学位論文

Shape evolution in neutron-rich midshell nuclei studied by γ-ray spectroscopy

（ガンマ線核分光による中性子過剰中重核の変形進化の研究）

平成 27 年 12 月博士（理学）申請

東京大学大学院理学系研究科
物理学専攻
横山　輪

Abstract

Deformed nuclei in the neutron-rich, midshell region $Z \sim 60$ and $N \sim 100$ have been studied using isomer and β-γ spectroscopy in order to investigate shape evolution. These neutron-rich isotopes were produced by in-flight fission of 345MeV/nucleon ^{238}U at the Radioactive Isotope Beam Factory, part of RIKEN Nishina Center. The beams were separated and identified using the BigRIPS separator. Separate experiments were performed with two different detector setups. The first experiment was an isomer search in the midshell region with 4 clover-type HP-Ge detectors. In the second experiment an active stopper, WAS3ABi, was introduced to enable β-γ spectroscopy in addition to isomer measurements, and an array of 12 EUROBALL cluster Ge detectors, EURICA, was employed to improve the γ-ray detection efficiency.

23 new isomers were identified in neutron-rich midshell nuclei with $59 \leq Z \leq 67$. $K^{\pi} = 4^{-}$ isomers were observed in the $N = 100$ isotones, while $K^{\pi} = 6^{-}$ isomers were identified in $N = 98$ isotones of Pm and Nd. Isomers with one-proton quasi-particle excitations were identified systematically in $100 \leq N \leq 104$ Tb isotopes. New excited states built on the ground-state band were identified in ^{157}Pm, ^{154}Ce and ^{150}Ba using β-γ spectroscopy. A candidate for a negative-parity state in an octupole band was observed at 697 keV in the most neutron-rich Ba isotope measured to date, ^{150}Ba.

Experimental signatures of large hexadecupole deformation in Nd isotopes were discovered using isomer spectroscopy. An increase in excitation energy of isomers in $N = 100$ Sm to Nd isotones and changes in isomer configurations in $N = 98$ Sm to Nd isotones cannot be explained solely by quadrupole deformation, although it can be described reasonably well by large hexadecupole deformation. There is also an indication of octupole collectivity in the very neutron-rich Ba isotope, ^{150}Ba. An RPA calculation successfully reproduces the negative-parity excitation with octupole collectivity as low as ~0.77 MeV. Our results highlight the importance of higher-order deformations, such as hexadecupole and octupole deformation, in the midshell nuclei around $Z \sim 60$ and $N \sim 100$. The systematics of level energies in ground-state rotational bands indicate a maximum in deformation at $Z = 60$ (Nd). This observation cannot be explained by any current theoretical calculations. $E(2^{+})$ and $E(4^{+})$ systematics display peaks at $N = 100$ along the $Z = 62$ (Sm) and 64 (Gd) isotopic chains. These characteristics were predicted by RMF and deformed-HF calculations that suggest a new neutron shell gap at N = 100; the present results support the calculations. However, similar peaks were not observed experimentally in Nd isotopes, in contrast to the theory. Such disagreements in the Nd isotopes may suggest that our understanding of higher-order deformation can be improved. The results related to the $N = 100$ shell gap presented here will provide important input for more precise calculations that aim to reproduce the r-process elemental abundance peak at $A \sim 160$.

Index

List of Figures

List of Tables

Chapter 1 Introduction

Atomic nuclei are finite quantum many-body systems consist of two different kinds of nucleons, protons and neutrons. The existence of two degrees of freedom, proton and neutron numbers, is one of the features adding variety to the nuclear phenomena. The quantum effect in a many-body system yields shell structure. The shell effect is one other key feature driving wide variety of phenomena in atomic nuclei.

The existence of closed shells in nuclei were first pointed out as "magic numbers" of protons and neutrons by M. G. Mayer in 1948 [1]. Experimental facts such as isotopic abundances, number of stable isotones or absorption cross section of a neutron indicated that nucleus get particularly stable with 20, 50 or 82 protons and 20, 50, 82 or 126 neutrons. The shell structures associated with the observed magic numbers were successfully explained by including spin-orbit interaction by Mayer [2] and Haxel, Jensen and Suess [3] independently in 1949. The nuclear shell structure also relates to a macroscopic characteristic, the shape of nucleus. The nuclei at closed shell have spherical shape as shown in Figure 1.1. As the number of particles in unfilled shell increased, nuclei break their symmetry spontaneously and get deformed even they are in the space with spherical symmetry. Study of the nuclear deformation of midshell nuclei is important to understand how the shell effect drives macroscopic shape of nuclei to have different shapes at different proton or neutron numbers.

Experimental investigations have been limited along the line of β stability due to experimental difficulties in production of unstable nuclei. The experimental first 2^+ energies of even-even nuclei are plotted over on the nuclear chart in Figure 1.1. Smaller energies of the first 2^+ level relate to more deformed nuclei. The experimental value around the line of β stability shows that deformation gets larger as going far from the magic numbers. However there is a lack of experimental data that covers the region around the center of midshell in which large deformation expected. The midshell region of $50 < Z < 82$ and $82 < N < 126$ looks one of the best case for the systematic study of shape evolution around the center of midshell, but it has not been well studied especially for neutron-rich side.

Recent studies of unstable nuclei have been revealed that there exists novel phenomena that have not been observed in stable nuclei. One attractive example is the disappearance of the magic numbers at $N = 8$ [4,5], $N = 20$ [6,7] and the appearance of new magic numbers $N = 16$ [8], $N = 34$ [9]. Such new phenomena in heavier unstable nuclei are still remained to be investigated. Theoretically, there is a prediction of the existence of new neutron shell gap at $N = 100$ by the infinite nuclear matter mass model (INM) and the relativistic mean field (RMF) theory [10]. Study of neutron-rich midshell nuclei is relevant to such new shell structure.

In addition to the quadrupole, the lowest-order deformation, onset of higher-order deformations such as octupole (β_3) or hexadecupole (β_4) deformations, are predicted in the neutron-rich midshell nuclei. Strong octupole correlation is expected in neutron-rich $Z \sim 56$

isotopes, and hexadecupole deformation is expected in neutron-rich $Z \sim 60$ isotopes (See Section1.4). Octupole and hexadecupole moments have been measured in stable nuclei (β_3 in ^{138}Ba [11] and β_4 in ^{152}Sm [12]) and the appearance of higher-order deformations itself is known. However, the number of experimental studies on higher-order deformations so far, is very limited and it is not well known how such deformations appear in nuclei and how these affect to the single particle levels. Recent study on *K*-isomers [13] indicates the presence of higher-order deformations in a neutron-rich midshell nucleus, ^{166}Gd. They discuss such deformations change the excitation energy of the isomer significantly (See Section1.3). It is thus, quite important study higher-order deformations in the neutron-rich midshell nuclei with $Z \sim 60$.

Study of neutron-rich nuclei far from the line of β stability is also important from the astrophysical point of view. Roughly half of nuclei heavier than iron in the solar system are supposed to be synthesized through the rapid-neutron-capture (*r*) process. How the *r*-process proceeded and produced the elements in the universe are not fully understood. The distribution of *r*-process abundance has a peak at $A \sim 160$ that is smaller than the peaks due to the shell closure along the path (See Section1.5). Origin of the peak at $A \sim 160$ is not understood well but it should relevant to the nuclides along the *r*-process path, $Z \sim 60$, $N \sim 100$.

This study focuses on the neutron-rich midshell nuclei with $Z \sim 60$, $N \sim 100$ aiming at understanding how nuclear shape, including higher-order, octupole and hexadecupole, deformations evolves with the increase of proton and neutron numbers. It is expected that the study of the $A \sim 160$ midshell nuclei will also provide important input to the calculations of *r*-process abundance.

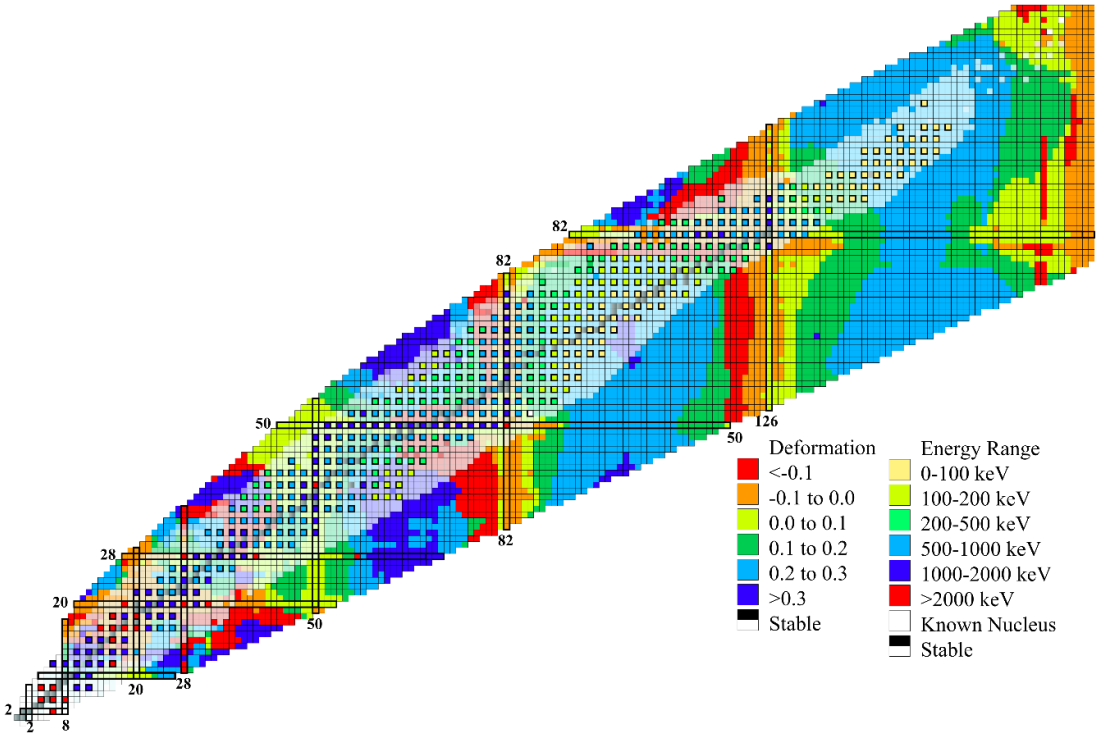

Figure 1.1 Nuclear chart of the experimental first 2^+ energies of even-even nuclei plotted over the theoretical prediction of quadrupole deformation by Möller *et al* [14].

1.1 Nuclear deformation

The first experimental evidence of non-spherical nuclear shape was the observation of a quadrupole component in a hyper-fine structure of optical spectra in 1930s [15]. The electric quadrupole moment of some nuclei were one order larger than that could be attributed to a single proton. In the beginning of 1950s, M. Goldhaber and A. W. Sunyar realized that some E2-transition rates are much larger than that could be explained by a single particle transition, especially in low-lying 2^+ (with spin 2 and even parity) states of even-even rare-earth nuclei [16]. Such experimental facts suggested that nuclei can be deformed and have quadrupole moments as a whole. An interpretation of collective rotation to the low energy spectra of even-even nuclei was first given by A. Bohr and B. R. Mottelson in 1953 [17]. They pointed out that those excitations were part of a level sequence with angular momenta $I = 0,2,4,...$ and energies proportional to $I(I+1)$, which was interpret as a rotational motion of the deformed nucleus. After their indication, such rotational band structures were observed in the rare-earth nuclei between the shells $Z = 50$ and 82, $N = 82$ and 126, and heavy nuclei between the shells $Z = 82$ and 126, $N = 126$ and 184. Since then, many theoretical works with different approach have been performed in order to reveal the mechanism of deformation and to make fair predictions.

Shapes of atomic nuclei are often expressed by multipole expansion with spherical harmonics, $Y_{\lambda\mu}$, as equation (1.1).

$$R(\theta,\phi) = R_0 \sum_{\lambda,\mu=0}^{\lambda=\infty,\mu=\lambda} \alpha_{\lambda\mu} Y_{\lambda\mu}(\theta,\phi) \tag{1.1}$$

Since the terms with $\lambda = 0$ and 1 can only express spherical shape, quadrupole ($\lambda = 2$) is the lowest order of deformation. Higher-order terms with $\lambda = 3$ and $\lambda = 4$ are called octupole and hexadecupole, respectively.

As an idea of the surface term in the nuclear mass formula by Weizsäcker [18] and Bethe and Bacher [19] in 1930s, which represents the loss of binding energy by the particles in the surface layer due to fewer neighbors there, nuclei with smaller surface area have lower energies. From such macroscopic point of view, spherical shape is expected to be preferred the most. This is appeared as the shapes of closed shell nuclei. However, shell effect of atomic nuclei often drives the shape deformed. In quadrupole deformed nuclei, single particle orbitals are degenerated and orbitals along longer axis have lower energy while those along shorter axis have higher energy. In midshell nuclei whose outermost shell is filled by half, total energy can become lower by having deformed shape and filling only the orbitals along longer axis, than having spherical shape. This is a very naive explanation of nuclear deformation driven by the shell effect. Some of theoretical calculations of the nuclear deformation will be shown in the following paragraph.

Figure 1.1 shows nuclear ground-state quadrupole deformations obtained from macroscopic-microscopic calculation (finite range droplet model, FRDM) by Möller *et al* [14]. The ground-state deformations were also predicted by the relativistic mean field (RMF) theory by Lalazissis *et al* [20], Hartree-Fock-Боголю́бов method by S. Hilaire *et al* [1], Hartree-Fock-BCS+MSk7

by S. Goriely *et al.* [21] and so on. The results of those calculations are not totally consistent especially in nuclei far from the line of β stability. Comparison of the calculations of nuclear ground-state deformations are shown in Figure 1.2, around neutron-rich midshell nuclei with $Z \sim 60$. In the midshell nuclei with $Z = 55$ to 66, the deformation suddenly appears at $N = 90$ as shown by the systematics of excitation energies of the first 2^+ states of even-even nuclei [22]. From the FRDM, the deformation is expected to develop towards $Z = 64$, $N = 102$, while RMF predicts deformation maximum at $Z = 66$, $N = 102$ and HFBCS predicts that at $Z = 64$, $N = 100$. It is not well understood how the quadrupole deformation develops and at where the deformation get maximum. Measurements of the excited states in the midshell nuclei will provide us information how nuclear deformation evolves in neutron-rich nuclei.

FDRM

Z \ N	84	86	88	90	92	94	96	98	100	102	104
70	0.09	0.142	0.171	0.195	0.219	0.246	0.267	0.285	0.299	0.304	0.301
68	0.093	0.147	0.177	0.203	0.231	0.255	0.277	0.298	0.312	0.317	0.313
66	−0.09	0.145	0.179	0.211	0.247	0.273	0.292	0.306	0.316	0.322	0.318
64	−0.08	0.135	0.178	0.228	0.266	0.282	0.296	0.308	0.318	0.323	0.32
62	−0.01	0.112	0.176	0.235	0.265	0.279	0.292	0.305	0.315	0.321	0.317
60	−0	−0.07	0.16	0.221	0.263	0.277	0.289	0.302	0.313	0.319	0.315
58	−0	−0.03	0.146	0.183	0.246	0.263	0.276	0.29	0.303	0.308	0.299
56	−0.01	−0.05	0.144	0.172	0.191	0.217	0.252	0.269	0.283	0.286	0.276

RMF

Z \ N	84	86	88	90	92	94	96	98	100	102	104
70	−0.01	0.125	0.161	0.208	0.225	0.264	0.274	0.284	0.295	0.296	0.287
68	−0.02	0.143	0.189	0.216	0.253	0.272	0.273	0.283	0.294	0.296	0.296
66	0	0.153	0.207	0.235	0.262	0.272	0.281	0.292	0.293	0.304	0.295
64	0	0.161	0.207	0.243	0.271	0.271	0.28	0.291	0.301	0.303	0.294
62	0	0.161	0.206	0.243	0.27	0.279	0.279	0.29	0.3	0.302	0.294
60	0	0.161	0.206	0.243	0.262	0.27	0.279	0.279	0.29	0.3	0.293
58	0	0.144	0.182	0.216	0.252	0.261	0.27	0.27	0.271	0.282	0.274
56	0	0.135	0.164	0.199	0.236	0.243	0.261	0.261	0.271	0.274	0.275

HFBCS+MSk7

Z \ N	84	86	88	90	92	94	96	98	100	102	104
70	0	0.09	0.19	0.23	0.27	0.27	0.28	0.28	0.28	0.32	0.31
68	0	0	0	0.23	0.27	0.26	0.29	0.32	0.3	0.31	0.3
66	0	0.16	0.23	0.27	0.28	0.29	0.3	0.32	0.33	0.29	0.3
64	0	0.13	0.23	0.27	0.28	0.3	0.28	0.3	0.34	0.3	0.29
62	0	0.17	0.19	0.26	0.28	0.29	0.3	0.28	0.3	0.29	0.31
60	0	0.13	0.19	0.25	0.27	0.29	0.3	0.3	0.3	0.32	0.33
58	0	0.13	0.16	0.22	0.25	0.27	0.29	0.29	0.3	0.32	0.31
56	0	0.11	0.16	0.2	0.22	0.25	0.27	0.29	0.28	0.28	0.29

Figure 1.2 Comparison of different theoretical calculations of ground-state deformation, β_2. The values were taken from [14] (FRDM), [20] (RMF) and [21] (HFBCS+MSk7).

1.2 Nilsson model and *K* isomers

Quadrupole deformation, is the most basic form of deformation. Quadrupole deformed shape with positive quadrupole moment, whose symmetry axis is the long axis, is called as prolate shape and the shape with negative moment, whose symmetry axis is the short axis, is called oblate shape. Single particle orbitals in an axially symmetric deformed potential were first given by Nilsson [23] in 1955. In the nucleus with axial symmetry, projections of quantum numbers on to the symmetry axis become good quantum numbers. These are called asymptotic quantum numbers (details are described in Appendix A). In the Nilsson model, single particle orbitals

are described by asymptotic quantum numbers. In this thesis the representation, $\Omega[Nn_z\Lambda]$ is used where Λ is z-component of orbital angular momenta, Ω is the composition of Λ and spin angular momenta, and N and n_z are total and z-component of the number of nodes. In a quadrupole deformed nucleus, orbitals with different asymptotic numbers are degenerated from those in a spherical nucleus. The plot of single particle energies of orbitals as a function of quadrupole deformation is called Nilsson diagram. Nilsson diagrams for $56 < Z < 82$ and $82 < N < 126$ are shown in Figure A.2 and Figure A.3 of Appendix A.

When the nuclear shape has axial symmetry, there are selection rules for single-particle transitions by the asymptotic quantum numbers. The *K* quantum number, which is the projection of total angular momentum on to the symmetry axis, provides strong selection to single-particle transitions by ΔK. If there is a state that has no available decay path with small ΔK, the decay will be hindered and may become an isomer (an excited state with longer half-life than usual). Such isomers are called as "*K* isomers". The estimation of single-particle transition probability and the empirical hindrance factor of large ΔK transition are described in Appendix B.

K isomers are very specific to the nucleus with large quadrupole deformation. Figure 1.3 (a) shows a schematic diagram of *K* quantum number. States with large *K* value have the angular momentum aligned to the symmetry axis that means the single particle motion is on the plane perpendicular to the symmetry axis. In a prolate deformed nucleus, the plane is on the direction of short axis. Therefore, the energy of large *K* orbital is expected to get higher in more prolate-deformed nucleus. This is shown in the schematic Nilsson diagram in Figure 1.3 (b). As shown in the figure, orbitals with large and small *K* quantum number from different orbitals in spherical basis cross each other as the deformation increased. Deformed nucleus with its Fermi surface of neutrons or protons around such crossing will have excitation with large ΔK at low excitation energy. Such excitation generates a *K* isomer.

The ground state of an even-even nucleus can be regarded as a condensate of pair motion. Excitations involved with adding or removing particles, or creating particle or hole, to the condensate vacuum requires pairing correction and called as quasiparticle excitations. The quasiparticle energy, E_{qp}, is written as,

$$E_{qp} = \sqrt{(\varepsilon_{sp} - \lambda)^2 + \Delta^2}, \tag{1.2}$$

where ε_{sp} is single-particle energy, λ is energy of Fermi surface and Δ is pairing energy. In the case of deformed nucleus with large mass number ($A > 100$), single-particle levels are so close to each other that the pairing interaction is not negligible, and quasiparticle picture is more suitable. (See Figure 1.4.) Excitation of an even-even nucleus with a broken pair can be regarded as two quasiparticle excitation. In this thesis, *K* isomers with a particle or a hole at a large *K* orbital $\Omega[Nn_z\Lambda]$ and a small *K* orbital $\Omega'[N'n_z'\Lambda']$ is denoted as two quasiparticle (2-qp) excitation with $\Omega[Nn_z\Lambda] \otimes \Omega'[N'n_z'\Lambda']$ configuration.

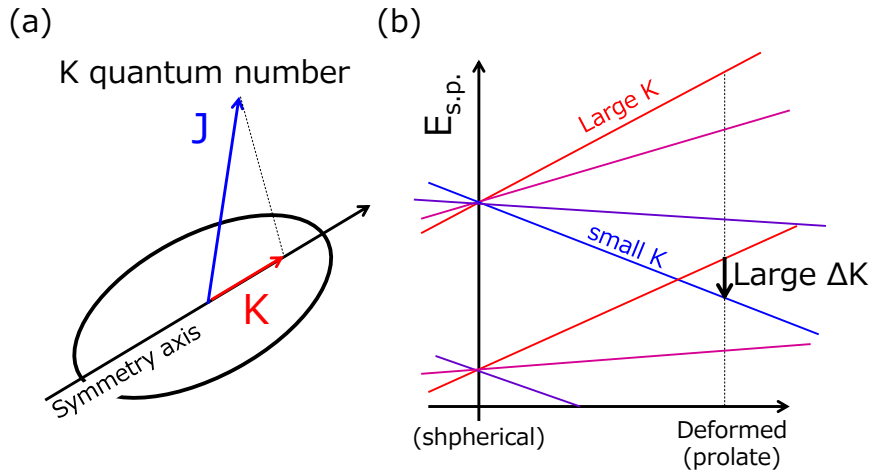

Figure 1.3 Schematic diagrams of K quantum number (a) and K isomer appears in deformed nuclei (b).

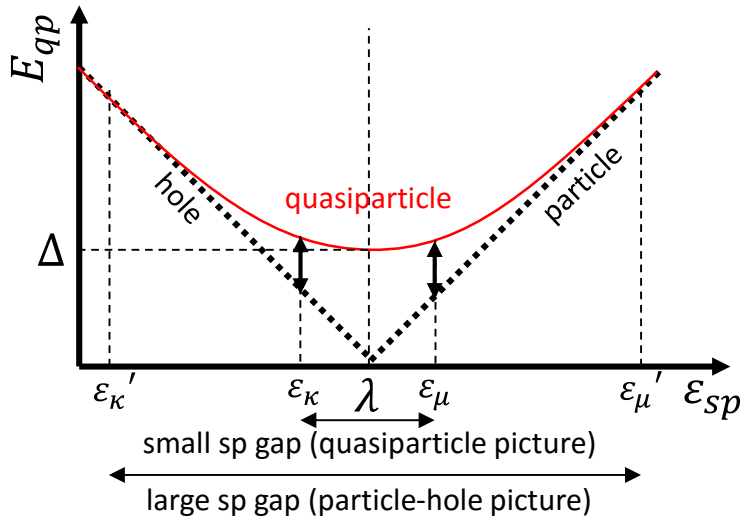

Figure 1.4 Schematic plot of quasiparticle energy as a function of single-particle energy. When single-particle levels are close, quasiparticle treatment is required.

1.3 K isomers in neutron-rich $Z \sim 60$ midshell nuclei

K isomers are known in midshell nuclei around $Z \sim 60$ to 70. In Hf isotopes, many long-lived K isomers are known [24]. The $K^\pi = 16^+$ isomer with the half-life of 31 years is one of the famous case of such K isomers. It has the configuration of $\nu 9/2[624] \otimes \nu 7/2[514] \otimes \pi 9/2[514] \otimes \pi 7/2[404]$ that has $\Delta K = 8$ hindrance of both neutron and proton excitation.

Neutron-rich $Z \sim 60$ nuclei have also attracted much attention due to their large prolate deformation and the existence of many quasi-particle K-isomers with micro second half-lives. γ-ray spectroscopy of neutron-rich $Z \sim 60$ isotopes has been carried out by using thermal neutron induced fission of heavy nuclei [25]. The work revealed that there exists many K isomers in $N = 60$ and 62 (Nd and Sm) isotopes up to $N = 98$. The existence of such K

isomers indicates that those nuclei have a shape with stable axial symmetry so that the transitions with large ΔK are hindered to become isomers. Similar isomers are expected in more neutron-rich isotopes. In stable $N = 100$ nuclei, ^{168}Er and ^{170}Yb, $K^{\pi} = 4^{-}$ isomers are known and considered to be neutron two quasi-particle excitation with the configuration of $\nu 7/2[633] \otimes \nu 1/2[521]$ [26,27]. Isomers produced by this quasi-particle excitation may also appear in neutron-rich $N = 100$ isotones. Figure 1.5 shows the systematics of the excited states of the ground-state bands and isomeric states of $N = 100$ isotones. The 2^{+} and 4^{+} energies are get lower as Z decreases. This fact indicates the deformation of the ground state is larger in nuclei with less atomic number. The excitation energies of isomeric states with $K^{\pi} = 4^{-}$ also get lower in less Z isotones. This may show that the neutron single-particle orbitals 7/2[633] and 1/2[521] get closer to each other, which can be explained by the development of quadrupole deformation. Those systematics make us expecting that the deformation is increasing from $Z = 70$ to 64. The theoretical expectations shown in Figure 1.2 predict deformation peak at $Z = 64$. Further experimental investigation of excitation energies for less Z isotones is required to see if the $Z = 64$ is deformation maximum and for further understanding of the development of deformation and single-particle levels in neutron-rich midshell nuclei.

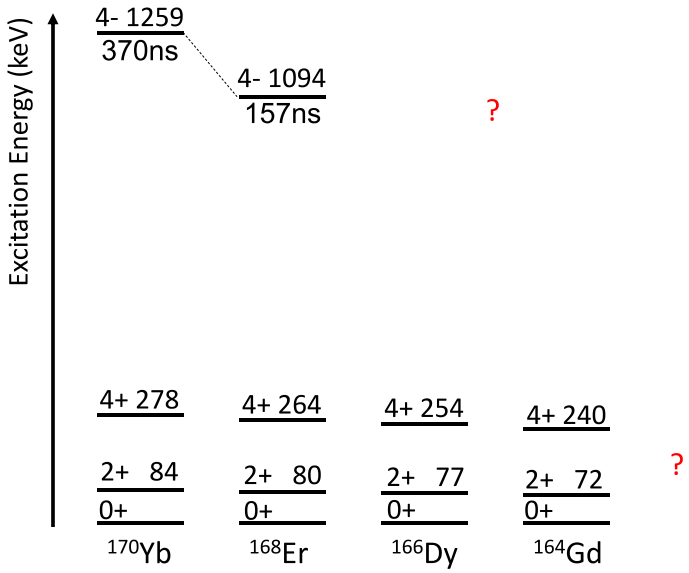

Figure 1.5 Systematics of the excitation energies of ground-band 4^{+} and 2^{+} states and $K^{\pi} = 4^{-}$ isomers in $N = 100$ isotones.

1.4 Higher-order deformations

One of the unique features of the nuclear shells is that they have intruder orbitals from larger N number by large spin-orbit interaction. Such intruder orbitals with large N quantum number are essential for large higher-order correlations to make higher-order deformed shape energetically favored. Recently, it is getting to be known that higher-order deformations such as octupole or hexadecupole deformation appear at nuclei in certain Z or N regions.

Although, in general, quadrupole deformation is sufficient to explain primary phenomena in nuclei, high-order deformations can cause significant change in the single particle structures. In the neutron-rich midshell nuclei, there are both regions expected to have large octupole deformation (around $Z = 56,\ N = 88$) and hexadecupole deformation (around $Z = 60$). Study of those nuclei is quite important to understand the mechanism of higher-order deformation and its influence to the nuclear level structures.

Octupole deformation is often illustrated as pear-like shape shown in the left-top of the Figure 1.6. It has been a long standing question whether there exist nuclei with this parity-violating collectivity as a stable state. Study of octupole deformation is also attracted attention for the measurement of atomic electric-dipole moments (EDMs). The existence of a finite permanent EDM violates the time reversal or equivalently charge-parity symmetry. All the experimental approach so far results in zero and some measurements of the atomic EDMs gives the tightest limit ([28] for example). Such experimental limits give constrains on proposed extensions beyond the standard model. Nucleus with static octupole deformation is expected to be much more sensitive to the atomic EDM measurement as discussed in [29].

The interaction between orbitals with $\Delta J = \Delta I = 3$ is responsible for strong octupole correlations and thus the nuclei with such orbits close to each other around the Fermi surface are expected to have large octupole correlation. It corresponds to the Z or $N =$ 34, 56, 88 and 134. A recent study on $Z \sim 88,\ N \sim 134$ region [30] revealed that there exists static octupole deformation in ^{224}Ra and ^{220}Rn. The neutron-rich Ba isotopes ($Z = 56,\ N \sim 88$) are also expected to have large octupole correlation and good candidates for octupole deformation. Orbitals with $\Delta J = \Delta I = 3$ in $Z \sim 56$ ($1h_{11/2}$-$2d_{5/2}$) and $N \sim 88$ ($1i_{13/2}$-$2f_{7/2}$) are shown with red and blue curves in Figure 1.7. Such orbitals are getting close with each other and the gaps at $Z = 56$ and $N = 88$ act as magic numbers for stable octupole deformation. The even-even Ba isotopes from $A = 140$ to 148 have been studied by spontaneous fission of ^{248}Cm [31] and negative parity bands which assumed to have some octupole collectivity were found. Observation of enhanced E1 transition rates of γ decays are one of the indication of such octupole correlation. Although the intuition that ^{144}Ba ($Z = 56,\ N = 88$) should show the largest E1 rates in the neighboring nuclides, Ref. [31] revealed that ^{148}Ba seems to have large E1 rates as much as those of ^{144}Ba, while ^{146}Ba has much smaller rates. Figure 1.8 shows the systematics of experimental dipole moments obtained from E1/E2 rate in [31] and a calculation by microscopic-macroscopic method [32]. The theoretical dipole moments are shown with macroscopic contribution and the shell correction by reflection asymmetric Woods-Saxon model separately. The calculation shows qualitative agreement with experimental dipole moments, which indicates that the shell effect is responsible for the octupole deformation. Quantitatively, however, the calculation in ^{148}Ba underestimate the dipole moment and it is difficult to say how it will be in ^{150}Ba. Theoretical calculations on octupole correlation so far have large uncertainty and differ with each other. For example, a calculation by microscopic-macroscopic method [32,33] predicts large β_3 value in ^{150}Ba while a Hartree-Fock calculation [34] argues that there is no state with octupole moment in ^{150}Ba. Therefore, experimental investigations on the further neutron-rich Ba isotopes is required to resolve the problem.

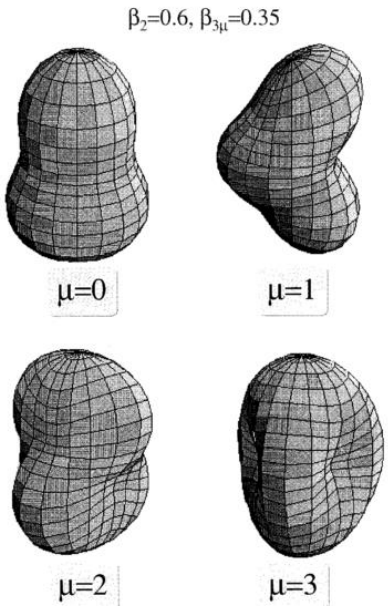

Figure 1.6 Illustration of the shapes of octupole deformations (taken from [33])

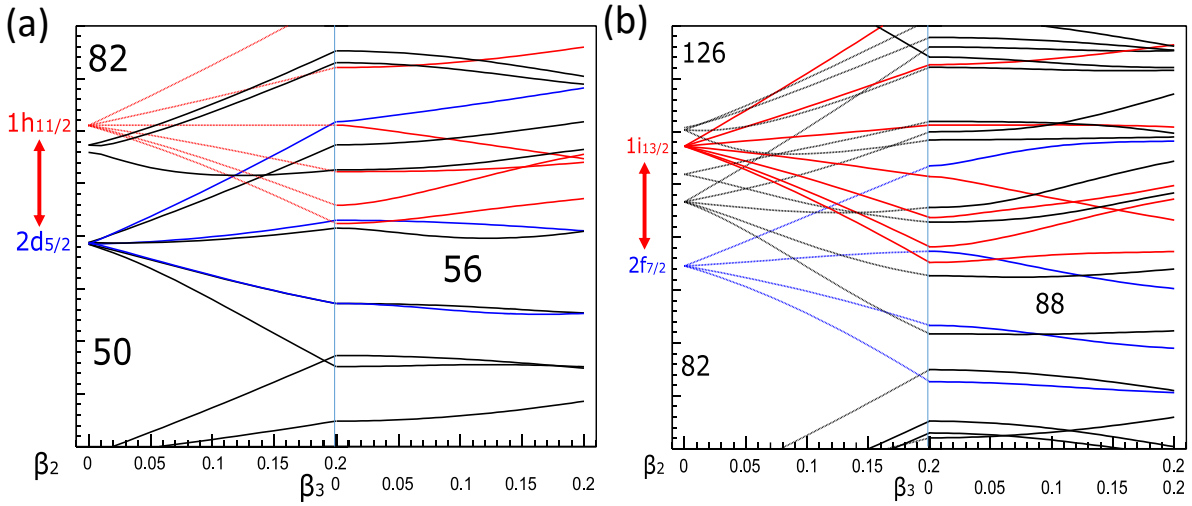

Figure 1.7 Proton single-particle levels (a) and neutron single-particle levels in a Woods-Saxon potential as a function of quadrupole and octupole deformation calculated by [35]

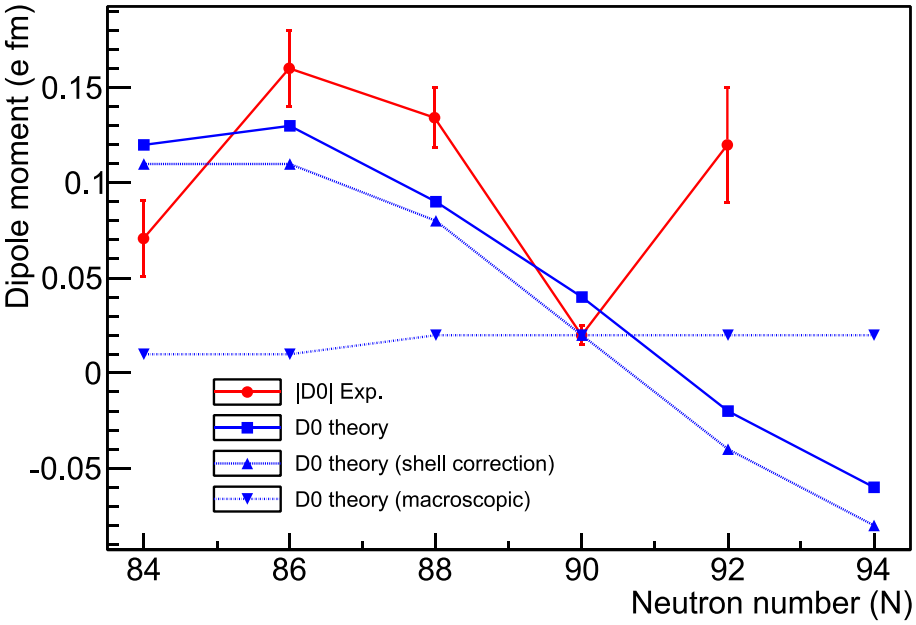

Figure 1.8 Experimental and theoretical values of intrinsic electric dipole moment of Ba isotopes. Note that experimental E1/E2 ratio is not sensitive to the sign of the dipole moment, therefore, the experimental plot shows the absolute values of the dipole moment.

Hexadecupole deformation (β_4) is even one order higher than the octupole deformation (β_3). However, it is getting to be known that this deformation plays important role in some rare-earth nuclei. Figure 1.9 shows the illustration of hexadecupole deformation with positive and negative hexadecupole moment on quadrupole (prolate) deformation. Nuclear hexadecupole deformation was first measured by scattering of α particles at energies well above the Coulomb barrier for stable rare-earth nuclei from Sm ($Z = 62$) to Hf ($Z = 72$) [36]. Since then, many experimental investigation have been performed on the rare-earth nuclei. Coulomb excitation method is one of the most direct and reliable technique to obtain electric multipole matrix element of nuclei. In ^{152}Sm, hexadecupole deformation was obtained from E4 transition probability by a Coulomb-excitation experiment. It became a strong convincing evidence for the existence of hexadecupole deformation in nuclei. So far, such measurement is limited to the stable nuclei due to the low probability of E4 transition. In stable rare-earth nuclei, Nd ($Z = 60$) have the largest hexadecupole moment $\beta_4 \sim 0.07$ [37]. Reference [14] also provide calculated values on β_4. This calculation reproduces the trend of hexadecupole deformation of stable rare-earth nuclei that Nd has the largest positive β_4 deformation and it gets smaller as Z increased. The calculation predicts large hexadecupole deformation also in neutron-rich isotopes. However, theoretical β_4 values are differ with each other as shown in Figure 1.10 and no experimental measurement of higher-order deformation is available for unstable nuclei. Recent measurement of *K*-isomers in ^{166}Gd [13] shows an indication of large β_4 and β_6 deformation. According to their potential energy surface calculation, significantly non zero β_4 and β_6 are required to reproduce the observed energy of the isomeric state, which is assumed to be neutron 2 quasi-particle excitation with the configuration of $\nu 5/2[512] \otimes \nu 7/2[633]$. Systematic study of the excited states may give us a hint on such effect of hexadecupole

deformation.

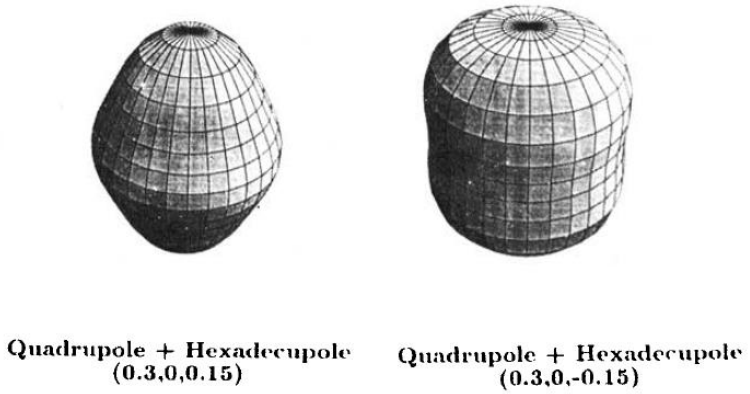

Figure 1.9 Illustration of the shapes of hexadecupole deformations on quadrupole deformed bases. (taken from [38])

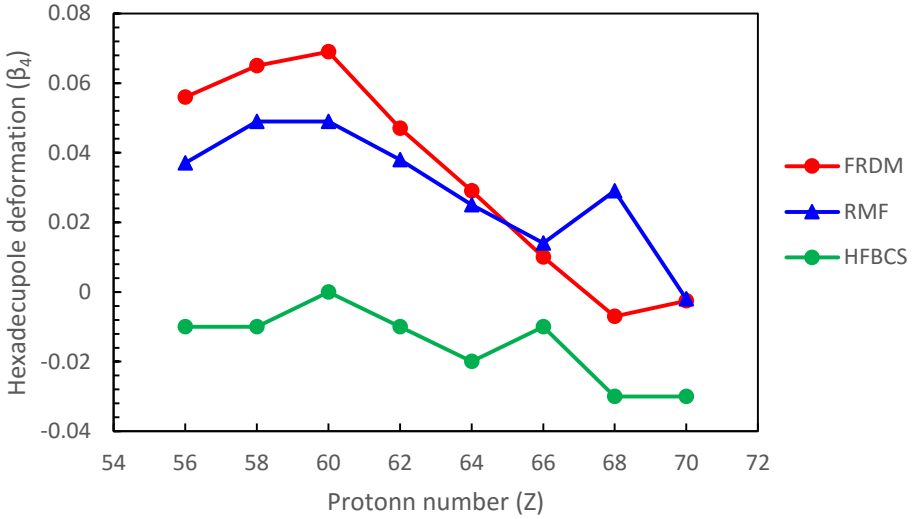

Figure 1.10 Comparison of theoretical β_4 values for $N = 100$ isotones. [14,20,21]

1.5 Deformed shell closure and *r*-process abundance

There are a great variety of elements and their isotopes exist on the earth. It has been a long standing question of astrophysics that how the almost 300 nuclides in nature produced in which kind of stellar sites in the universe. At the beginning of the universe just after the "big bang", hydrogen, the simplest stable nucleus made of a single proton, was almost only the elements. All the rest of $\sim$300 nuclides are assumed to be produced in some different stellar sites. Burning processes inside stars can produce elements with $Z \leq 26$ (Fe) by fusion reactions. However, more catastrophic phase of stars is expected to be responsible for the synthesis of heavier elements since Fe has the largest binding energy per nucleon and it becomes difficult to produce heavier elements by fusion reactions. The rapid-neutron-capture (*r*) process is one

of the main process responsible for the synthesis of nuclei with $Z > 26$ up to uranium. This is the process of neutron capture on a very short time-scale, ~ 0.01 to 10 sec, and the captures occur at a rapid rate compared to the β decays. [39]

Figure 1.11 shows the decomposition of the solar abundances of nuclei with mass number A into final mass distributions of three processes, *s*-, *r*- and *p*-process, that are assumed to be responsible for the synthesis of the elements heavier than iron. The *r*-process abundance distribution has large peaks at $A \sim 80, 130$ and 195. These have been understood as the effect of neutron shell closure. Since the nuclei with shell closure have long beta-decay lifetimes and capture neutrons reluctantly, *r*-process flow passes through neutron-closed-shell nuclei acts like a bottleneck and abundances build up on it. This mechanism has been known for many years [39]. There is a smaller but still distinct peak at $A \sim 160$, rare-earth nuclei. In contrast to the large peaks, the origin of this peak has not been understood clearly. R. Surman *et al.* argues that this is due to the deformation maximum [40]. Existence of a deformation maximum can acts like a neutron closed shell if the next isotope is less stable for the deformation and the binding energy drops with the addition of a neutron. Theoretical models predict deformation maximum at around $N = 100$. Macroscopic-microscopic calculation [14] and RMF calculation [20] place the maximum at $N = 102$. Hartree-Fock calculations with different Skyrme parametrization were performed in [41]. Calculations with SIII and SkM* predict the maximum deformation at $N = 102$ while Sk14 and Sly4 results in β_2 maximum at $N = 100$. Exact placement of the deformation maximum by experimental study is necessary to understand the sub peak of solar abundances at $A \sim 160$.

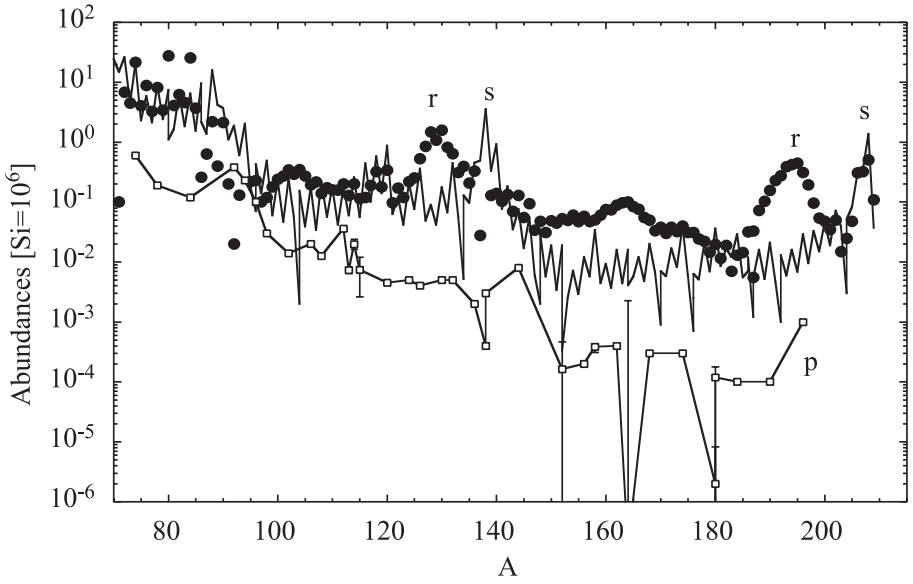

Figure 1.11 Decomposition of the solar abundances into *s*-, *r*- and *p*-process (taken from [42]). The dots shows the abundance of *r*-process.

Recent calculations of *r*-process abundance [43,44] reproduces the peak at $A \sim 160$ as a sum of different models, of neutron star mergers and core-collapse supernovae. However, the theoretical calculations still have large uncertainties and the origin of $A \sim 160$ nuclei is different in theories. Ref. [44] argues that most $A \sim 160$ nuclei are from fissions of the nuclei

at the terminal of *r*-process, while Ref. [43] says only ~10% of the yields of $A \sim 160$ nuclei are from fissions of such nuclei. Experimental nuclear data are required for better understanding.

As experimental studies getting available to the neutron-rich isotopes, it is getting to be recognized that the first 2^+ energies are slightly larger at $N = 100$ than other isotopes in Gd [45]. Calculations in infinite nuclear matter (INM) mass model and RMF theory showed new neutron magic number, $N = 100$ in $Z \sim 60$ nuclei [10]. They also calculated the first 2^+ energies, $E(2_1^+)$, of Sm isotopes and it showed a peak at $N = 100$ [46]. Existence of such shell gap lying on the β-decay path of $A \sim 160$ *r*-process nuclei may have a great importance in the explanation of the peak at $A \sim 160$ in *r*-process abundances. Since the calculations [10] suggest larger shell gap in $Z \leq 60$ nuclei, experimental investigation of $N = 100$ isotones with smaller proton numbers is required. Existence of a shell gap is often identified as the discontinuity of two neutron or proton separation energies. Figure 1.12 shows the two neutron separation energies of $Z \sim 60$ isotopes deduced from the masses of nuclei. $N = 82$ shell gap is apparent as a sudden decrease of the separation energies. According to the latest atomic mass evaluation, AME2012 [47], the masses of such neutron-rich nuclei are not known. Measurement of the excited states of those nuclei will help understanding the new shell gap since the excitation energies of the first 2^+ states may reflect shell gap.

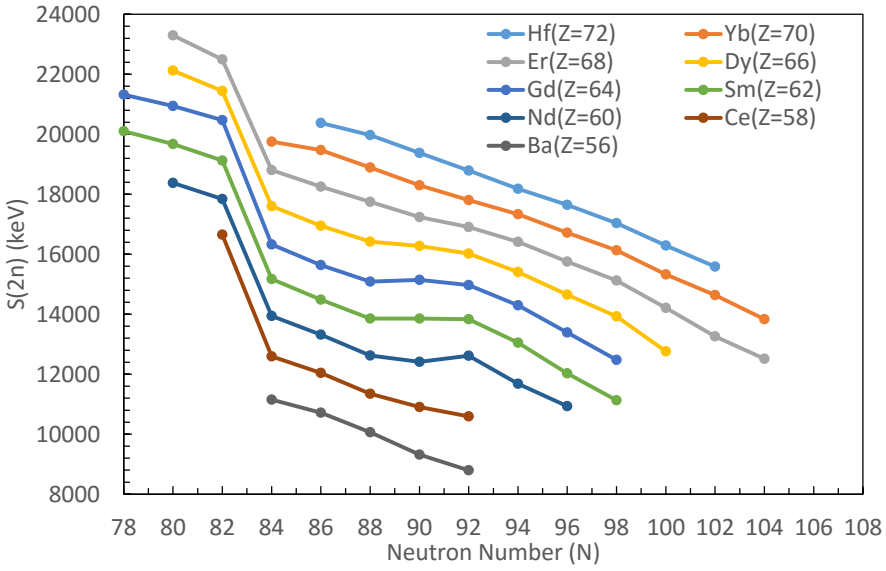

Figure 1.12 Two neutron separation energies $(S(2n))$ of $56 < Z < 72$ isotopes [47].

1.6 Thesis objectives

This thesis reports a systematic study of excited states of neutron-rich midshell nuclei with $Z \sim 60$ and $N \sim 100$, aiming at further understanding of nuclear deformation and shape evolution in unstable nuclei including higher-order deformations. Measurement of the excited states in this work includes the different approaches as follows.

- Systematic measurement of E_1^{2+} and E_1^{4+} values in order to obtain the evolution of quadrupole deformation in more neutron-rich nuclei ever known.

- Investigation of quasi-particle excitations which are sensitive to the single-particle orbitals of deformed nuclei, to obtain information on the shell structure of midshell nuclei, especially the shell gap at $N = 100$.
- Search for excited states specific to higher-order deformation especially for the octupole negative-parity state in Ba isotopes for the better understanding of the mechanism and the effect of higher-order deformations in nuclei.

In order to measure the excited states of neutron-rich midshell nuclei, two different method, β-γ spectroscopy and isomer spectroscopy were employed. For the production of neutron-rich unstable nuclei, in-flight fission of ^{238}U beam at 345MeV/nucleon was employed. This thesis based on two experiments. One focused only on isomer spectroscopy of neutron-rich nuclei with $Z = 60$ to 70 (MS-11 exp.). The other was a simultaneous measurement of both isomer and β-γ spectroscopy performed on neutron-rich $Z = 56$ to 61 nuclei (RIBF-86 exp.).

The author joined entire preparation and experiment of both experiments, and was responsible for the analysis of γ-ray spectroscopy. The contributions of the author are listed as follows.

- Preparation of the setup of clover-type Ge γ-ray detectors at F12 in MS-11 experiment. This includes construction of the signal shaping and data acquisition circuit; setup and monitoring for the liquid nitrogen filling system to automatically fill liquid nitrogen to the Ge detectors; taking calibration data for energy, timing, efficiency of each detector; monitoring the energy resolution and reduction of the noises on the signals.
- Online analysis of the γ-ray detectors in MS-11 experiment, which includes; writing program codes for the online analysis of Ge detectors to see the isomer spectra; monitoring the soundness of detectors during the beam time; online search for new isomers.
- Offline analysis of the isomers in order to obtain energies, half-lives and relative intensities of new isomeric γ rays in MS-11 experiment, which includes; energy, timing and gain shift calibrations of all γ ray data; Monte Carlo simulation using Geant4 for the efficiency curve of γ-ray detection; consistency check of the result of the analysis on known isomers with the known values.
- Design of the secondary beam production with BigRIPS group for RIBF-86 experiment, which includes; performing LISE++ calculations for the estimation of production rates in order to optimize beam settings for the nuclei of interest; deciding if and how we divide runs into different beam settings to optimize the statistics of isomer and β-γ data; participating in the beam tuning of BigRIPS at the beginning of the experiment.
- Online analysis in RIBF-86 experiment, which includes; online beam reconstruction and PID analysis; merging data from three different DAQ (for the active stopper, γ-ray detectors and beam line detectors) by the timestamp information; plotting isomer and β-γ spectra; searching for new excited states.
- Offline analysis of the entire data of RIBF-86 experiment, which includes; analysis of the beam line detectors and beam reconstruction for obtaining better particle identification than that performed online; energy, timing and efficiency calibrations of γ-ray detectors and active stopper detectors; isomer analysis for

obtaining energies, half-lives and relative intensities of new isomeric γ rays; analysis of beam implantation position and β-ray emission in at the active stopper and merging events with beam and β correlation for β-γ analysis.

- Investigation and discussion of the shape evolution of neutron-rich midshell nuclei from the combined results of the two experiments. There was no extensive discussion on the shape evolution of such neutron-rich midshell nuclei combining the effect of higher-order deformations and the systematics of quadrupole deformation. This study may also provide some indication on the $N = 100$ shell gap in deformed nucleus.

Chapter 2 Experiment

This study aimed at measuring the excited states of highly neutron-rich $Z \sim 60$ nuclei systematically in order to investigate the nuclear shape evolution at the midshell region. In this work, the neutron-rich nuclei were produced at RIBF, RIKEN Nishina Center by using in-flight fission of high-intensity ^{238}U beam. Fission fragments were separated and identified by an in-flight separator, BigRIPS, and transported to the experimental sites for γ-ray spectroscopy. First, the primary ^{238}U beam with ∼0.5 pnA was achieved and measurement for new isomer search was performed (MS-11 exp.). In this experiment, the secondary beam was implanted into a stack of 14 Si detectors placed at F12 focal plane. Delayed γ rays from the implanted RIs were measured by 4 clover-type Ge detectors placed around the Si stack detectors. Then, the intensity of the primary beam was upgraded to more than 5 pnA and measurement of further neutron-rich nuclei was performed by isomer and β-γ spectroscopy using the high-efficiency γ-ray detector array, EURICA (EUROBALL-RIKEN Cluster Array) at F11 focal plane (RIBF-86 exp.). In RIBF-86 experiment, an active stopper, WAS3ABi (Wide-range Active Silicon Strip Stopper Array for β and ion detection) was introduced in order to enable β-γ measurement with event-by-event particle identification of the secondary beam with ∼100 Hz of total implantation rate.

This chapter first describes the principal and then experimental setups of production of neutron-rich RI beam using in-flight fission of ^{238}U at RIBF in Section 2.1, which is basically common for the both experiments. Then, the method of isomer and β-γ spectroscopy using EURICA system in RIBF-86 are explained. The detector setups of the EURICA system is explained in Section 2.2, and the data acquisition of the system is shown in Section 2.3. The last section of this chapter, Section 2.4, describes the experimental details which are specific to the experiment, MS-11.

2.1 Production and identification of neutron-rich nuclei

2.1.1 Production of unstable nuclei

Production of unstable nuclei is based on adding or removing nucleons from stable nuclei using various nuclear reactions. Nuclear fission, fusion and fragmentation are often used in order to produce unstable nuclei far from the line of β stability. This subsection discusses on various RI production methods and compare which is suitable for the production of neutron-rich midshell nuclei $A \sim 160$. Basically, fusion reaction of stable nuclei is suitable for production of proton-rich or neutron-deficient nuclei, while fission or fragmentation is more suitable for production of neutron-rich nuclei. This is because the ratio of neutrons in stable

nuclei gets larger in heavier mass nuclei due to the Coulomb force between protons. Since the stable nuclei with lighter mass have less neutron fraction than those with heavier mass, fusion products tend to have less neutrons than the stable isotopes of compound element, and fission products tend to have more neutrons. When producing neutron-rich nuclei using fission or fragmentation reaction, a nuclide with higher mass is preferable as the primary nuclide. This is because the higher mass nuclei are more neutron-rich, and these reactions only produce nuclei with smaller mass than the original mass. There are some methods that produces neutron-rich nuclei using fission or fragmentation.

One uses spontaneous fission of heavy nuclei such as ^{252}Cf. The example is [45] at Argonne National Laboratory in the US. Induced fission of heavy nuclei by photon or thermal neutron is also used to study unstable nuclei. Lohengrin mass spectrometer at Institut Laue-Langevin, Grenoble can select unstable nuclei recoiling from the fission target at a high-flux reactor [48]. In such methods, the fission fragments have asymmetric mass and distributes mostly around $A \sim$ 100 and 140. They have low cross section for the other mass region such as the region of interest of this study, $A \sim 160$.

There is one another method to produce unstable nuclei called as ISOL (isotope separation on line). In this technique, the driver beam such as protons from an accelerator is bombarded to a thick target of heavy nuclei to break them by spallation, fragmentation or fission reactions. The produced unstable nuclei are ionized and accelerated for the on-line separation and then provided as RI beams. ISOLDE at CERN [49] and TRIUMF in Canada [50] are the example of the facility based on ISOL technique. In this method, efficiency of RI beam extraction at an ion source depends on the atomic property of the nucleus.

In in-flight method, ions of heavy elements such as ^{238}U are accelerated up to hundreds of MeV per nucleon and bombarded to a production target to induce in-flight fission or fragmentation reactions. The fragments of unstable nuclei fly out from target and can be obtained as RI beams after separation and identification along the beamline. In this method, nuclei across a wide range of mass region can be produced, which is suitable for the systematic study of $A \sim 160$ region. The flight time from the production target to experimental sites is hundreds of nanoseconds, which is shorter than the other methods described above. Therefore, it have sensitivity to the isomers with short half-lives as $\sim$100 ns. RIBF at RIKEN Nishina Center is an example of the facility employs this method. This in-flight method is employed in this study since it is suitable for the production of neutron-rich $A \sim 160$ nuclei and measurement of isomers with micro-seconds half-lives.

2.1.2 Principle of RI beam separation and identification in in-flight method

There are huge numbers of nuclides produced by in-flight fission. They should be separated or identified in order to investigate certain nuclides. This subsection describes the basic idea of in-flight fragment separation and identification.

The curvature ρ of a charged-particle track in a uniform magnetic field B is written in a proportional expression as,

$$\rho \propto \frac{p}{Q} B \propto \frac{A}{Q} \frac{\beta}{\sqrt{1-\beta^2}} B, \tag{2.1}$$

where p, Q and A are the momentum, charge and mass number of the particle, respectively. This relation gives us mass-to-charge ratio (A/Q) from the curvature and velocity of the particle. The value, $B\rho$ is called as "magnetic rigidity" and proportional to A/Q when the velocity of the particle is fixed. Energy loss (ΔE) in an enough thin material is expressed using nuclear charge (Z) as follows.

$$\Delta E \propto Z^2/\beta^2 \tag{2.2}$$

These two relations enables particle separation. A fragment separator basically consists of two dipole magnets. The first magnet separates ions with different magnetic rigidity ($B\rho$). By installing a slit after the magnet, ions with a certain rigidity can be selected. By installing position detector, the magnetic rigidity of ions can be identified one by one. The second magnet separates ions with different atomic number (Z). The degrader before the magnet reduces more energy of ions with larger atomic number according to the equation (2.2) then ions with larger atomic number turn with smaller radius in the second magnet. Ions with a certain atomic number can be selected by a slit after the magnet. A ΔE detector is often used to identify the atomic number of ions. The wedged shape of the degrader is designed to focus the energy spread of the beam. Ions deviated to higher momentum have larger magnetic rigidity, and thus, pass thicker part of the wedged degrader to reduce much energy. Ions with lower momentum pass thinner part of the degrader and reduce fewer energy.

2.1.3 Accelerator facility

In order to obtain high intensity ^{238}U beam for the production of neutron-rich $A \sim 160$ nuclei by in-flight fission, facilities for multistage acceleration at RIKEN, Nishina Center was used. Figure 2.1 shows the schematic view of the accelerator facility at RIBF. ^{238}U beam was accelerated by five sequential accelerators, RILAC2 (RIKEN Heavy Ion LINAC 2), RRC (RIKEN Ring Cyclotron), fRC (fixed-frequency Ring Cyclotron), IRC (Intermediate-stage Ring Cyclotron) and SRC (Superconducting Ring Cyclotron), to increase beam energy step by step. The energy of the $^{238}U^{86+}$ beam from the last Cyclotron, SRC, reaches up to 345 MeV/u, which corresponds to ~70 % of the speed of light. The beam intensity as much as ~5pnA was achieved in this experiment.

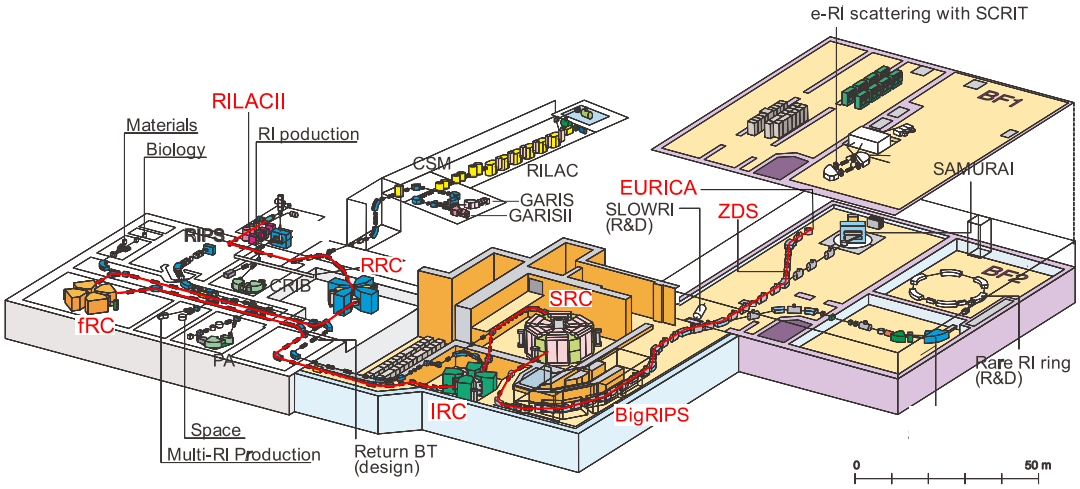

Figure 2.1 Overview of RIBF facility. The beam line used for ^{238}U acceleration in this work is indicated by the red line.

2.1.4 RI beam separation and identification using BigRIPS at RIBF

The RI Beam Factory (RIBF) at RIKEN, Nishina Center enabled to accelerate very intense ^{238}U beam up to 345 MeV/u using a super conducting ring cyclotron. Figure 2.2 shows the beam line of a fragment separator, BigRIPS [51] at RIBF. The primary uranium beam is bombarded to a primary target placed at the F0 focal plane and produces wide range of radioactive isotopes by in-flight fission. The BigRIPS consists of two stages of fragment separators. The first stage, from the F0 to F3 focal plane, selects nuclei in a certain range of $B\rho$ and Z from the intense beam of product fragments using slits. In the second stage of the BigRIPS that is from the F3 to F7 focal plane, has detectors in each focal plane in order to enable event-by-event identification of the fragment particles. The magnetic rigidity is obtained from the horizontal position at the F5 and the magnetic field of the dipole magnets. The velocity of particles is deduced from the time of flight (TOF) between the F3 and F7. From the magnetic rigidity and the velocity, mass to charge ratio (A/Q) can be obtained. An ion chamber or Si detectors is used to measure ΔE to get atomic number, Z. The nuclide of particles can be identified from the A/Q and Z values.

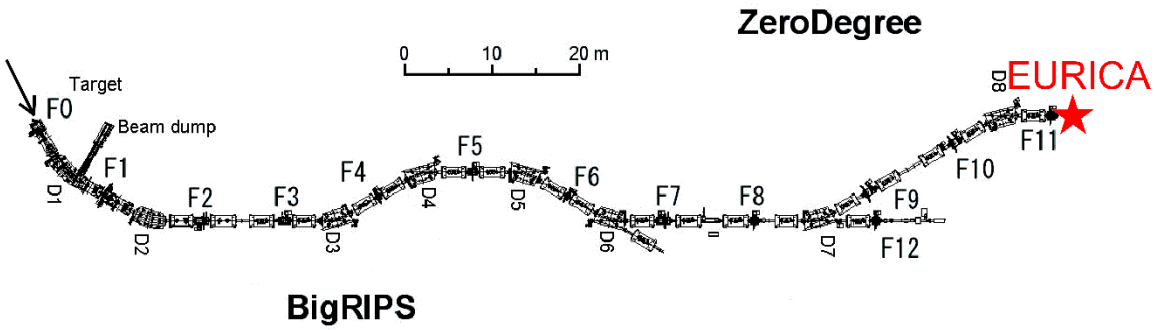

Figure 2.2 The BigRIPS beam line

2.1.5 Determination of the optimal BigRIPS settings

Since the total implantation rate of an active stopper, WAS3ABi (See [52].) introduced for β-γ spectroscopy is limited up to ∼100 cps, we decided to divide our beam time in order to obtain optimal statistics of both β-γ and isomer data. For isomer measurement, the active stopper is not necessary. The first nine hours were optimized for isomer measurement by installing passive stopper made of Cu plate with 1-mm thickness. The beam implantation rate was ∼1 kcps for this setting. The isomer setting with passive stopper centered ^{158}Pm and nuclei from $Z = 56$ to 64 were accepted. The rest of four days run with the active stopper in order to enable both β-γ and isomer measurement at the same time. Since the total implantation rate was limited with the active stopper, runs were divided into two settings in order to increase the implantation rate of interested nuclides by focusing on limited number of nuclides. One of the β-γ setting was centered ^{150}Ba and the other did ^{155}Pr. The BigRIPS settings for the three different runs are summarized in Table 2.1.

Table 2.1 Summary of the BigRIPS settings for three different settings

	Isomer setting	Nd beta setting	Ba beta setting
Be target thickness [mm]	4.0	4.0	3.0
Beam dump left [mm]	40.0	70.0	50.0
Beam dump right [mm]	124.9	124.9	124.9
$B\rho$ D1 [Tm]	7.3100	7.5602	7.7000
Degrader at F1	Al 2.0 mm	Al 2.0 mm	Al 2.0 mm
F1 slit left [mm]	42.8	42.8	27.0
F1 slit right [mm]	64.2	64.2	64.2
$B\rho$ D2 [Tm]	6.6931	6.9680	7.2732
F2 slit left [mm]	25.0	18.0	10.0
F2 slit right [mm]	5.0	5.0	2.0
Thickness of F3 plastic [mm]	0.2	0.2	0.2
$B\rho$ D3, D4 [Tm]	6.6447	6.9093	7.2309
Degrader at F5	Al 3.5 mm	Al 3.5 mm	Al 3.5 mm
F5 slit left [mm]	120.0	120.0	120.0
F5 slit right [mm]	120.0	120.0	50.0
$B\rho$ D5, D6 [Tm]	5.6095	5.9459	6.3860
F7 slit left [mm]	25.0	20.0	15.0
F7 slit right [mm]	9.0	9.0	4.0
Thickness of F7 plastic [mm]	0.2	0.2	0.2
$B\rho$ D7, D8 [Tm]	5.5455	5.9136	6.3705
F11 slit left [mm]	170	170	170
F11 slit right [mm]	170	170	170
Degrader at F11	Al 1.3 mm	Al 0.6+1.0+0.3 mm	Al 1.5+2.1 mm

2.1.6 RI implantation

The secondary beams produced and identified by BigRIPS were implanted into the stoppers at the final focal plane, F11. During the isomer runs, the beam was implanted into a passive stopper made of 1-mm-thick copper plate, while an active stopper, WAS3ABi, which made of 5 layers of 1-mm-thick silicon was used for the beta runs. There were aluminum degraders installed just after the F11 chamber in order to reduce and adjust the beam energy so that the nuclei of interest are stopped inside the stoppers. The degrader thicknesses were estimated before the experiment by LISE++ calculation. The calculated range distribution of secondary beam nuclei are shown in Figure 2.3. This shows that our region of interest ($Z =$ 56 to 61) are covered by the five layers of DSSSDs. The degrader thicknesses used in the three experimental settings are shown in the Table 2.1.

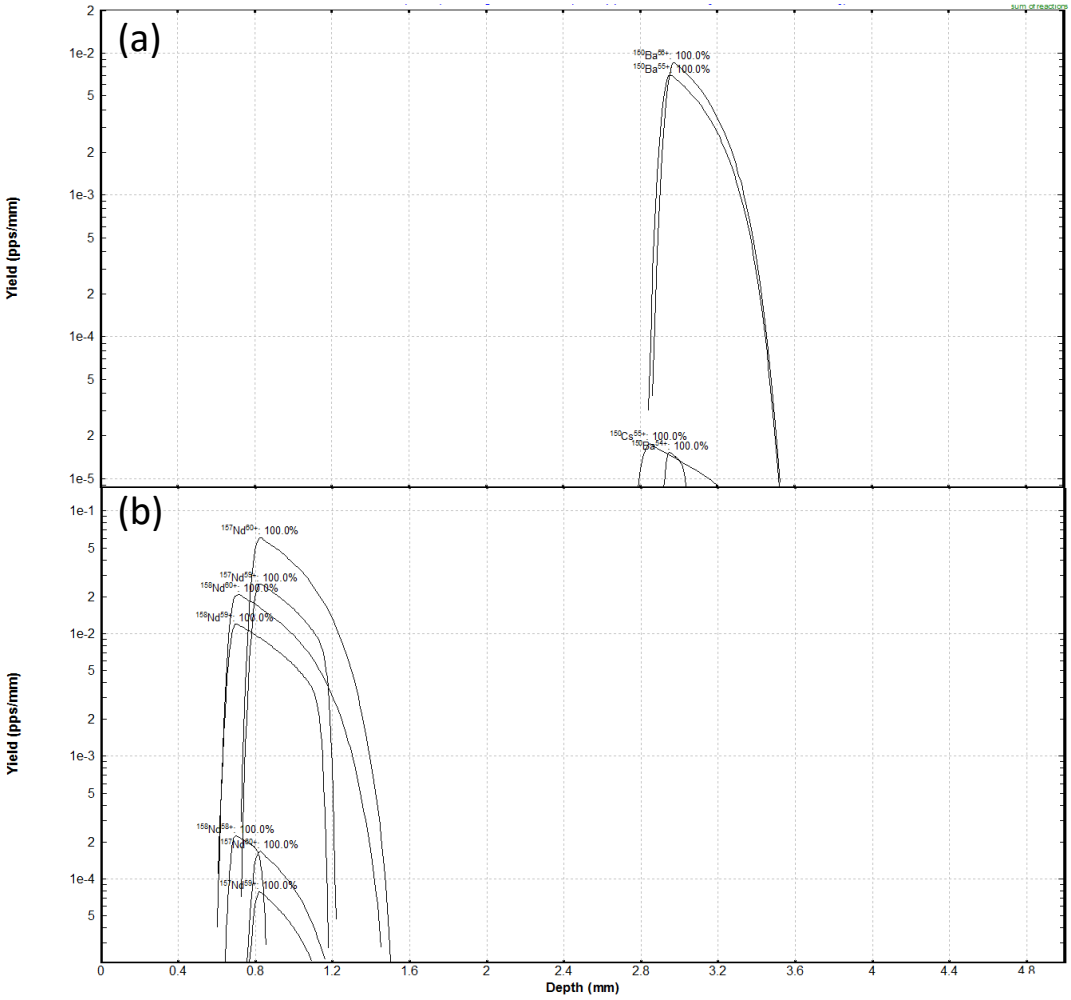

Figure 2.3 Range distribution of Ba ($Z = 56$) isotopes (a) and Nd ($Z = 60$) isotopes (b) in the DSSSDs by LISE++.

2.2 Detectors

2.2.1 Beam-line detectors

In order to obtain ΔE, $B\rho$ and TOF values for the event-by-event particle identification, beam-line detectors were installed at the second stage of the BigRIPS, from F3 to F7, and the final focal plane, F11. Parallel plate avalanche counters (PPAC) [53] were installed at F3, F5, and F7, for tracking the beam trajectory. The PPAC enables to obtain the x and y positions by the delay-line readouts of two cathodes stripped in x and y directions, respectively, as shown in Figure 2.4. The position is derived from the timing difference between the signals of the two delay-line readouts. Typically, the PPAC can achieve position resolution $\sim$1 mm in FWHM with $>$95% efficiency. Two PPACs were installed at each focal plane chamber in order to obtain both the x, y positions and angles of the beam trajectory.

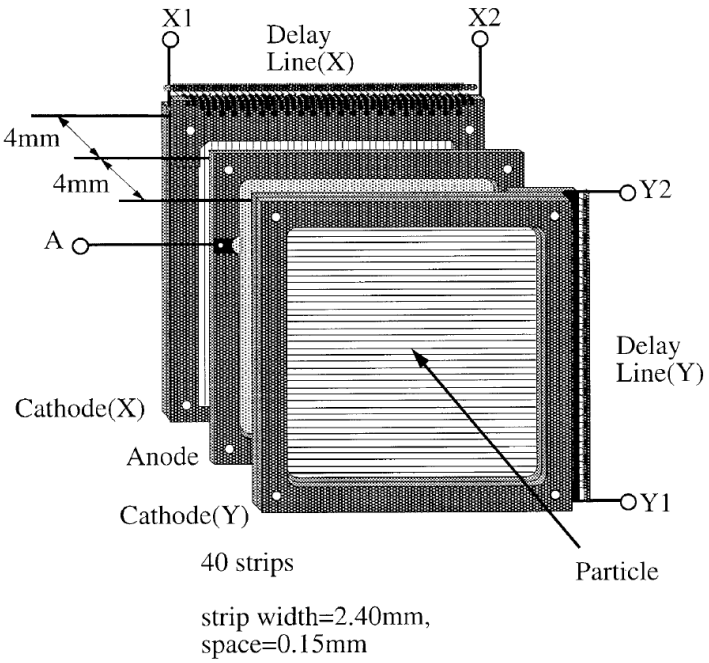

Figure 2.4 Exploded view of the delay-line PPAC (taken from Figure 1 of the reference [53]).

Plastic scintillation counters were installed at the F3 and F7 foci for the TOF measurement. The type of the scintillators was EJ-230 of ELJEN Technology which was intended for fast timing measurement with $\sim$0.5-ns rise time. The thickness was 0.2mm. Two photo multiplier tubes (PMTs) were attached on both the right and left sides of the plastic scintillators. This enables cancelling the position dependency of the detection timing by averaging both signals.

An ionization chamber was installed at the F11 focal plane for the energy loss measurement. The MUSIC (Multi-sampling ionization chamber) detector [54] which consists of 12 anodes with 6 readouts and 13 grounded cathodes placed alternately. The thin anode-cathode gap, 20 mm, reduces the drifting time and enables high-rate counting above 100 kHz.

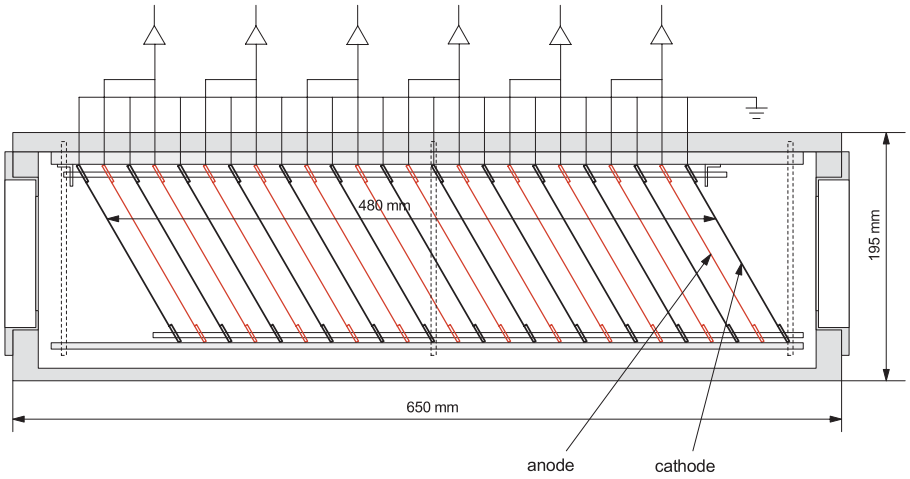

Figure 2.5 Cross-sectional view of the ionization chamber, MUSIC (taken from Figure 1 of the reference [54]).

2.2.2 γ-ray detector array (EURICA)

The EUROBALL-RIKEN Cluster Array, EURICA [55], consists of 12 clusters of HPGe detectors from EUROBALL [56]. Each cluster consists of 7 crystals packed closely in hexagonal way. This enables adding back Compton-scattered events with neighboring crystals. The array was placed at F11, the final focal plane, where the secondary beams were implanted. Figure 2.6 shows the detector setup at F11. The rectangular chamber with WAS3ABi detector inside was placed at the center of the array, and 12 clusters mounted to surround it. The angles of each detector are listed in Table 2.2, which do not have symmetry for vertical nor horizontal inversion. $LaBr_3$ γ-ray detectors were installed at vacant slots for lifetime measurement of γ decays with sub-nanoseconds half-lives, which will be explained in next section.

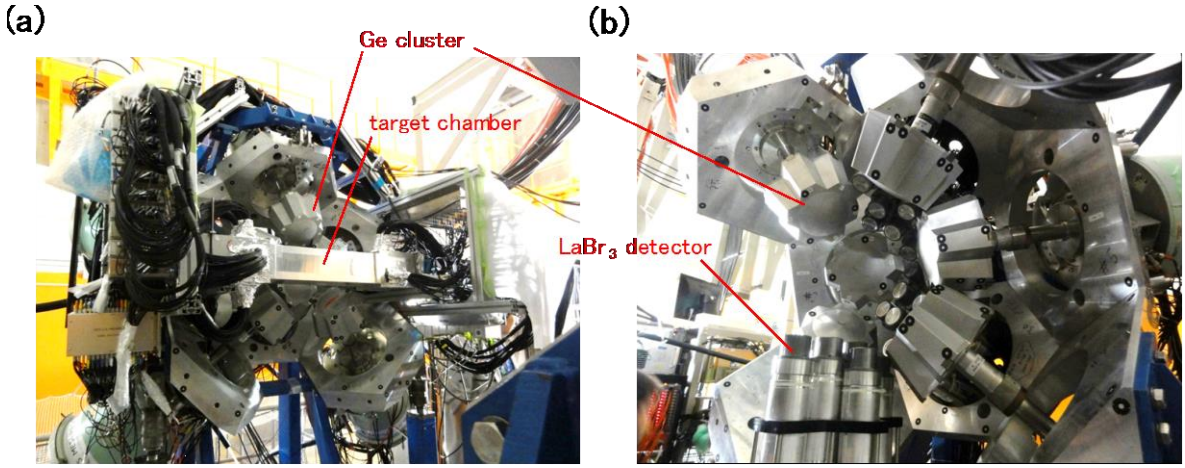

Figure 2.6 Photographic pictures of the left half (a) and the right half (b) of the cluster array.

Table 2.2 List of detector angles of the cluster array. θ represents the angle from the beam axis, while ϕ shows the angle of clockwise rotation around the beam axis from left direction viewing from upstream side.

Detector id	θ (deg.)	ϕ (deg.)
1	51	234
2	51	162
3	51	90
4	129	234
5	129	162
6	129	90
7	90	54
8	90	342
9	51	306
10	51	18
11	129	306
12	129	18

2.2.3 $LaBr_3$ detectors

$LaBr_3$:Ce scintillation crystals are used as fast-timing γ-ray detectors aimed at measuring sub-nanosecond half-lives. They have timing resolution of ~ 100 ps which is one order faster than that of Ge semiconductor detectors, and have energy resolution $\sim 3\%$ for 662 keV γ rays in FWHM [57]. 18 $LaBr_3$ crystals with ϕ1.5 x 2 inches cylindrical shape readout by a H10570 Hamamatsu PMT were mounted. These $LaBr_3$ detectors were supplied by the University of Surrey and the University of Brighton in the U.K. [58]

2.2.4 WAS3ABi

WAS3ABi is a double-sided silicon strip detector (DSSSD) array designed as an active stopper for the decay spectroscopy of the secondary beams of RIBF with large momentum acceptance and high implantation rate [52,59]. WAS3ABi stands for Wide-range Active Silicon-Strip Stopper Array for Beta and ion detection. 5 layers of DSSSDs were installed in this work in order to stop all the ions of interest ($Z = 55$ to 61). Each layer was horizontally segmented into 60 strips and vertically done into 40 strips. The width of the strips was 1 mm and the thickness of the Si of a single layer was 1 mm. The picture of WAS3ABi mounted on a frame is shown in Figure 2.7. WAS3ABi enables taking correlations between a beam implantation event and a β-decay event that are implanted and emitted at the same position. This made it possible to combine γ-ray data of a β-decay event to the PID of an implantation events whose time difference is as long as 1 second with the total implantation rate of ~ 100 cps.

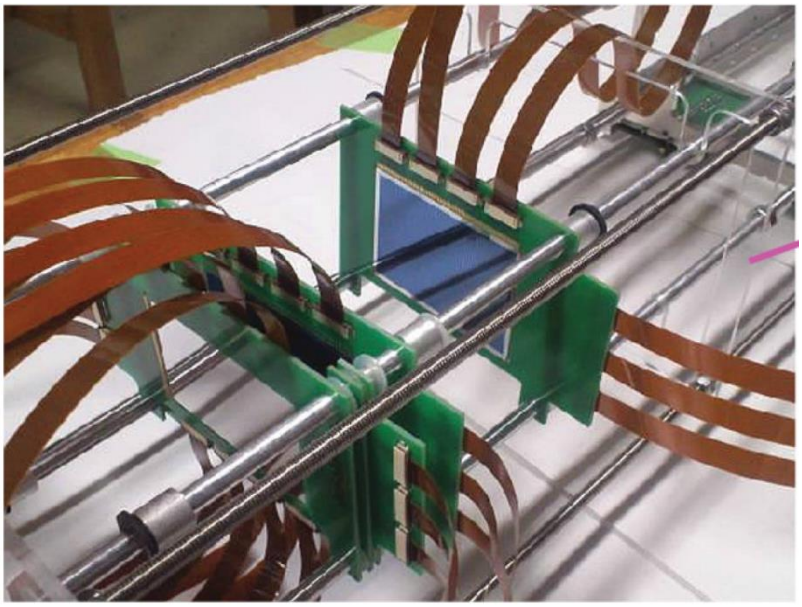

Figure 2.7 Photographic picture of WAS3ABi (taken from Figure 5 of the reference [59]).

2.3 Data acquisition

Three independent data acquisition (DAQ) systems were operated to record data of EURICA, WAS3ABi and BigRIPS detectors. Each DAQ system records the absolute time information called timestamp which is counted in every 10 ns by programmable FPGA logic modules (LUPO) synchronized by a common 25-MHz clock [60]. Data for the same physical event can be merged together by using this timestamp information. Beam implantation events during the β-decay measurement trigger all three DAQ systems, while β-emmission events trigger only WAS3ABi and EURICA DAQ systems. During the isomer setting runs, only the EURICA and BigRIPS DAQ systems are triggered.

2.3.1 DAQ system for BigRIPS

The DAQ system for BigRIPS takes data of all the beam-line detectors. Since this DAQ covers detectors in different focal planes, signals of each detectors were sent from each focal plane to the counting room by optical fibers to avoid electric contact between different halls. The block diagram of the BigRIPS DAQ is shown in Figure 2.8. The two-dot chain lines in the figure represent optical lines. Signals of plastic scintillators and PPACs at each focal planes were sent by the optical fibers to the counting room and processed for producing the trigger signal and for taking the timing and charge data by TDCs and QDCs. The trigger signal was sent back to experimental hall for taking data of ionization chambers at F7 and F11 by ADCs placed around the focal planes because they were not expected to join the trigger and it was not necessary to send the signals if ionization chambers to the counting room.

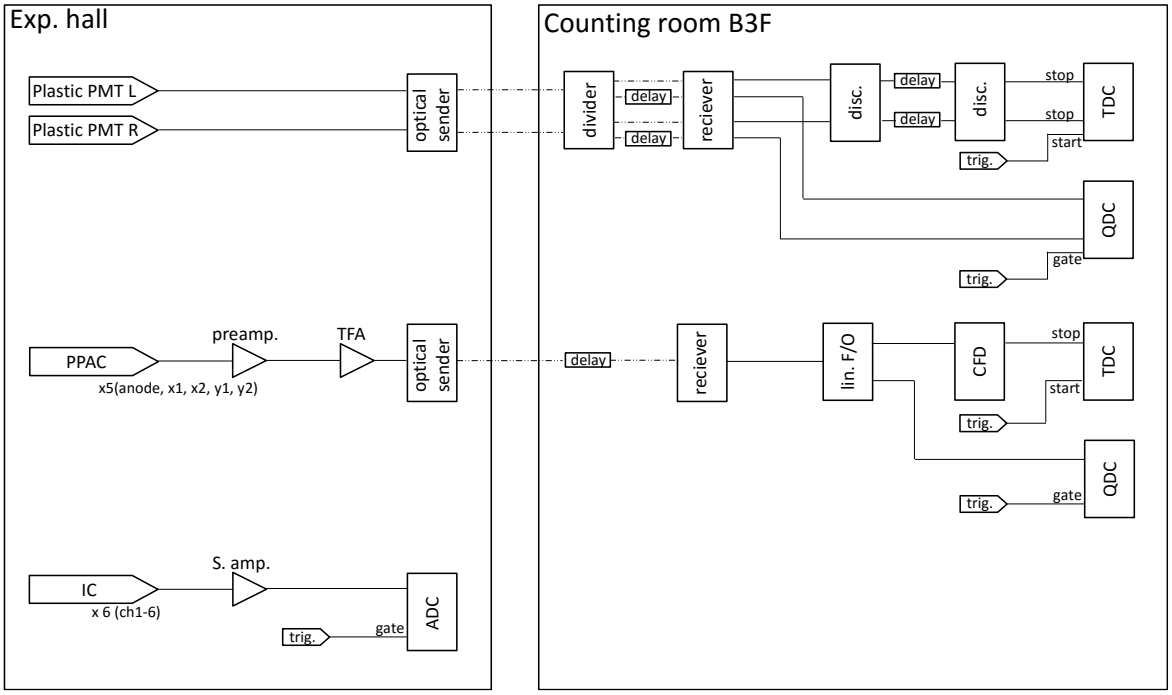

Figure 2.8 Block diagram of BigRIPS DAQ system.

2.3.2 DAQ system for WAS3ABi

The energies and timing information of all strips of DSSSDs were taken by DAQ system for WAS3ABi. Signals from the strips of ground side (x direction) and bias side (y direction) were shaped and amplified by CAEN N568B S. Amps. The slow pulse outputs for energy measurement were measured by ADCs, CAEN V785. The fast outputs were discriminated by the leading edges and measured by TDCs, CAEN V1190. Since the number of read out channels are large, gains of the ADCs were adjusted only for β rays (high gain) and events of heavy ion implantation were only identified as overflowed channel. However, timing information of leading edge discriminator is sensitive to the pulse height, and thus, the energy information of implantation events were roughly obtained by the leading edge timings. The WAS3ABi DAQ was triggered by a sum of front-back coincidence of DSSSDs or plastic counters at F11. The events triggered by WAS3ABi were identified as β events and those triggered by F11 plastic were considered to be beam events.

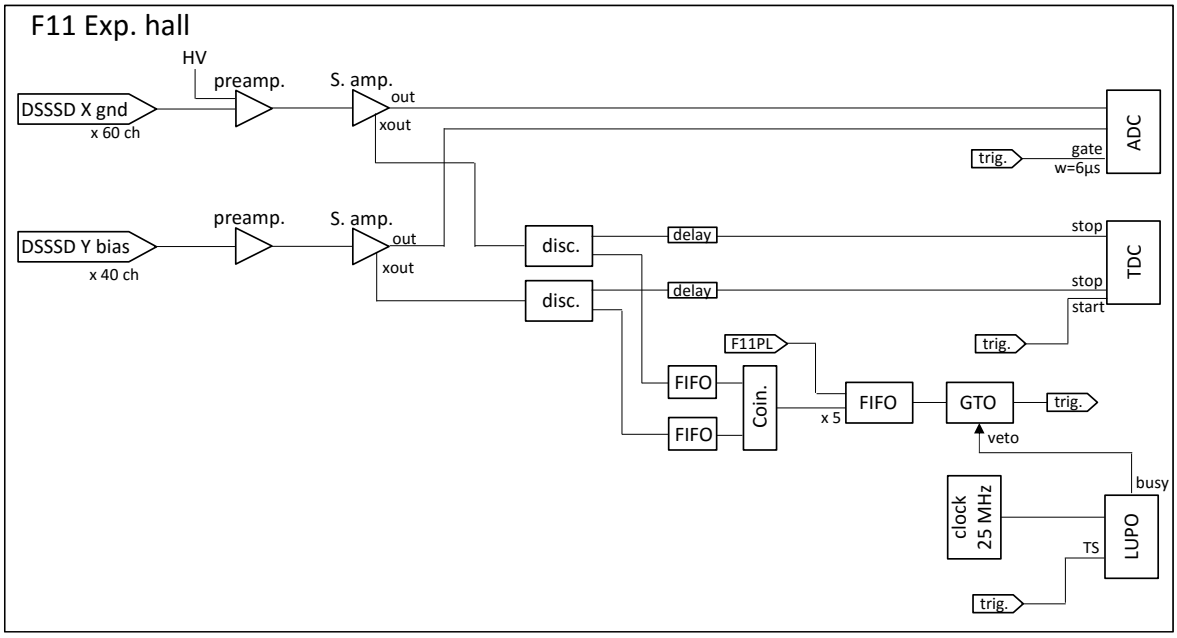

Figure 2.9 Block diagram of WAS3ABi DAQ system

2.3.3 DAQ system for EURICA

The signals of cluster Ge detectors were mainly processed by digital module called DGF (digital gamma finder) of XIA [61]. This module digitize the raw signals from preamplifiers and processes the pulse shape to obtain the pulse height information. Time stamp of the pulses are also recorded. Timing information were also recorded by two types of TDCs with different time ranges. Short-Range TDC (CAEN V775) have the shortest time window but the best digital time resolution and Long-Range TDC (CAEN V767) have longer time window than Short-Range TDC but lower digital resolution. The time stamp of DGFs have the digital resolution of 25 ns which is worse than TDCs, but it is still good enough to measure isomers with the half-life of hundreds of nanoseconds. TDC information was dedicated for the measurement of the half-lives of first 2^+ states. Data of $LaBr_3$ detectors and Beta plastic counters were also recorded by the TDCs and ADCs of EURICA DAQ system. All the DGFs, TDCs and ADCs were controlled by VME board computers, RIO3 [62], and the events were built by MBS event builder. The trigger of EURICA DAQ was identical to that of WAS3ABi DAQ.

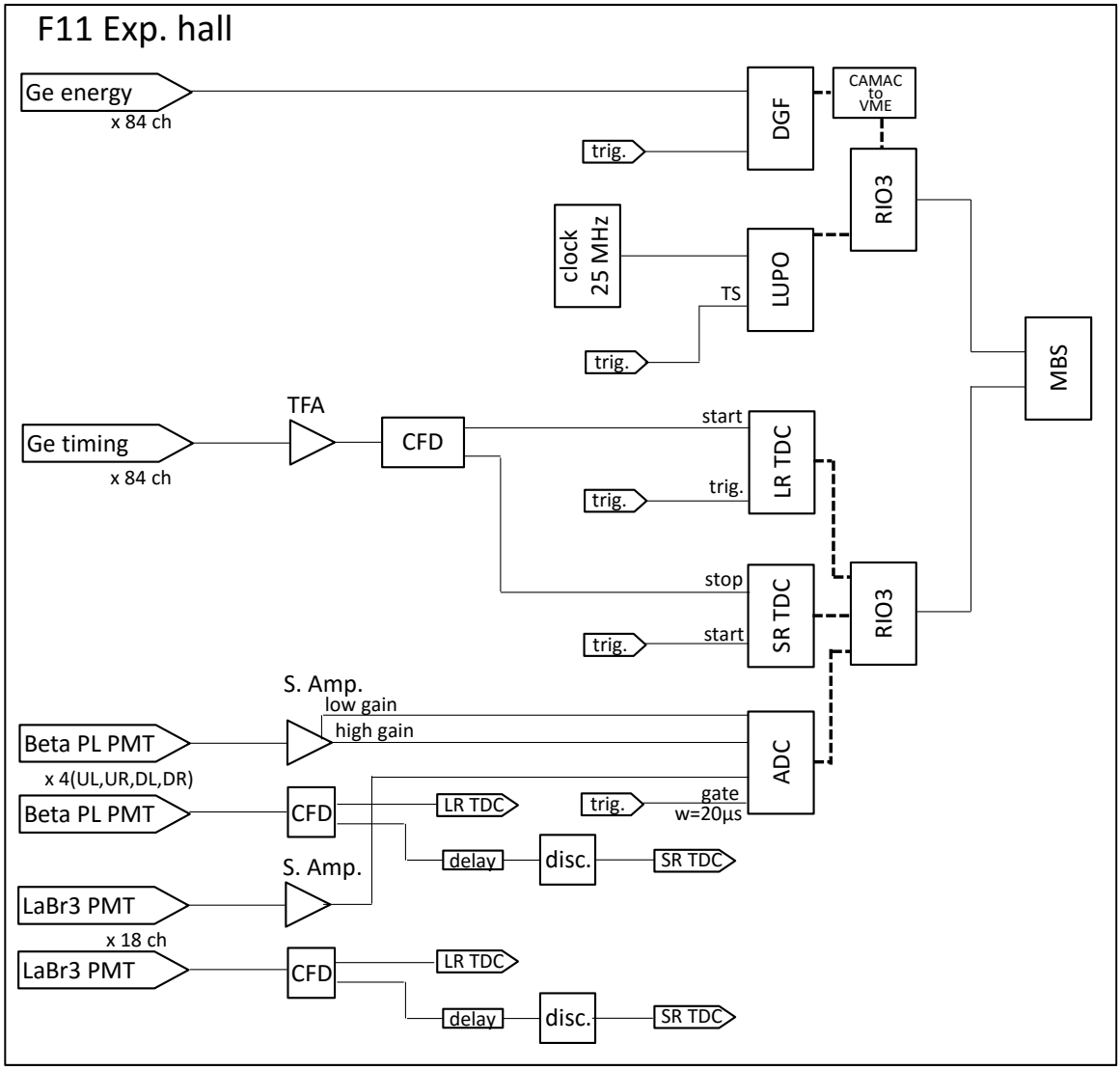

Figure 2.10 Block diagram of EURICA DAQ system

2.4 Experiment with clover-type Ge detectors at F12 (MS-11)

In this section, experimental setups of the MS-11 experiment of isomer spectroscopy on neutron-rich $Z \sim 65$ nuclei are described. The basic idea of the beam production and isomer measurement are the same as the RIBF-86 experiment, which are already shown in Section 2.1 to 2.3. Only the points specific to this experiment are mentioned in this section. The beam settings, detector setups and DAQ system of this experiment are explained in the following subsections. β-γ spectroscopy was not possible in this experimental setup.

2.4.1 Beam settings

Neutron-rich nuclei were produced by in-flight fission of 345 MeV/u ^{238}U beam. Fission fragments were separated and identified by BigRIPS and implanted into the final focal plane, F12. $B\rho$ and TOF were measured at the second stage of the BigRIPS, F3 to F7, and ΔE was

measured by a stack of Si detectors at F12. Runs were divided in to two BigRIPS settings. One centers $Z = 61$ and the other does $Z = 64$. These two settings were named as "Top setting" and "Bottom setting". Summary of the two settings are shown in Table 2.1.

Table 2.3 Major information of the BigRIPS settings in the prior experiment.

Settings	Bottom setting	Top setting
^{238}U intensity	0.13 pnA	0.31 pnA
Total running time	44h	58h
Total dose on target	1.2×10^{14}	3.9×10^{14}
Target	Be 3.96mm	Be 4.93mm
F1 degrader	Al 1.27mm (curved)	Al 1.27mm (curved)
F5 degrader	Al 1.40mm (wedge)	Al 1.40mm (wedge)
$B\rho$ of the central path	7.306 Tm	6.950 Tm
Central particle	^{150}Pm	^{168}Gd
Momentum acceptance	±3%	±3%
Trigger rate	620 cps	260 cps

2.4.2 Detector setups

Secondary beam of neutron-rich nuclei were implanted into a stack of Si detectors placed at F12 focal plane (you can find F12 in Figure 2.2). The Si stack detector is shown in blue color in Figure 2.11. It consists of 14 layers of Si detectors in total; 2 layers with 0.5 mm thickness and 12 layers with 1.0 mm thickness. The size of the sensitive area was 50 × 50 mm^2 for both thicknesses of Si. The Si stack was designed to stop all the nuclei of interest and the lighter nuclei were detected by a CSI veto counter just behind the Si stack. Delayed γ rays from implanted ions were measured by four clover-type HPGe detectors around the Si stack (shown in red in Figure 2.11). One clover detector consists of four crystals packed closely and is able to addback among the four crystals in order to enhance full energy peak counts. The flight distance of the particles from F0 to F12 was 102.9 m that corresponds to ∼550 ns for a typical particle. Thus, the lower limit of the measureable half-life of the isomers was ∼100 ns.

2.4.3 DAQ system

Data acquisition of the BigRIPS is basically the same as described in Section 2.3.1. DAQ for isomer spectroscopy at F12 runs with the same trigger as the other BigRIPS DAQ systems. All the data of F12 and the other BigRIPS DAQ for one trigger were built to one event. The block diagram of F12 DAQ system is shown in Figure 2.12. Energy information of clover detectors were measured by ADC, ORTEC AD413, which was adjusted to have the dynamic range around 4 MeV. Signals were shaped and amplified by ORTEC 671, before putting into the ADC. Timing signals of clover detectors were produced by CFD, ORTEC 935, and measured by TDC, Lecroy 3377. This TDC have time window up to 32 μs. The stop signal was delayed 30 μs from the trigger (produced by F3 plastic) to have the prompt γ rays in the beginning 2 μs of

the time window and 30 μs available for delayed γ rays.

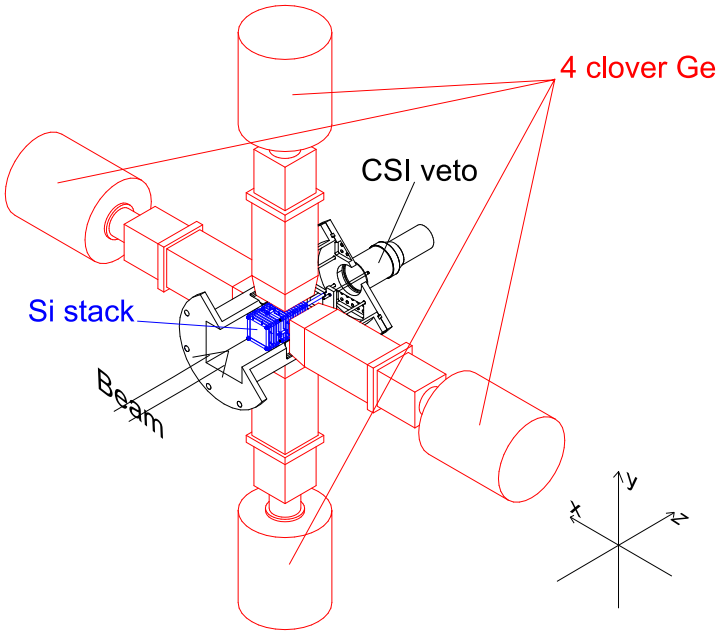

Figure 2.11 Detector setups for isomer spectroscopy at F12.

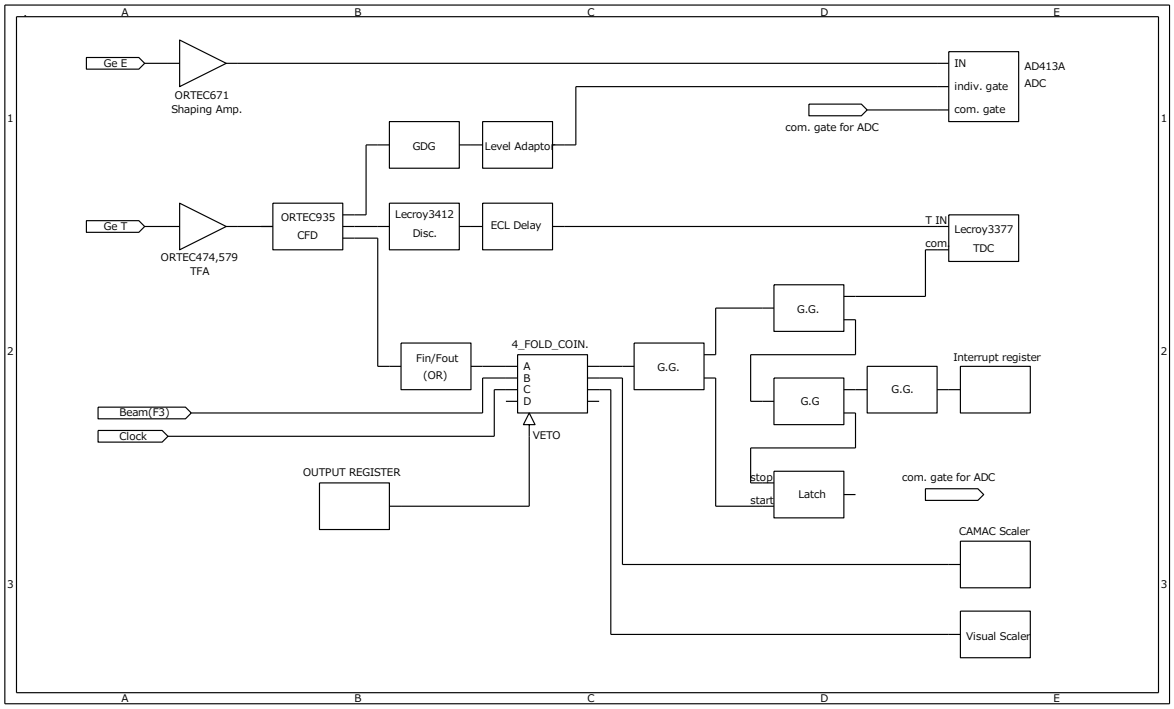

Figure 2.12 Block diagram of the DAQ electronics for the isomer spectroscopy at F12

Chapter 3 Analysis

In this chapter, detailed procedure of the data analysis is explained. The analysis to obtain the particle identification is shown in Section 3.1, then the calibration of Ge detectors and Si detectors are given in Section 3.1.4 and 3.3, respectively. The procedure for the analysis of isomer spectroscopy is shown in Section 3.4 and that of β-γ spectroscopy is in Section 3.5.

3.1 Particle identification

Particle identification (PID) is to tag the secondary beam implanted to the detector system event-by-event by using the beamline detectors in the second stage of the BigRIPS. Basically, the PID is provided as loci on the Z (nuclear charge) vs. A/Q (mass-to-charge ratio) plot. In this section, detailed procedure for obtaining the Z and A/Q from the energy loss (ΔE), magnetic rigidity ($B\rho$) and time-of-flight (TOF) measured by the beamline detectors is shown. Many of the ideas of PID analysis in this section referred to [63].

3.1.1 Determination of A/Q

The A/Q value was determined from the TOF and $B\rho$ measurement made by trajectory reconstruction. The TOF is defined as,

$$\mathrm{TOF} = L/\beta c, \tag{3.1}$$

where β is the velocity, and L is the flight length of the beam particle. This can be obtained from the time difference between plastic scintillators at two different foci. In this experiment, TOF was measured at F3 and F7 foci shown as following equation.

$$\mathrm{TOF}_{37} = T_{F7plastic} - T_{F3plastic} + T_{offset} \tag{3.2}$$

The T_{offset} is a timing offset of the measurement and can be calibrated by known particle for example, first it can be roughly calibrated by the primary beam and then by known fragments once they were tagged by isomers. The plastic scintillators at each focal plane were read out by two PMTs on the left and right side as described in the section 2.2.1. Timing was obtained simply from the equation,

$$T_{plastic} = (T_{Left} + T_{right})/2. \tag{3.3}$$

The magnetic rigidity, $B\rho$, is defined by the radius of the circular motion of a particle ρ in a magnetic field B, and can be expressed as,

$$B\rho = p/q = \frac{\gamma m \beta c}{q}, \tag{3.4}$$

where p, q and m shows the momentum, charge and the mass of the particle. γ here shows the relativistic Lorentz factor. From this notation, the A/Q is given by,

$$\frac{A}{Q} = \left(\frac{m}{m_u}\right) \Big/ \left(\frac{q}{e}\right) = \frac{e}{\beta c \gamma m_u} B\rho. \tag{3.5}$$

From TOF_{37}, we can derive TOF_{35} and TOF_{57} which are different from each other because of the energy loss at the F5 degrader, without timing detector at F5 focal. By assuming the mass and charge of the particle does not change before and after the F5, $B\rho/\beta\gamma$ is conserved as follows.

$$\frac{B\rho_{35}}{\beta_{35}\gamma_{35}} = \frac{B\rho_{57}}{\beta_{57}\gamma_{57}} \tag{3.6}$$

From the equation (3.6) and the obvious equation,

$$\mathrm{TOF}_{37} = \mathrm{TOF}_{35} + \mathrm{TOF}_{57} = \frac{L_{35}}{\beta_{35}c} + \frac{L_{57}}{\beta_{57}c}, \tag{3.7}$$

the TOF_{35} and TOF_{57} can be expressed by using TOF_{37}, L_{35}, L_{57}, $B\rho_{35}$ and $B\rho_{57}$.

The $B\rho$ value was obtained from the trajectory reconstruction. The $B\rho$ of the particle off the center trajectory can be expressed by the momentum dispersion, δ and the magnetic rigidity along the center trajectory, $B\rho_0$,

$$B\rho = (1+\delta)B\rho_0. \tag{3.8}$$

Since the $B\rho_0$ value was monitored and recorded by the measurement of the magnetic field by NMR, $B\rho$ can be derived from reconstructed δ.

When we define a horizontal vector that represents the motion of the particle at the i-th focal plane $\boldsymbol{X_i}$ as,

$$\boldsymbol{X_i} = \begin{pmatrix} x_i \\ a_i \\ \delta_i \end{pmatrix}. \tag{3.9}$$

The transfer matrix to the next focal, $\boldsymbol{R_{ij}}$ can be described as,

$$\boldsymbol{R_{ij}} = \begin{pmatrix} (x|x) & (x|a) & (x|\delta) \\ (a|x) & (a|a) & (a|\delta) \\ (\delta|x) & (\delta|a) & (\delta|\delta) \end{pmatrix}, \tag{3.10}$$

where x shows the horizontal position and a shows the horizontal angle of the trajectory. Using the transfer matrix, the horizontal vector of the next focal plane can be derived as,

$$\boldsymbol{X_j} = \boldsymbol{R_{ij}}\boldsymbol{X_i}. \tag{3.11}$$

Therefore, the momentum dispersion at F5 can be obtained as,

$$\delta = (x_5 - (x|x)_{35}\mathrm{x}_3 - (x|a)_{35}a_3)/(x|\delta)_{35}. \tag{3.12}$$

The elements of the transfer matrix were obtained from the linear correlations by gating on two of the x, a or δ values around a certain value, for example, correlation between x position of F5 vs F3 with $a, \delta \sim 0$ particles was used for obtaining the $(x|x)$ element. The correlation plot for this case is shown in Figure 3.1. The red line in the figure shows the result of linear fitting. The slope of the line, 0.177(4) corresponds to the matrix element, $(x|x)_{35}$. All the other elements of the matrix for F3 to F5 were obtained in similar way. Since the beam line from F3 to F5 and F7 to F5 are symmetry, the matrix for F5 to F7 were obtained as the inverse matrix of that for F7 to F5. The matrices for all the settings are shown in Table 3.1.

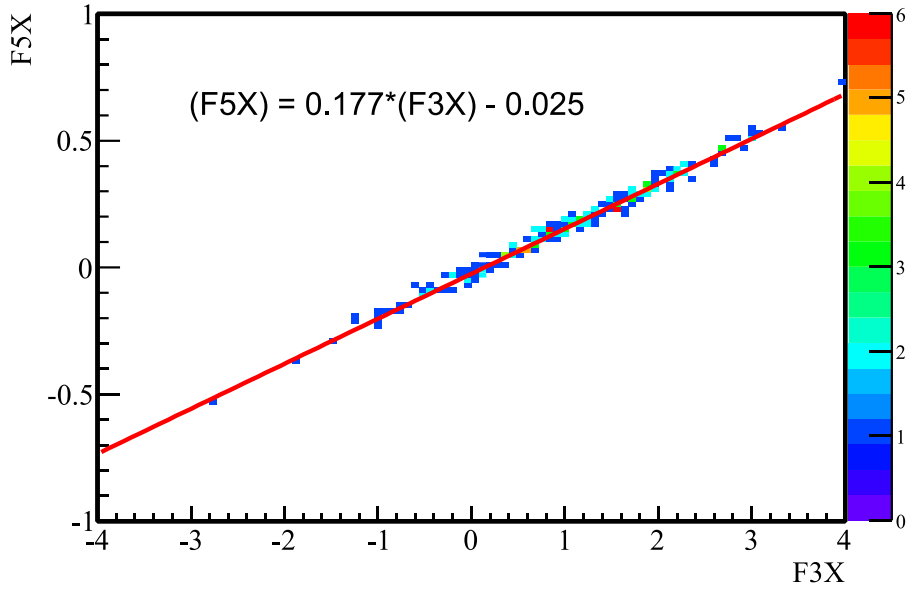

Figure 3.1 Correlation between the x position at F5 and F3 gated on the particles with zero angle and dispersion at F3. The gate conditions were $-1 < a_3 < 1$ and $-0.001 < \delta_3 < 0.001$.

Table 3.1 Transfer matrices for F3 to F5 and F5 to F7 in the three settings.

Isomer run	F3-F5						F5-F7					
	$(x\|x)$	1.05	$(x\|a)$	0.23	$(x\|\delta)$	36.5	$(x\|x)$	1.18	$(x\|a)$	0.01	$(x\|\delta)$	-37.4
	$(a\|x)$	0.02	$(a\|a)$	1.03	$(a\|\delta)$	0.55	$(a\|x)$	-0.16	$(a\|a)$	1.17	$(a\|\delta)$	0.58
Nd beta run	F3-F5						F5-F7					
	$(x\|x)$	0.98	$(x\|a)$	0.01	$(x\|\delta)$	31.6	$(x\|x)$	1.14	$(x\|a)$	-0.01	$(x\|\delta)$	-34.4
	$(a\|x)$	-0.02	$(a\|a)$	1.01	$(a\|\delta)$	-0.01	$(a\|x)$	-0.02	$(a\|a)$	1.12	$(a\|\delta)$	0.59
Ba beta run	F3-F5						F5-F7					
	$(x\|x)$	0.18	$(x\|a)$	0.01	$(x\|\delta)$	31.6	$(x\|x)$	1.09	$(x\|a)$	-0.01	$(x\|\delta)$	-34.4
	$(a\|x)$	-0.02	$(a\|a)$	1.09	$(a\|\delta)$	-0.01	$(a\|x)$	-0.02	$(a\|a)$	0.92	$(a\|\delta)$	0.59

3.1.2 Determination of Z

The Z value was derived from the energy loss in the F11 ion chamber and the TOF value. The energy loss of a heavy ion can be calculated by the Bethe formula,

$$\frac{dE}{dx} = \frac{4\pi e^4 Z^2}{m_e v^2} Nz \left[\ln \frac{2m_e v^2}{I} - \ln(1-\beta^2) - \beta^2 \right]. \quad (3.13)$$

Here, $v = \beta c$ is the velocity of the heavy ion, m_e is the electron mass and e is the elementary charge. N, z, I show the atomic density, atomic number and mean excitation potential of the counter gas. The gain shift was corrected by scaling the gain in order to adjust the center of the island of Ba isotopes to be 56. The gain shift before the correction is shown in Figure 3.2.

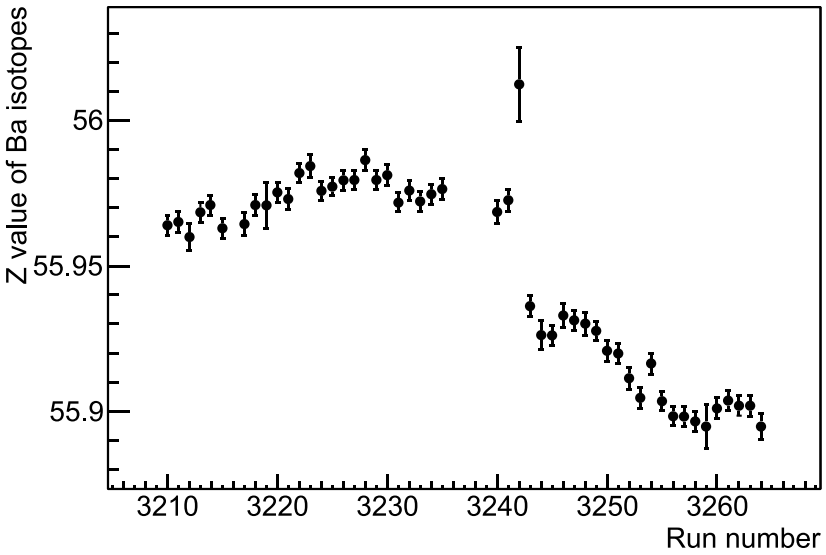

Figure 3.2 Gain shift of the F11 ion chamber. The horizontal axis shows the run number of Ba beta runs. The vertical axis shows the calibrated Z value of the center of the island of Ba isotopes.

3.1.3 Removal of background events

By plastic scintillation counter

The plastic scintillators at F3 and F7 for the TOF measurement, have two photomultiplier (PMT) readouts on the left and right edge. Charge and timing information of a PMT depends on the distance from the position of an incident particle. The charge attenuates exponentially as the distance increases, while the timing delays linearly. Since the sum of the distances from an incident position to the left and right PMTs is a constant (the length of the scintillator), there is a following correlation.

$$\ln(q_l/q_r) \propto t_r - t_l \tag{3.14}$$

Figure 3.3 shows the correlation between $\ln(q_l/q_r)$ and $t_r - t_l$ of the plastic scintillator at F7. By using this kind of plots, background events in plastic scintillators at F3 and F7 were removed.

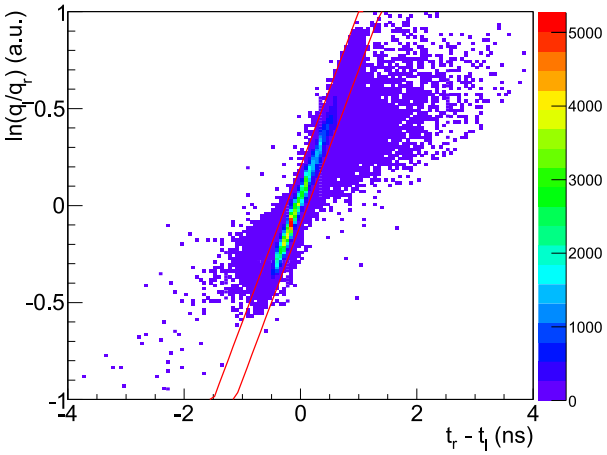

Figure 3.3 $\ln(q_l/q_r)$ vs. $t_r - t_l$ plot of the plastic scintillator at F7 focal plane. Sound events should follow the linear correlation. Events outside the area between two red lines were regarded as backgrounds and excluded from the following analysis.

By PPAC detector

The PPACs are position sensitive detectors installed at F3, F5 and F7 foci for reconstruction of the beam trajectory. The position is determined from the time difference between two delay line readouts of cathodes. Since the sum of the timings from two readouts should be a constant, inconsistent events can be removed by gating on $t_1 + t_2$ value. Events outside the gate were excluded in each layer of the PPACs. Sample spectrum for F7 PPAC 1 X is shown in Figure 3.4.

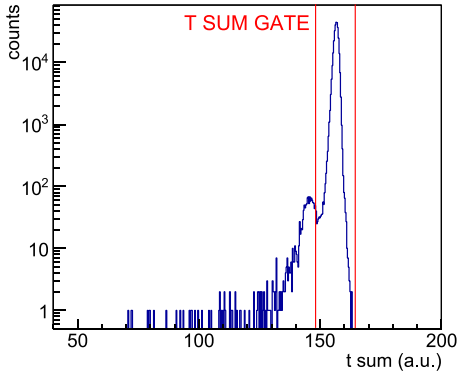

Figure 3.4 T sum spectrum for the F7 PPAC 1 X. The events between the two red lines are accepted.

By ΔE detector

The MUSIC detector, an ion chamber used for the ΔE measurement, consists of 12 anode pads with 6 readouts in total. They are averaged to obtain ΔE, however, the events reacted with the nucleus in the electrodes or the gas inside the detector may become background. Such events were excluded by gating on the ratio of ADC values between the n^{th} and $(n+1)^{\text{th}}$ readouts, which should be about 1. Figure 3.5 shows the ratio of the 0^{th} to the 1^{st} ADC value of F11 ion chamber. Similar gates were applied to all the other layers in this detector.

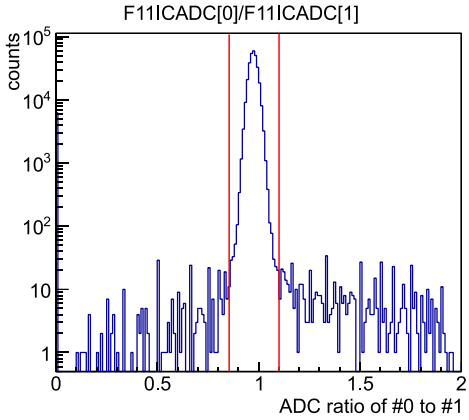

Figure 3.5 Spectrum of ADC value of the first anode readout divided by that of the second one for the F11 ion chamber. Events between the two red lines were selected.

Events whose charge state changes at F5 focus

Events whose charge state changes at the energy degrader or the PPACs at F5 can be background because the A/Q values cannot be derived correctly. Such events were identified by using ratio of A/Q values calculated from the TOF and $B\rho$ values between F3 to F5 and F5 to F7. As shown in Figure 3.6, events whose charge state +1 appear in the right down side in Z vs. $(A/Q)_{35}/(A/Q)_{57}$ plot. Those events were excluded to reduce the background.

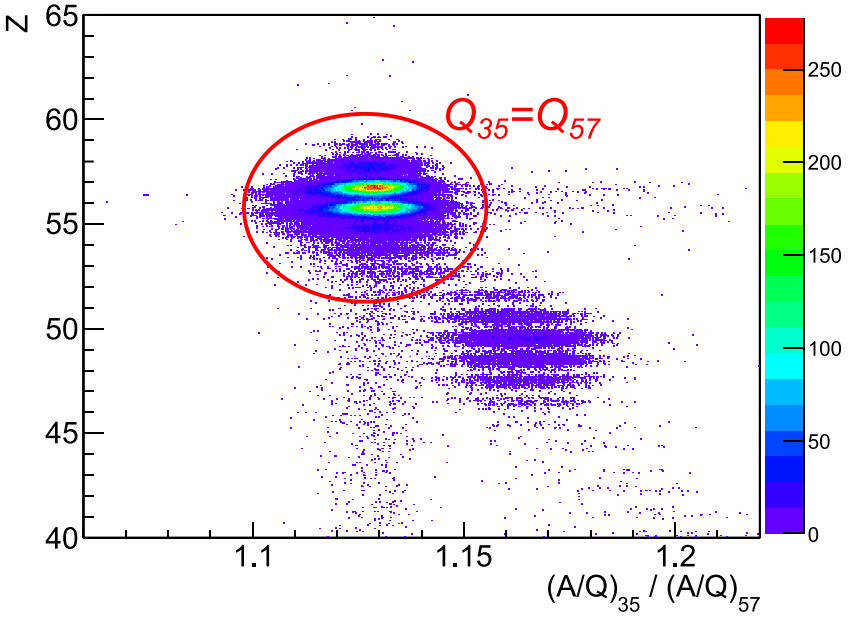

Figure 3.6 Z vs. $(A/Q)_{35}/(A/Q)_{57}$ plot of a Ba β run. $(A/Q)_{35}$ and $(A/Q)_{57}$ shows the A/Q values calculated from the TOF and $B\rho$ between F3 to F5 and F5 to F7, respectively.

3.1.4 PID for three different settings

The Z vs. A/Q plot for the PID of three settings are shown in the following figures, from Figure 3.7 to Figure 3.9.

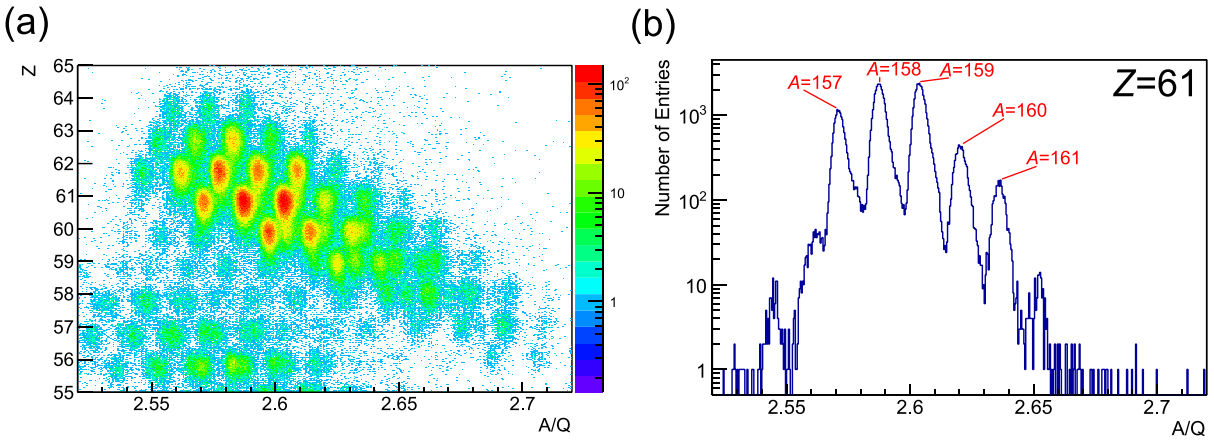

Figure 3.7 (a) The PID plot for the isomer runs. (b) A/Q spectrum of $Z = 61$ (Pm) isotopes.

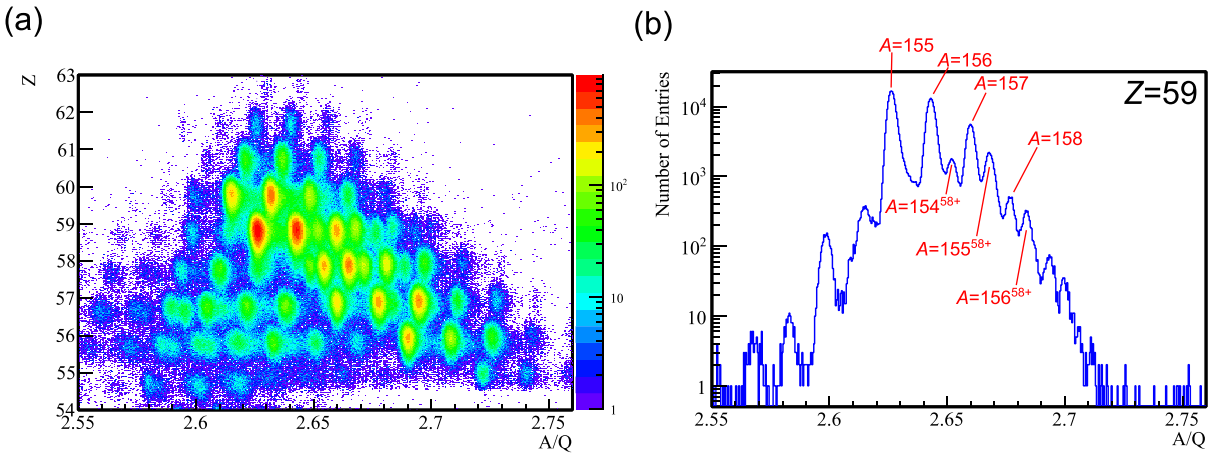

Figure 3.8 (a) The PID plot for the Nd beta runs. (b) A/Q spectrum of $Z = 59$ (Pr) isotopes.

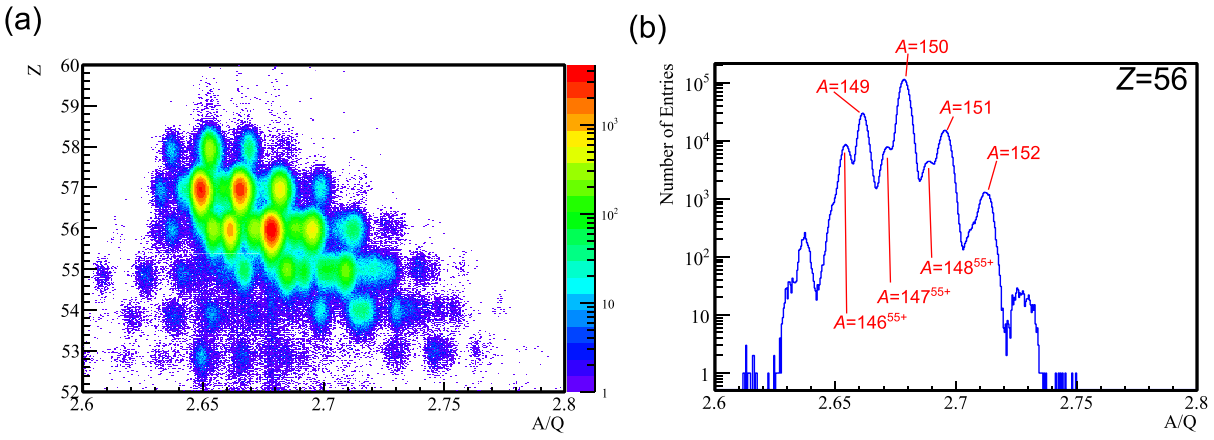

Figure 3.9 (a) The PID plot for the Ba beta runs. (b) A/Q spectrum of $Z = 56$ (Ba) isotopes.

3.2 Analysis of Ge detectors

3.2.1 Peak fitting

A function that consists of the following components was used for fitting peaks of γ-ray energy spectra.

A) A quadratic function
B) Gaussian functions
C) Skewed Gaussian functions
D) Error functions

As a default, the quadratic term of (A) and the functions (C) and (D) were set to be zero. If the peak had a tail, (C) was set to be on. If there was a stair-wise background that went down from lower energy side to higher energy side, the component (D) was added. The expression of each function is shown as below.

A) $y = p_0 + p_1 x + p_2 x^2$
B) $y = \frac{p_3 p_9}{\sqrt{2\pi} p_5} \exp\left(\frac{(x-p_4)^2}{2p_5^2}\right)$
C) $y = (1-p_6) p_3 p_9 \exp\left(\frac{(x-p_4)}{p_7}\right) \mathrm{Erfc}\left(\frac{(x-p_4)}{\sqrt{2}p_5}\right) + \frac{p_5}{\sqrt{2}p_7}$
D) $y = p_8 p_3 p_9 \mathrm{Erfc}\left(\frac{(x-p_4)}{\sqrt{2}p_5}\right)$

The parameter p_9 corresponds to the width of a bin of the histogram. In this peak fitting, the parameter p_3 directly shows the integrated counts of the peak. Figure 3.10 is an example of the peak fitting with a sample spectrum.

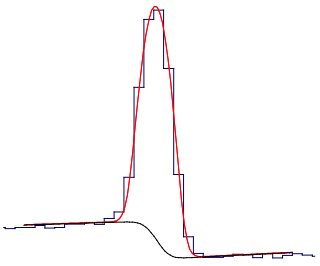

Figure 3.10 An example of the peak fitting of a sample spectrum with stair-wise background. The black line shows the background component of the fitting function (red line).

3.2.2 Energy calibration

Pulse heights of the Ge-detector signals were computed to 16 bit precision on the DGF processor. Pulse-height-to-energy calibration of the Ge detectors was carried out before and after the experiment using two standard sources, ^{152}Eu and ^{133}Ba. The ^{133}Ba source emits γ ray with 81 keV. Since the targeted nuclei of this study in $A \sim 150$ to 160 region tend to have low first 2^+ energy as ~ 60 keV, the low energy γ ray of ^{133}Ba was employed in the calibration. The γ-ray spectrum of ^{152}Eu and ^{133}Ba measured at the same time is shown in Figure 3.11. The calibration function for each crystal was obtained by chi-square fitting of γ-ray energy (E_γ) vs.

peak centroid (A_{DGF_ch}) plot with linear function,

$$E_\gamma = p_0 + p_1 A_{DGF\_ch}. \quad (3.15)$$

The gain shifts were estimated by comparing the γ-ray peaks of ^{152}Eu source before and after the experiment. The plot of the energy differences are shown in Figure 3.12. The standard deviation of the energy differences (σ_{std_dev}) was ~ 0.03 keV, while the statistical error σ_{stat} was,

$$\sigma_{stat} = \left(\sqrt{\sum \frac{1}{\sigma_i^2}}\right)^{-1} \sim 0.004 \text{ keV}. \quad (3.16)$$

This indicates that the deviation of the energy differences are mainly from gain shifts and thus the uncertainty due to gain shifts during the experiment was estimated to be ~ 0.03 keV.

Figure 3.13 shows the energy resolution of the whole array which was deduced from the peak width of ^{152}Eu spectrum. The energy resolution at 1408 keV was 0.09 % in sigma (2.9 keV in FWHM). The effect of the gain shift is much smaller than the energy resolution and will not significantly broaden the peak.

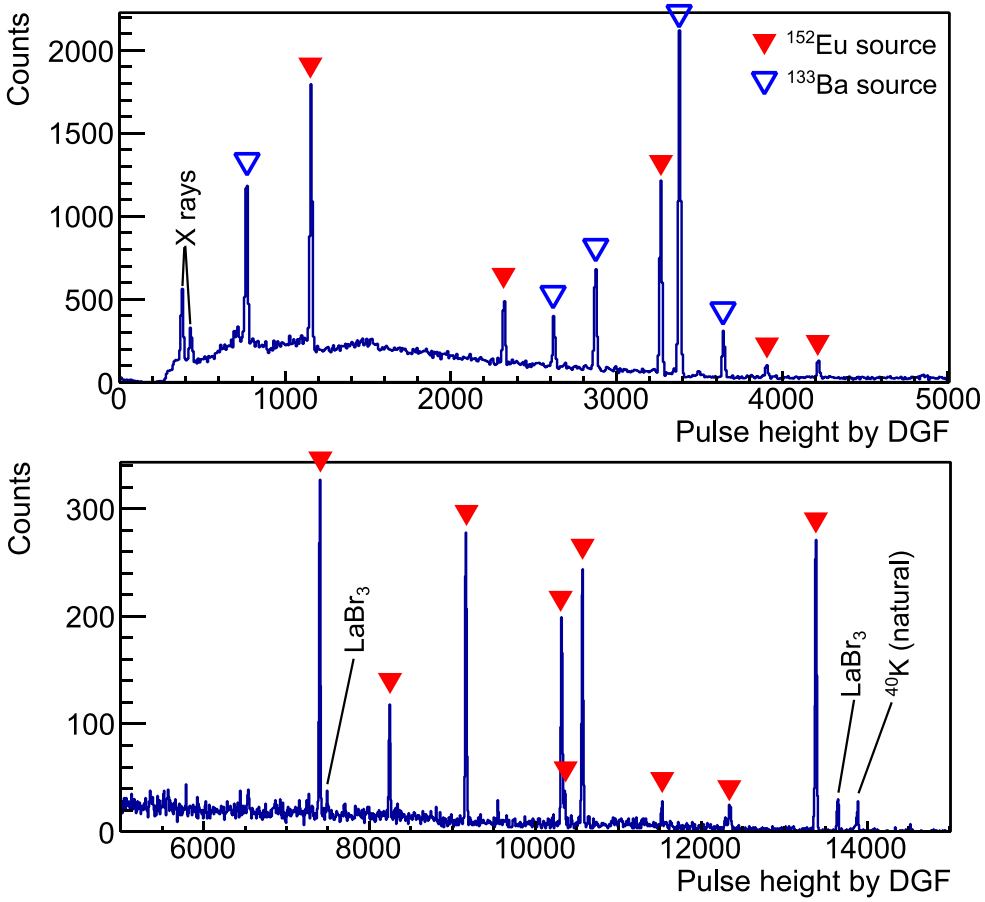

Figure 3.11 A sample γ-ray spectrum of a single crystal with ^{133}Ba and ^{152}Ba sources. The two peaks that corresponds to 789 and 1436 keV originate in ^{138}La in the $LaBr_3$ detectors.

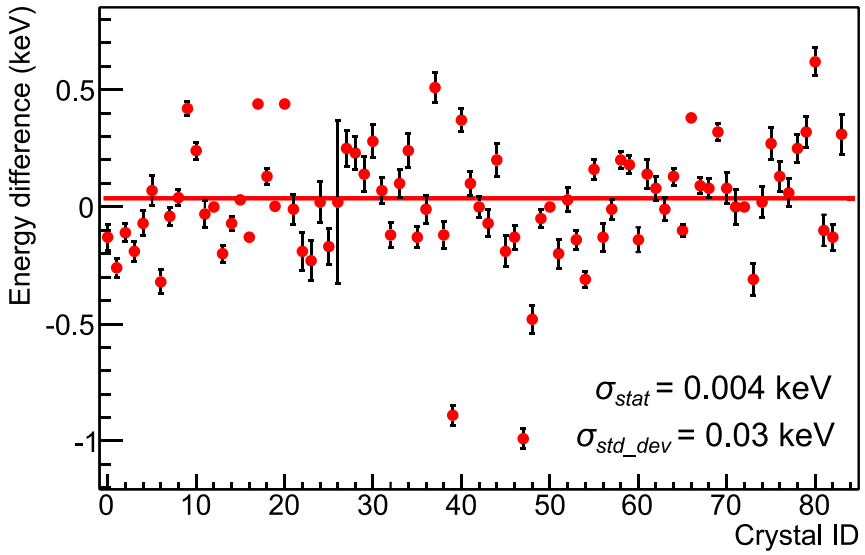

Figure 3.12 Energy differences of the 1408 keV peak in ^{152}Eu spectra obtained before and after the experiment.

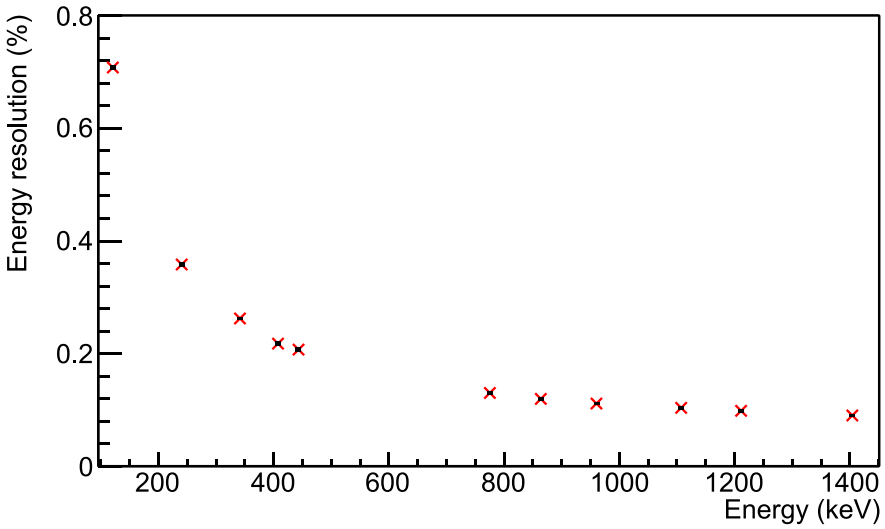

Figure 3.13 Energy resolution of the total spectrum of EURICA array.

3.2.3 Timing and slew correction

Timing information of the hit of Ge crystals relative to the timing of beam implantation is required to obtain the time spectra for isomer analysis. Figure 3.14 shows the timing vs. energy spectrum of beam implantation events for one Ge crystal. The prompt component of low energy part "slews" to later direction due to the characteristic of discrimination. This slewing curve is obtained by fitting the peak points of each energy bin by the function (3.17).

$$T = T_0 - p_0 - \frac{p_2}{\sqrt{E - p_1}} - \frac{p_3}{E - p_1} - \frac{p_4}{(E - p_1)^2} \tag{3.17}$$

By using this function, the prompt components of all the energies and all the crystals are corrected to be zero so that one can obtain the timings of γ hits relative to those of beam implantation.

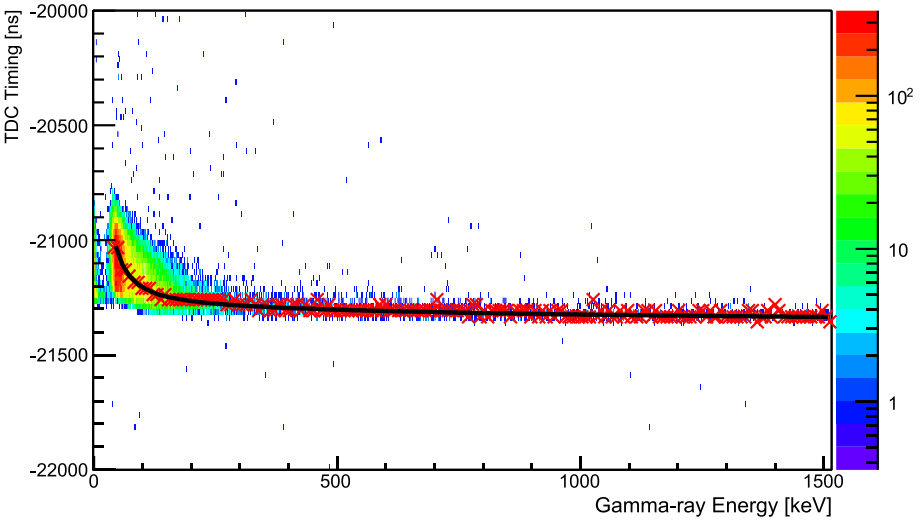

Figure 3.14 Timing vs. energy correlation of a Ge crystal. The black line shows the function of slew correction that is obtained by fitting the points shown in red x-marks.

3.2.4 Efficiency calibration

The efficiency of detecting a γ ray as a full energy peak depends on its energy. The efficiency curve of the Ge cluster array was deduced by measuring standard γ-ray sources whose activities are known. Basically, in the range of γ-ray energy from tens keV to a few MeV, detection efficiency gets lower as the γ-ray energy gets higher. However, the absorption of the low energy γ rays by the target chamber and the detector window decreases the efficiency of the γ rays with ~100 keV or lower energy. Taking the absorption into an account, formula (3.18) was adopted as the efficiency curve [64].

$$\varepsilon(E_\gamma) = \exp\left[\{(p_0 + p_1X + p_2X^2)^{-p_6} + (p_3 + p_4Y + p_5Y^2)^{-p_6}\}^{-\frac{1}{p_6}}\right], \quad (3.18)$$

where,

$$X(E_\gamma) = \log(E_\gamma/E_1) \quad (3.19)$$

$$Y(E_\gamma) = \log(E_\gamma/E_2). \quad (3.20)$$

From p_0 to p_6 are free parameters and obtained by fitting data points measured with standard sources. E_1 and E_2 were fixed to be 100 keV and 1 MeV respectively in order to express lower energy part where the absorption is significant and higher energy part where it is not.

Standard sources of ^{152}Eu and ^{133}Ba were used to obtain the efficiency curve. The calibration data were taken with 1-kHz clock trigger, and the γ rays detected within 15 μs after the trigger were analyzed. The detection efficiency for a certain γ ray, ε_γ, is given by,

$$\varepsilon_\gamma = \frac{N_\gamma}{I_\gamma T_{real} f_{clock} T_{window}}, \quad (3.21)$$

where N_γ is the total number of counts in a certain γ-ray peak, I_γ is the absolute emission rate of the γ-ray, T_{real} is the real time of the measurement, f_{clock} is the frequency of the trigger clock (1 kHz), and T_{window} is the time window opened in one trigger (15 μs). The I_γ values were taken from the specification notes of the standard sources at RIBF. Addback

algorithm was not implied in this efficiency and all the analysis related to intensity of γ rays.

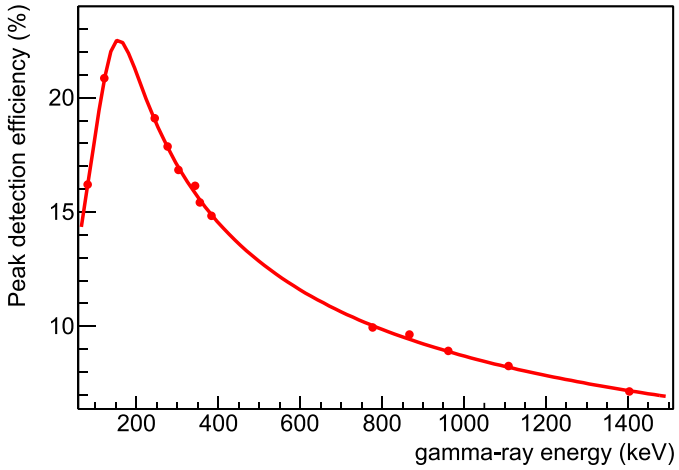

Figure 3.15 The efficiency curve of the Ge cluster array for γ-ray detection as a full energy peak.

3.2.5 Add back

The cluster-type Ge detector consists of 7 crystals with hexagonal cylindrical shape which are arranged one in the center and the other six surrounds it hexagonal way. Since the full energy peak of a γ ray is the interest, Compton-scattered events with its energy deposit on to several crystals should be added back to reconstruct the original energy of the γ ray. Energies of neighboring crystals in a detector within a time window of 300 ns were assumed to be a Compton-scattered event, and added to be one hit. Timing information of the crystal with highest energy deposit was regarded as the timing of the added hit. This is because the time resolution is better in the events with higher energy. Schematic view of this algorithm is shown in Figure 3.16. The effectiveness of add back algorithm was shown in Figure 3.17 with standard sources of ^{152}Eu and ^{133}Ba. The background level of the Compton part, especially in low energy region, reduced and the peak counts enhanced. By applying this add back algorithm, the full energy peak to Compton background ratio improves in γ-ray spectra.

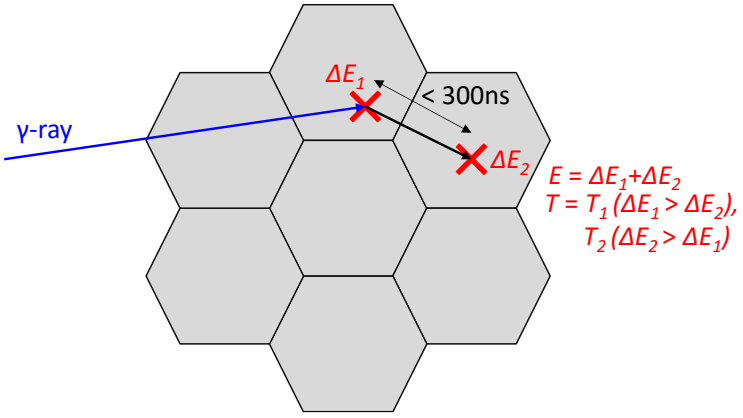

Figure 3.16 Schematic illustration of the addback algorithm for the cluster Ge detector.

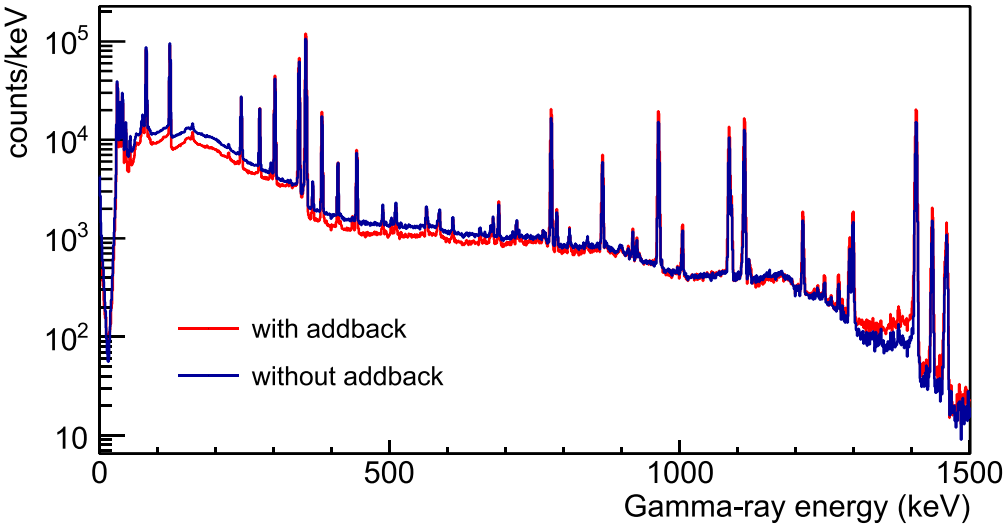

Figure 3.17 Comparison between spectra with and without add back. Standard sources of ^{152}Eu and ^{133}Ba were placed at the center of the array.

3.2.6 γ-γ coincidence

Coincidence hits of neighboring crystals of a cluster were added back to reconstruct full energy peak as shown in Section 3.2.5. On the other hand, coincidence hits between different clusters are not likely to be Compton-scattered events, but events with multiple γ-ray emission. The analysis of such γ-γ coincidence events is important in order to assign excited levels from γ-ray spectrum. The time difference window was set to ±300 ns from the time difference spectra between different Ge detectors shown in Figure 3.18.

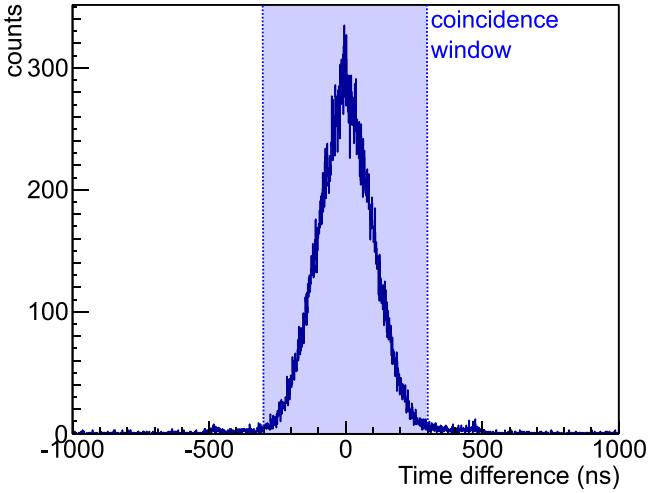

Figure 3.18 Time difference between different Ge detectors. The coincidence window was set to ±300 ns

3.3 Analysis of Si detectors

3.3.1 Timing calibration

Timing signals of the Si strips relative to the beam implantation are used to derive the x and y positions of the beam implantation in WAS3ABi. Thus, it is important to correct relative

offsets between strips. Slew correction improve the timing resolution of low energy part which may improve the signal to noise ratio when cutting out γ events correlated with β decay. Slewing effects of the Si strips were corrected by fitting the timing vs. energy spectra of Si detector for Compton scattered γ rays of ^{60}Co source, relative to the slew-corrected timing of Ge hits. Figure 3.19 (a) shows the slewing curve of a Si timing. The curve was fitted by the function of (3.17) with p_4 fixed to be zero and corrected as shown in Figure 3.19 (b). The relative offset of timing is defined as the fastest peak in the time spectrum of beam implantation events. As shown in Figure 3.20, the fastest component of the timing spectra of each strip for the beam implantation events were fitted and aligned with each other.

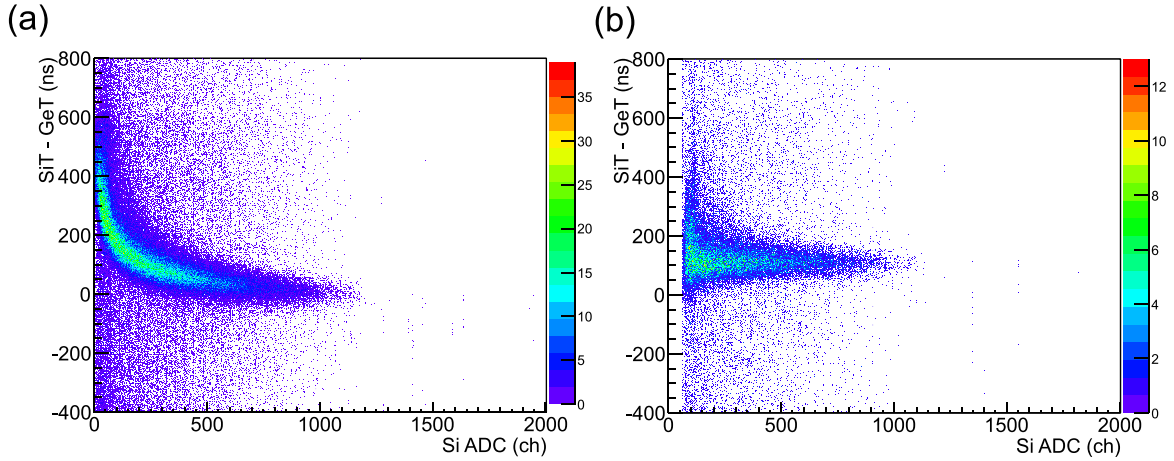

Figure 3.19 Timing vs. energy spectra of a Si strip before (a) and (b) after the slewing correction.

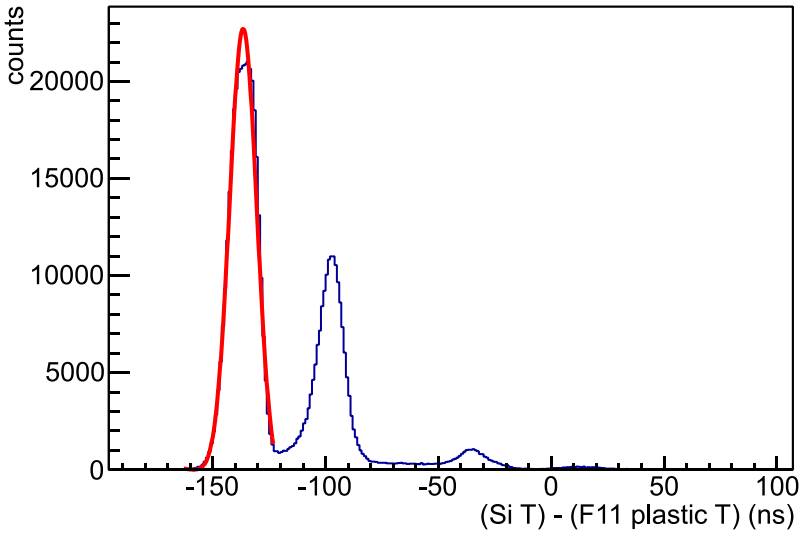

Figure 3.20 Timing spectrum of a Si strip relative to the timing of beam implantation at the F11 plastic scintillator. The fastest component was fitted by Gaussian function with linear background which is plotted in the red curve.

3.3.2 Energy calibration

The pulse height information of each strip of the WAS3ABi detector was digitized by ADC modules with the dynamic range up to ~ 4 MeV. For the energy calibration of WAS3ABi,

Compton scattered γ rays of ^{60}Co source was employed. When a γ ray is scattered in the Si and the scattered photon deposits its energy in a Ge detector, the sum of the energy losses at Ge and Si detectors will equal to the energy of the original γ ray. The linear correlations of 1173 and 1333 keV γ rays of ^{60}Co between Ge and Si detectors can be observed as shown in Figure 3.21. The energy can be calibrated by using these correlations.

The ADC gains were extracted from the linear correlations by minimizing the peak width of the Compton events projected on to a rotated axis by changing the rotation angle. Figure 3.22 (a) and (b) shows the projected spectrum and the fitting of the peaks of the Compton events, respectively. The fitting was repeated again and again by changing the rotation angle, then the angle minimizing the peak width was deduced as shown in the Figure 3.22 (c). The gain of the Si strip can be obtained as $\tan\theta_{min}$. Since the energy resolution of Ge detector is much better than that of Si, the peak width of the projected spectrum σ_{peak} can be approximated as,

$$\sigma_{peak} \approx \sigma_{SiADC} \cdot \sin\theta_{min}, \tag{3.22}$$

where σ_{SiADC} is the energy resolution of Si in channel. The gain of the Si energy is $\tan\theta_{min}$, therefore, the energy resolution of the Si strip can be expressed as follows.

$$\sigma_{\mathrm{SiE}} = \sigma_{peak}/\cos\theta_{min} \tag{3.23}$$

The typical peak width at θ_{min} varies in the range from 8 to 13, which means the typical energy resolution of Si strips is from 14 to 23 keV in FHWM.

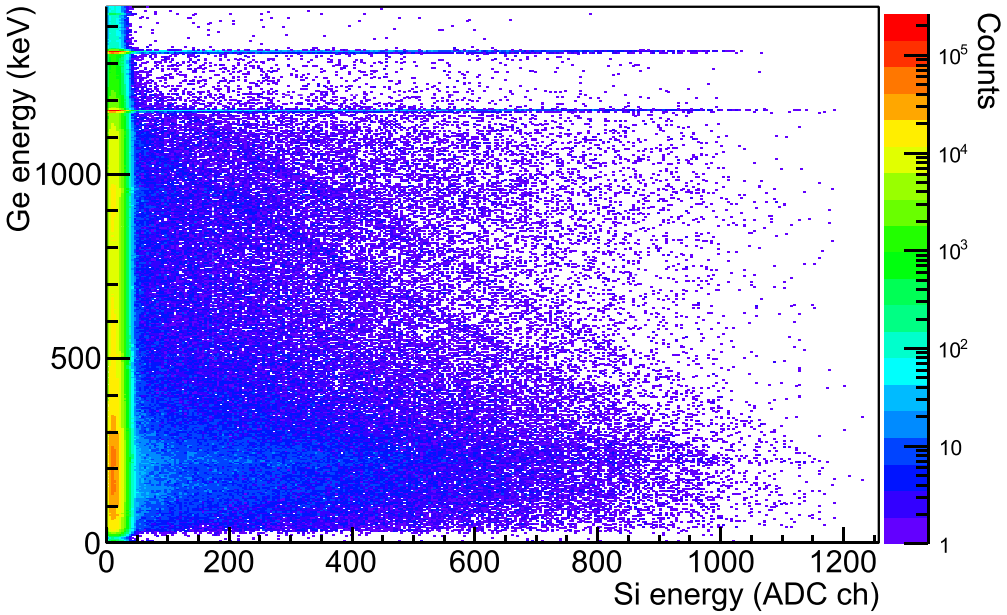

Figure 3.21 Energy correlation between Ge detectors and a certain Si strip of WAS3ABi. The energy of the Ge detectors are calibrated as described in Section 3.2.2

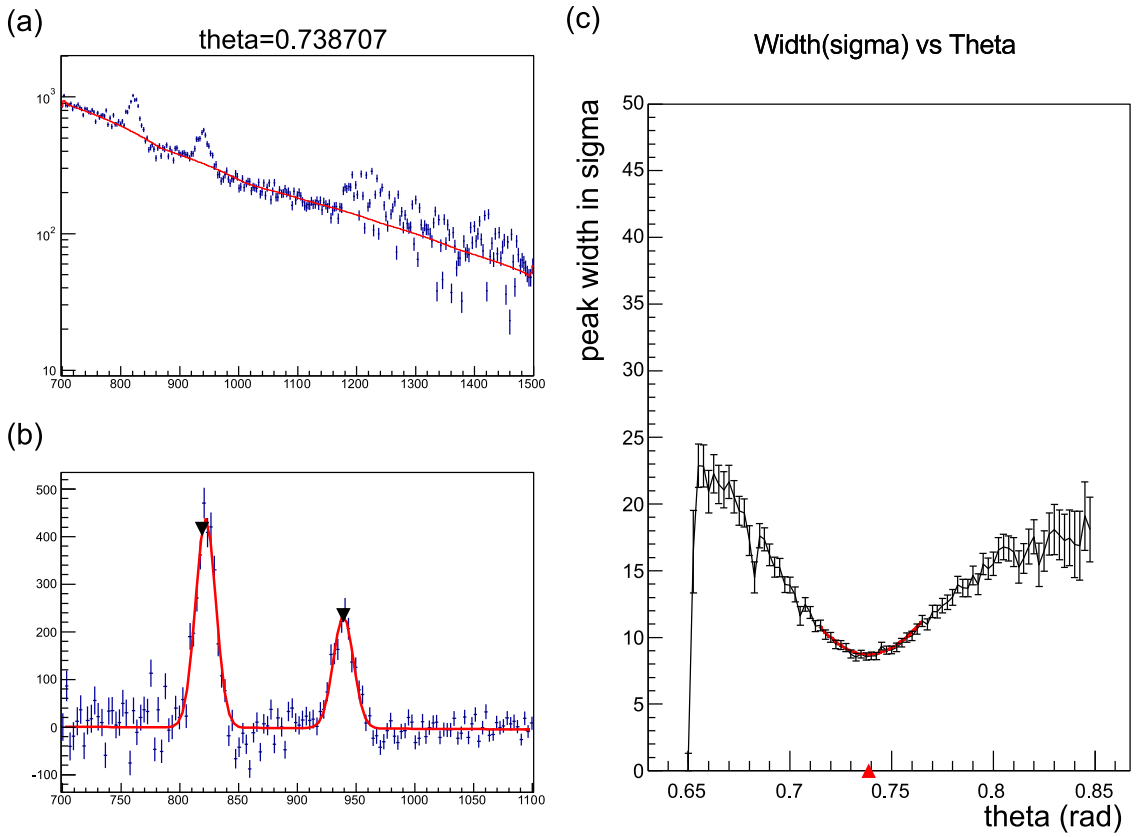

Figure 3.22 (a) Projection of the spectrum in Figure 3.21 on to the axis rotated 0.74 rad from the x axis. The red line shows the background to be subtracted in figure (b). (b) Two peaks of the Compton scattered events with linear correlation between Ge and WAS3ABi, fitted by two Gaussian functions. (c) A plot of the width of the peaks vs. the rotation angle of projection axis. The red marker on the x axis shows the minimum point of the width.

3.4 Procedure of isomer analysis

For isomer analysis, only the beam implantation events were analyzed. The DAQ system of EURICA cluster is triggered by F11 plastic or WAS3ABi, while the DAQ of BigRIPS is triggered by F7 plastic. The time stamp of the EURICA events which were triggered by F11 plastic was compared with that of BigRIPS and merged if the time difference is in a certain time window.

3.4.1 Energy spectra of delayed γ rays

The γ-ray hits close to the timing of beam implantation are contaminated with a background with continuum energy. This prompt background was cut by the following condition.

$$T_\gamma > \frac{p_0}{\sqrt{E_\gamma}} + p_1 \tag{3.24}$$

This curve is shown in Figure 3.23 as a red curve with $p_0 = 3000$, $p_1 = 50$. For the analysis of γ-ray intensities, $p_0 = 0$, $p_1 = 400$ was employed to avoid energy dependent cut. Energy spectra were obtained by projecting delayed hits on to the E_γ axis. The upper time limit was

changed depending on the life of the isomer.

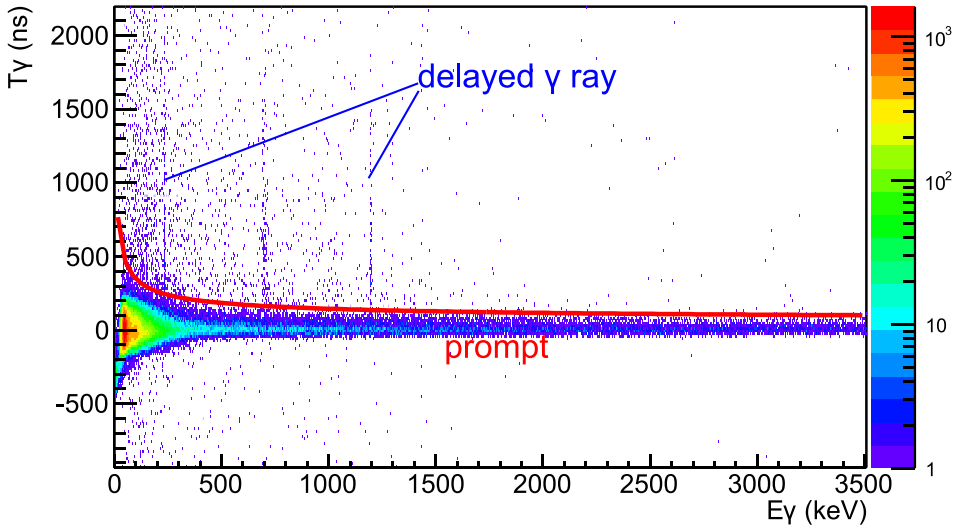

Figure 3.23 The timing vs. energy histogram of Ge detectors for ^{158}Nd. The hits below the red curve were regarded as the prompt background and excluded. The vertical stripes pointed by the blue lines show the full energy peaks of delayed γ rays.

3.4.2 Timing spectra and half-life analysis

The half-lives of the delayed γ rays were obtained by fitting the timing spectrum with the function that consists of exponential decay and constant background. The fitting function is,

$$I(t) = I_0 2^{-t/T_{1/2}} + C. \quad (3.25)$$

There is a known K-isomer in ^{156}Nd reported in [25]. Figure 3.24 shows the timing spectrum of the isomeric γ ray at 155 keV. The half-life of the decay was obtained to be 0.31(3) μs by fitting the timing spectrum which agrees with the known half-life of the isomer, 0.37(15) μs, within the range of the errors.

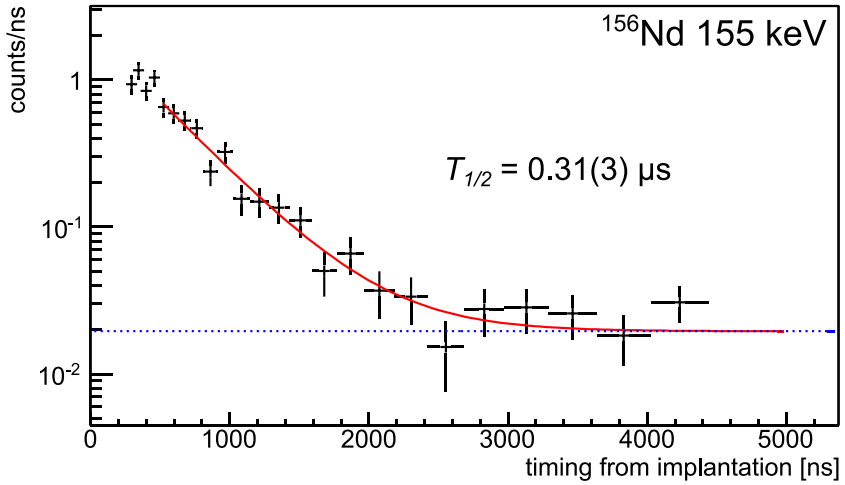

Figure 3.24 Timing spectrum of the 155 keV γ ray of ^{156}Nd. The red line shows the fitting function described as equation (3.25). The dashed blue line shows the fitted constant background parameter, C. The half-life of this decay spectrum is obtained as 0.31(3) μs.

3.5 Procedure of β-γ analysis

For β-γ analysis, the events of EURICA and WAS3ABi DAQ systems were merged and the events with which no BigRIPS event was merged were analyzed as β-γ events. The events with BigRIPS data were analyzed to obtain which nuclide implanted to which pixel of WAS3ABi. The A/Q and Z values of implanted ions were stored pixel-by-pixel with the timestamp. Position of the β-ray emission was obtained for each β-γ event and the event was tagged by the information of parent nuclide stored in the pixel at the deduced position if the timestamp difference was less than 10 s. The procedure of the analysis for obtaining the position of implantation and β emission is described in the following subsections.

3.5.1 Analysis of the beam implant position

Energy information of the DSSSD strips of WAS3ABi was optimized for β-ray energy and implantation energies of heavy ions were not measured because of the huge number of readout strips. The x-y position of beam implantation at WAS3ABi was derived from leading-edge timing information of each x and y strips of the DSSSD. Figure 3.25 shows the principle of energy determination. Even when the analog signal was so large that ADC was overflowed, leading edge timing (up-cross point of a threshold level) distribute by the pulse height of the signal. As the timing offset of each strip aligned as shown in section 3.3.1, the strip with the largest pulse height will have the fastest leading edge timing. Figure 3.26 (a) shows the timing spectrum of beam implantation events as a function of strip ID for the second layer of DSSSD. There are several components after the fastest component aligned to $t = 0$ by the calibration. The same spectrum only with the events when the strip #40 of the first layer of DSSSD was hit by heavy ion is plotted in Figure 3.26 (b). The fastest component was appeared only in strip #40 which is expected to be hit by heavy ion. This plot shows that the strip on a heavy ion trajectory can be identified by taking the strip with fastest timing around $t = 0$. The implantation depth was deduced by looking at the last layer with overflowed ADC data along the beam axis. Dynamic range of the ADC was adjusted to be 3.5 to 4 MeV for β-ray measurement, which is much smaller than the energy deposit of heavy ions. Therefore, layer without overflow ADC channel was assumed that heavy ion did not passed.

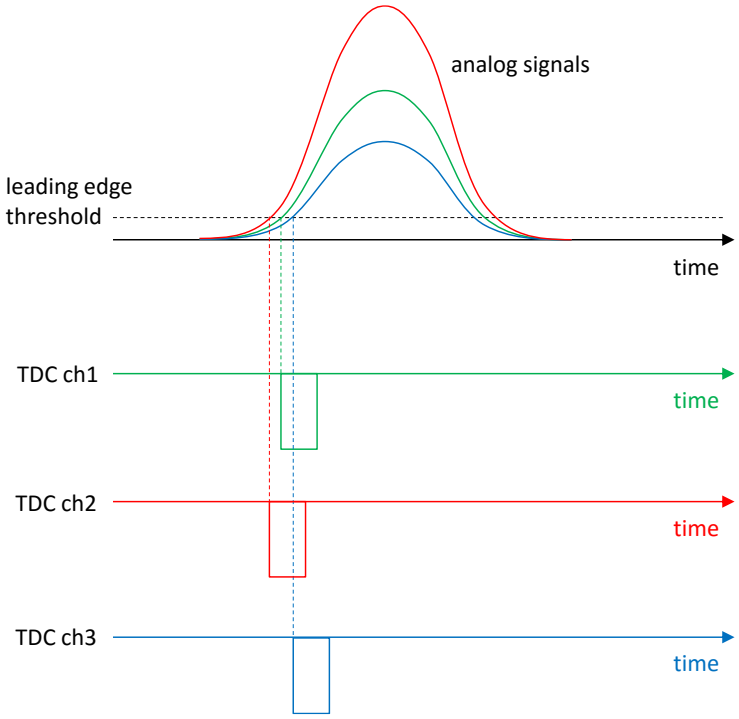

Figure 3.25 Principle for obtaining energy information from leading edge timing of analog signal from DSSSD.

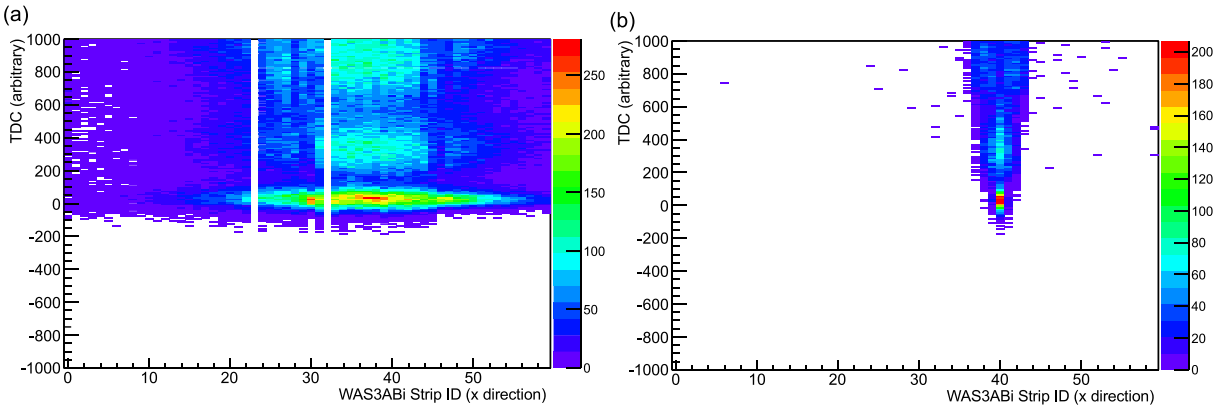

Figure 3.26 Timing spectra as a function of strip ID for the ground side (x direction) of WAS3ABi DSSSD. (b) is gated on the condition that strip ID = 40 in one layer upstream was hit by heavy ion.

3.5.2 Analysis of the position of beta emission

Analysis to obtain the position of the β-ray emission was applied to the events with no BigRIPS event merged and those in which the plastic counters at F11 focal was not fired. Since the width of DSSSD strips was as narrow as 1 mm, energy deposit of a β ray often distributed into several strips. The addback algorithm similar to that applied for cluster Ge detectors (described in Section 3.2.5) was also applied for β-ray events of DSSSDs. Energies in neighboring strips of a DSSSD with 200-ns window were summed up as one β-ray hit. Energies detected in non-neighboring strips were regarded as independent β-ray hit. Position of a β-ray emission was defined as the weighted mean position of energy deposits in summed

strips. This addback and position extraction procedures were applied each of the ground and bias side of a DSSSD, and then, the x, y positions of a β-ray emission.

β-decay events were obtained by merging events with heavy ion implantation and β-ray emission. In this thesis, β-ion correlation of the following condition was employed.

$$\sqrt{\left(x_\beta - x_{ion}\right)^2 + \left(y_\beta - y_{ion}\right)^2} < 1, \left|z_\beta - z_{ion}\right| = 0 \tag{3.26}$$

The position of ion implantation was only obtained as an ID of strip, position of the center of the strip was regarded as the implantation position. The correlation was taken only in one layer of DSSSD.

3.5.3 Determination of β-decay half-life

The β-decay half-lives were derived from the decay curves in timing spectra of the time stamp difference between β-ray detection events and the corresponding beam implantation events. Since the nuclei of interest in this study are quite neutron-rich, the total β-decay events consists of all the β decays of descendant nuclides. In order to obtain half-lives of one nuclide from the total decay curves without γ-ray coincidence, components of such descendant nuclides should be included to the fitting function.

The total number of β decays, N_β, of parent nuclide, X_0, and all the descendant nuclides, X_i, in an unit time can be written as,

$$\frac{N_\beta}{dt} = \sum_i \lambda_i X_i(t) + C, \tag{3.27}$$

where, λ_i is the decay constant of the nuclide, X_i, and $X_i(t)$ is the number of the nuclei, X_i. When the initial number of the parent nuclide is N_0, the number of parent nuclei is,

$$X_0(t) = N_0 e^{-\lambda_0 t}. \tag{3.28}$$

The differential equation of the number of descendant nuclei can be written by two components, feeding from their parent nuclei and decay of the descendant nuclei, as follows.

$$\frac{dX_i}{dt} = \lambda_{i-1} X_{i-1} - \lambda_i X_i \tag{3.29}$$

When $X_1(t=0) = 0$, the number of daughter nuclei is,

$$X_1(t) = N_0 \lambda_0 \left(\frac{e^{-\lambda_0 t}}{\lambda_1 - \lambda_0} + \frac{e^{-\lambda_1 t}}{\lambda_0 - \lambda_1} \right). \tag{3.30}$$

If β delayed neutron branch is open at the parent nuclide, the equation (3.29) should be,

$$\frac{dX_i}{dt} = P_{\beta n} \lambda_{i-1} X_{i-1} - \lambda_i X_i, \tag{3.31}$$

for the descendant nuclides of neutron branch, and,

$$\frac{dX_i}{dt} = P_\beta \lambda_{i-1} X_{i-1} - \lambda_i X_i, \tag{3.32}$$

for those of β^- branch. P_β and $P_{\beta n}$ shows the branching ratio of β decay and β delayed neutron decay respectively. All the components with half-life longer than the average interval of beam implantation at one pixel of WAS3Abi, say tens of seconds, are included as constant background, C. Decay curves in the timing spectra without γ-ray coincidence were fitted by the function (3.27). If the half-life of a descendant nuclide was known, it was fixed to the known

value in the fitting.

Once the γ rays of parent nuclide was identified, decay curves can be obtained by gating on the γ-ray energies. It selects the β-decay events only to the nuclide which have corresponding γ decay. The half-life can be derived by fitting the decay curve with γ ray coincidence by the function with much simpler formula,

$$\frac{N_{\beta\gamma}}{dt} = N_0 e^{-\lambda_0 t} + C. \tag{3.33}$$

Half-life determination for the nuclides whose $P_{\beta n}$ or the half-life of daughter nuclide is not known well, the latter method, fitting decay curves with γ-ray coincidence, is regarded as more reliable in this study.

Chapter 4 Experimental results

In this chapter, the results of the isomer and β-γ spectroscopy for each nuclide are presented in the following sections. The spectra shown in this chapter are from RIBF-86 experiment for $Z \leq 61$ isotopes and MS-11 experiment for those of $62 \leq Z$. There were isomers with similar half-lives and excitation energies observed systematically in $N = 98$ and $N = 100$ isotones and $Z = 65$ isotopes respectively. Each of those systematic isomers are assumed to originate in the same quasi-particle excitations. The results of the γ-ray spectroscopy on $N = 98$, $N = 100$ and $Z = 65$ nuclides are shown in Section 4.1 to 4.3. New candidate for a negative parity state of an octupole band was observed in ^{150}Ba by β-γ spectroscopy. The results on ^{150}Ba are shown in Section 4.4. There were excitations assigned to be the first 2^+ and 4^+ states in the most neutron-rich Ce isotope ever measured, ^{154}Ce. The results on ^{154}Ce are shown in Section 4.5. A ground-state rotational band was identified in ^{157}Pm by β-γ spectroscopy, which is shown in Section 4.6. Known isomer in ^{156}Nd was identified consistently with the previous work and some new γ rays were additionally observed by β-γ spectroscopy as shown in Section 4.7. Other results of the isomer spectroscopy are listed in Appendix C.

4.1 New isomers in $N = 98$ isotones

New isomers were systematically observed in $N = 98$ isotones. These isomers are assumed to be neutron two quasi-particle excitation with $K^\pi = 6^-$. Results of isomer spectroscopy on each nuclide and the level scheme construction are shown in the following subsections.

4.1.1 ^{159}Pm ($Z = 61$, $N = 98$)

New isomer and β decay were observed in this nuclide. Figure 4.1 shows the delayed γ-ray spectrum of ^{159}Pm. There were a lot of peaks observed in the spectrum. The time spectra of those peaks were shown in Figure 4.2 and Figure 4.3. The last figure in Figure 4.3 is a sum of the timing spectra of some intense γ rays. The half-life of the isomeric state was obtained to be 4.97(12) μs from the summed spectrum. Decay scheme of ^{159}Pm was proposed as Figure 4.4. The ground state was assumed to be $5/2^-$ from systematics [65] and a theoretical prediction [66]. A rotational band structure up to $(17/2^-)$ state at 654 keV was identified. As shown in Figure 4.5, the 330-keV γ ray has coincidences with 801, 669, 921 and 871 keV and also the γ rays of the ground-band members. The 644-keV γ ray has coincidences with the γ rays in the side band shown on the right-hand part of the figure. There were no coincidence observed between 330 and 664 keV. These results support the decay scheme. J^π of the isomeric state was tentatively assigned as $17/2^+$ which is interpreted as the coupling of the neutron two quasi-particle isomer with $K^\pi = 6^-$ (will be discussed in the next chapter) and odd proton in $\pi 5/2[532]^-$ orbital.

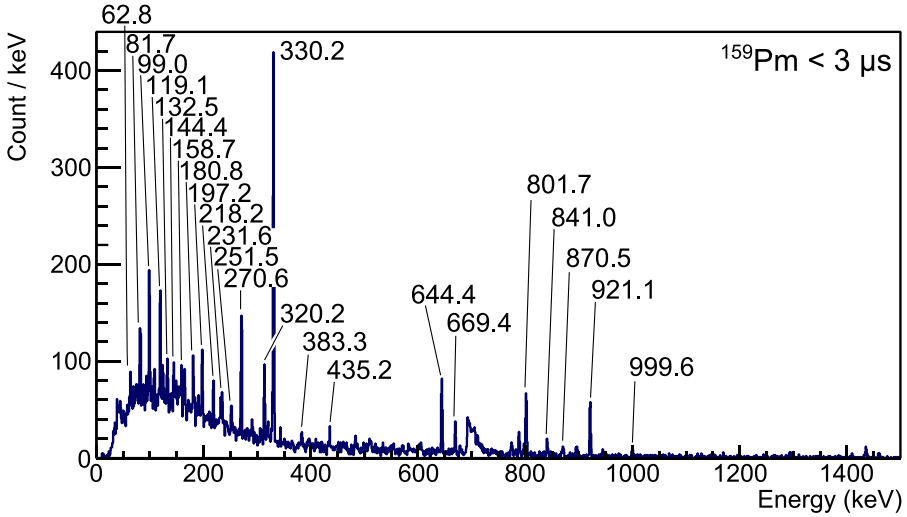

Figure 4.1 Energy spectrum of delayed γ rays from ^{159}Pm. The time window is up to 3 μs after the implantation.

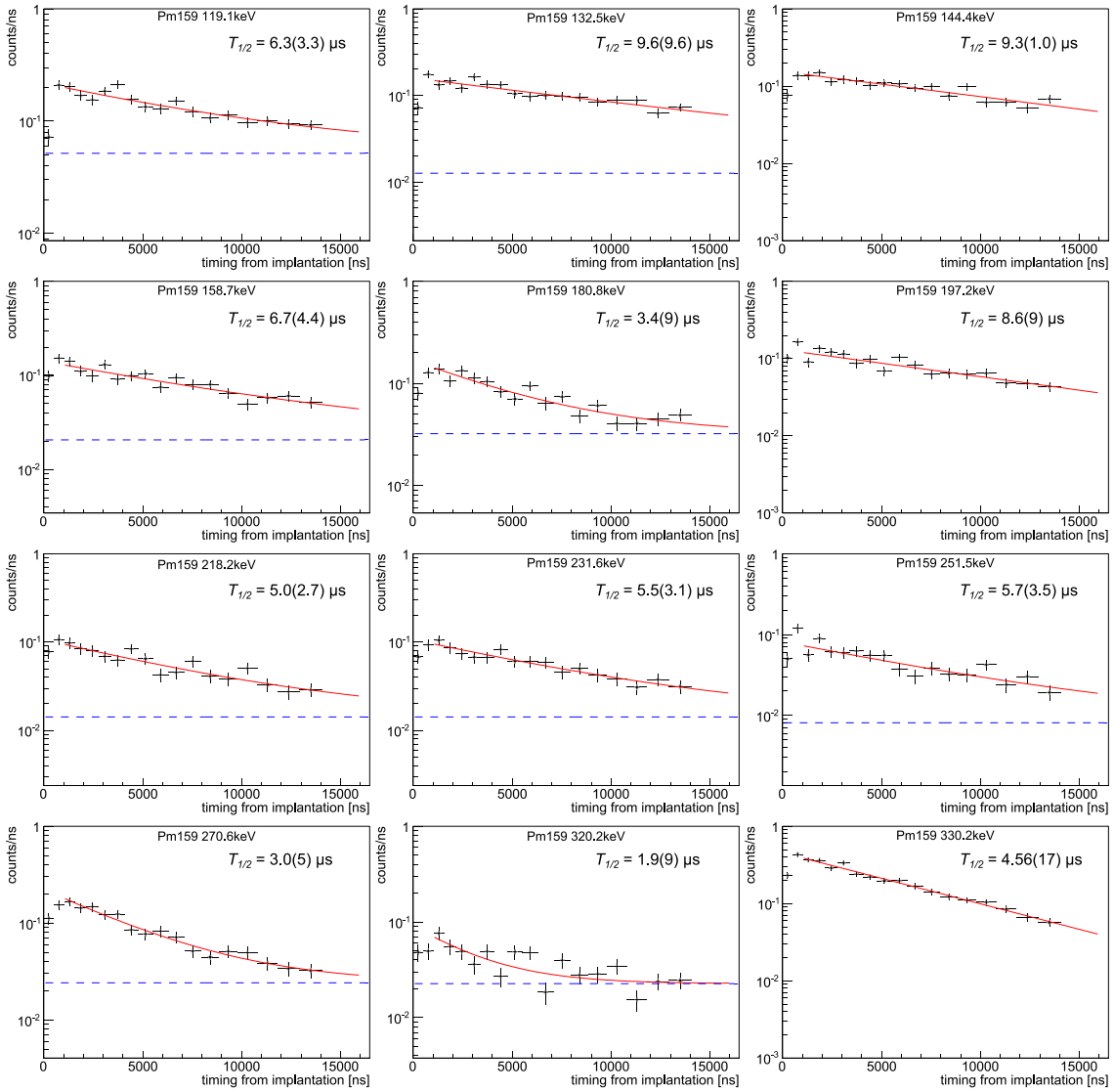

Figure 4.2 Time spectra gated on the peaks of delayed γ rays from ^{159}Pm.

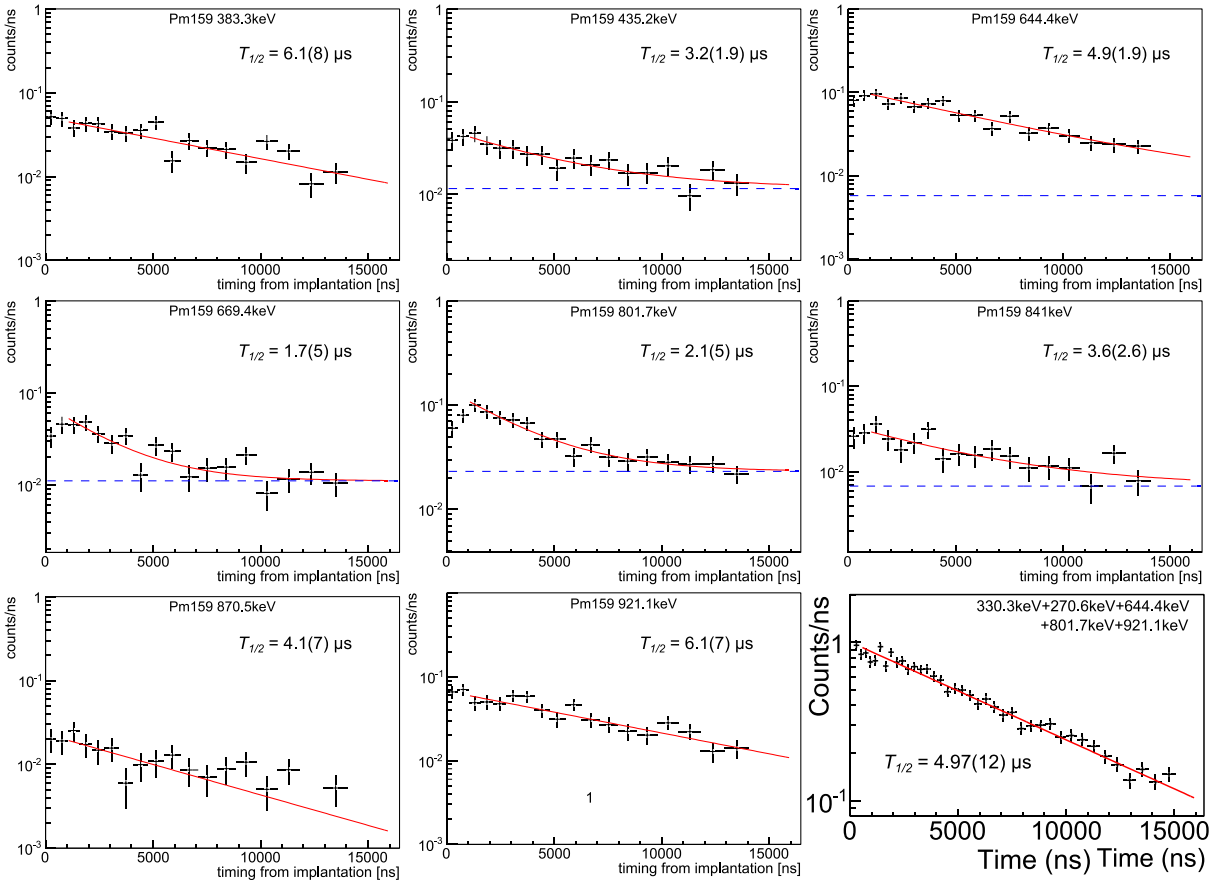

Figure 4.3 Time spectra gated on the peaks of delayed γ rays from ^{159}Pm.

Table 4.1 Summary of the new delayed γ rays observed in ^{159}Pm. $N_{implanted}$ is the total number of particles implanted in the experiment. I_{γ_rel} is the relative intensity of γ rays where I_{rel} represents the relative intensity of the decay derived by correcting internal conversion using BrIcc [67]. The 61.5-, 80.2-, 96.7- and 118.2-keV γ rays were assumed to be M1 transition, and the 177 keV γ ray was assumed to be E2 transition for the correction of internal conversion.

$N_{implanted}$	E_γ (keV)	$T_{1/2}$ (μs)	I_{γ_rel} (%)	I_{rel} (%)
	62.8	-	12(6)	84(41)
	81.7	-	33(8)	123(31)
	99.0	-	42(9)	110(22)
	119.1	6.3(3.3)	32(6)	62(11)
	132.5	9.6(9.6)	12(3)	20(5)
4.8×10^5	144.4	9.3(1.0)	6.3(2.3)	10(4)
	158.7	6.7(4.4)	8.1(2.7)	11(4)
	180.8	3.4(9)	8.7(1.9)	11.2(2.5)
	197.2	8.6(9)	14.2(2.3)	17(3)
	218.2	5.0(2.7)	9.3(1.7)	10.8(1.9)
	231.6	5.5(3.1)	8.2(2.1)	8.2(2.1)

$N_{implanted}$	E_γ (keV)	$T_{1/2}$ (μs)	I_{γ_rel} (%)	I_{rel} (%)
	251.5	5.7(3.5)	9.9(2.2)	10.8(2.4)
	270.6	3.0(5)	28.4(2.7)	28.4(2.7)
	320.2	1.9(9)	4.3(1.9)	4.3(1.9)
	330.2	4.56(17)	100(6)	100(6)
	383.3	6.1(8)	4.9(1.3)	4.9(1.3)
	435.2	3.2(1.9)	5.0(1.0)	5.0(1.0)
4.8×10^5	644.4	4.9(1.9)	34.5(2.3)	34.5(2.3)
	669.4	1.7(5)	11.8(1.5)	11.8(1.5)
	801.7	2.1(5)	35.1(2.4)	35.1(2.4)
	841.0	3.6(2.6)	8.7(1.3)	8.7(1.3)
	870.5	4.1(7)	6.5(1.1)	6.5(1.1)
	921.1	6.1(7)	31.4(2.3)	31.4(2.3)
	999.6	-	5.4(1.1)	5.4(1.1)

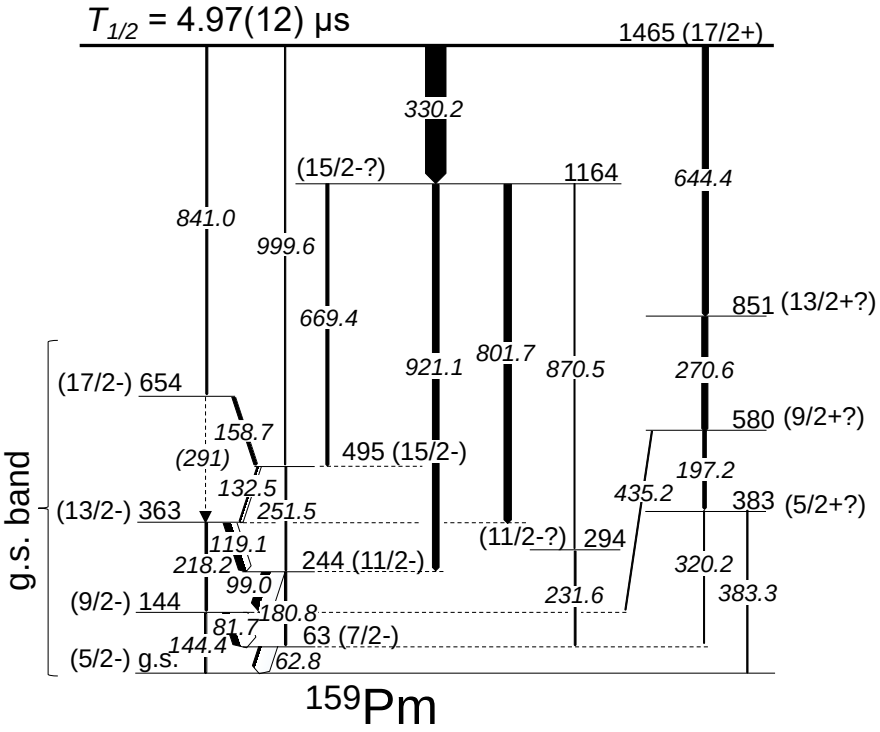

Figure 4.4 Decay scheme of the isomer in ^{159}Pm proposed in this work. The widths of the black part of the arrows are proportional to the γ-ray intensity, and the total widths of the arrows represent the decay intensities including internal conversions. The 291-keV γ ray with dashed arrow was distinguished only in γ-γ coincidence spectra.

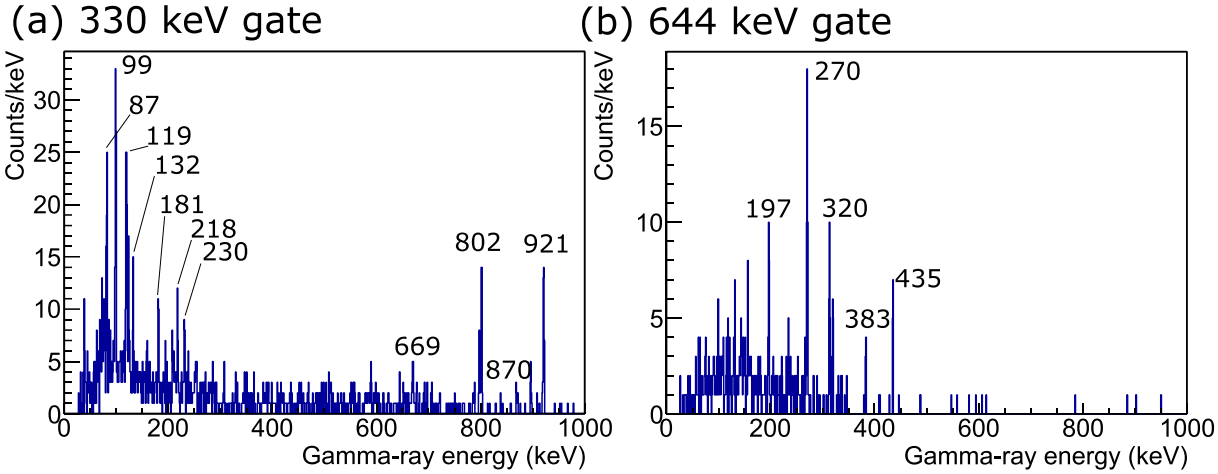

Figure 4.5 γ-ray energy spectra in coincidence with (a) 330- and (b) 644-keV γ rays.

4.1.2 ^{158}Nd ($Z = 60,\ N = 98$)

New isomer was observed in ^{158}Nd. Figure 4.6 shows the delayed γ-ray spectrum of ^{158}Nd with time window < 3 μs. Three γ-ray peaks were observed at 151.6, 233.4 and 1197.1 keV. Time spectra of those three γ rays agreed with each other as shown in Figure 4.7. The weighted average of the half-lives was 0.31(2) μs. Coincidences between all combinations of the three γ rays were confirmed as shown in Figure 4.8 and summarized in Table 4.2. From the coincidence result, the three γ rays can be assigned in a single cascade as shown in the decay scheme in Figure 4.9. The single cascade decay scheme is also supported by the relative intensities of the three γ rays as shown in the summary of the observed γ rays in Table 4.3. The 151.6- and 233.4 keV γ rays were assigned as $4^+ \rightarrow 2^+$ and $6^+ \rightarrow 4^+$ decays, respectively, because the energies are close to those of ^{152}Nd, ^{154}Nd and ^{156}Nd [25,68]. A delayed γ ray with energy corresponds to $2^+ \rightarrow 0^+$ was not observed. The energy of this transition was estimated to be 65.9(4) keV from the energy of $4^+ \rightarrow 2^+$ decay by using the average value of $E(4^+)/E(2^+)$ ratio, 3.31(1) (^{156}Nd) and 3.30(2) (^{160}Nd). One reason for not observing the 65.9 keV γ ray in this experiment is that it is expected to be highly converted to electron. The conversion coefficient of this decay calculated by BrIcc [67] is 10.2 that means only $\sim 9\%$ of the decay emit γ rays. One other reason is that ^{158}Nd was only well produced in the run using passive stopper made of Cu. This stopper plate absorbs low-energy photons more strongly than the WAS3ABi stopper that made of Si. The spin of the isomeric state at 1648 keV was assigned to be 6 because it only decays to 6^+ state. If the spin was 5, both the decays to 6^+ and 4^+ states should be observed, and if it was 7, the decay to 8^+ state should be observed. By assuming the 1197-keV peak as a decay from the state with spin 5 to that with 6^+, there should be $\sim$250 counts around 1431 keV as a direct decay to 4^+ state. It was estimated from the number of counts in 1197-keV peak by assuming branching ratio of $\Delta J = 1$ decays to be proportional to E_γ^3, and taking detection efficiencies into account. A peak with such a number of counts should be clearly seen in the spectrum and therefore, the assignment of spin 5 is refuted. By similar argument, spin 7 assignment is also refuted by non-observation of 8^+ to 6^+ decay which should be observed $\sim$150 counts at around 330 keV. The negative parity of the

isomeric state was tentatively assigned from the possible quasi-particle excitations which will be discussed in the next chapter.

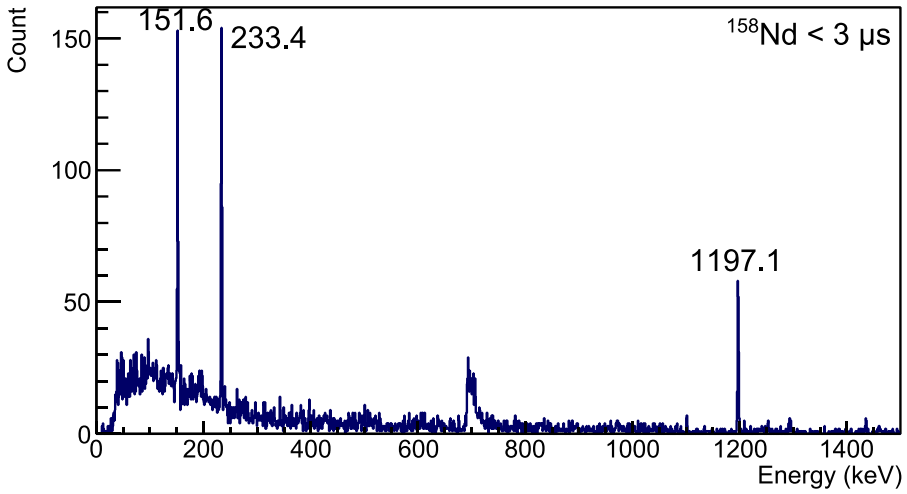

Figure 4.6 Energy spectrum of delayed γ rays from ^{158}Nd. The time window is up to 3 μs after the implantation.

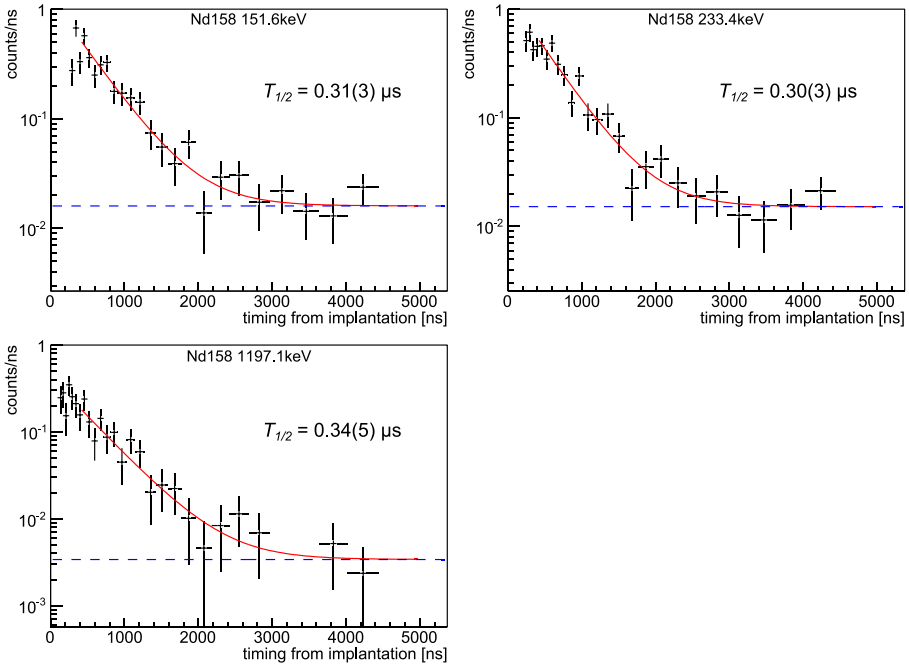

Figure 4.7 Time spectra gated on the peaks of delayed γ rays from ^{158}Nd.

Table 4.2 List of γ-ray coincidences in the isomeric decay of ^{158}Nd. Coincident γ rays are marked by ticks.

Energy (keV)	151.6	233.4	1197.1
151.6	gate	✔	✔
233.4	✔	gate	✔
1197.1	✔	✔	gate

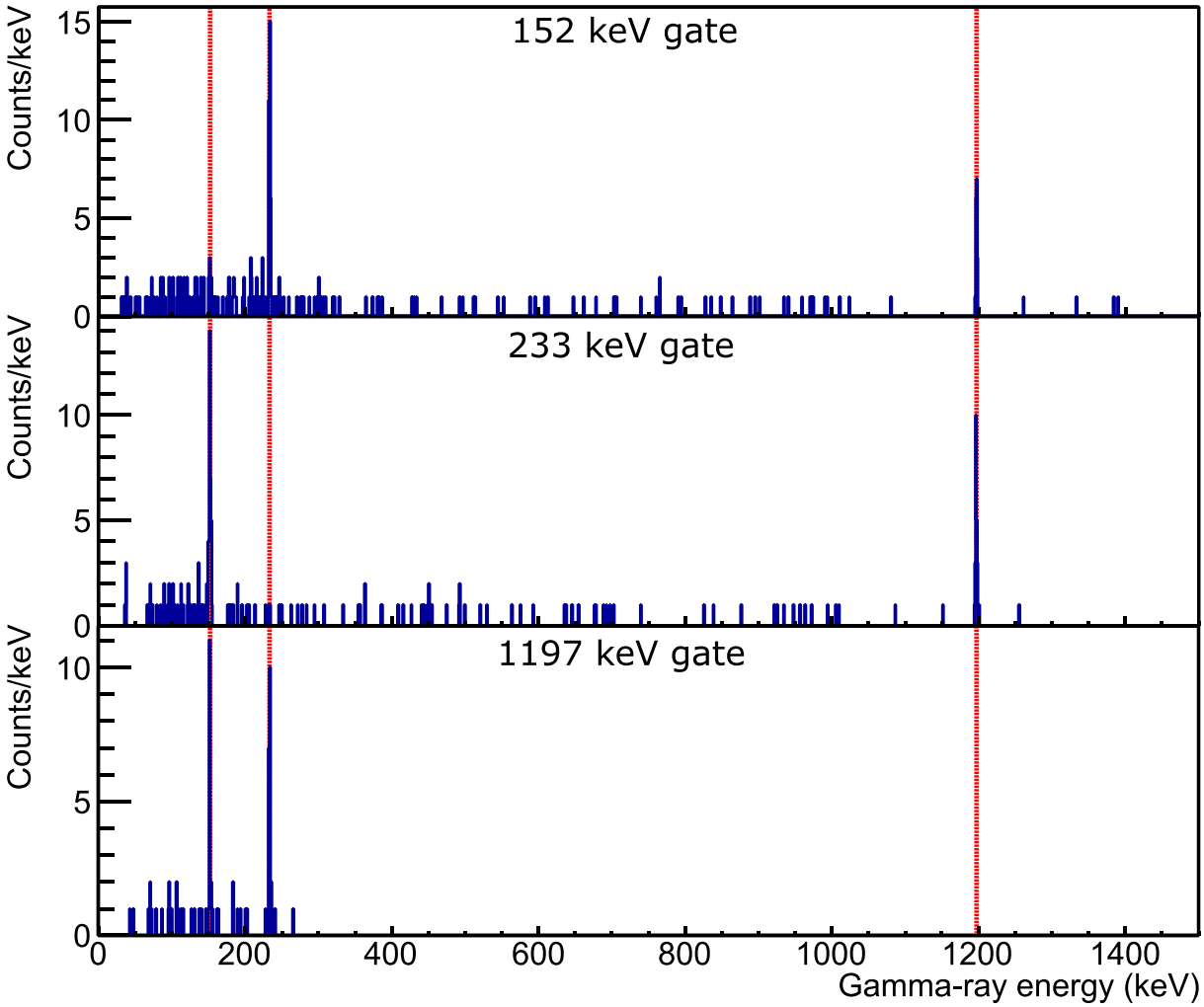

Figure 4.8 γ-γ coincidence spectra gated by 152-, 233- and 1197-keV γ rays.

Table 4.3 Summary of the new delayed γ rays observed in ^{158}Nd. $N_{implanted}$ is the total number of particles implanted in the experiment. I_{γ_rel} is the relative intensity of γ rays where I_{rel} represents the relative intensity of the decay derived by correcting internal conversion using BrIcc [67]. The 151.6- and 233.4-keV γ rays were assumed to be E2 transition for the correction of internal conversion.

$N_{implanted}$	E_γ (keV)	$T_{1/2}$ (μs)	I_{γ_rel} (%)	I_{rel} (%)
2.9×10^5	151.6	0.31(3)	57(4)	100(8)
	233.4	0.30(3)	81(5)	105(7)
	1197.1	0.34(5)	100(8)	116(9)

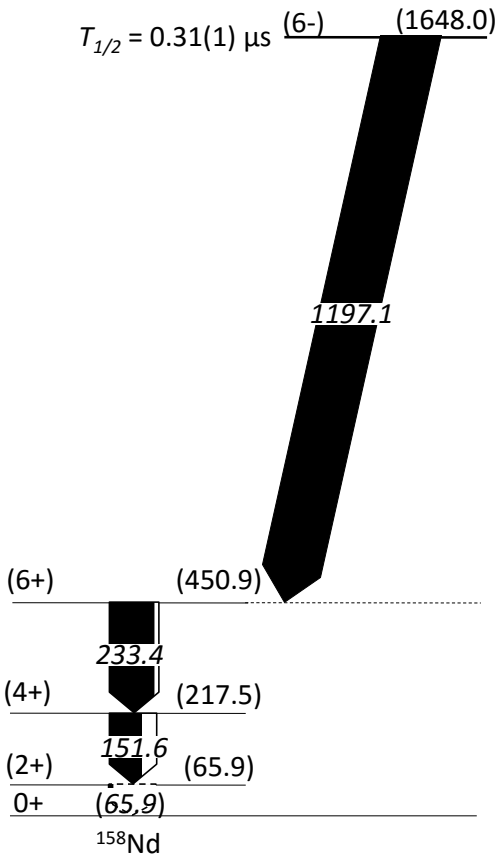

Figure 4.9 Decay scheme of the isomer in ^{158}Nd proposed in this work. The widths of the black part of the arrows are proportional to the γ-ray intensity, and the total widths of the arrows represent the decay intensities including internal conversions.

4.2 New isomers in $N = 100$ isotones

New isomers were systematically observed in $N = 100$ isotones. These isomers are assumed to be neutron two quasi-particle excitation with $K^{\pi} = 4^{-}$. Results of isomer spectroscopy on each nuclide and the level scheme construction are shown in the following subsections.

4.2.1 ^{164}Gd ($Z = 64,\ N = 100$)

The 72.0 and 168.0 keV γ rays in ^{164}Gd had been reported as $2^{+} \rightarrow 0^{+}$ and $4^{+} \rightarrow 2^{+}$ transition of the ground-state band [69]. In this work, new delayed γ rays were observed at 60.2, 854.1 and 961.9 keV as shown in Figure 4.10. Half-lives of those γ rays were obtained as shown in Figure 4.12. The weighted mean value of the half-lives was 0.57(2). The proposed decay scheme of ^{164}Gd was shown in . The isomeric state was assigned at 1094 keV since the energy sum of 961.9- and 60.2-keV γ rays and those of 168.9 and 854.1 keV were in good agreement. The spin of the isomeric state at 1094 keV was assigned as 4 because it only decays to 4^{+} state of the ground-state band and not to 2^{+} nor 6^{+} states. The parity was tentatively

assigned as negative from the systematics of 4^- isomers in $N = 100$ isotones which will be discussed in the next chapter. The transition with 60.2-keV γ rays was assigned as an E1 transition because the internal conversion coefficient of E1 transition reproduces the intensity conservation between 60.2- and 961.9-keV decays the best. On the assumption that the spin and parity of the isomeric state is 4^-, the 1034 keV state is expected to have 3^+, 4^+, or 5^+. $J^\pi = 3^+$ is the most probable candidate because it decays only to the 2^+ state of the ground-state band and does not decay to the 4^+ state. In the case of ^{168}Er, decay from $K^\pi = 4^-$ isomer to $J^\pi = 3^+$ state of a $K^\pi = 2^+$ γ-vibrational band is observed [70].

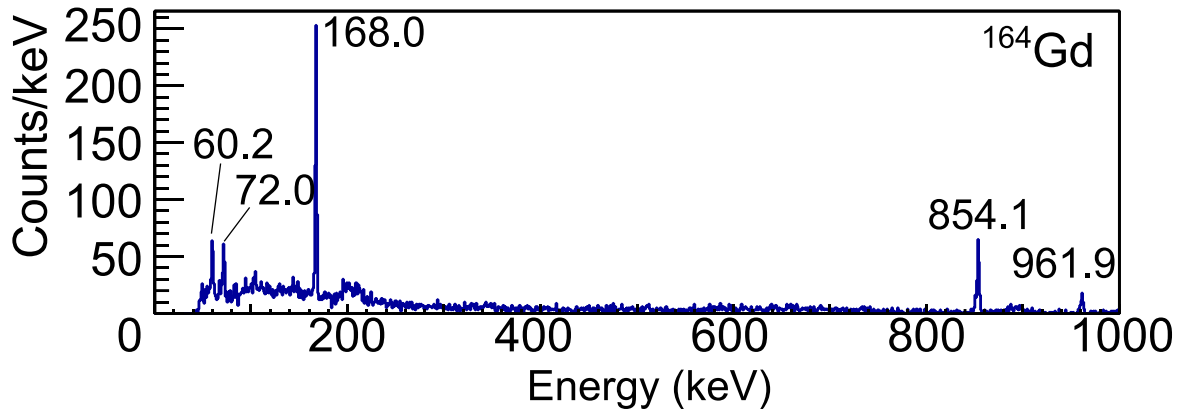

Figure 4.10 Energy spectrum of delayed γ rays from ^{164}Gd.

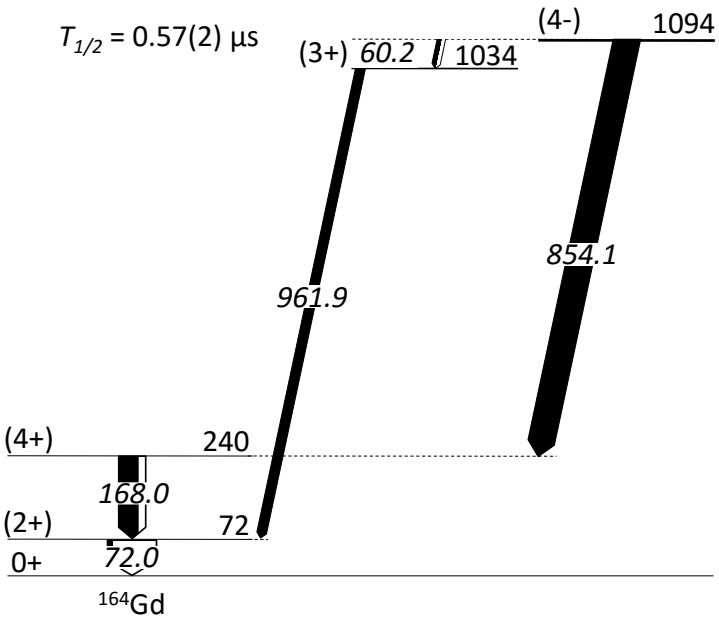

Figure 4.11 Decay scheme of the isomer in ^{164}Gd proposed in this work. The widths of the black part of the arrows are proportional to the γ-ray intensity, and the total widths of the arrows represent the decay intensities including internal conversions.

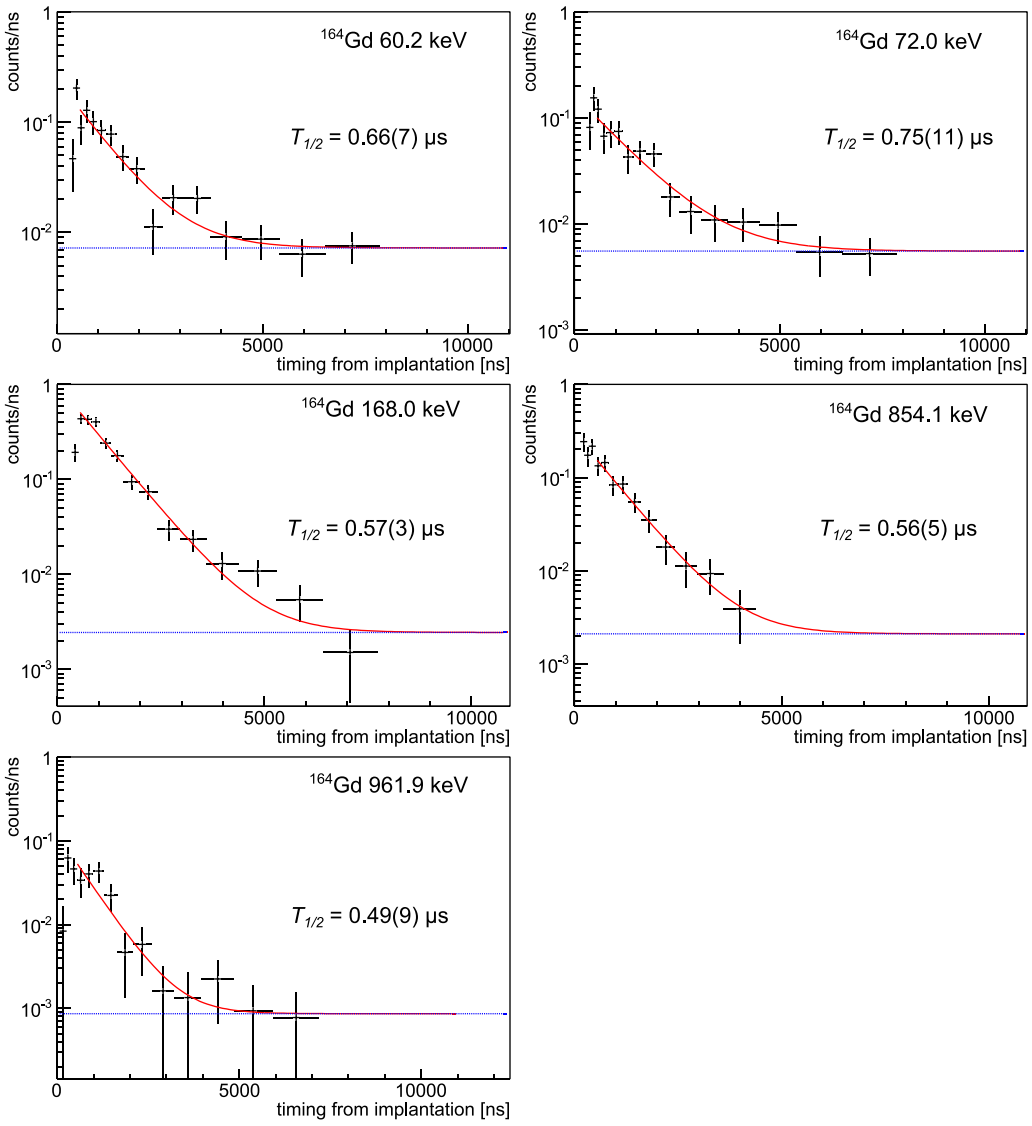

Figure 4.12 Time spectra gated on the peaks of delayed γ rays from ^{164}Gd.

Table 4.4 Summary of the new delayed γ rays observed in ^{164}Gd. $N_{implanted}$ is the total number of particles implanted in the experiment. I_{γ_rel} is the relative intensity of γ rays where I_{rel} represents the relative intensity of the decay derived by correcting internal conversion using BrIcc [67]. The 72 and 168 keV γ rays were assumed to be E2 transition, and that of 60 keV was assumed to be E1 transition for the correction of internal conversion.

$N_{implanted}$	E_γ (keV)	$T_{1/2}$ (μs)	I_{γ_rel} (%)	I_{rel} (%)
2.9×10^5	60.2	0.66(7)	14(3)	17(5)
	72.0	0.75(11)	19(4)	100(19)
	168.0	0.57(3)	71(5)	55(11)
	854.1	0.56(5)	100(11)	55(12)
	961.9	0.49(9)	37(7)	20(5)

4.2.2 ^{163}Eu ($Z = 63,\ N = 100$)

In ^{168}Eu, 8 delayed γ rays were newly observed in this work as shown in Figure 4.13. Half-lives of each γ-ray peaks were obtained as shown in Figure 4.14. The decay scheme proposed in this study is shown in Figure 4.15. The ground state of ^{163}Eu was tentatively assigned to be $5/2^+$ in [71] from systematics. In this case, the ground state is assumed to have the configuration of $\pi 5/2[413]$. The ground-state band was constructed up to 289-keV ($11/2^+$) state. The energies of the ground-state excitation well agree with the systematics in less neutron-rich Eu isotopes ^{157}Eu and ^{159}Eu [72]. Spin of the isomeric state was assigned as 13/2 since it decays only to $11/2^+$ state of the ground-state band. If the spin is higher or lower than 13/2, decays to other member of the ground-state band should be observed. The isomeric state can be interpreted as the coupling of the $K^\pi = 4^-$ neutron quasi-particle excitation known in $N = 100$ even-even nuclei and the $\pi 5/2[413]$ orbit as the ground state. Spin of the 708-keV state was assigned as 11/2 since it decays to $9/2^+$ state of the ground-state band. M1 assignment for the 256.1-keV transition rather explains relative intensities of the γ rays by the difference of conversion coefficient, which may indicate negative parity for the 708-keV state.

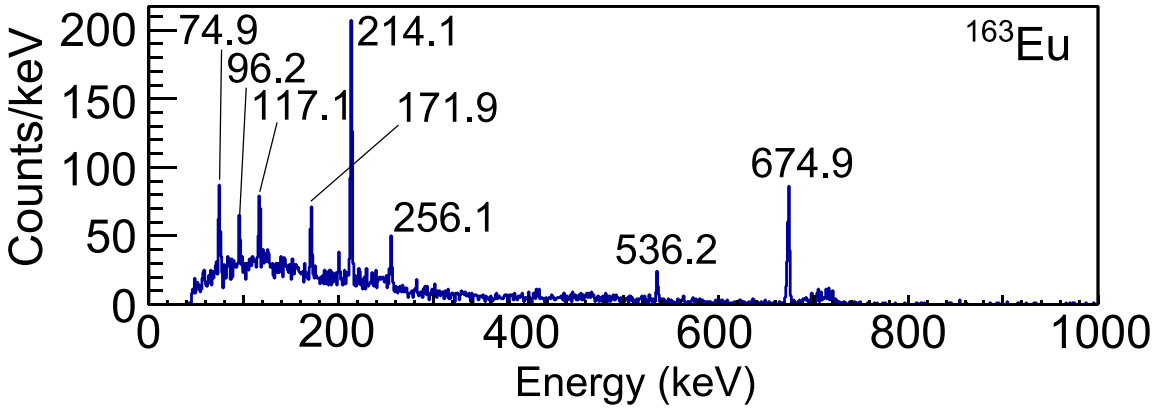

Figure 4.13 Energy spectrum of delayed γ rays from ^{163}Eu.

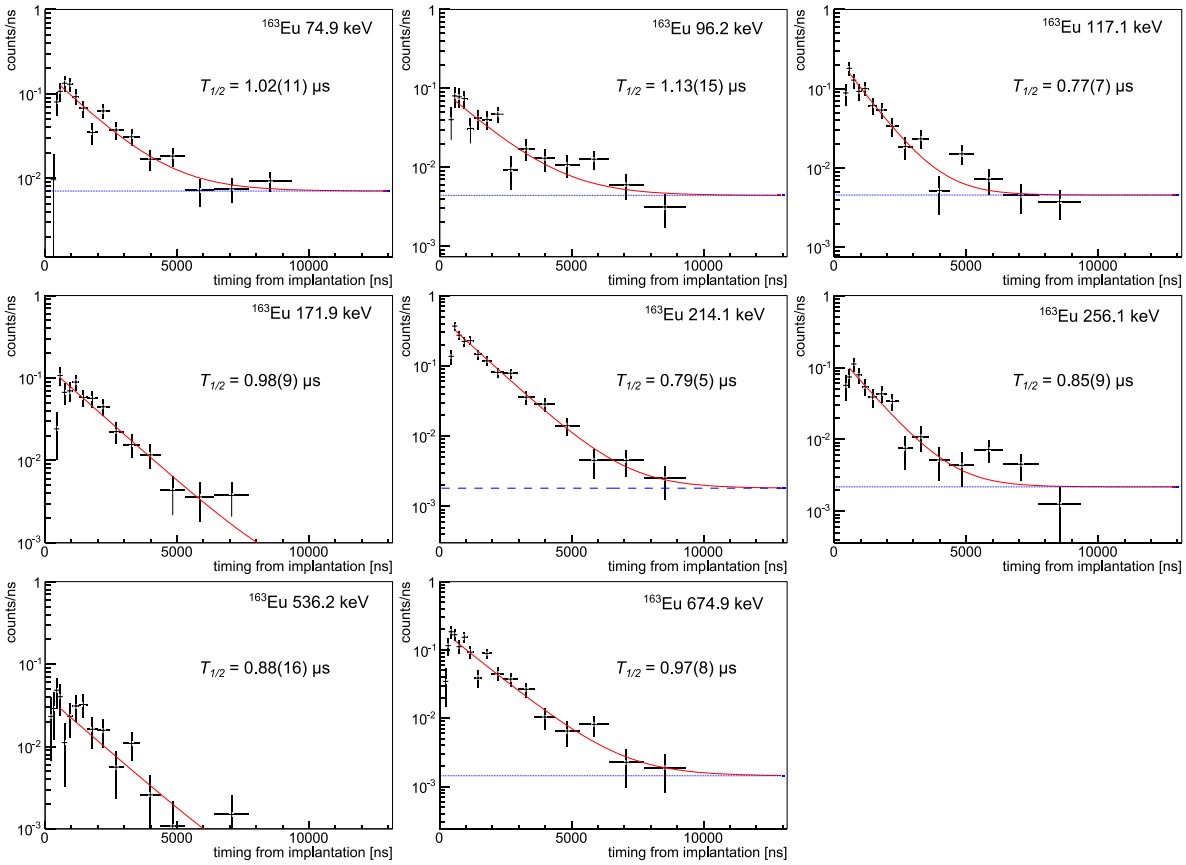

Figure 4.14 Time spectra gated on the peaks of delayed γ rays from ^{163}Eu.

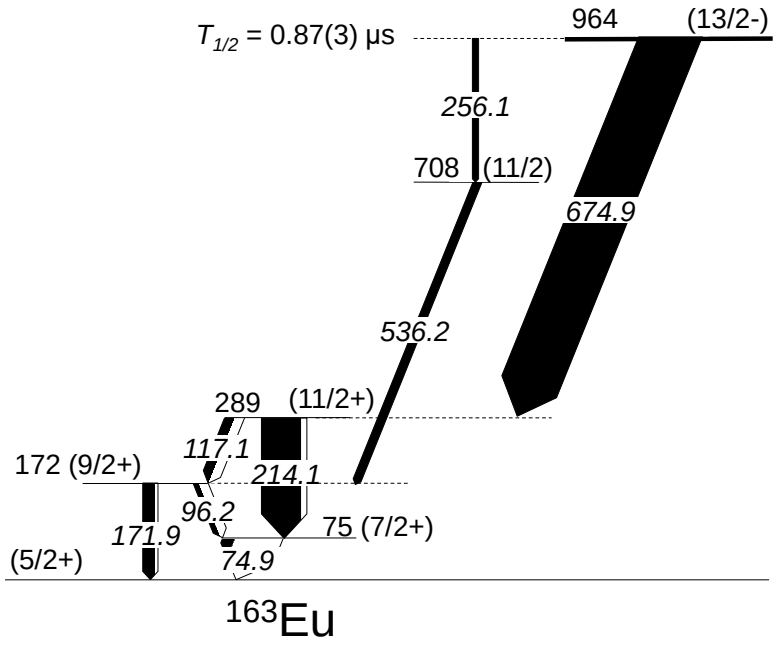

Figure 4.15 Decay scheme of the isomer in ^{163}Eu proposed in this work. The widths of the black part of the arrows are proportional to the γ-ray intensity, and the total widths of the arrows represent the decay intensities including internal conversions.

Table 4.5 Summary of the new delayed γ rays observed in ^{163}Eu. $N_{implanted}$ is the total number of particles implanted in the experiment. I_{γ_rel} is the relative intensity of γ rays where I_{rel} represents the relative intensity of the decay derived by correcting internal conversion using BrIcc [67]. The 74.9-, 96.2-, 117.1- and 256.1-keV γ rays were assumed to be M1 transition, and that of 171.9 and 214.1 keV was assumed to be E2 transition for the correction of internal conversion.

$N_{implanted}$	E_γ (keV)	$T_{1/2}$ (μs)	I_{γ_rel} (%)	I_{rel} (%)
3.1×10^5	74.9	1.02(11)	18(3)	96(6)
	96.2	1.13(15)	7.8(2.2)	24(7)
	117.1	0.77(7)	15(3)	32(7)
	171.9	0.98(9)	19(3)	26(4)
	214.1	0.79(5)	66(5)	77(6)
	256.1	0.85(9)	9(3)	10(3)
	546.2	0.88(16)	14(4)	14(4)
	674.9	0.97(8)	100(9)	100(9)

4.2.3 ^{162}Sm ($Z = 62,\ N = 100$)

Three delayed γ rays were observed in an even-even nuclide, ^{162}Sm, as shown in Figure 4.16. Half-lives were obtained for the three γ rays (Figure 4.17). The weighted average of those half-lives were 1.78(7) μs. Decay scheme of this isomer was proposed as shown in Figure 4.18. The two peaks at 71.0 and 164.3 keV were assigned as the γ rays from $2^+ \rightarrow 0^+$ and $4^+ \rightarrow 2^+$ transition of the ground-state band. The excitation energies of 2^+ and 4^+ states agreed well with the systematics of less neutron-rich Sm isotopes such as ^{158}Sm and ^{160}Sm [25]. The peak at 774.1 keV is assumed to be emitted from the transition between an isomeric state and the 4^+ state of the ground-state band. The decay scheme with a single cascade line is supported from the result that relative intensities of the three γ rays agree with each other as shown in Table 4.6. The spin of the isomeric state was tentatively assigned to be 4 because it only decays to 4^+ state of the ground-state band. If the spin of the isomeric state was 3, there should also be a decay branch to 6^+ state. Excitation energy of 6^+ state is expected to be around 452 keV by assuming rotational band with energies proportional to $I(I+1)$. By assuming the branching ratio is proportional to the third power of the ratio of γ-ray energies for $\Delta J = 1$, and detection efficiency ratio, a γ-ray peak at around 656 keV should be observed ~70 counts in the case of spin 5 assignment. A peak with such counts should be clearly seen in the spectrum, and therefore, the spin assignment of the isomeric state to be 5 is refuted. The negative parity of the isomeric state was assumed from the systematics of $K^\pi = 4^-$ isomers in $N = 100$ isotones, which will be discussed in the next chapter.

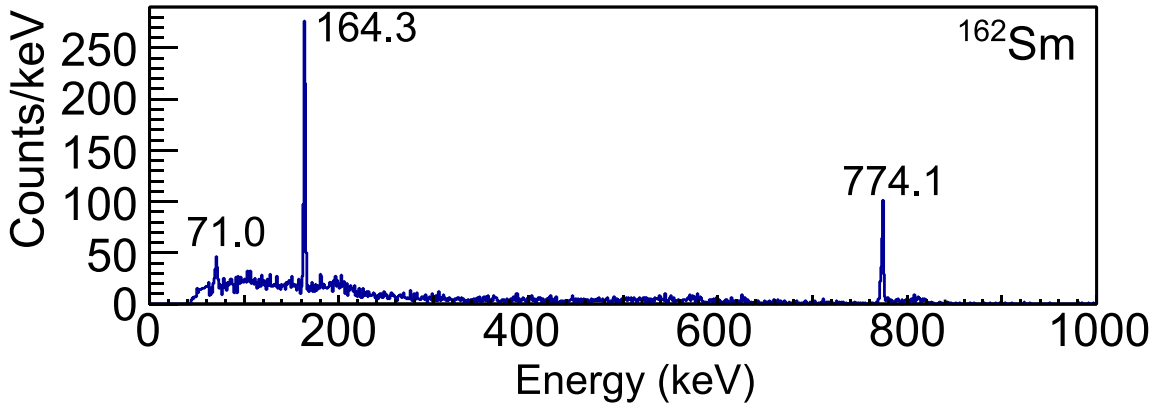

Figure 4.16 Energy spectrum of delayed γ rays from ^{162}Sm.

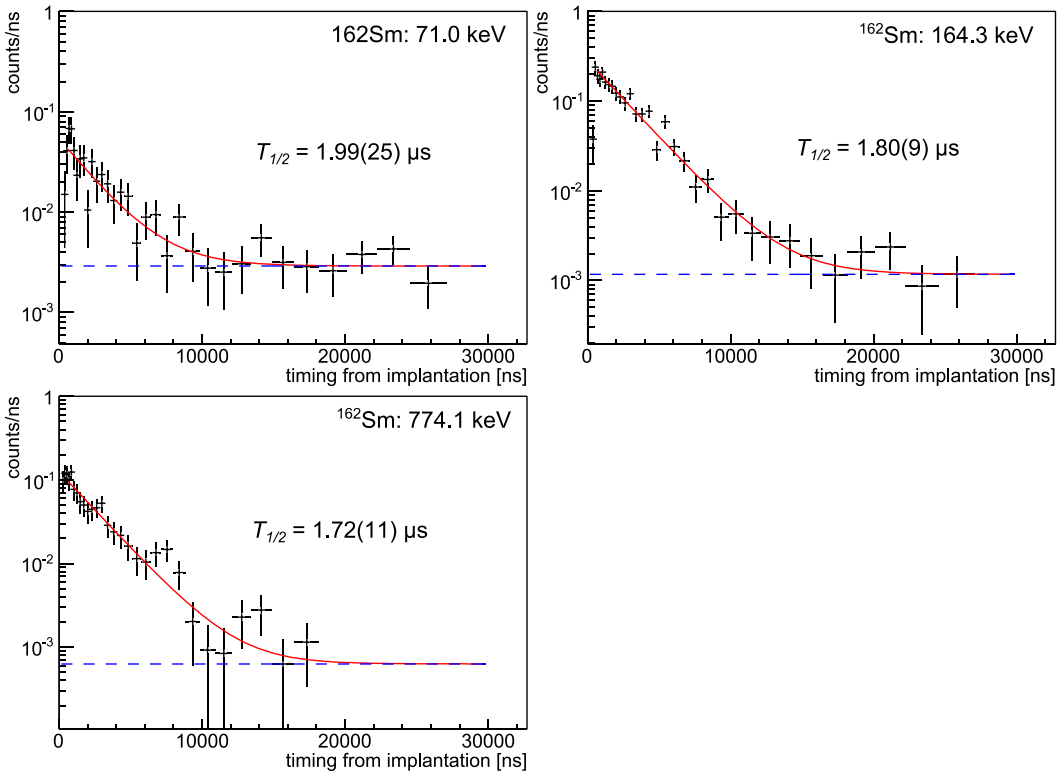

Figure 4.17 Time spectra gated on the peaks of delayed γ rays from ^{162}Sm.

Table 4.6 Summary of the new delayed γ rays observed in ^{162}Sm. $N_{implanted}$ is the total number of particles implanted in the experiment. I_{γ_rel} is the relative intensity of γ rays where I_{rel} represents the relative intensity of the decay derived by correcting internal conversion using BrIcc [67]. The 71.0- and 164.3-keV γ rays were assumed to be E2 transition for the correction of internal conversion.

$N_{implanted}$	E_γ (keV)	$T_{1/2}$ (μs)	I_{γ_rel} (%)	I_{rel} (%)
1.8×10^5	71.0	1.99(25)	9.8(1.6)	93(15)
	164.3	1.80(9)	62(3)	88(4)
	774.1	1.72(11)	100(7)	100(7)

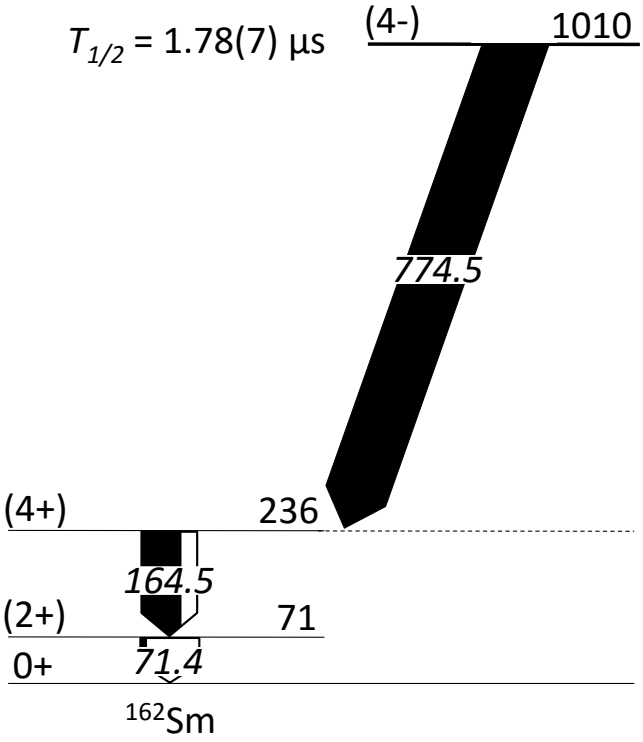

Figure 4.18 Decay scheme of the isomer in ^{162}Sm proposed in this work. The widths of the black part of the arrows are proportional to the γ-ray intensity, and the total widths of the arrows represent the decay intensities including internal conversions.

4.2.4 ^{161}Pm ($Z = 61,\ N = 100$)

New isomer was observed in ^{161}Pm. Figure 4.19 shows the energy spectrum of the delayed γ rays. There are 7 peaks with similar half-lives with each other as shown in Figure 4.21. The weighted average of the half-lives of these γ rays was 0.66(3) μs. γ-γ coincidences were examined for each γ rays as shown in Table 4.7. Figure 4.20 shows the coincidence spectra with 728- and 609-keV gate. From the coincidence analysis, the level scheme of ^{161}Pm isomer was constructed (Figure 4.22). Non-observation of the coincidence between 728- and 609-keV γ rays and the coincidence between 118- and 609-keV γ rays support the level scheme decaying with two branches from the isomeric state. The spin and parity of the ground state of ^{161}Pm was tentatively assumed to be 5/2- from the systematics of Pm isotopes [65] and theoretical prediction [66]. A rotational band structure was constructed on the ground state up to (13/2-) state at 347 keV. The excitation energies of this band is similar to those of ^{153}Pm and ^{155}Pm known in [73], which shows the consistency of the assignment. The isomeric state was built at 966 keV. The spin of the isomeric state was assigned to be 13/2 since it decays both to (13/2-) and (11/2-) state. The isomeric state was interpreted as the coupling of the neutron configuration as $K^{\pi} = 4^{-}$ isomer know in even-even $N = 100$ nuclei (will be discussed in the next chapter) and odd proton in $\pi 5/2[532]^{-}$ orbital.

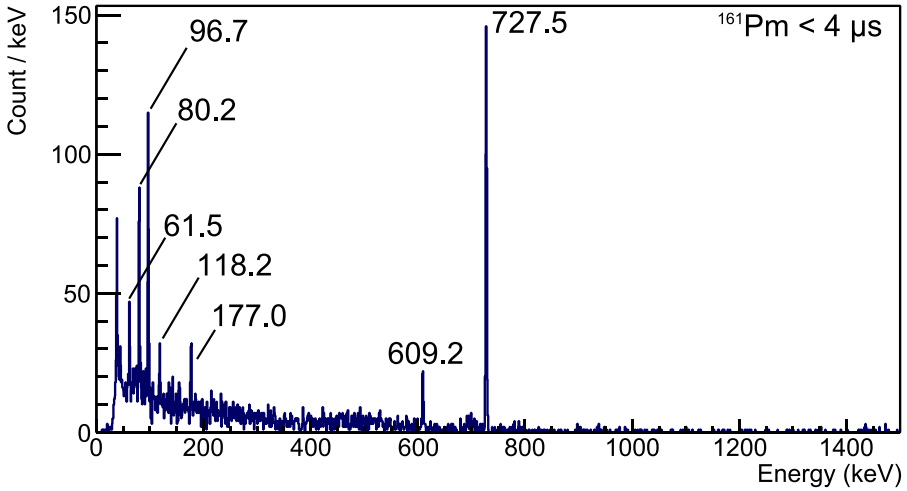

Figure 4.19 Energy spectrum of delayed γ rays from ^{161}Pm. The time window is up to 4 μs after the implantation.

Table 4.7 List of γ-ray coincidences in the isomeric decay of ^{161}Pm. Coincident γ rays are marked by ticks. The 177-keV peak was too small to observe coincident events.

Energy (keV)	62	80	97	118	177	609	728
62	gate	✔	✔				✔
80	✔	gate	✔	✔		✔	✔
97	✔	✔	gate	✔		✔	✔
118		✔	✔	gate		✔	
117					gate		
609				✔		gate	
728	✔	✔	✔				gate

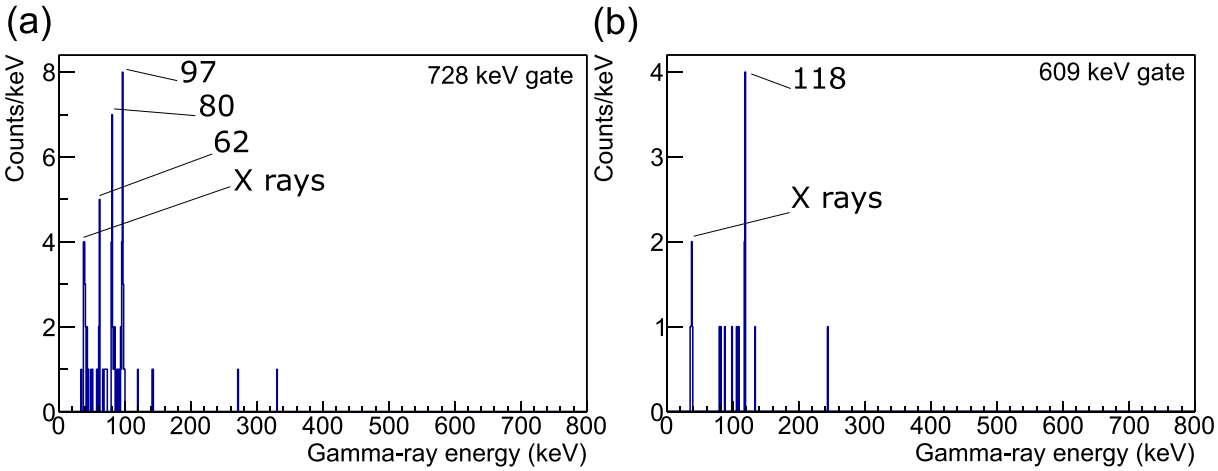

Figure 4.20 γ-γ coincidence spectra with (a) 728- and (b) 609-keV gate.

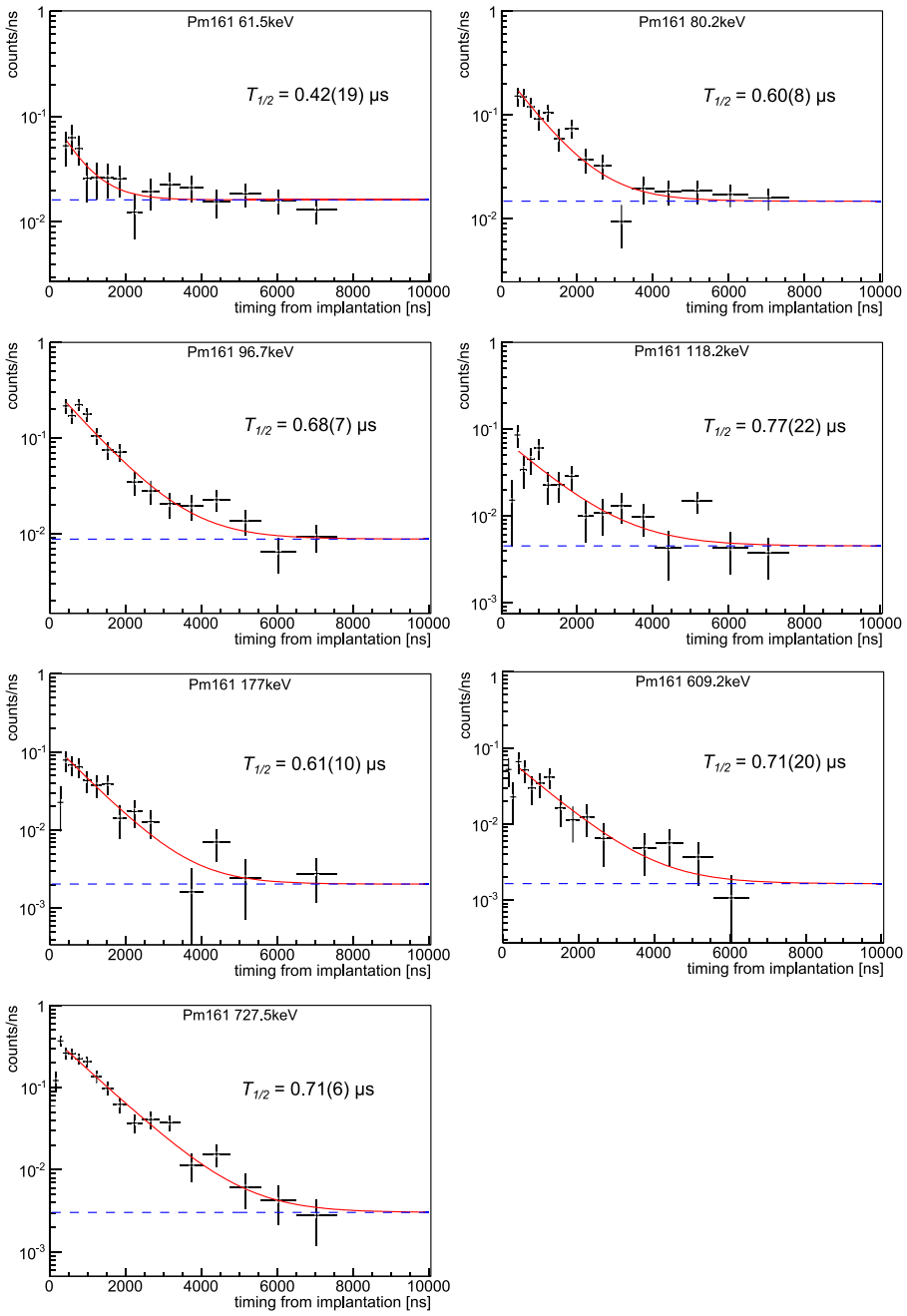

Figure 4.21 Time spectra gated on the peaks of delayed γ rays from ^{161}Pm.

Table 4.8 Summary of the new delayed γ rays observed in ^{161}Pm. $N_{implanted}$ is the total number of particles implanted in the experiment. I_{γ_rel} is the relative intensity of γ rays where I_{rel} represents the relative intensity of the decay derived by correcting internal conversion using BrIcc [67]. The 61.5-, 80.2-, 96.7- and 118.2-keV γ rays were assumed to be M1 transition, and the 177-keV γ ray was assumed to be E2 transition for the correction of internal conversion.

$N_{implanted}$	E_γ (keV)	$T_{1/2}$ (μs)	I_{γ_rel} (%)	I_{rel} (%)
	61.5(2)	0.42(19)	12(3)	86(25)
	80.2	0.60(8)	34(5)	132(20)
	96.7	0.68(7)	43(6)	117(15)
5.5×10^4	118.2	0.77(22)	4.8(2.0)	9(4)
	177.0	0.61(10)	8.6(1.8)	11.2(2.4)
	609.2	0.71(20)	14.7(2.5)	14.7(2.5)
	727.5	0.71(6)	100(6)	100(6)

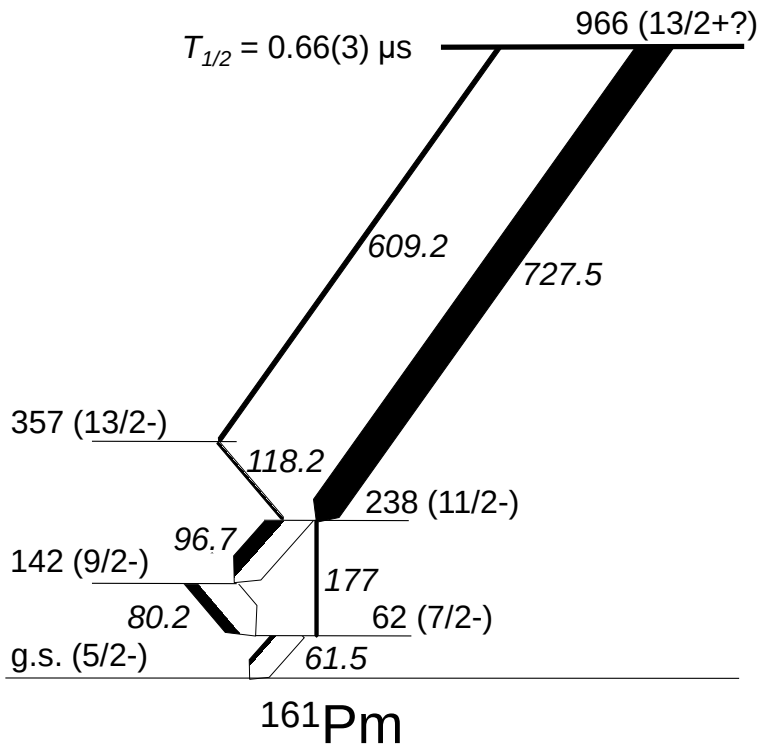

Figure 4.22 Decay scheme of the isomer in ^{161}Pm proposed in this work. The widths of the black part of the arrows are proportional to the γ-ray intensity, and the total widths of the arrows represent the decay intensities including internal conversions.

4.2.5 ^{160}Nd ($Z = 60,\ N = 100$)

New isomeric γ rays were observed in ^{160}Nd at 65.2, 150.0 and 892.8 keV as shown in the energy spectrum, Figure 4.23. The half-lives obtained from decay curves of the 150.0 and 892.8 keV γ rays shown in Figure 4.24 agreed with each other within the errors. The weighted mean value of the half-life was 1.33(9) μs. The γ-γ coincidence was examined for the three γ rays. The coincidence between 150.0- and 892.8-keV γ rays were distinguished as shown in Table 4.9. There were also some events at 65.2 keV in coincidence with 150.0- and 892.8-keV peaks but they were not significant since the peak counts was so small. The 65.2- and 150.0-keV transition was assigned to be $2^+ \rightarrow 0^+$ and $4^+ \rightarrow 2^+$ decays respectively, from the

systematics of less neutron-rich Nd isotopes [25,68]. The spin of the isomeric state at 1108 keV was assigned to be 4 because it only decays to 4^+ state. If the spin was 3, both the decays to 4^+ and 2^+ states should be observed, and if it was 5, the decay to 6^+ state should be observed. By assuming the 893-keV peak as a decay from the state with spin 3 to that with 4^+, there should be ~270 counts around 1043 keV as a direct decay to 2^+ state. It was estimated from the number of counts in 1108-keV peak by assuming branching ratio of $\Delta J = 1$ decays to be proportional to E_γ^3, and taking detection efficiencies into account. A peak with such a number of counts should be clearly seen in the spectrum and therefore, the assignment of spin 3 is refuted. By similar argument, spin 5 assignment is also refuted by non-observation of 6^+ to 4^+ decay which should be observed ~150 counts at around 239 keV. The negative parity for the isomeric state was assigned from the systematics of $K^\pi = 4^-$ isomers in $N = 100$ isotones which will be discussed in the next chapter.

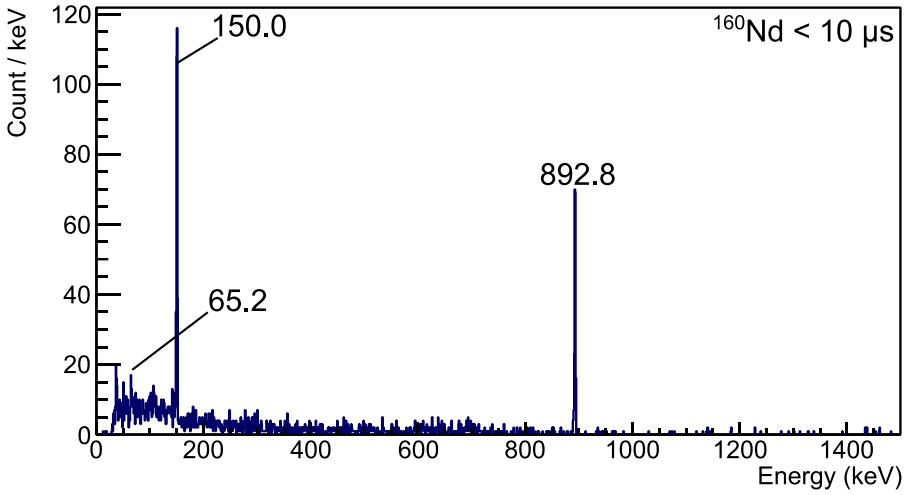

Figure 4.23 Energy spectrum of delayed γ rays from ^{160}Nd. The time window is up to 10 μs after the implantation.

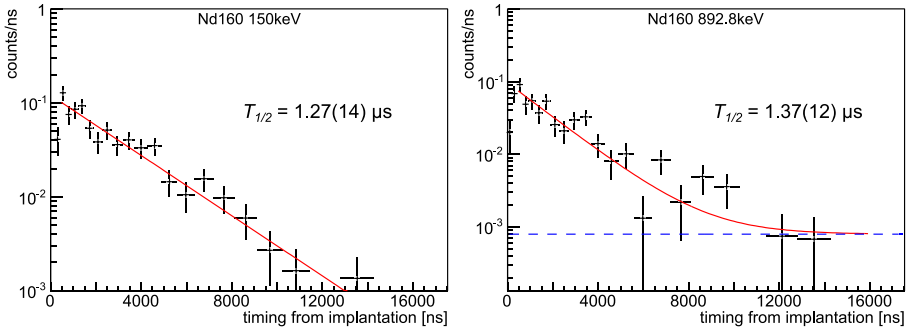

Figure 4.24 Time spectra gated on the peaks of delayed γ rays from ^{160}Nd.

Table 4.9 List of γ-ray coincidences in the isomeric decay of ^{160}Nd. Coincident γ rays are marked by ticks. The ticks with parenthesis indicate that there were some coincident events but the statistics was not sufficient to say it was significant.

Energy (keV)	65	150	893
65	gate	(✔)	(✔)
150	(✔)	gate	✔
893	(✔)	✔	gate

Table 4.10 Summary of the new delayed γ rays observed in ^{160}Nd. $N_{implanted}$ is the total number of particles implanted in the experiment. I_{γ_rel} is the relative intensity of γ rays where I_{rel} represents the relative intensity of the decay derived by correcting internal conversion using BrIcc [67]. The 65.2- and 150.0-keV γ rays were assumed to be E2 transition for the correction of internal conversion.

$N_{implanted}$	E_γ (keV)	$T_{1/2}$ (μs)	I_{γ_rel} (%)	I_{rel} (%)
1.3×10^4	65.2(5)	-	100(46)	100(46)
	150.0	1.27(14)	739(46)	97(6)
	892.8	1.37(12)	1111(82)	95(7)

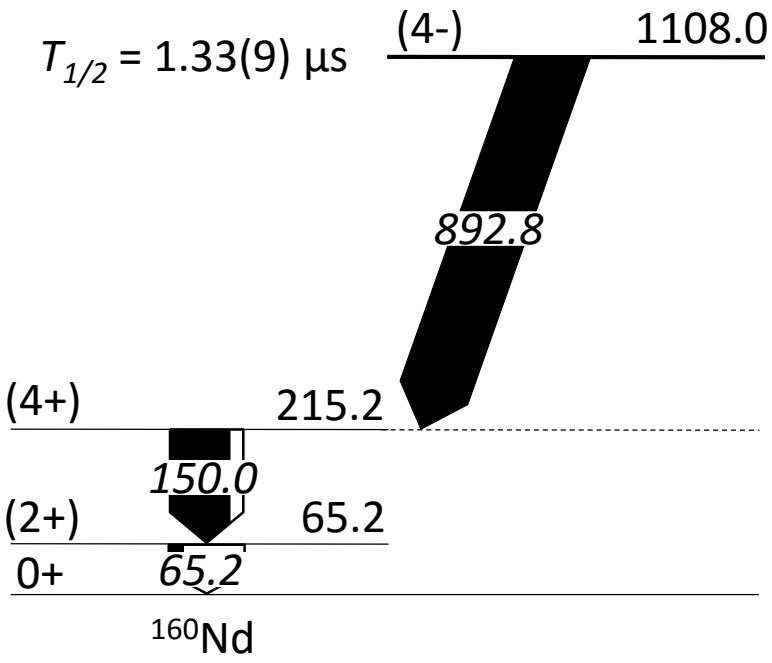

Figure 4.25 Decay scheme of the new isomer in ^{160}Nd proposed in this work.

4.3 New isomers in Tb ($Z = 65$) isotopes

New isomers were systematically observed in $N = 100$ to 104 Tb isotopes. Those are assumed to originate in one quasi-particle excitation of proton. Results of isomer spectroscopy on each nuclide and the level scheme construction are shown in the following subsections.

4.3.1 ^{165}Tb ($Z = 65,\ N = 100$)

Three delayed γ-ray peaks were newly observed at 54.8, 75.9 and 152.4 keV in ^{165}Tb as the energy spectrum shown in Figure C.9. Half-lives obtained from the two peaks at 75.9 and 152.4 keV were agreed with each other as shown in Figure 4.27. The weighted average of the half-lives was 0.82 (4) μs. There are small peaks at ~45 and ~50 keV which were assigned as K_α and K_β X rays from Tb atom emitted after an electron internal conversion. The energies of the $K_{\alpha1}$, $K_{\alpha2}$, $K_{\beta1}$, $K_{\beta2}$ and $K_{\beta3}$ X rays are 44.5, 43.8, 50.4, 51.7 and 50.2 keV respectively [74]. The isomer in Tb isotopes are expected to be one quasi-particle excitation of proton and not likely to be a 2 quasi-particle excitation of neutrons since the excitation energy of the isomeric state is smaller than 300 keV, the sum of the energies of the observed γ rays. The appearance of similar isomers in Tb isotopes also indicates that the isomer is due to the proton excitation. The γ rays at 54.8 and 75.9 keV are tentatively assigned as the M1 decays of the rotational band of ground state from the comparison with the systematics of less neutron-rich Tb isotopes [75–78].

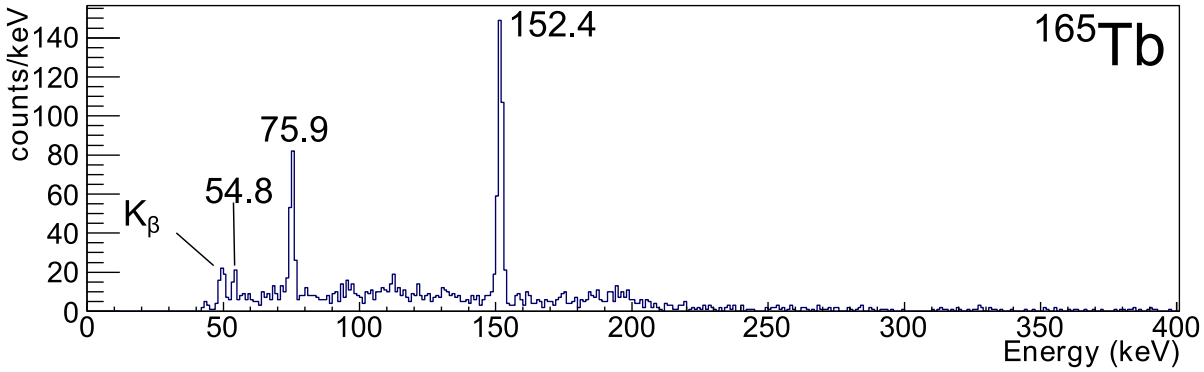

Figure 4.26 Energy spectrum of delayed γ rays from ^{165}Tb.

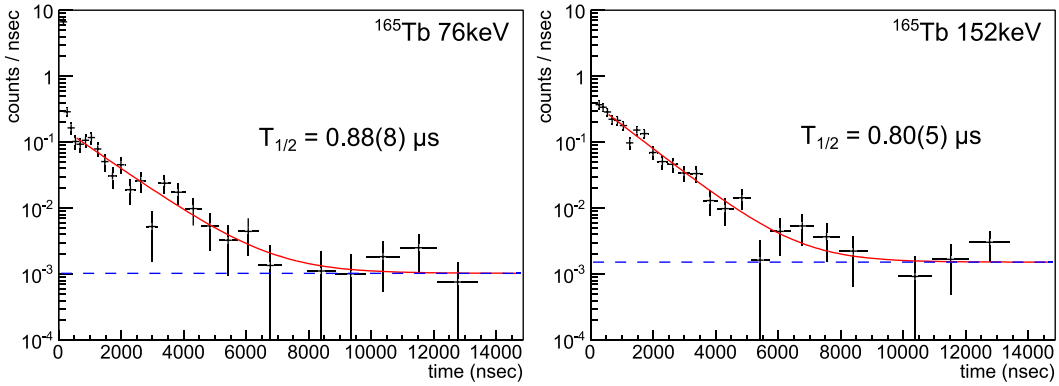

Figure 4.27 Time spectra gated on the peaks of delayed γ rays from ^{165}Tb.

4.3.2 ^{166}Tb ($Z = 65,\ N = 101$)

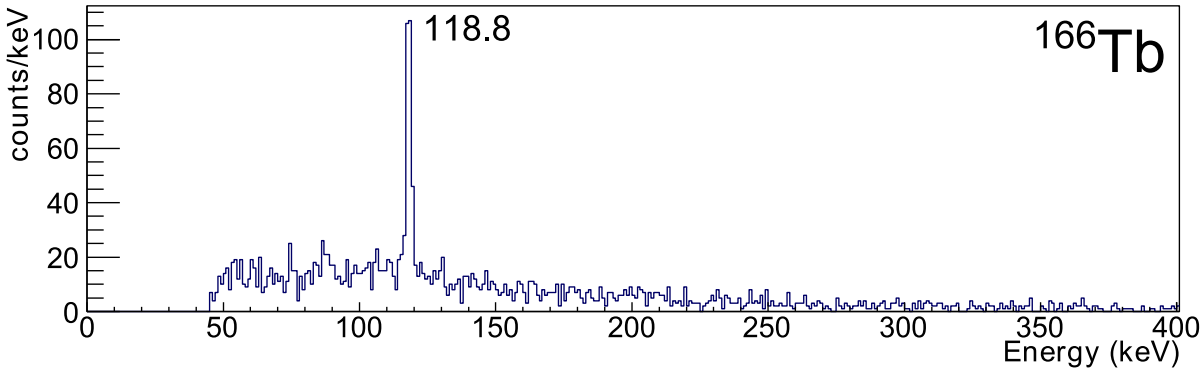

Figure 4.28 Energy spectrum of delayed γ rays from ^{166}Tb.

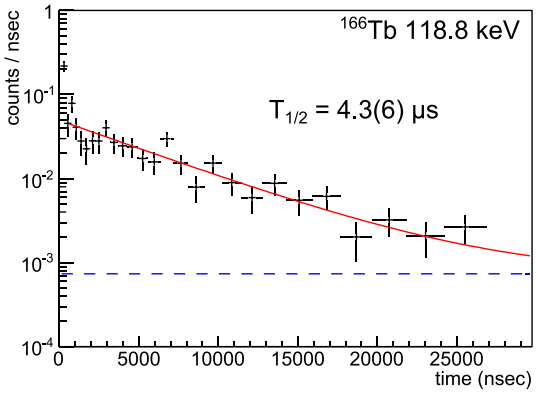

Figure 4.29 Time spectra gated on the peaks of delayed γ rays from ^{166}Tb.

4.3.3 ^{167}Tb ($Z = 65,\ N = 102$)

Three delayed γ-ray peaks were newly observed at 73.6 and 152.4 keV in ^{167}Tb as the energy spectrum shown in Figure 4.30. Half-lives obtained from the two peaks at 73.6 and 152.4 keV were agreed with each other as shown in Figure 4.31. The weighted average of the half-lives was 2.47 (17) μs. There are small peaks at ~45 and ~50 keV which were assigned as K_α and K_β X rays from Tb atom emitted after an electron internal conversion. The origin of the isomer of ^{167}Tb seems to be the same as that of ^{165}Tb The γ rays at 75.9 keV is tentatively assigned as the M1 decay ($7/2^+ \rightarrow 5/2^+$) of the rotational band of ground state from the comparison with the systematics of less neutron-rich Tb isotopes [75–78]. Since the peak at 50 keV is broad, it probably consists of K_β X rays and the γ ray of the $5/2^+ \rightarrow 3/2^+$ decay around 52 keV.

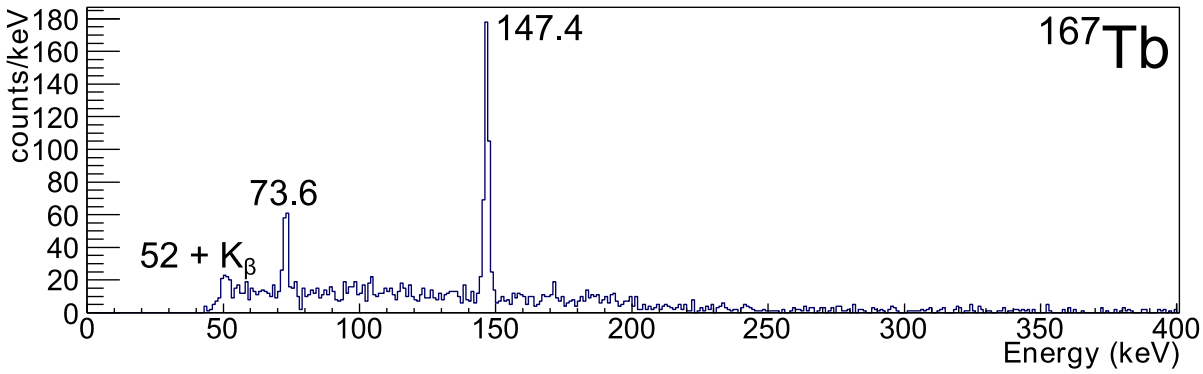

Figure 4.30 Energy spectrum of delayed γ rays from ^{167}Tb.

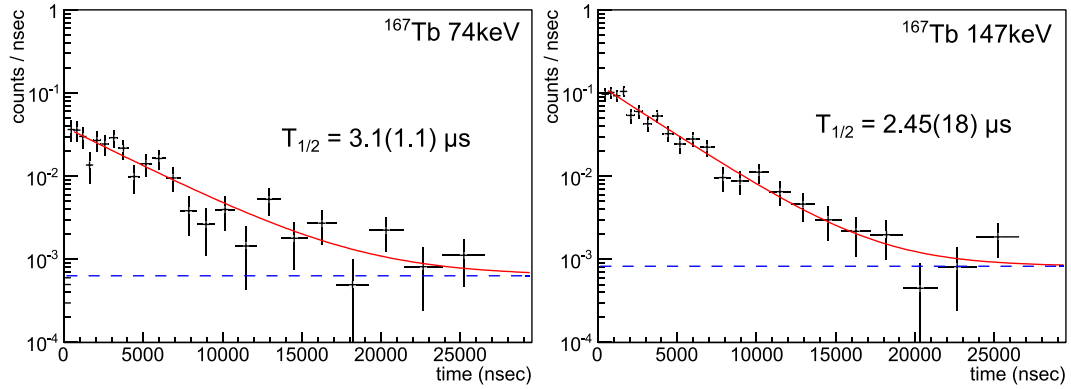

Figure 4.31 Time spectra gated on the peaks of delayed γ rays from ^{167}Tb.

4.3.4 ^{168}Tb ($Z = 65,\ N = 103$)

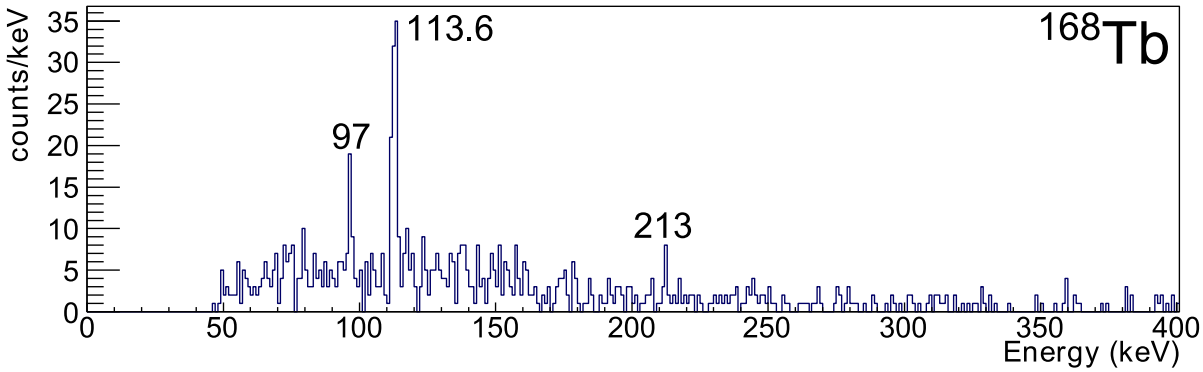

Figure 4.32 Energy spectrum of delayed γ rays from ^{168}Tb.

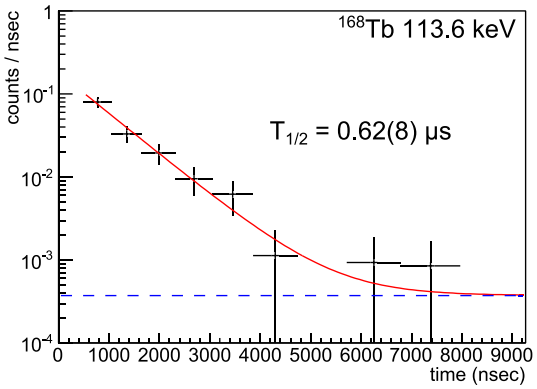

Figure 4.33 Time spectra gated on the peaks of delayed γ rays from ^{168}Tb.

4.4 Candidate for new octupole excitation in ^{150}Ba ($Z = 56,\ N = 94$)

There are two peaks observed at 100 and 597 keV in ^{150}Ba.. Figure 4.34 shows the half-life determination of the decay from ^{150}Cs to ^{150}Ba without γ-ray coincidence. The half-lives of ^{150}Ba, La, Ce and Pr were fixed to the known values, 0.3 s [79], 0.86 s [80], 4.0 s [81] and 6.19 s [82], respectively. The half-life of ^{150}Ba was obtained as 141(29) ms. Unlike the $Z \geq 56$ isotopes, Cs isotopes are known to have large β-delayed neutron branch $\sim 25\%$ [83]. The branching ratio of β-delayed neutron channel of ^{150}Cs is not known but expected to be larger than 25%. The fitting here did not consider the neutron branch and may not be exact. However, the half-life of the daughter nuclide of neutron branch, ^{149}Ba, is 0.324 s [83] which is close to that of ^{150}Ba, 0.3 s. Therefore, the half-life of ^{150}Cs obtained by the fitting without including the neutron branch is expected to be precise enough to see γ rays with appropriate time window. The γ-ray energy spectra of ^{150}Ba with and without addback (See Section3.2.5) are shown in Figure 4.35 (a) and (c). Although the statistics is limited, two peaks can be identified at 100 and 597 keV. For the low energy γ rays ~100 keV, the chance of missing a part of γ-ray energy by Compton scattering is lower than that of high energy γ rays, and thus the addback algorithm can reduce peak counts by accidental coincidence with neighboring crystals more than it is gained. The peak at 100 keV can be seen clearer in the spectrum without addback.

Since the peak counts were small, log likelihood ratio test was performed to the two spectra in order to see if those peaks are significant. Figure 4.35 (b) and (d) shows the significance spectra of the test statistics σ_i, which defined as,

$$\sigma_i = \sqrt{y_i + n_i \ln(n_i/y_i)}, \tag{4.1}$$

where, n_i is the number of counts at i-th bin from the true event distribution $D(E)$, and y_i is the estimated counts of background events at i-th bin. The back ground was estimated by smoothing and scaling the spectrum with time window $2 < t < 10$ s, since this region is expected to be mainly consists of the constant component from Figure 4.34. The true distribution $D(E)$ was assumed to be the sum of Gaussian of all the events, which is,

$$D(E) = \sum_{j=0}^{nevent} \frac{1}{\sqrt{2\pi}\sigma(E_{\gamma j})} \exp\left(-\frac{(E - E_{\gamma j})^2}{2\sigma(E_{\gamma j})^2}\right), \quad (4.2)$$

where $\sigma(E_\gamma)$ is the energy resolution of Ge detector array, and $E_{\gamma j}$ is the γ-ray energy of the j-th event. The σ_i corresponds to that of χ^2 test for Gaussian distribution:

$$\chi^2 = \sum_i (y_i - n_i)^2 / 2\sigma_i \quad (4.3)$$

In this case, we defined the χ^2 of likelihood ratio test as,

$$\chi^2 = -2\ln(\mathcal{L}_{null}/\mathcal{L}_{true}). \quad (4.4)$$

$\mathcal{L}_{null}$ is the likelihood for null model, that is, the estimated background in this case. $\mathcal{L}_{true}$ is the likelihood for the true distribution which was assumed from the actual energy spectrum. The statistics of the counts in the spectra can be regarded to follow the Poisson distribution. In the case of Poisson distribution, the likelihood is written as,

$$\mathcal{L}_{null} = \prod_i \exp(-y_i) y_i^{n_i} / n_i! \,. \quad (4.5)$$

Then, we obtain σ_i in equation (4.1) from the χ^2 equation (4.3) and (4.4).

The significance of the peak at 100 keV in the spectrum without addback is almost 5σ. In the case of 597-keV peak, the significance was 4.6σ in the spectrum with addback. The probability of having counts more than 4.6σ at a certain energy is less than 10^{-5}. The probability of having such counts at anywhere in the spectrum is roughly speaking less than 10^{-2} since we have our energy range of interest $\sim 10^3$ times of the energy resolution. Therefore the confidence levels of the two peaks at 100 and 597 keV are more than 99%. There is also a peak at 200 keV with significance of $4.3\,\sigma$ in Figure 4.35 (b). Though the confidence level of the peak at 200 keV is lower than those at 100 or 597 keV, it can be a candidate for the γ ray.

In order to confirm that the those peaks are from the decay of ^{150}Cs to Ba, two spectra shown in Figure 4.36 was checked. One possibility for the origin of the peaks other than the β decay from ^{150}Cs to Ba is the daughter or other descendant nuclides. Figure 4.36 (a) shows the energy spectrum with time window from 0.5 to 2 s. If the two peaks originate in the decay of descendant nuclides, those peaks should also appear in this spectrum. The red dashed lines in the figure indicate that there is no significant peak at 100 nor 597 keV. However, there is a small peak at 200 keV, which shows the peak may originate in the decay of descendant nuclides. One other possibility for the other origin is the β-delayed neutron channel. Figure 4.36 (b) shows the spectrum of the β decay from ^{149}Cs to Ba. If the peaks at 100 and 597 keV originate in the neutron channel, those will also appear in the spectrum. From the figure, there is no peak at the energies. From those evidence, the peaks at 100 and 597 keV are from the decay of ^{150}Cs to Ba. The peak at 200 keV is one more candidate but it cannot be concluded that the peak is from the β decay of ^{150}Cs.

From the comparison with the level scheme of ^{148}Ba as shown in Figure 4.37, the peak at 100 and 597 keV were tentatively assigned to be the decay, $2^+ \rightarrow 0^+$ and $3^- \rightarrow 2^+$. The 3^- state is a candidate for the octupole band excitation. The peak at 200 keV may correspond to $4^+ \rightarrow 2^+$ decay if it is from ^{150}Ba. The spin and parity of the parent nuclide, ^{150}Cs is not known. The proton configuration is assumed as $3/2^+[422]$ from the J^π of ^{143}Cs and ^{145}Cs measured by

atomic beam magnetic resonance method in [84]. The neutron configuration is not clear because the spin and parity is not known neither ^{151}La nor ^{153}Pr. The possible configuration from Nilsson diagram is 5/2$^-$[523] and those will be $J^\pi = 4^-$ for the ground state of ^{150}Cs. This assumption of the J^π do not exclude the possibility of feeding to the 3$^-$ state. However, it does not limit the J^π of ^{150}Cs because there is possibility of having more excited states decay with high energy γ rays above 1 MeV. The efficiency for such high-energy γ rays were lower than those with lower energies and were not sensitive in the statistics of this experiment.

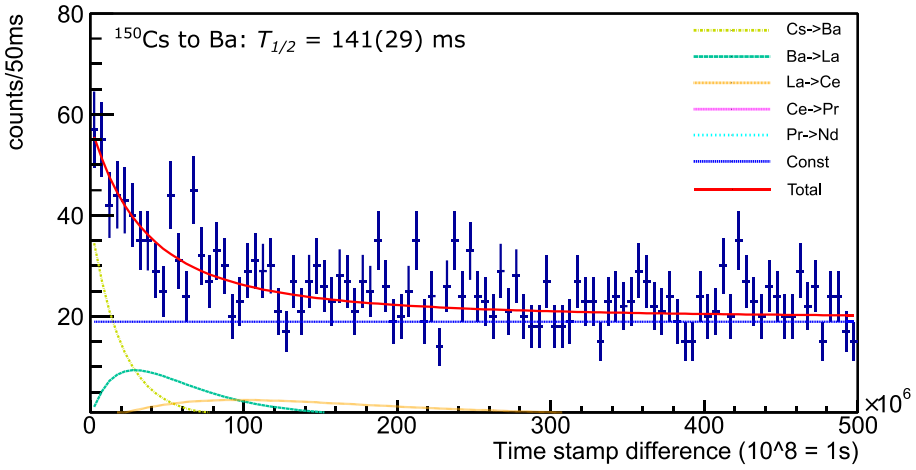

Figure 4.34 Decay curve of ^{150}Cs showing from 0 to 5 s fitted by the function including the component of ^{150}Ba, La, Ce and Pr. The half-life of the ^{150}Cs was deduced as 141(29) ms.

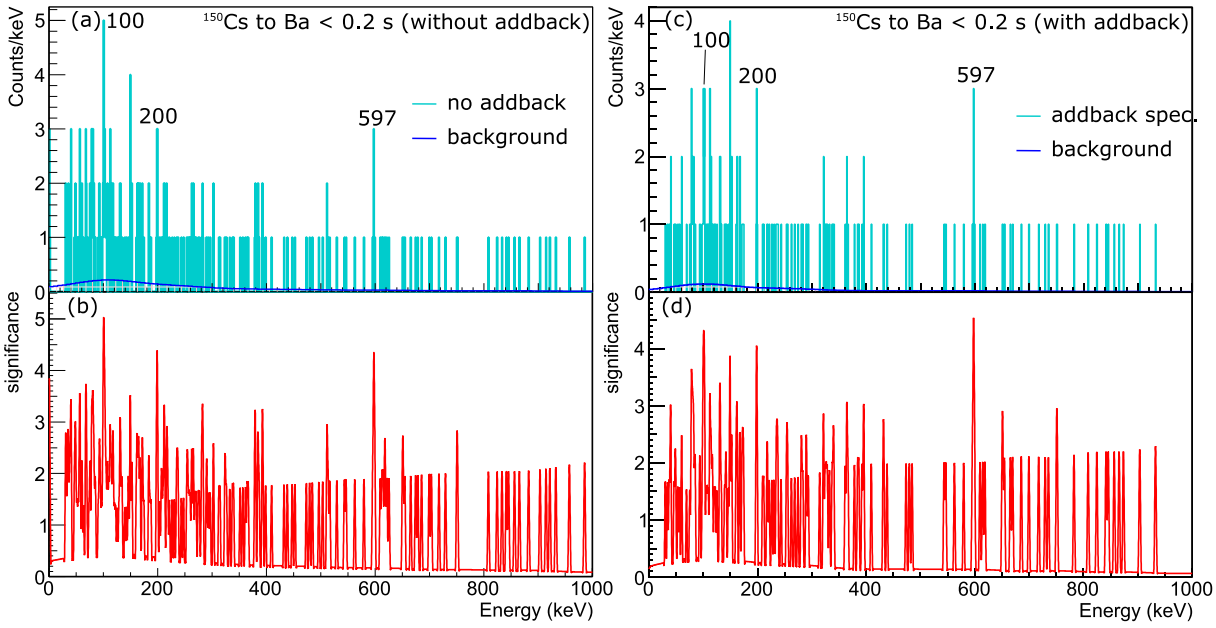

Figure 4.35 Energy spectrum of the β decay from ^{150}Cs to Ba with (c) and without (a) addback. β-decay events with the time stamp difference from the beam implantation smaller than 0.2 s were plotted. (b) and (d) shows the likelihood ratio test significance.

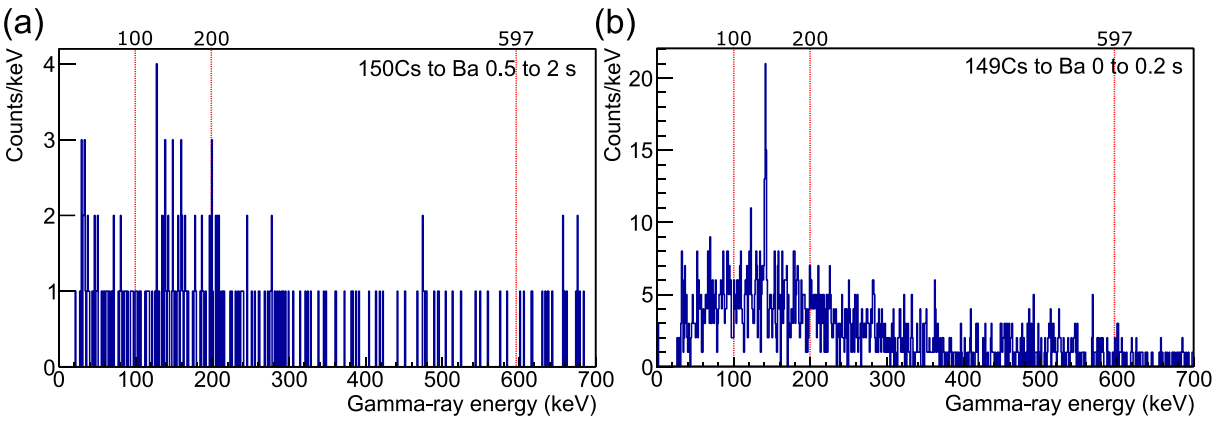

Figure 4.36 Energy spectrum of the β decay from (a) descendant nuclides of ^{150}Cs and (b) ^{149}Cs which might be observed as a delayed neutron channel. 100, 200 and 597 keV are indicated by red arrows.

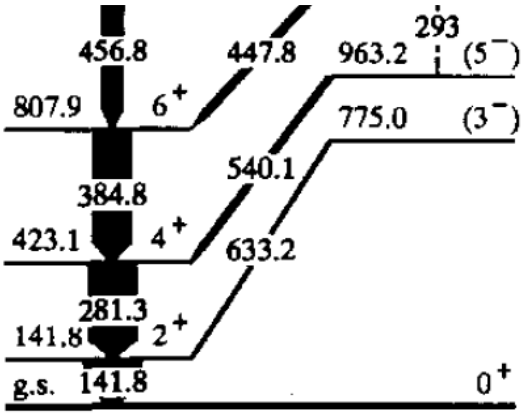

^{148}Ba

Figure 4.37 Level scheme of ^{148}Ba from [31]

4.5 The first 2^+ and 4^+ excitation in ^{154}Ce ($Z = 58$, $N = 96$)

^{154}Ce is the most neutron-rich even-even Ce isotope ever measured. Candidates for $4^+ \rightarrow 2^+$ and $2^+ \rightarrow 0^+$ decays were observed. Figure 4.38 shows the half-life determination of the decay from ^{154}La to ^{154}Ce. The half-life of the decay of ^{154}Ce was obtained to be 0.7 s as shown in Figure 4.39. The half-lives of ^{154}Pr and Nd were fixed to the known values, 2.3 s [85] and 23.5 s [86]. The half-life of the decay of ^{154}La was obtained as 430(117) ms. γ-ray energy spectrum with time window 0 to 0.7 s is shown in Figure 4.40 (a). There were peaks observed at 72 and 164 keV. The events between 2 to 5 s after the beam implantation were plotted in the spectrum (b). There is no peak observed at 72 and 164 keV, which indicates that those peaks are not originated in β decays of descendant nuclides.

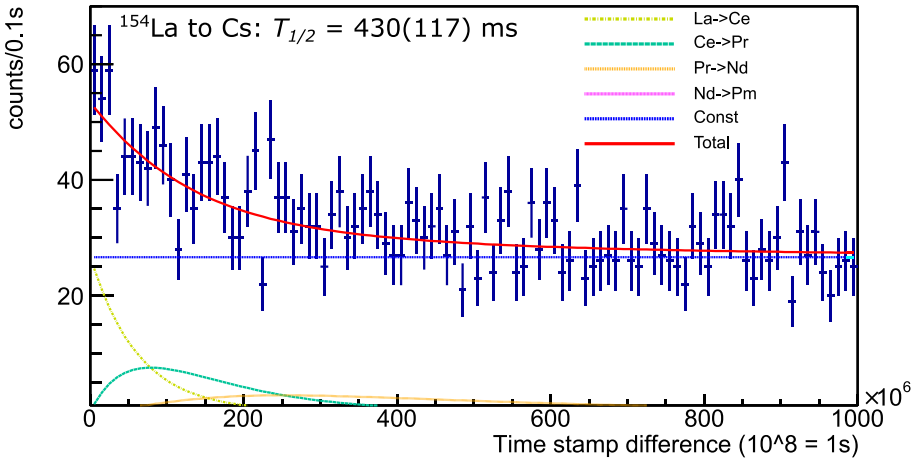

Figure 4.38 Decay curve of ^{154}La showing from 0 to 10 s fitted by the function including the component of ^{154}Ce, Pr and Nd. The half-life of the ^{154}La was deduced as 430(117) ms.

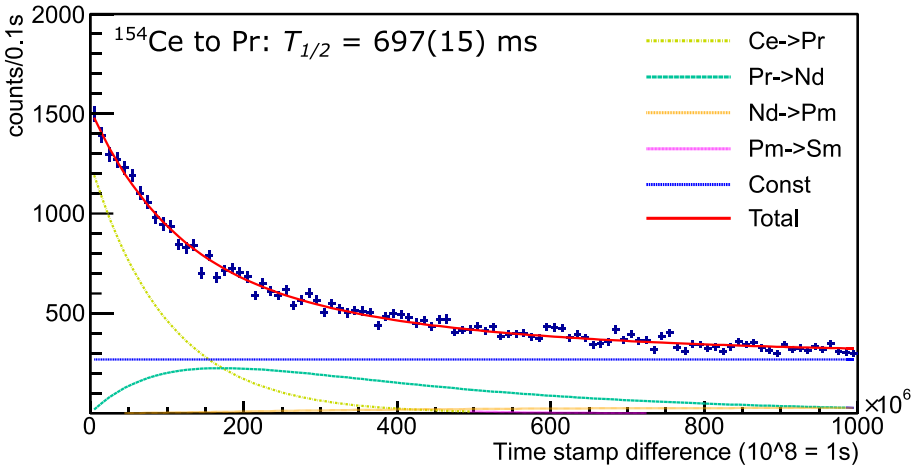

Figure 4.39 Decay curve of ^{154}Ce showing from 0 to 10 s fitted by the function including the component of ^{154}Pr, Nd and Sm. The half-life of the ^{154}Ce was deduced as 697(15) ms.

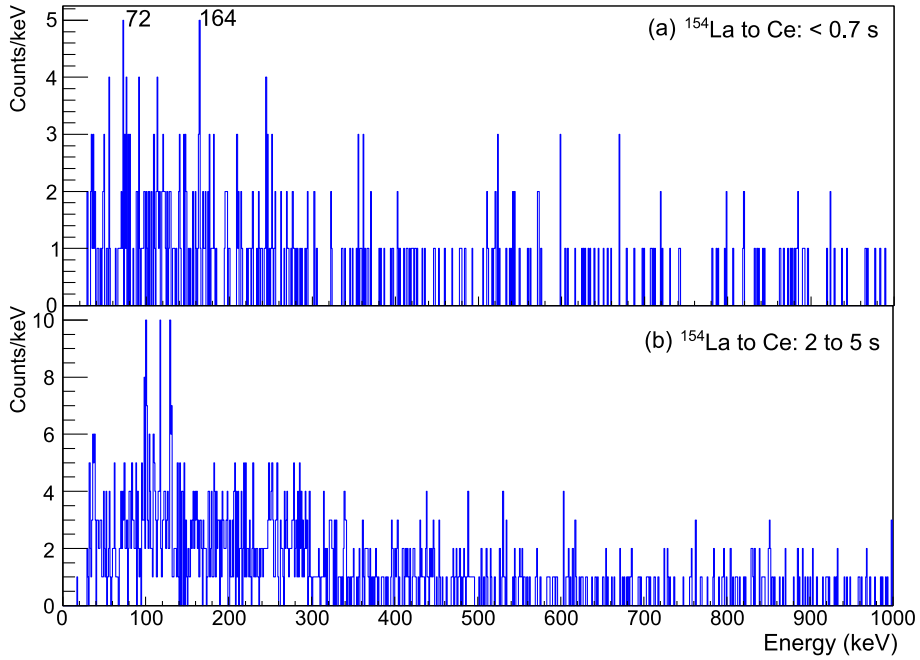

Figure 4.40 Energy spectrum of the β decay from ^{154}La to Ce. β-decay events with the time stamp difference from the beam implantation smaller than 0.7 s were plotted in (a) and those with 2 to 5 s were plotted in (b).

4.6 Ground-state rotational band in ^{157}Pm ($Z = 61$, $N = 96$)

Some γ rays were observed by the measurement of β decay from ^{157}Nd. No isomeric γ ray was observed in this nuclide. Figure 4.41 shows the half-life determination by fitting the decay curve without γ-ray coincidence. The blue and yellow lines show the β-decay components of daughter and grand-daughter nuclides. The half-life of the daughter nuclide, ^{157}Pm, and the grand-daughter nuclide, ^{157}Sm were fixed to 10.5 and 483 s, known in [87]. The energy spectrum of the β decay is shown in Figure 4.42. There are three γ-ray peaks observed at 66, 85 and 1703 keV. They have half-lives with 1.5(6), 1.3(5) and 1.4(5) s, respectively, which agree, within the errors, with the half-life obtained without γ-ray coincidence: 1.22(4) s. Other peaks seemed to have much longer half-lives and assumed to be the γ rays of descendant nuclides. The γ rays at 66.0 and 84.9 keV are tentatively assigned as the M1 decays of ground-state band from the comparison with the rotational band of $5/2[521]$ known on the ground state of ^{155}Pm ($N = 94$) [73].

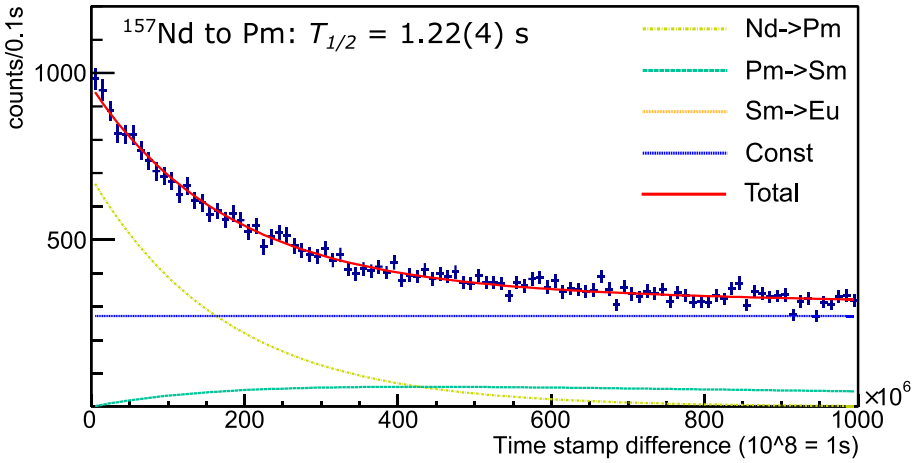

Figure 4.41 Decay curve of ^{157}Nd showing from 0 to 10 s fitted by the function (3.27) shown in the section 3.5.3. The half-life of the ^{157}Nd was obtained as 1.22(4) s.

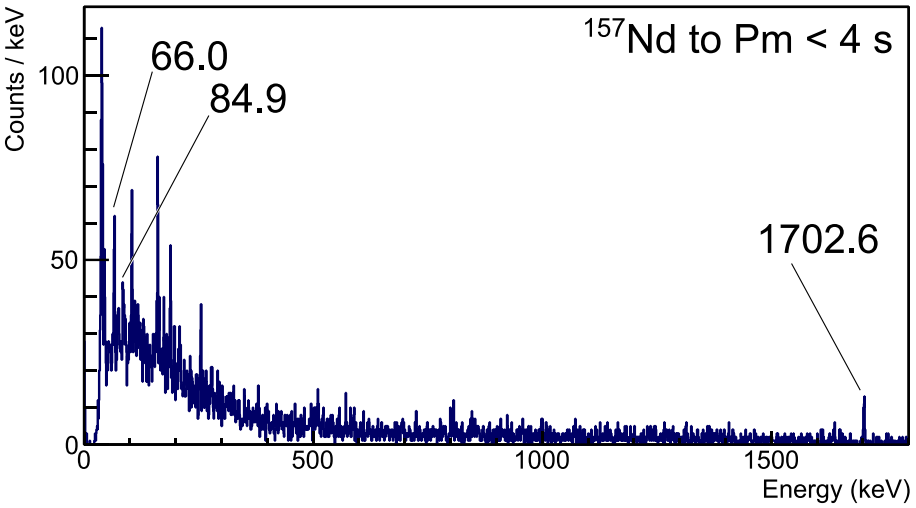

Figure 4.42 Energy spectrum of the β decay from ^{157}Nd to Pm. β-decay events with the time stamp difference from the beam implantation smaller than 4 s were plotted.

Table 4.11 Summary of the new γ rays observed in the β decay of ^{157}Nd to ^{157}Pm. $N_{implanted}$ is the total number of particles implanted in the experiment. I_{γ_rel} is the relative intensity of γ rays.

$N_{implanted}$	E_γ (keV)	$T_{1/2\_\beta}$ (s)	I_{γ_rel} (%)
7.5×10^4	66.0	1.5(6)	100(19)
	1702.6	1.4(5)	100(16)

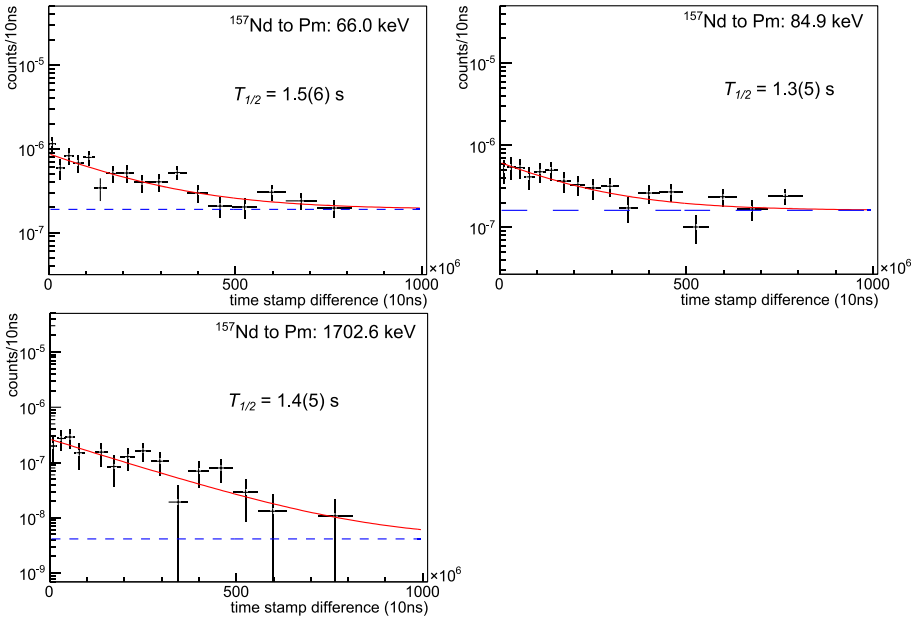

Figure 4.43 Time spectra gated on the peaks of γ rays from the β decay of ^{157}Nd to ^{157}Pm.

4.7 Known and new γ rays in ^{156}Nd ($Z = 60$, $N = 96$)

There is an isomeric state known at 1431 keV in ^{156}Nd by spontaneous fission [25]. This know isomer was consistently observed by the isomer spectroscopy in this work. Figure 4.44 shows the isomer spectrum of ^{156}Nd. There are four isomeric γ rays observed and the half-lives of each delayed γ-ray peaks were derived from the time spectra as shown in Figure 4.45. All the half-lives agree with each other within the errors. The weighted average of them was 280(15) ns, which is consistent with the known value, 365(145) ns, and improved the accuracy. γ-γ coincidences of the four peaks were examined as shown in Figure 4.46 and summarized in Table 4.12. This is also consistent with the known level scheme shown in Figure 4.49. The 2^+ to 0^+ decay was not observed in the isomer spectroscopy in this work, which is because we had lower detection efficiency for low energy γ rays and also the γ rays were highly converted to electrons (the conversion coefficient is 9.5 according to BrIcc [67]).

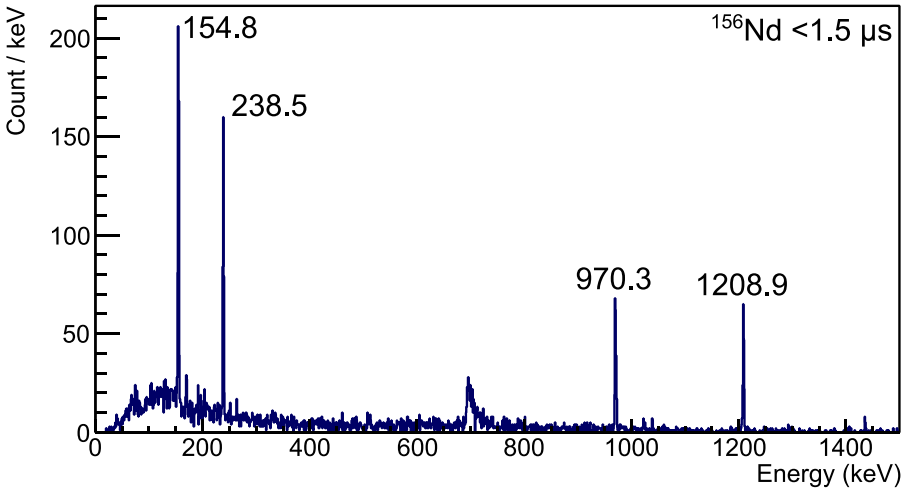

Figure 4.44 Energy spectrum of delayed γ rays from ^{156}Nd. The time window is up to 1.5 μs after the implantation.

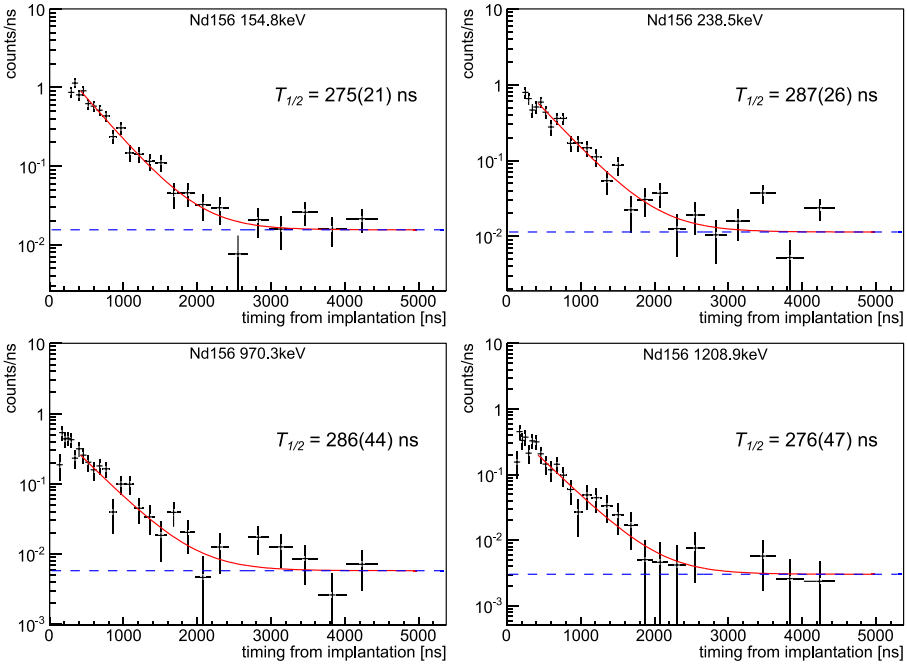

Figure 4.45 Time spectra gated on the peaks of delayed γ rays from ^{156}Nd.

Table 4.12 List of γ-ray coincidences in the isomeric decay of ^{156}Nd. Coincident γ rays are marked by ticks.

Energy (keV)	154.8	238.5	970.3	1208.9
154.8	gate	✔	✔	✔
238.5	✔	gate	✔	
970.3	✔	✔	gate	
1208.9	✔			gate

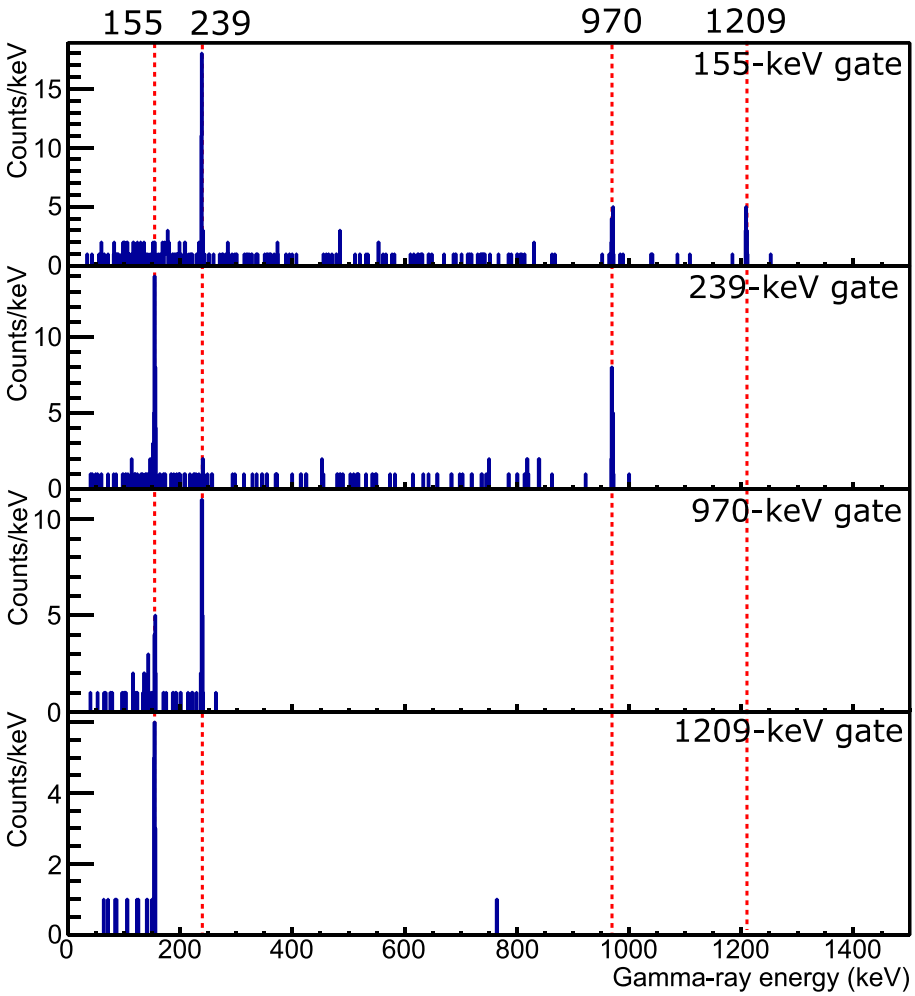

Figure 4.46 γ-γ coincidence spectra of ^{156}Nd gated by each γ ray.

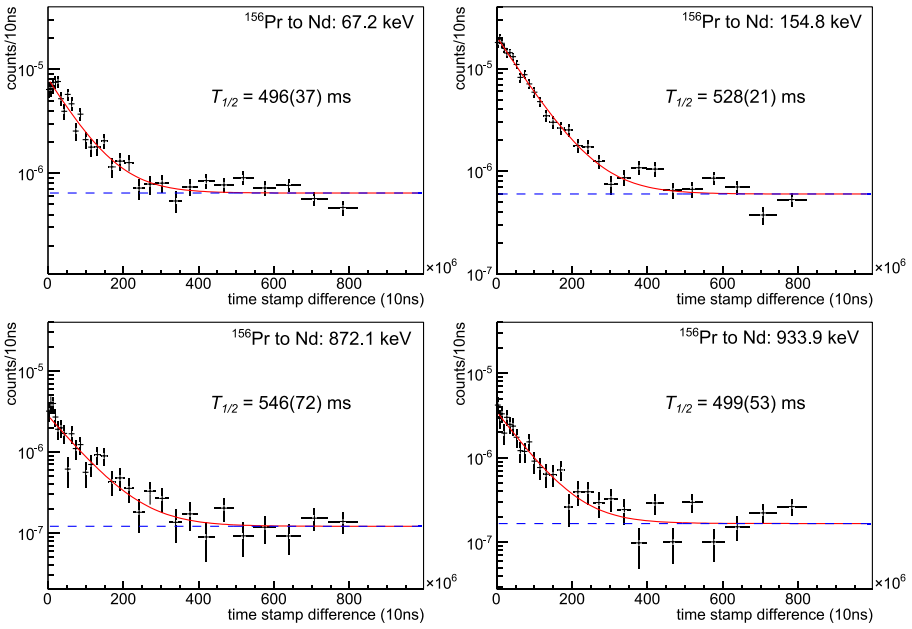

Figure 4.47 Time spectra gated on the peaks of γ rays from the β decay of ^{156}Pr to ^{156}Nd.

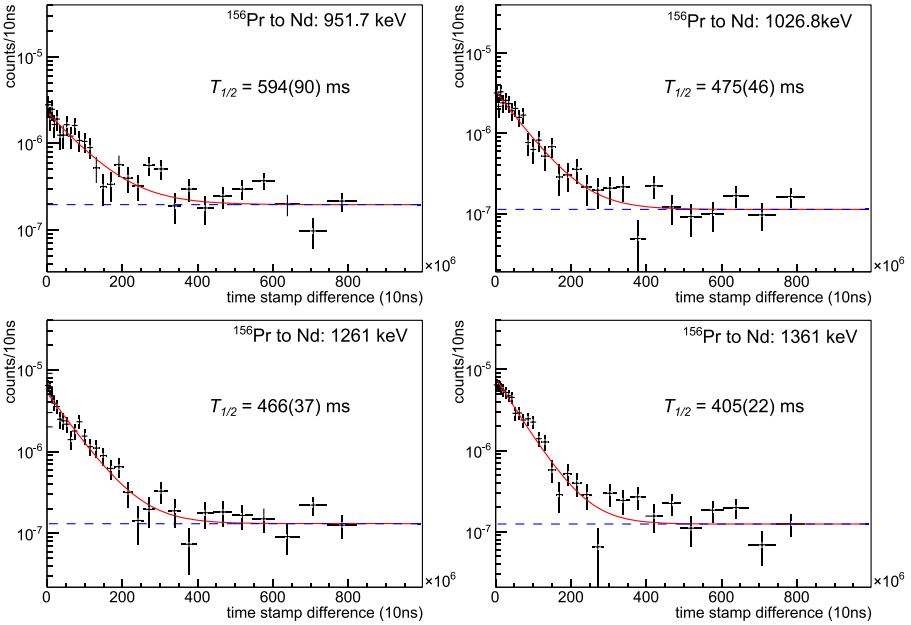

Figure 4.48 Time spectra gated on the peaks of γ rays from the β decay of ^{156}Pr to ^{156}Nd.

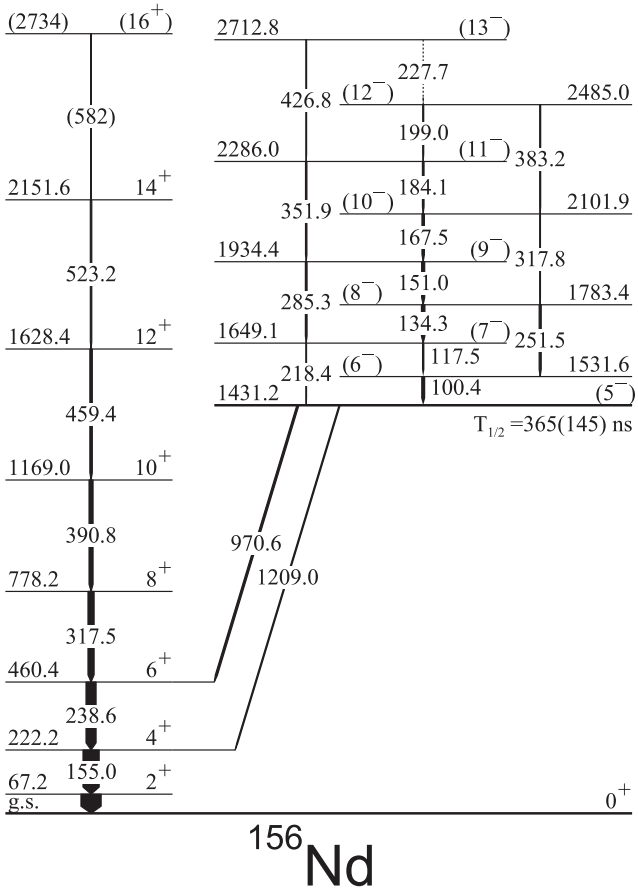

Figure 4.49 Level scheme of ^{156}Nd by a measurement of spontaneous fission [25]. Levels above the isomeric state is accessible by measuring prompt γ rays, which is not observed in this work.

β decay of ^{156}Pr to ^{156}Nd was also observed. Figure 4.50shows the half-life determination without γ-ray coincidence. The half-life of daughter (^{156}Nd), grand-daughter (^{156}Pm) and grand-grand-daughter (^{156}Sm) nuclides were fixed to 5.06 [88], 26.7 [86] and 3.4×10^4 [89] s respectively. The energy spectrum of γ rays with 3 s time window was plotted in Figure 4.51. There are 8 peaks observed whose half-lives were obtained to be around 500 ms. The decay curves of these γ rays are shown in Figure 4.51. The weighted mean value of the half-lives was 478(12) ms. The $4^+ \rightarrow 2^+$ and $2^+ \rightarrow 0^+$ decays of ground-state band were observed at 67.2 and 154.8 keV.

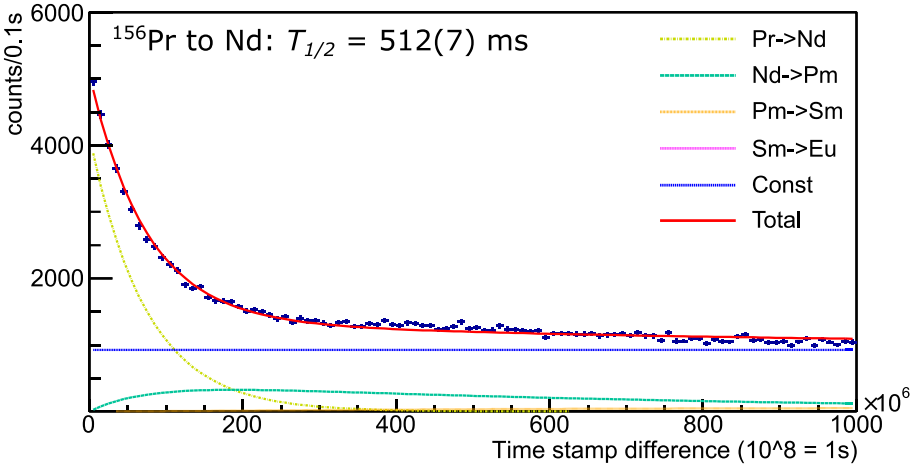

Figure 4.50 Decay curve of ^{156}Pr showing from 0 to 10 s fitted by the function including the component of ^{156}Nd, Pm and Sm. The half-life of the ^{156}Pr was deduced as 512(7) ms.

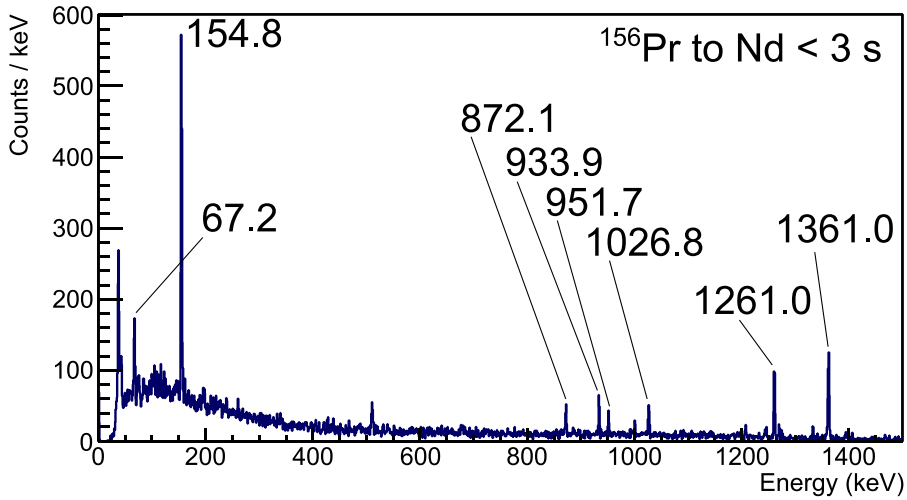

Figure 4.51 Energy spectrum of the β decay from ^{156}Pr to Nd. β-decay events with the time stamp difference from the beam implantation smaller than 3 s were plotted.

Table 4.13 List of γ-ray coincidences in the β-decay measurement of ^{156}Pr to ^{156}Nd. Coincident γ rays are marked by ticks. The column titled "else" on the right shows the coincident γ rays which were not identified as peaks in the singles γ-ray spectrum but observed in γ-γ coincident spectrum.

Energy (keV)	67	155	871	934	952	1027	1261	1361	else
67	gate	✔						✔	
155	✔	gate	✔				✔		
871		✔	gate						
934				gate					427
952					gate			✔	
1027						gate			235
1261		✔					gate		
1361	✔				✔			gate	

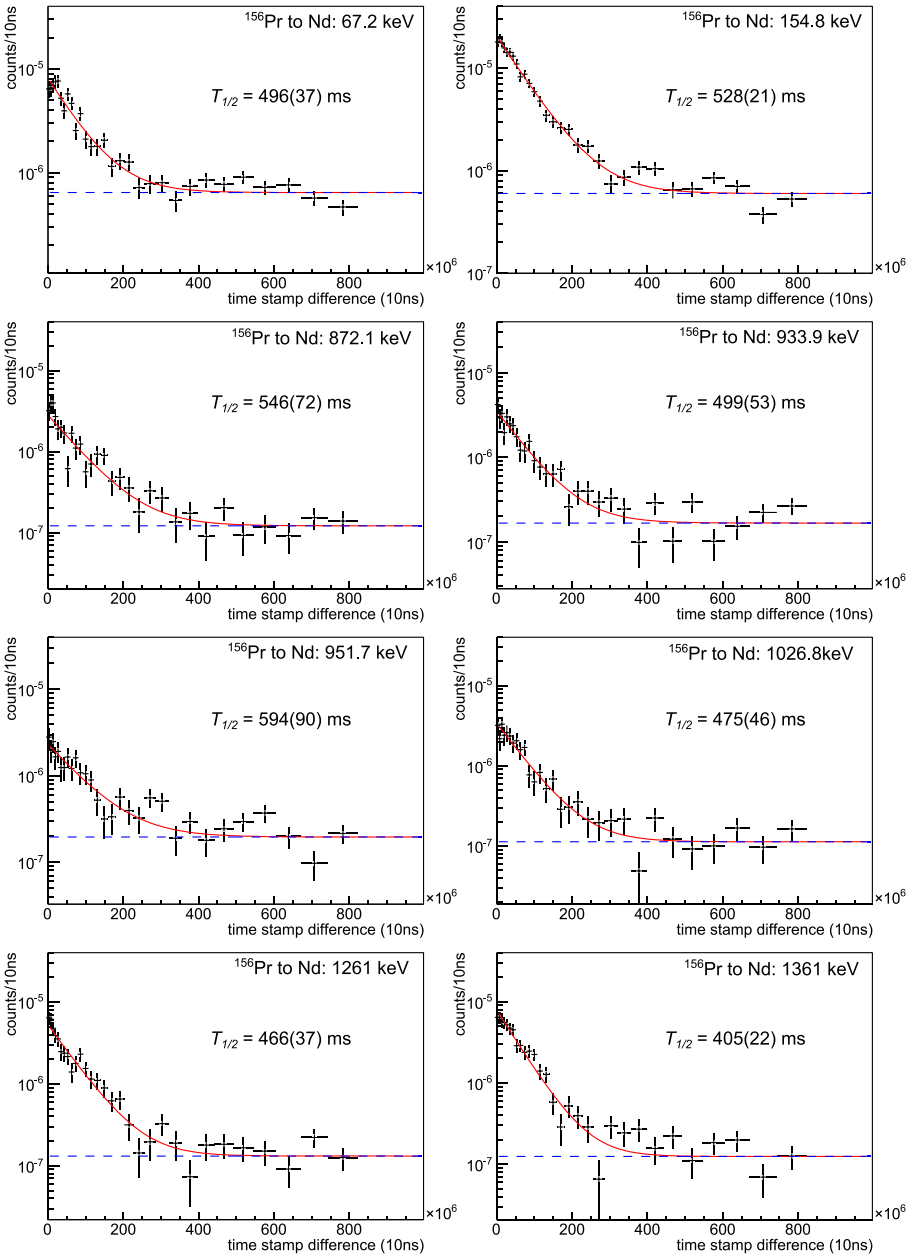

Figure 4.52 Time spectra gated on the peaks of γ rays from the β decay of ^{156}Pr to ^{156}Nd.

Chapter 5 Discussion

In the previous chapter, experimental results of neutron-rich midshell nuclei with $Z \sim 60$ are shown. Many new excited states were newly observed in this work. This chapter first discusses on the systematics of excitation energies of ground-state bands, which gives us information on the deformation, moment of inertia of the nuclei. Then, the systematics of the isomeric states will be discussed. Excitation energies and half-lives of quasi-particle isomers provide us some insights to the development of single-particle orbitals associated with the hexadecupole deformation in such deformed nuclei. In the last, octupole deformation in Ba isotopes will be discussed.

5.1 Systematics of the deformation of ground states

5.1.1 The first 2^+ and 4^+ energies of even-even nuclides

Excitation energies of the first 2^+ and 4^+ states of even-even nuclei reflect collective characteristics of the nucleus and widely used as an index of nuclear deformation since the levels at low excitation region of even-even nuclei are much simpler than those of odd nuclides. Eigenenergy of rotational motion, $E(I)$, with the angular momentum I, and the moment of inertia $\Im$, can be expressed as following equation.

$$E(I) = \frac{\hbar^2}{2\Im} I(I+1) \tag{5.1}$$

From the equation (5.1), kinematic moment of inertia, $\Im^{(1)}$ can be defined as follows.

$$\Im^{(1)}(I-1) = 2(I-1)/E_\gamma[I \to I-2] \tag{5.2}$$

$E_\gamma[I \to I-2]$ represents the energy of the γ decay from the state with spin I to $I-2$. From the energy of first 4^+ to 2^+ decay, one can obtain $\Im^{(1)}(3)$ for example. Since the rotational moment of inertia has a 5/3-rd power of mass dependence, $\Im^{(1)}/A^{5/3}$ is a good guideline for the nuclear deformation.

In Figure 5.1, the empirical β_2 values calculated from $\Im^{(1)}(1)$ are compared with experimental values of β_2 obtained from more direct measurement, lifetime or Coulomb excitation measurement, for Er isotopes. The plot shows nice agreement in the systematic trends of experimental and empirical values. It shows the $\Im^{(1)}$ values obtained from E_γ can be used as an indicator of the deformation, β_2. For an ideal rigid rotor, the ratio of the excitation energies of the first 4^+ and 2^+ states is equal to $I(I+1)_{I=4}/I(I+1)_{I=2} = 20/6 \approx 3.33$. The $E(4_1^+)$ to $E(2_1^+)$ ratio is a good measure to see the collective property of the nucleus, whether it is rotational $E(4_1^+)/E(2_1^+) \approx 3.33$ or vibrational $E(4_1^+)/E(2_1^+) \approx 2.0$.

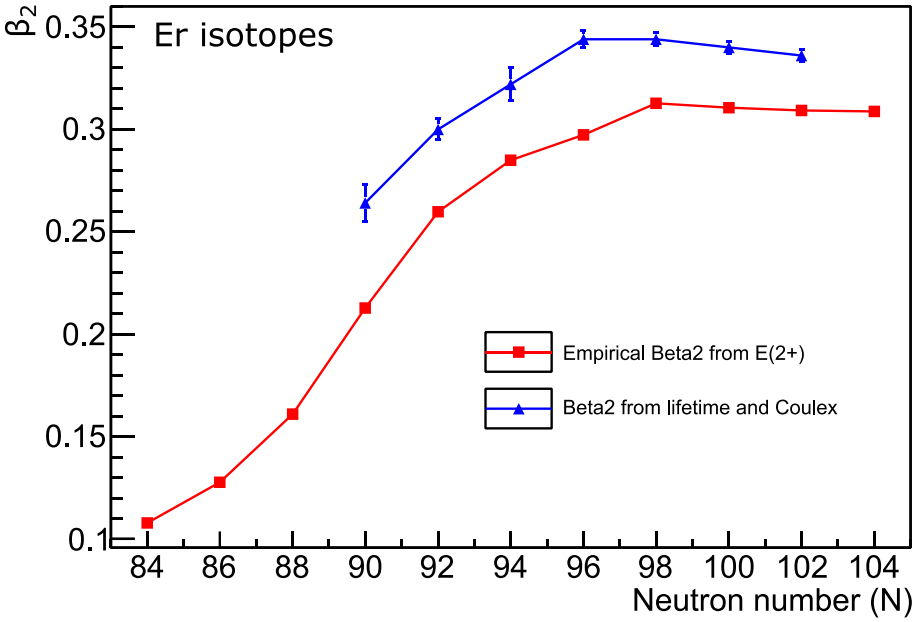

Figure 5.1 Comparison between β_2 values deduced from lifetime or Coulomb excitation measurements and empirical β_2 values calculated from the excitation energies of the first 2^+ states for Er isotopes. The values of the experimental β_2 and $E(2_1^+)$ energies are from [90].

Figure 5.2 shows the systematics of the experimental $E(4_1^+)/E(2_1^+)$ values of $Z \sim 60$ midshell nuclei. As already discussed in [22], there is a steep increase of the $E(4_1^+)/E(2_1^+)$ value at $N = 88$ to 90. $N \sim 100$ nuclei have values almost 3.3, which indicates that those nuclei are well deformed and can be regarded as good rotors. The steepness at $N = 88$ to 90 is largest at Gd ($Z = 64$) and gets smoother in lower or higher Z isotopes. This is explained by the $Z = 64$ sub-shell closure in $N \leq 88$ nuclei in [22]. Figure 5.3 and Figure 5.4 shows the systematics of nuclear moment of inertia obtained from $E_\gamma[4^+ \rightarrow 2^+]$ and $E_\gamma[2^+ \rightarrow 0^+]$ respectively. Those systematics also shows the sudden onset of the deformation at $N = 88$ to 90 and large deformation in $N \sim 100$ nuclei. From the plots (a) in Figure 5.3 and Figure 5.4, there is a local minimum of the moment of inertia at $N = 100$ nuclei. This has been reported in Gd [69] and has been discussed as due to the new shell gap at $N = 100$ predicted in [10,91]. The key feature of the new result of present work is the systematics of Sm and Nd isotopes. It looks that the kink at $N = 100$ is also present in Sm but absent in Nd contrary to the prediction of $N = 100$ shell gap [10]. The result on Sm isotopes support the theory which predicts $N = 100$ shell gap but it may not be the case in Nd. One other feature is that Nd ($Z = 60$) isotopes seems to have largest quadrupole deformation as shown in the plots (b). Figure 5.5 shows β_2 values of $N = 100$ isotones calculated by three different theoretical methods. None of the calculation in the figure shows deformation maximum at $Z = 60$. This result may also indicate new phenomena in neutron-rich nuclei which is not included in current theoretical calculations.

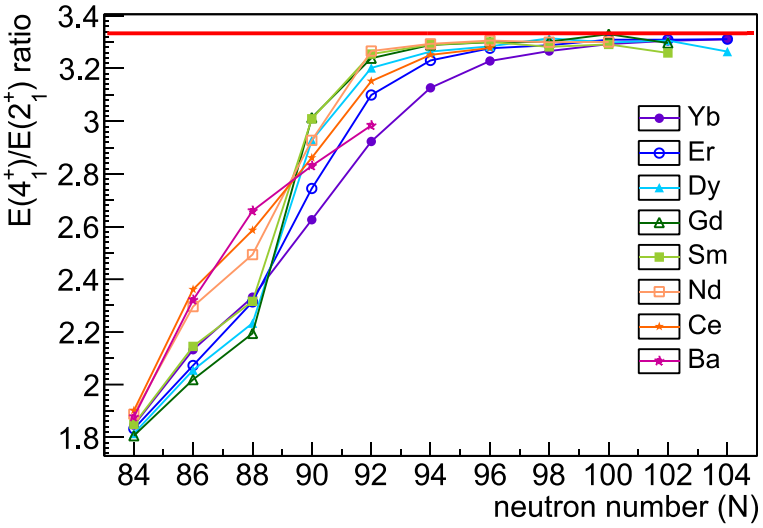

Figure 5.2 Systematics of the energy ratio of the first 4^+ and 2^+ states of $Z = 56$ to 70 even-even isotopes. The red line indicates the ideal value of a rigid rotor, 3.33. Known values were taken from [92].

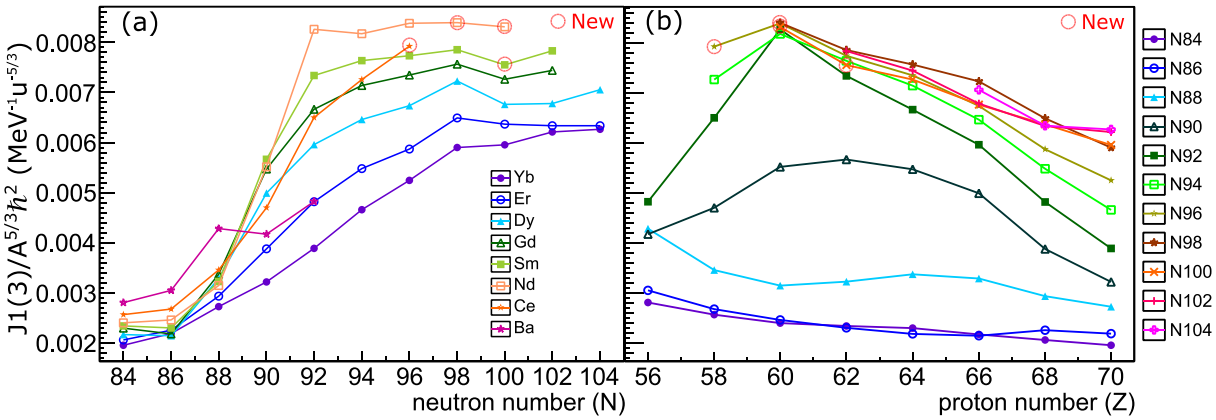

Figure 5.3 Systematics of the moment of inertia scaled by $A^{5/3}$ obtained from $E(4_1^+)$ values ($\Im^{(1)}(3)$). (a) is plotted by isotopes and (b) is plotted by isotones. Known values were taken from [92].

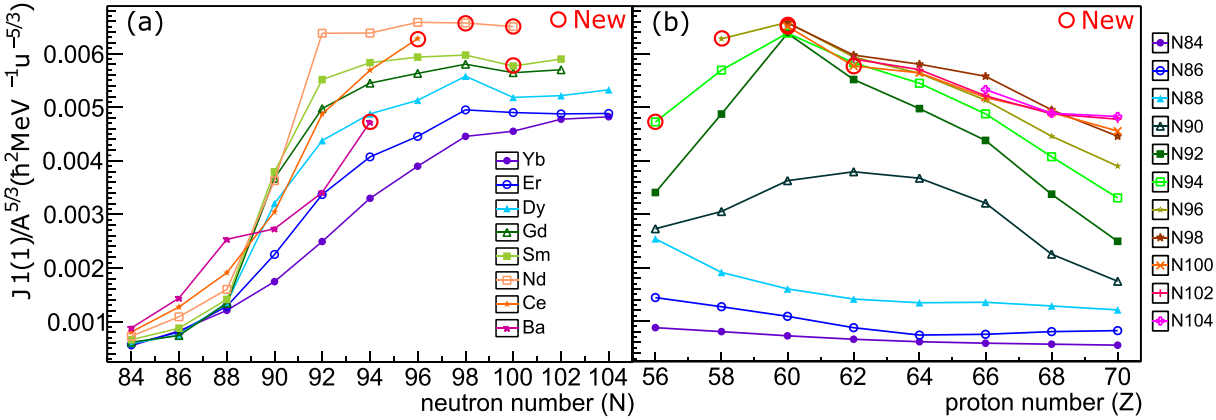

Figure 5.4 Systematics of the moment of inertia scaled by $A^{5/3}$ obtained from $E(2_1^+)$ values ($\Im^{(1)}(1)$). (a) is plotted by isotopes and (b) is plotted by isotones. Known values were taken from [92].

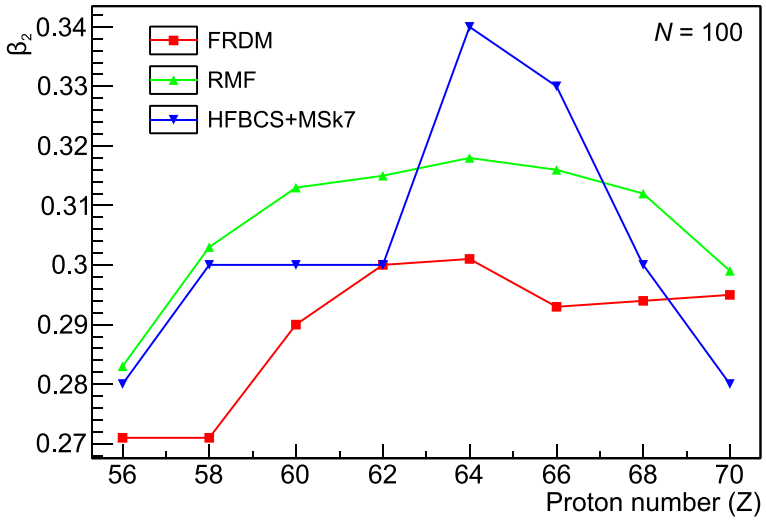

Figure 5.5 Theoretical calculations of ground-state β_2 values for $N = 100$ isotones. Those values were taken from [14] (FRDM), [20] (RMF) and [21] (HFBCS+MSk7)

Indication of hexadecupole deformation in Nd isotopes

Increase of quadrupole and hexadecupole deformation when going from Dy to Nd is a possible explanation for the disappearance of the kink at $N = 100$. From the plots (b) of Figure 5.3 and Figure 5.4, the moments of inertia peak at Nd ($Z = 60$) in $N \geq 92$ isotones that indicate increasing quadrupole deformation. ^{152}Nd is the most neutron-rich Nd isotopes with an experimental value of quadrupole deformation, which is $\beta_2 = 0.349(12)$ [93]. From the systematics of the moment of inertia, ^{160}Nd is expected to have deformation equivalent to or even larger than ^{152}Nd. Nd isotopes are also expected to have large hexadecupole deformation [14]. The trends of hexadecupole deformation that Nd isotopes have larger β_4 values than other $Z \sim 60$ isotopes can be explained qualitatively. As shown in Appendix A, an orbital of a single particle in a potential with axial symmetry is expressed by asymptotic quantum numbers, N, n_z, Λ. In the case of deformed harmonic oscillator potential, hexadecupole moment of an orbital defined by asymptotic quantum numbers, $|N, n_z, \Lambda\rangle$, can be written as,

$$\begin{aligned}\langle N n_z \Lambda | r^4 Y_{40} | N n_z \Lambda \rangle \\ = \left(\frac{9}{4\pi}\right)^{\frac{1}{2}} \frac{3}{4} (27 n_z^2 - 22 n_z N + 3N^2 - \Lambda^2 - 6 n_z \\ - 2N) \left(\frac{\hbar}{2M\omega_0}\right)^2 .\end{aligned} \tag{5.3}$$

Plot of the equation above for the Nilsson orbitals originate from $h_{11/2}$ spherical orbit is shown in Figure 5.6 (a). From the plot, the orbital with $N = n_z$ has large hexadecupole moment, while orbitals with n_z value somewhere in the middle will have negative moment. In quadrupole deformed nuclei with $\beta_2 \sim 0.2$ to 0.3, the $h_{11/2}$ orbitals are starting to be filled from larger n_z orbital in Ce ($Z = 58$) as shown in the Nilsson diagram in Figure 5.6 (b). Since the orbitals with $n_z = 4, 5$ have positive while those with $n_z = 3, 2, 1$ have negative

hexadecupole moment from the plot (a), Nd ($Z = 60$) isotopes are expected to have the largest hexadecupole moment. Such discussion using deformed harmonic oscillator potential was given by A. Bohr and B. R. Mottelson [94].

Large hexadecupole deformation of a nucleus will lower the energies of orbitals with large hexadecupole interaction. This can happen for neutron orbitals. For example, 1/2[651] orbital from $g_{9/2}$ spherical orbit have $n_z = 5$ and be lowered in hexadecupole deformed nucleus. The β_2 of ^{160}Nd expected to be as large as that of ^{152}Nd ($\beta_2 = 0.349$). The β_4 is also expected to be large since $\beta_4 \sim 0.07$ is reported in ^{148}Nd [37]. Single particle levels with and without hexadecupole deformation were calculated using deformed Woods-Saxon potential [35] as shown in Figure 5.7. As hexadecupole moment increased, the 1/2[651] orbital becomes lower energy and crosses with 7/2[633] orbital at around $\beta_2 \sim 0.35$. Eventually, the termination of deformed gap at $N = 100$ will occur in ^{160}Nd as shown in Figure 5.7. This can change the systematics of moment of inertia of Nd isotopes.

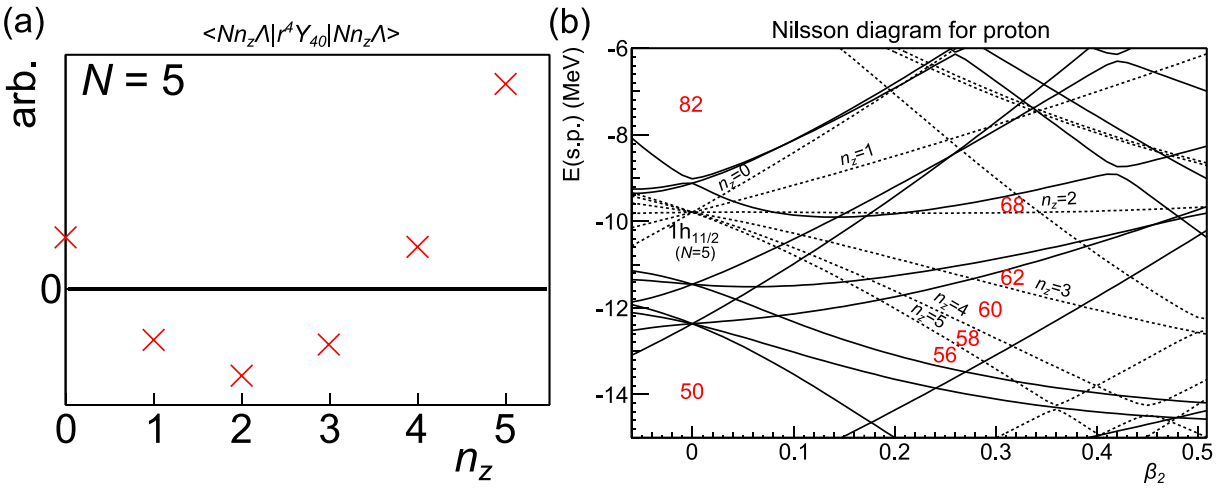

Figure 5.6 (a) Plot of the equation (5.3) for the orbitals originate from $h_{11/2}$ spherical orbit. (b) Nilsson diagram for proton around the Fermi surface of $Z \sim 60$ nuclei.

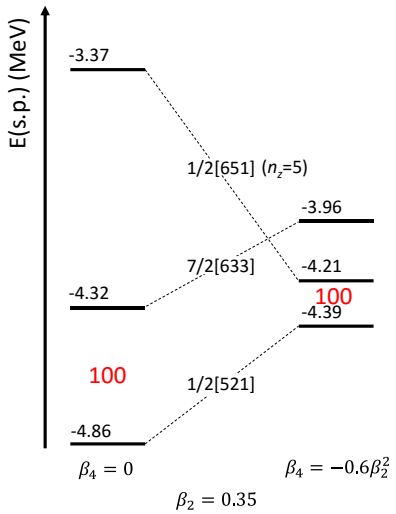

Figure 5.7 Single particle energies of Nilsson levels at $N = 100$ with and without hexadecupole deformation calculated by [35].

5.1.2 Rotational bands on the ground state of odd mass isotopes

One quasi-particle states of deformed odd mass nuclei also have rotational structures. Moments of inertia of odd mass nuclei show larger variations than those of even-even nuclei, due to the second-order effects of the Coriolis coupling acting on the last odd particle as discussed in [94]. However, systematics of the rotational bands with the last odd particle in the same orbit will show some systematics on the deformation of the core. In Tb isotopes, rotational bands of $3/2[411]$ have been known on the ground states systematically [75–78]. The same rotational bands were newly observed for $N = 100$ and 102 isotopes by the isomer spectroscopy in this work. In Pm isotopes, the rotational band of $5/2[521]$ has been known on the ground state of ^{155}Pm ($N = 94$) [73]. Similar excitations were newly observed in ^{157}Pm by β-γ spectroscopy and in ^{159}Pm and ^{161}Pm by isomer spectroscopy. The systematics of the moment of inertia for Tb and Pm isotopes are shown in Figure 5.8. Two new data points of Tb revealed the existence of $N = 100$ shell gap. The moment of inertia decrease at $N = 100$ and increase again at $N = 102$. On the other hand, the new data point of Pm at $N = 100$ does not show clear decrease which is consistent with the plot of the disappearance of $N = 100$ shell gap in $Z < 62$ described in Section 5.1.1. This results on odd mass isotopes suggest larger hexadecupole deformation in Pm ($Z = 61$) than Tb ($Z = 65$) which is consistent with the discussion in the previous subsection.

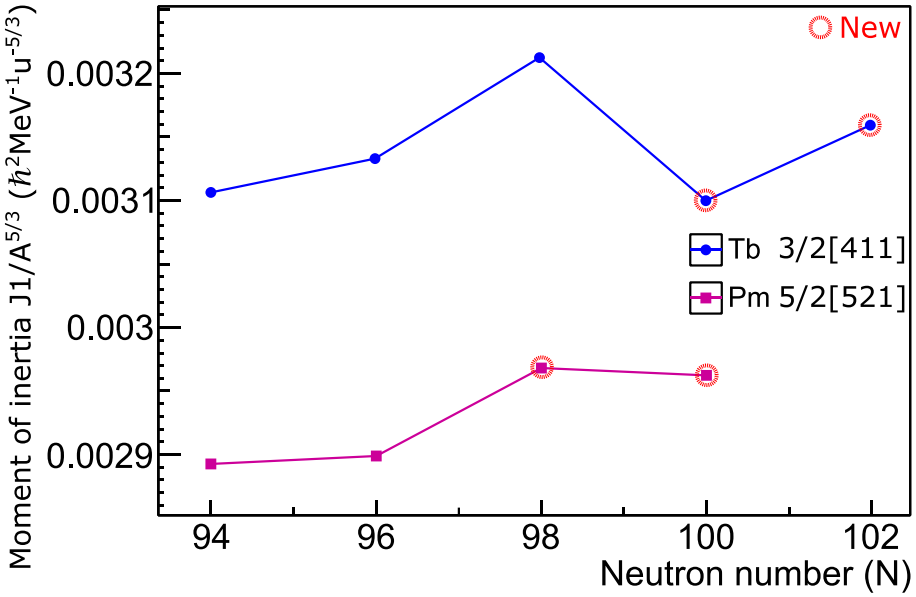

Figure 5.8 Systematics of the moment of inertia scaled by $A^{5/3}$ obtained from $E(7/2^+)$ for Tb isotopes and $E(9/2^-)$ for Pm isotopes.

5.2 Systematics of K isomers

Many isomers that assigned as neutron 2 quasi-particle excitation were observed at the excitation energy around 1 to 2 MeV in $N \sim 100$ midshell nuclei. In order to excite a 2-qp state, one of the neutron pairing should be broken. Therefore, there exists a lower limit of the excitation energy of 2-qp state. Neutron pairing energies can be estimated from the difference of the binding energies of neighboring odd-N and even-N nuclei. Figure 5.9 shows the neutron pairing energies of $Z = 58$ to 64 even-Z isotopes deduced from the mass table in AME2003 [95,96]. The pairing energies are gradually decreased as the neutron number increases. At $N \sim 100$, the pairing energy get as low as ~700 keV. The excitation energies of the 2-qp isomers, ~1 MeV, are reasonable as the sums of the energy for breaking neutron pairing and that of quasi-particle excitation.

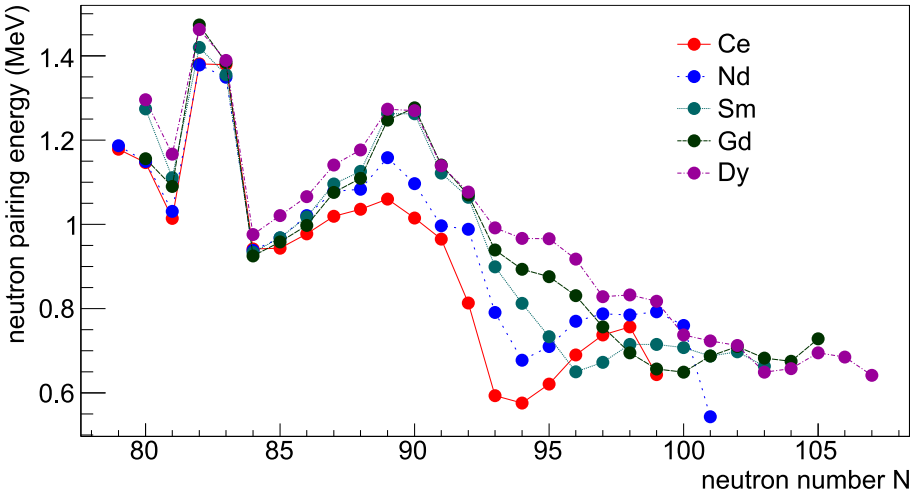

Figure 5.9 Neutron pairing energies of $Z = 58$ to 64 isotopes.

5.2.1 $K^{\pi} = 4^{-}$ isomers at $N = 100$ isotones

Isomers with similar excitation energy and half-life have been newly observed in $N = 100$ isotones from $Z = 60$ to 64. The isomer energies and hindrance factors are summarized in Table 5.1. The hindrance factors of all the isomeric decays in $N = 100$ isotones are on the order of 10^9. This suggests that all of these isomers may have same origin. Figure 5.10 shows the excitation energies of even-even $N = 100$ isotones. There has been isomers reported in ^{170}Yb [26] and ^{168}Er [27] ($Z = 68$ and 70). These known isomers are assigned as 2 quasi-particle (2-qp) excitation with the configuration of $\nu 7/2[633] \otimes \nu 1/2[521]$ whose $K^{\pi} = 4^{-}$. The empirical rule by F. D. Kondev *et al.* [97] (See Appendix B) gives $\Delta K = 4$ hindrance with an E1 decay as $\log F_w = 8.3 + 1.4 - 1.6$. The hindrance factor of the isomer at $N = 100$ isotones are consistent with the empirical rule.

Indication of hexadecupole deformation in Nd isotopes from isomers

The excitation energies of the isomeric states show slight decrease from Yb to Sm but one interesting feature is that it gets higher again in Nd. The gradual decrease of isomeric state can be explained by Nilsson-model calculation with Woods-Saxon potential. Figure 5.11 shows the Nilsson diagram for neutrons. From this diagram, the gap between $\nu 7/2[633]$ and $\nu 1/2[521]$ gets smaller as quadrupole deformation increases. As the moment of inertia from $E(2^+)$ and $E(4^+)$ indicates increase of β_2 from Yb to Nd, it is expected that excitation energy of the isomeric state decreases. The increase of the energy at Nd cannot be explained from the quadrupole deformation. The configuration of the isomeric states have been examined with projected shell-model (PSM) calculation [98]. The model has successfully described the 2-qp isomeric states of ^{154,156}Nd, ^{156,158,160}Sm as reported in [25,99]. The PSM calculations predict a $K^{\pi} = 4^{-}$ state with a $\nu 7/2[633] \otimes \nu 1/2[521]$ configuration at an energy of 1.1 MeV for ^{162}Sm and 1.2 MeV for ^{160}Nd by Y.-C. Yang *et al.* [99]. They predicted slightly higher energies but reproduced the increase of the excitation energy by ~ 100 keV from ^{162}Sm to ^{160}Nd. For this calculation, quadrupole and hexadecupole deformation were assumed to be $\beta_2 = 0.318$, $\beta_4 = 0.008$ for ^{162}Sm and $\beta_2 = 0.332$, $\beta_4 = 0.032$. They employed larger β_4 value for ^{160}Nd comparing to that for ^{162}Sm [14], and the change of β_4 value may have resulted in larger excitation energy of the isomer in ^{160}Nd. In order to identify the effect of hexadecupole deformation, we have calculated quasi-particle energies of $\nu 7/2[633] \otimes \nu 1/2[521]$ excitation by using similar PSM code [100]. By using exactly the same deformation parameters as the calculation in [99], we obtained quasi-particle energies of 1.03 MeV for ^{162}Sm and 1.15 MeV for ^{160}Nd. As we decreased input β_4 value of ^{160}Nd to 0.008, the quasi-particle energy got lower to 1.01 MeV. This suggests that the increase of quasi-particle energy due to the large hexadecupole deformation in Nd is responsible for the increase of the excitation energy of the isomer from Sm to Nd.

Table 5.1 Partial half-lives ($T_{\gamma 1/2}$) and the hindrance factors of a γ decay from each isomeric state in $N = 100$ isotones. The isomers in ^{170}Yb and ^{168}Er are from [26] and [27].

Nuclide	E_{isomer} (keV)	E_γ (keV)	$T_{\gamma 1/2}(exp.)$ (s)	F_w
^{170}Yb	1259	981.1	3.7×10^{-7}	1.6×10^{9}
^{168}Er	1094	830.0	1.1×10^{-6}	2.9×10^{9}
^{164}Gd	1094	854.1	7.1×10^{-7}	2.0×10^{9}
^{163}Eu	964	674.9	9.1×10^{-7}	1.2×10^{9}
^{162}Sm	1010	774.5	1.8×10^{-6}	3.6×10^{9}
^{161}Pm	966	727.5	7.6×10^{-7}	1.3×10^{9}
^{160}Nd	1108	892.8	1.3×10^{-6}	4.0×10^{9}

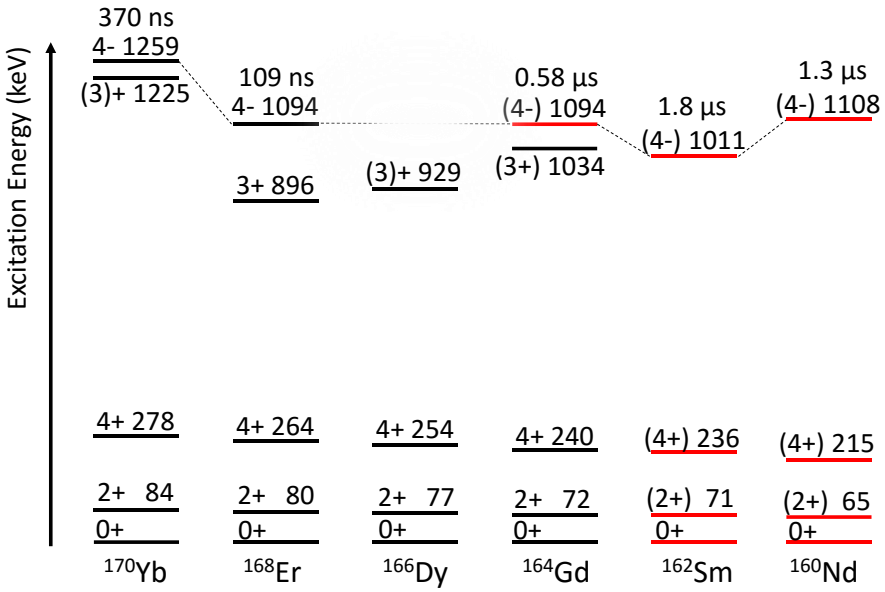

Figure 5.10 Systematics of the excitation energies of $K^\pi = 4^-$ isomers in $N = 100$ isotones. The levels newly observed in this work are shown in red lines.

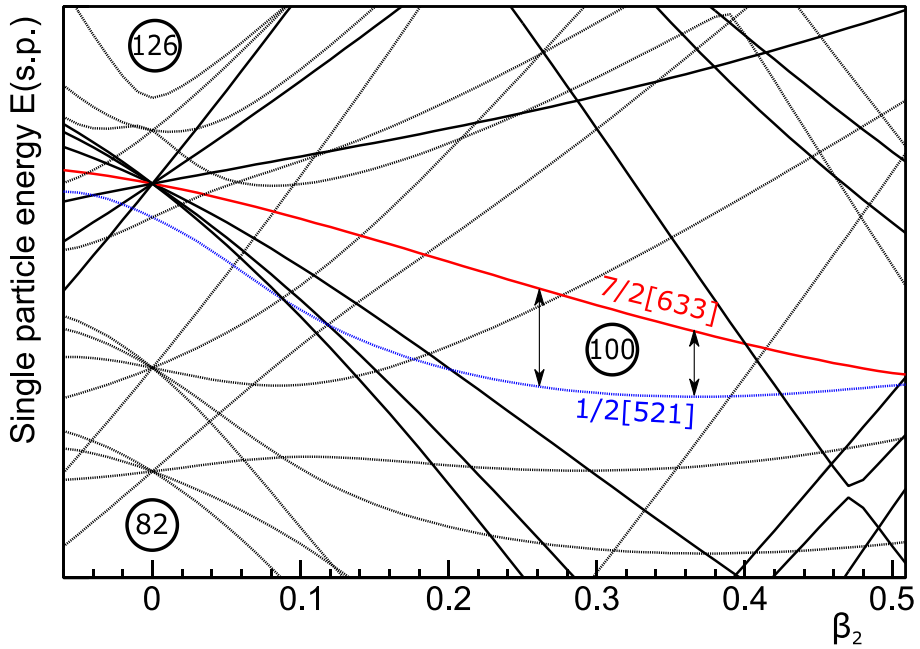

Figure 5.11 Nilsson diagram for neutrons around $N = 100$ calculated by [35]. Energy differences between 7/2[633] (red solid curve) and 1/2[521] (blue dashed curve) are shown by black arrows.

Systematics of γ-vibrational bands

One other feature of the systematics in Figure 5.10 is that there was no $J^\pi = 3^+$ excitation observed for Sm and Nd that has been observed in the isomeric decay of Yb to Gd. The 3^+ states in Yb and Er are reported as a member of $K^\pi = 2^+$ γ-vibrational band [26,27]. Disappearance of the 3^+ state may imply that the energy of the γ-vibrational excitation gets higher than that of $K^\pi = 4^-$ isomer in Sm and Nd. The trends of γ-vibrational state can also be explained qualitatively by calculations of deformed harmonic oscillator potential. The operator r^2Y_{22} that is responsible for γ-vibration, has a selection to the interaction between orbitals with $\Delta n_z = 0$ for $\Delta N = 0$. The detail was discussed by A. Bohr and B. R. Mottelson in [94]. As the quadrupole deformation develops in nucleus, the single particle levels with same n_z will get closer than those with different n_z. This will cause significant subshell effects for the transitions with $\Delta n_z = 0$. The blue lines in Figure 5.12 shows a subshell with $N = 4$, $n_z = 1$ orbitals for proton. At the deformation $\beta_2 \sim 0.3$, this subshell is started to be filled from $Z = 64$ (Gd) and be closed at $Z = 70$. It is expected that γ-vibrational excitation appears at relatively low energy and with large strength in the nucleus whose Fermi surface on the subshell $62 < Z < 70$. This reasonably explains the experimental systematics that the 3^+ state of Yb ($Z = 70$) have higher energy than those of Gd to Er ($Z = 64$ to 68) and again get higher in Sm and Nd ($Z = 62$ and 60).

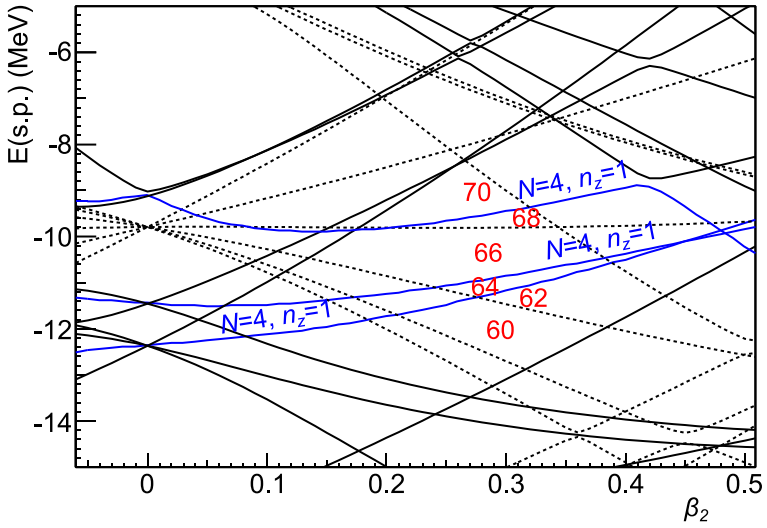

Figure 5.12 Nilsson diagram for proton around $Z = 60$. Blue lines show the orbitals with $N = 4,\ n_z = 1$.

5.2.2 K isomers in $N = 98$ isotones

In ^{159}Pm and ^{158}Nd, the isomers were assigned as a $K^\pi = 6^-$ neutron two quasi-particle excitation. There is $K^\pi = 5^-$ isomer with a configuration of $\nu 5/2[642] \otimes \nu 5/2[523]$ in ^{160}Sm. In the case of ^{160}Sm, the isomeric state decays both to 6^+ and 4^+ states of the ground-state band while in the case of ^{158}Nd, the isomeric state only decays to the 6^+ state. It suggests that the spin of the isomeric state in ^{158}Nd is not 5 but 6. The possible configuration for $K = 6$ isomer around $N = 98$ is $\nu 1/2[651] \otimes \nu 11/2[505]$. The hindrance factor of ^{158}Nd, $F_w = 2.3 \times 10^9$ as listed in Table 5.2, is in the range of empirical rule for $\Delta K = 6$ isomer, $8.3 < \log F_w < 12.5$ [97]. The change of isomer configuration from $K^\pi = 5^-$ in ^{160}Sm to $K^\pi = 6^-$ in ^{158}Nd may be explained by the increase of hexadecupole deformation in Nd. Single particle levels around the Fermi surface of $N = 98$ with and without hexadecupole deformation were calculated using deformed Woods-Saxon potential by the code [35] as shown in Figure 5.13. As discussed in Section 5.1.1, hexadecupole deformation lower the orbit with large n_z. The $1/2[651]$ orbital gets lower as β_4 increased, that can result in lowering the excitation energy of the $K^\pi = 6^-$ two quasi-particle state, $\nu 1/2[651] \otimes \nu 11/2[505]$ at Nd to become an isomer. This result supports the onset of hexadecupole deformation at Nd isotopes also in $N = 98$.

Table 5.2 Partial half-lives ($T_{\gamma 1/2}$) and the hindrance factors of a γ decay from each isomeric state in $N = 98$ isotones.

Nuclide	E_{isomer} (keV)	E_γ (keV)	$T_{\gamma 1/2}(exp.)$ (s)	F_w
^{160}Sm	1361	1128.2	1.2×10^{-7}	1.1×10^9
^{159}Pm	1465	841.0	5.0×10^{-6}	2.2×10^{11}
^{158}Nd	1648	1197.1	3.1×10^{-7}	2.3×10^9

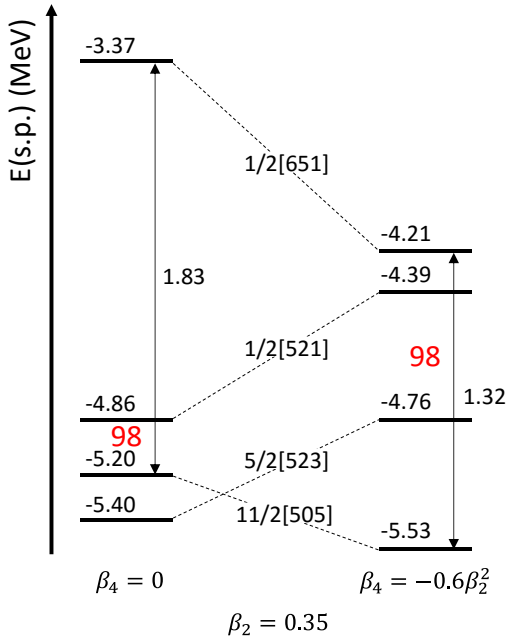

Figure 5.13 Single particle energies of Nilsson levels at $N = 98$ with and without hexadecupole deformation calculated by [35].

5.3 Octupole bands in Ba isotopes

The even-even Ba isotopes from $A = 140$ to 148 have been studied by spontaneous fission of ^{248}Cm [31] and negative parity bands with octupole collectivity are known. In this work, a candidate for the octupole negative parity state was observed in the most neutron-rich isotope ever measured, ^{150}Ba. Systematics of the $J^\pi = 3^-$ state of the octupole band is shown in Figure 5.14. Excitation energy of the 3^- state is getting lower as neutron number increased, and ^{150}Ba has the lowest energy, 697 keV, among the known Ba isotopes. Quadrupole deformation of the ground state seems to get larger as N increased from the systematics of the first 2^+ and 4^+ energies. The existence of the 3^- state at low excitation energy indicates that ^{150}Ba also have some octupole collectivity.

Theoretical calculations on octupole correlation so far have large uncertainty and differ with each other. Microscopic-macroscopic calculation [32,101] predicts large β_3 values ~ 0.074 in ^{150}Ba while a Hartree-Fock calculation [34] argues that there is no state with octupole moment in ^{150}Ba. In this study, new calculation was carried out using recent method solving random-phase approximation (RPA) in totally self-consistent Hartree-Fock theory [102,103]. Up to recent, there had been only a few attempts of fully self-consistent RPA calculations, that is, with full residual interactions, especially for deformed nuclei. In this calculation, representation by fully three-dimensional real space (without any spatial symmetry) was employed in order to allow the shape breaking any spatial symmetry such as the octupole deformed shape with reflection asymmetry. The SkM* force [104] was employed for the calculation and the LS force was also taken into account, while pairing term was ignored.

Results of the RPA calculation on Ba isotopes are shown in Figure 5.15. From this calculation,

we obtained static octupole deformation on the ground states of Ba isotopes $N = 84$ to 94. Figure 5.16 shows the comparison of the β_2 and β_3 values by the RPA calculation with experimental values that related to quadrupole and octupole deformation. The octupole deformation of ^{144}Ba was as large as $\beta_3 = 0.162$ and this is larger than the calculation by Möller *et al.* [14], $\beta_3 = 0.126$. A local minimum of the octupole deformation at $N = 90$ was appeared in the calculation, which is consistent with the systematics of experimental dipole moments as shown in Figure 5.16 (b). The gradual increase of the quadrupole deformation as going to neutron-rich isotopes is also consistent with the systematics of the experimental $E(2_1^+)$ values as shown in Figure 5.16 (a). $J^\pi = 3^-$ excitation was also calculated for ^{146}Ba to ^{150}Ba. Figure 5.17 shows the energy spectra of the octupole strength for $K = 0$ and $K = 1$ excitation by the calculation. The black dots in the figure shows the calculated points. Peaks in the spectra were fit by Lorentzian in order to obtain the excitation energy from the centroid and the octupole strength from the area of the peak. There were excited states with the energy reasonably low to regard as the state experimentally observed. The lowest $K = 1$ excitation of ^{150}Ba has 35 W.u. of octupole strength and the lowest $K = 0$ state has 20 W.u of strength. Those strength are too large for the contribution of a single particle (1 W.u.), and thus, the states appeared in the calculation have significant octupole collectivity. It is difficult to conclude whether the 697 keV state observed in this study corresponds to the states obtained from the calculation. However, this calculation supports that excited states with octupole collectivity can appear at low energy as experimentally observed in ^{150}Ba.

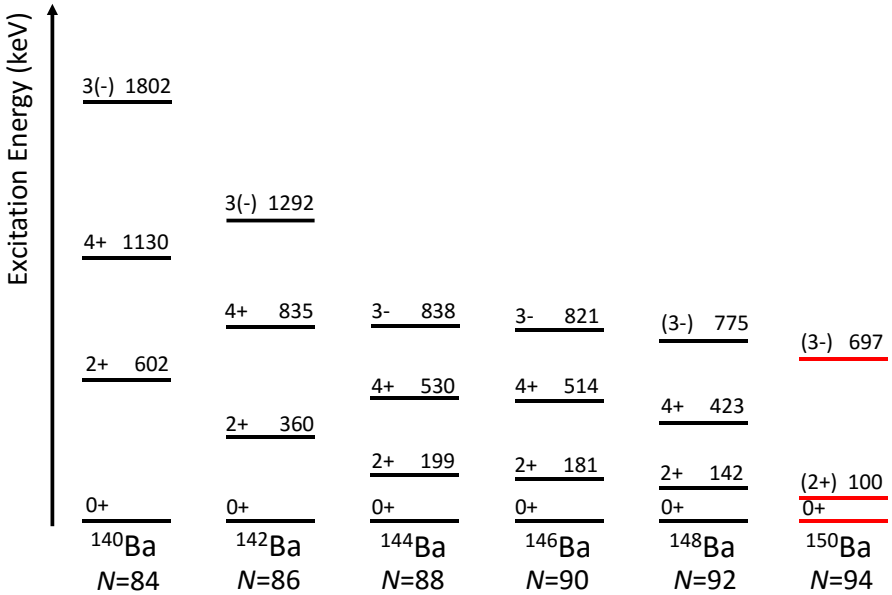

Figure 5.14 Systematics of the excitation energies of the first 2^+, 4^+ states of the ground-state band and 3^- states which are assumed to be an octupole excitation.

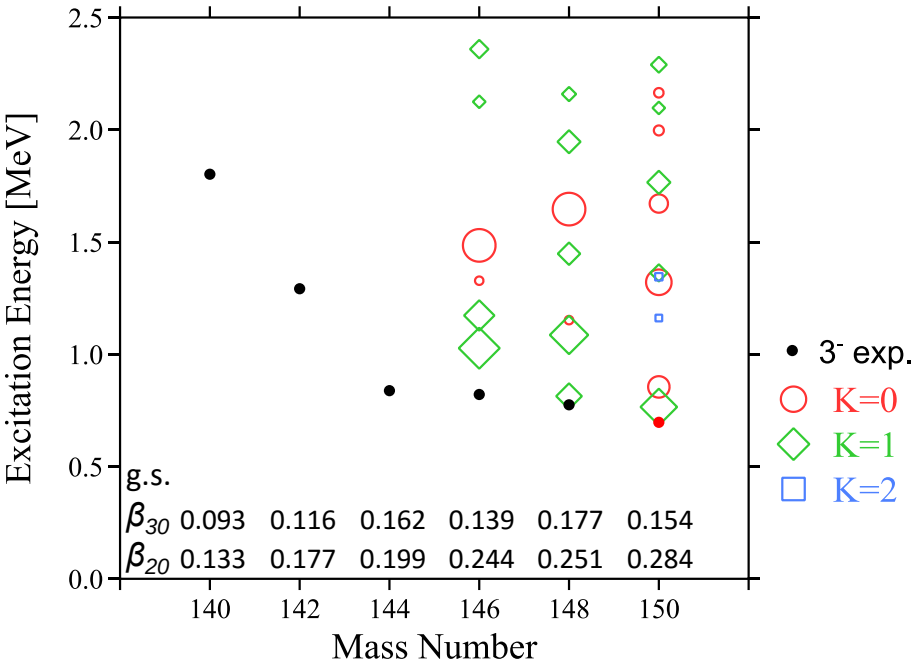

Figure 5.15 Excitation energies of 3^- states obtained by RPA calculation. The size of the points represents the octupole strength of each state. Quadrupole and octupole moment of the ground states are shown in the plot.

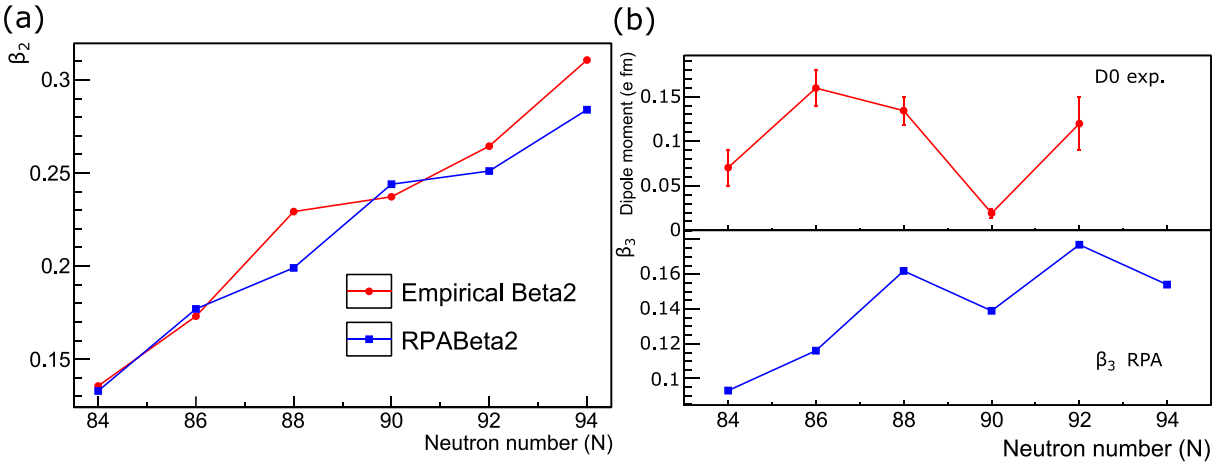

Figure 5.16 (a) Comparison of the β_2 values empirically deduced from $E(2_1^+)$ and the RPA calculation. (b) Comparison between experimental dipole moments [31] and β_3 values by the RPA calculation.

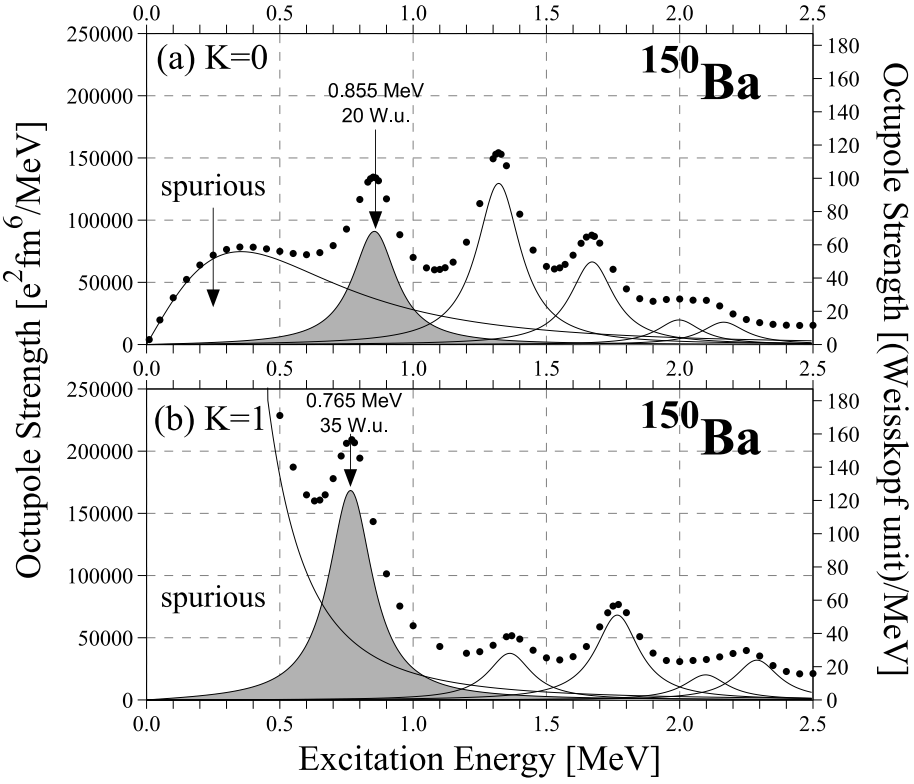

Figure 5.17 Energy spectra of octupole strength for $K = 0$ (a) and $K = 1$ (b) of ^{150}Ba by the RPA calculation.

5.4 Summary and perspectives

We have identified numerous new isomers and excited states in neutron-rich midshell nuclei around Z ~ 160. The increase in excitation energy of $K^\pi = 4^-$ isomers in $N = 100$ isotones and the change of isomer configuration from $K^\pi = 5^-$ to 6^- in $N = 98$ isotones from Sm to Nd can be explained by the effect of hexadecupole deformation. Recent self-consistent RPA calculations exhibit $J^\pi = 3^-$ states with octupole collectivity at low excitation energies (< 1 MeV), opening the possibility that the 697-keV level in ^{150}Ba is the corresponding 3^- state that has been identified in other neutron-rich Ba isotopes. This suggests that ^{150}Ba may also exhibit octupole collectivity. From the systematics of the $E(4_1^+)/E(2_1^+)$ ratio in even-even nuclei, the most neutron-rich isotopes in the $56 \leq Z \leq 70$ region have values ~3.3 and the ground states are expected to be good rotors. From the systematics of the moment of inertia, Nd isotopes ($Z = 60$) have the largest quadrupole deformation which is not consistent with any theoretical predictions so far. There is a local minimum in the moment of inertia at $N = 100$ in $62 \leq Z \leq 66$ isotopes, which provides an indication of a new deformed shell gap that is predicted at $N = 100$ by the calculations by L. Satpathy [10]. The calculations also predict that the $N = 100$ shell gap exists in $Z < 62$ isotopes; however, our results showed no local minimum in the moment of inertia at $N = 100$ in Nd ($Z = 60$) isotopes. Similar systematics were also observed in odd-mass nuclei: Tb ($Z = 65$) isotopes showed a local minimum in the moment of inertia at $N = 100$, while Pm ($Z = 61$) isotopes did not. These observations may relate to large hexadecupole deformation in Nd.

There are many *K* isomers in neutron-rich midshell nuclei. Figure 5.18 illustrates a distribution of isomers in the $Z \sim 60$, $N \sim 100$ region. Nuclides shaded orange or green contain isomers with half-lives longer than 100 ns. The number of isomers produced at the primary target was estimated for some of the new isomers from the γ-ray counts by correcting for the detection efficiencies and decay losses during the times of flight listed in Table 5.3—these values are tentative because the systematic errors were not evaluated, although the relative values can be compared between nuclides from the same experiment. The detection threshold of an isomer with a 1-μs half-life, a 2% isomer ratio, and a 1-MeV γ decay in the RIBF-86 experiment is $\sim 1.6 \times 10^4$ particles when the minimum number of counts in the peak is set to 20. Nuclides with >104 implantations are shaded grey in Figure 5.18. The figure indicates that either there are no isomers, the half-life is shorter than 1 μs, or the isomer ratio is relatively small in $Z < 58$ isotopes. Distribution of the *K* isomer indicates how well the nucleus is deformed with axial symmetry. The lifetime of a *K* isomer becomes shorter when either the quadrupole deformation is decreased or the axial symmetry of the nucleus is broken. In these circumstances the isomer cannot be observed using delayed γ-ray spectroscopy. The appearance of intermediate-*K* states below the excitation energies of high-*K* quasi-particle states can also shorten the half-life of high-*K* isomers by creating a decay path with smaller ΔK transitions. The reason for the disappearance of the *K* isomers in $Z \leq 58$ isotopes needs to be investigated further, although it provides an indication of changes in the nuclear shape or an increase of γ-softness.

In the present study, nuclear shapes in neutron-rich midshell nuclei with $A \sim 160$ were investigated. Maximums of deformation or neutron shell gaps around $N = 100$ are expected to be responsible for the sub peak around $A = 160$ in the *r*-process abundance (see Section 1.5). As indicated in Figure 5.2 to Figure 5.4, $N \sim 100$ nuclei have large deformation but the locations of maximum deformation depend on the proton number. The shell gap at $N = 100$ probably plays an important role in the *r*-process abundance peak at $A \sim 160$. Further theoretical and experimental investigation on $N = 100$ isotones with $Z < 60$ is required for more precise calculations of *r*-process abundances. Octupole deformation is also expected to be significant in $Z < 60$ nuclei and further studies of such higher-order deformations is also important.

The discussions given in the present work were based on the systematics of excitation energies. The excitation energies of rotational bands provide moments of inertia and the energies of quasi-particle isomers provide information on single particle levels. In turn, information on nuclear deformation can be extracted from those quantities; however, this is not an exclusive way to measure quadrupole, octupole and hexadecupole deformations. In order to obtain the quadrupole deformation of the ground state, a lifetime measurement of the first 2^+ state is one possibility. The β_2 can be obtained from the half-life by the following equation,

$$B(\mathrm{E2}; 2^+ \rightarrow 0^+) = \frac{1}{5}\left\{\frac{3}{4\pi} ZeR^2\right\}^2 \beta_2^2. \tag{5.4}$$

In the RIBF-86 experiment, 18 $LaBr_3$ detectors were installed for lifetime measurements of first 2^+ states with sub-nanosecond half-lives. However, the detection efficiencies of the $2^+ \rightarrow 0^+$ transitions in the neutron-rich midshell nuclei, which have energies as low as ~60 keV, was

very low due to absorption by other materials. It is, therefore, advantageous to reduce the absorption by changing the geometrical arrangements of the active stopper, chamber window and $LaBr_3$ detectors to reduce the substantial thickness of material along the paths of the γ rays.

In stable nuclei, octupole and hexadecupole moments have been deduced from reduced transition probabilities of E3 and E4 transitions by Coulomb excitation (138Ba [11], 152Sm [12]). Application of Coulomb excitation technique to unstable nuclei is necessary for the next step of the study of higher-order deformation.

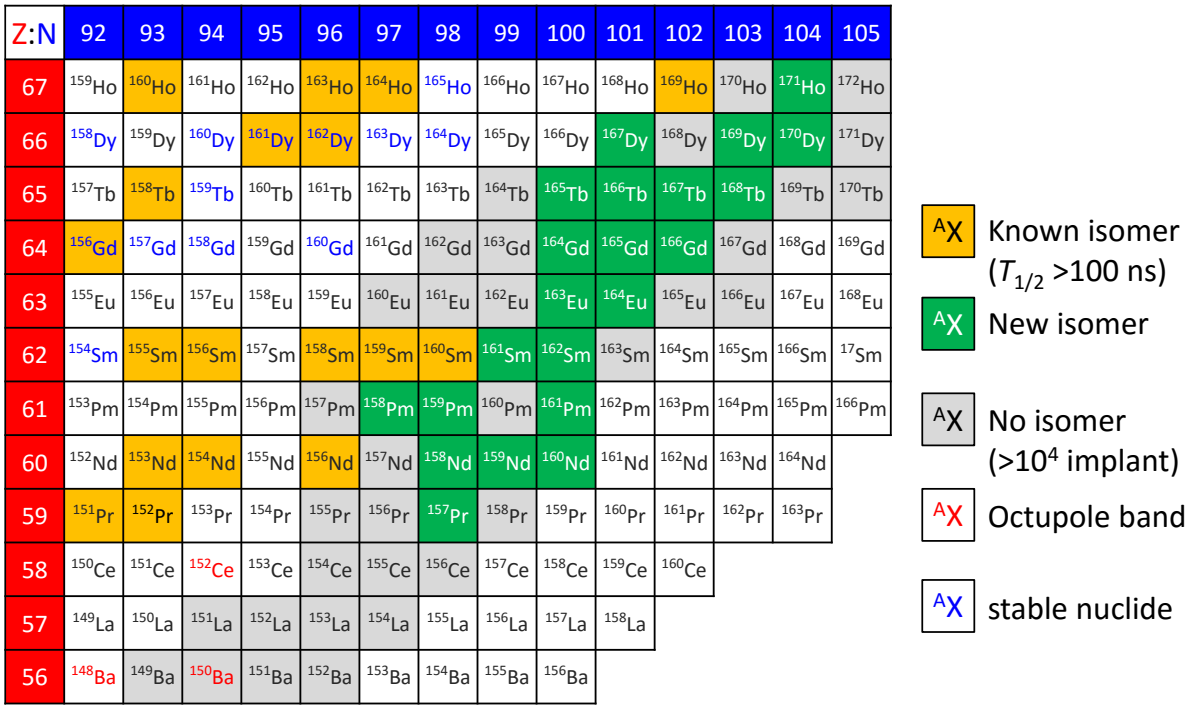

Figure 5.18 A part of the chart of nuclides showing disappearance of isomers in $Z < 58$ nuclei. The nuclides colored in green have isomers newly observed in this work. The nuclides colored in orange have known isomers and those with red character shows that an octupole band is observed in the nuclide.

Table 5.3 Tentative ratio of estimated number of isomers to the number of implanted ions for four nuclides with new isomers.

Nuclide	$\frac{N_\gamma}{\varepsilon_\gamma \exp(-t_{flight}/\tau)} / N_{implant}$
^{158}Nd	2.4×10^{-2}
^{160}Nd	2.0×10^{-1}
^{162}Sm	2.3×10^{-2}
^{164}Gd	2.0×10^{-2}

Chapter 6 Conclusion

Nuclear shape evolution in neutron-rich midshell nuclei with $A \sim 160$ was investigated using systematic measurements of excited states that were identified via isomer and β-γ spectroscopy. Neutron-rich nuclei were produced from in-flight fission of ^{238}U projectiles with the energy of 345 MeV/nucleon at the RIKEN Radioactive Isotope Beam Factory. The secondary beam was separated and identified using the BigRIPS beam line. Experiments were performed using two different detector setups. The first one was an isomer search in the midshell region with 4-clover type HP-Ge detectors. In the second experiment, an active stopper, WAS3ABi, was introduced in order to enable β-γ spectroscopy in addition to isomer measurements. An array of 12 EUROBALL cluster Ge detectors, EURICA, was installed to improve the γ-ray detection efficiency. The latter experiment focused on more neutron-rich nuclei with lower atomic numbers compared to the earlier one.

23 new isomers were observed in neutron-rich midshell nuclei with $59 \leq Z \leq 67$. $K^{\pi} = 4^{-}$ isomers were systematically observed in $N = 100$ isotones. $K^{\pi} = 6^{-}$ isomers were observed in $N = 98$ Pm and Nd isotones. Isomers with one-proton quasi-particle excitations were observed systematically in $100 \leq N \leq 104$ Tb isotopes. Excitation of the ground-state band were identified for the first time in ^{157}Pm, ^{154}Ce and ^{150}Ba using β-γ spectroscopy. A candidate for a negative-parity state of an octupole band was observed at 697 keV in ^{150}Ba, the most neutron-rich Ba isotope measured to date.

From the systematics of all the results, experimental indications of octupole and hexadecupole deformations have been revealed. The increase in excitation energy of the $K^{\pi} = 4^{-}$ isomers in $N = 100$ isotones, and the change of isomer configuration from $K^{\pi} = 5^{-}$ to 6^{-} in $N = 98$ isotones from Sm to Nd, can be explained by assuming large hexadecupole deformation in Nd isotopes. Self-consistent RPA calculations predict $J^{\pi} = 3^{-}$ states with octupole collectivity at excitation energies below 1 MeV. The excited state in ^{150}Ba observed in the present work provides a candidate for a state that exhibits octupole deformation, and may suggest that octupole collectivity remains also at $N = 94$. From the systematics of the moment of inertia obtained from the excitation energies of ground-state bands, Nd isotopes ($Z = 60$) appear to have the largest quadrupole deformation, which is not consistent with theoretical predictions. A local minimum in the moment of inertia exists at $N = 100$ in $62 \leq Z \leq 66$ isotopes, which was discussed to be an indication of the new deformed shell gap predicted at $N = 100$. However, this characteristic was not observed in Nd ($Z = 60$) and Pm ($Z = 61$) isotopes, in contrast to the predictions, which could be due to large hexadecupole deformation in Nd isotopes. These results may, therefore, indicate new phenomena in neutron-rich nuclei that is not included in current theoretical calculations.

The present study provides experimental indications of significant hexadecupole deformation in Nd and octupole collectivity in Ba isotopes with $N \sim 100$. Moreover, it highlights the

importance of further theoretical and experimental studies of higher-order deformations, namely as hexadecupole and octupole deformation. The new results on $N = 100$ nuclei will also provide important input for more precise calculations aiming to reproduce the $A \sim 160$ *r*-process elemental abundance peak. The next step of this study is to further improve experimental setups to measure the lifetimes of the excited states for more direct measurements of β_2. Furthermore, application of the Coulomb excitation technique to unstable nuclei will provide more exclusive information on higher-order deformations over a wide range of neutron and proton numbers. Such studies will enrich our understanding of how the shell effect drives macroscopic shapes at different proton and neutron numbers, including higher-order deformations.

Appendix

Appendix A. Asymptotic quantum numbers and Nilsson diagram

In a nucleus with axial symmetric shape such as quadrupole deformed nuclei, projection of the total angular momentum on to the symmetry axis is a good quantum number. Figure A.1 shows the quantum angular momenta in an axial deformed nucleus. The total angular momentum, J, is represented by the composition of the orbital angular momentum (I) and the intrinsic spin (s) of nucleons and the angular momentum of the rotational motion of the hole nucleus (R). The projection of l, s, $l+s$, and J on to the symmetry axis are defined as Λ, Σ, Ω, and K, respectively. In quadrupole deformed nuclei, motion of the nucleons can be expressed independently by one along the symmetry axis (z-axis) and the other on the plane perpendicular to the z-axis. Energies assuming harmonic potential are written as,

$$E = \left(n_z + \frac{1}{2}\right)\hbar\omega_z + (n_\perp + 1)\hbar\omega_\perp. \tag{A.1}$$

The subscripts, z and $\perp$ show the component along symmetry axis and that perpendicular to the z-axis respectively. In the case of harmonic potential, energy levels only depend on $[n_z, n_\perp]$. When $N = n_z + n_\perp$ and $\omega_0 = \omega_z\omega_\perp^2$ are defined from volume conservation, and $\varepsilon = (\omega_\perp - \omega_z)/\omega_0$ (A.1) can be written as,

$$E = \hbar\omega_0\left(N + \frac{3}{2} + (n_\perp - 2n_z)\frac{\varepsilon}{3}\right). \tag{A.2}$$

ε corresponds to deformation parameter and positive value means prolate deformation and negative value does oblate shape. Equation (A.2) shows that single-particle levels with large n_z are downsloping with increase of prolate deformation and those with small n_z are upsloping. The single particle orbitals with different deformations are first given by Nilsson [23] and a plot of the single particle energies of the orbitals as a function of deformation parameter is called Nilsson diagram.

The levels with same $[n_z, n_\perp]$ are degenerated by different Λ as,

$$\Lambda = \pm n_\perp, \pm(n_\perp - 2), \ldots, \pm 1 \text{ or } 0. \tag{A.3}$$

In more realistic potential such as Woods-Saxon potential, the degeneration will be resolved. A state with same $[n_z, n_\perp, \Lambda]$ will be resolved even more by adding spin-orbital interaction as,

$$\Omega = \Lambda \pm \Sigma. \tag{A.4}$$

Therefore, orbitals in an axial deformed nucleus in a realistic potential can be written with four asymptotic quantum numbers, $[n_z, n_\perp, \Lambda, \Omega]$. In this thesis, Nilsson orbitals are written by the expression, $\Omega[Nn_z\Lambda]$. The Nilsson diagram for the $82 \le N \le 126$, $50 \le Z \le 82$ midshell are show in Figure A.2 and Figure A.3.

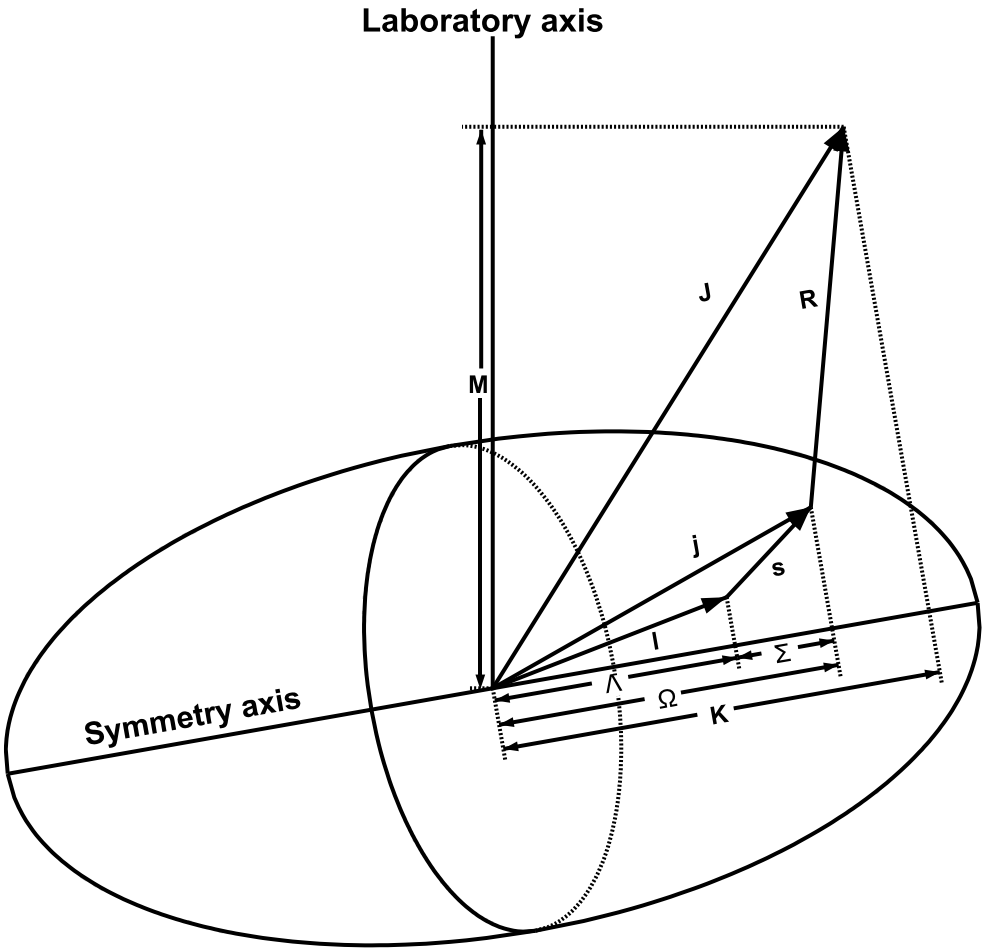

Figure A.1 asymptotic quantum numbers in axial deformed nuclei.

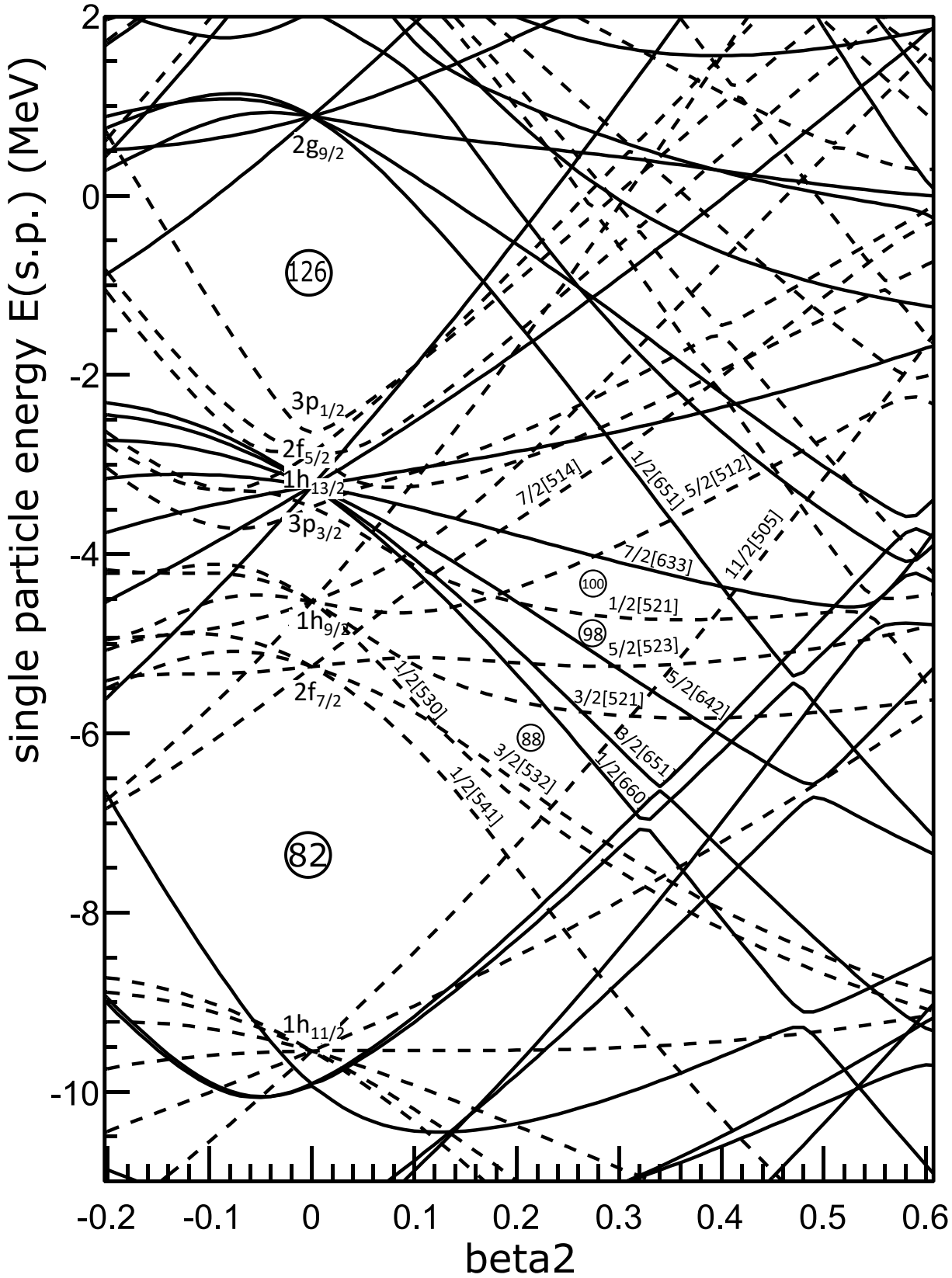

Figure A.2 Nilsson diagram for neutrons, midshell $82 \leq N \leq 126$ $(\beta_4 = 0.16\beta_2^2)$ calculated by [35]

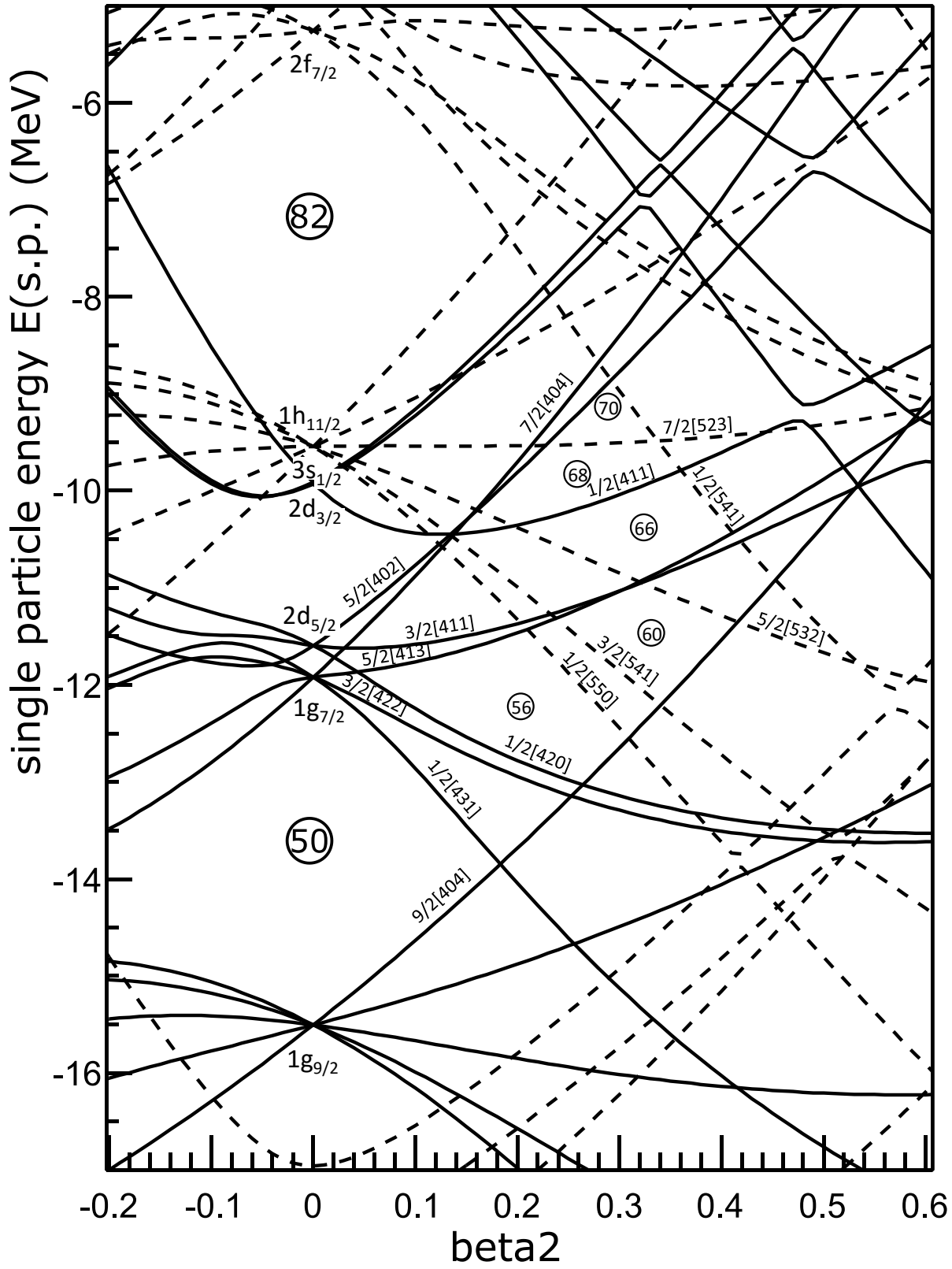

Figure A.3 Nilsson diagram for neutrons, midshell $50 \leq Z \leq 82$ $(\beta_4 = 0.16\beta_2^2)$ calculated by [35]

Appendix B. Weisskopf transition probability and hindrance of K-isomer

An estimation of transition probabilities of γ decays are given by Weisskopf [105]. Table B.1 shows the Weisskopf estimation for different transition types as a function of γ-ray energy and mass number of the nucleus. The ratio of the Weisskopf half-life and experimental one is called as "reduced transition probability". The Weisskopf estimation based on the assumption that only a single particle transition takes place. Therefore, the reduced transition probability corresponds to the number of particles contributed in the transition. In this thesis, reduced transition probability is defined as follows.

$$B(W.u.) = \frac{T_{1/2}(W.u.)}{T_{1/2}(exp.)} \tag{B.1}$$

If $B(W.u.)$ is large, the excitation is expected to have some collectivity. If $B(W.u.)$ is small, it is expected that a large difference of the configuration, the shape, or something between the initial and the final states hinders the transition. In such cases, the inverse of reduced transition probability is often used. This is called "hindrance factor", which is written as,

$$F_w = \frac{T_{1/2}(exp.)}{T_{1/2}(W.u.)}. \tag{B.2}$$

For K-isomers, an empirical formula of the hindrance factor is given by Rusinov [106], which is,

$$\log F_w = 2(|\Delta K| - L). \tag{B.3}$$

The order of the hindrance factor can be estimated from the difference of the K quantum number ΔK and the multiplicity L. This empirical rule was examined by Löbner [107] and there he mentioned that the hindrance factor is 10^2 times larger in the case of E1 transition. Recently, more precise empirical rule was given by F. G. Kondev *et al.* [97] for high-*K* isomers in deformed nuclei with $A > 100$, which is,

$$\log F_w = \log F_0 + (|\Delta K| - L)\log f_0. \tag{B.4}$$

The parameters F_0 and f_0 was obtained by fitting known *K* isomers with various ΔK values. The list of these parameters for E1, M1 and E2 transitions are shown in Table B.2.

The Weisskopf estimate is also used to limit possible transition type of unknown decays. Upper limits of reduced transition probability for $A > 150$ nuclei are given by Martin [108], which is shown in Table B.3.

Table B.1 Estimation of single particle transition half-lives by Weisskopf

Electric	$T_{1/2}$ (s)	Magnetic	$T_{1/2}$ (s)
E1	$\frac{6.76 \times 10^{-6}}{E_\gamma^3 A^{2/3}}$	M1	$\frac{2.20 \times 10^{-5}}{E_\gamma^3}$

E2	$\frac{9.52 \times 10^{6}}{E_{\gamma}^{5} A^{4/3}}$	M2	$\frac{3.10 \times 10^{7}}{E_{\gamma}^{5} A^{2/3}}$
E3	$\frac{9.52 \times 10^{19}}{E_{\gamma}^{7} A^{2}}$	M3	$\frac{6.66 \times 10^{19}}{E_{\gamma}^{7} A^{4/3}}$
E4	$\frac{6.50 \times 10^{31}}{E_{\gamma}^{9} A^{8/3}}$	M4	$\frac{2.12 \times 10^{32}}{E_{\gamma}^{9} A^{2}}$

Table B.2 Fit parameters of the empirical rule of K hindrance given by F. D. Kondev *et al.* [97]

σλ	F_0	f_0
E1	$1.0^{+37}_{-8} \times 10^{5}$	12.5^{+124}_{-62}
M1	$1.7^{+55}_{-3} \times 10^{3}$	6.7^{+65}_{-33}
E2	$1.2^{+17}_{-7} \times 10^{2}$	3.2^{+28}_{-15}

Table B.3 Recommended upper limits of reduced transition probability for $A > 150$ nuclei.

Electric	$B(W.u.)$	Magnetic	$B(W.u.)$
E1	0.01	M1	2
E2	1000	M2	1
E3	100	M3	10
E4		M4	10

Appendix C. Energy and timing spectra of isomers

The delayed γ-ray spectra and the timing spectra of isomers which were not shown in Chapter 4 are listed in the following subsections.

C.1 ^{171}Ho ($Z = 67,\ N = 94$)

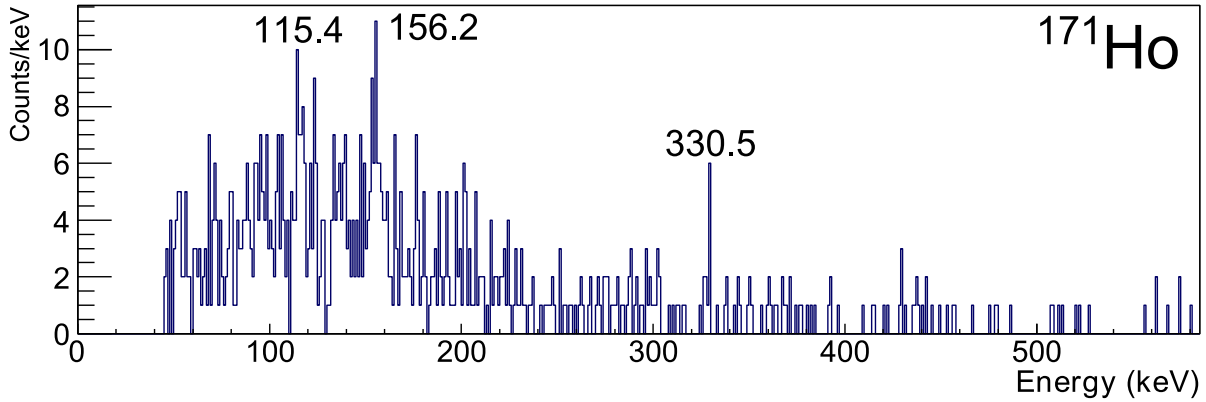

Figure C.1 Energy spectrum of delayed γ rays from ^{171}Ho.

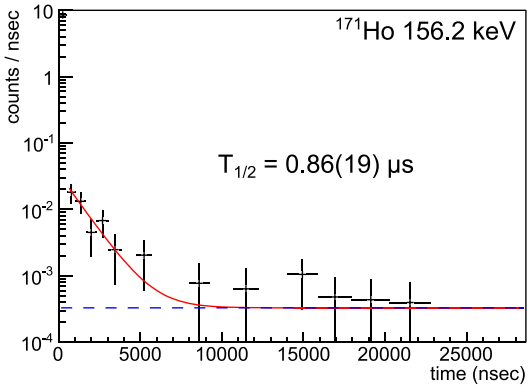

Figure C.2 Time spectra gated on the peaks of delayed γ rays from ^{171}Ho.

C.2 ^{167}Dy ($Z = 66,\ N = 101$)

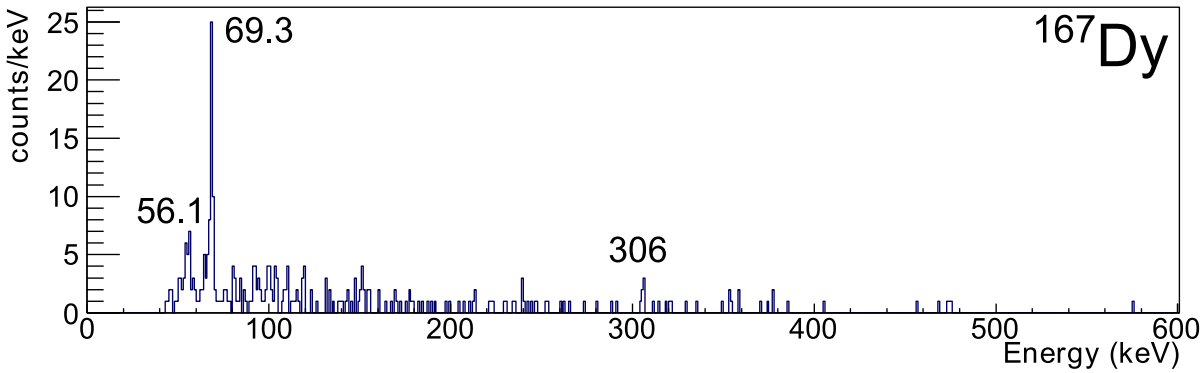

Figure C.3 Energy spectrum of delayed γ rays from ^{167}Dy.

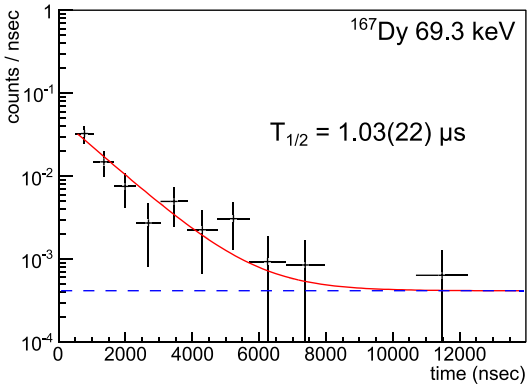

Figure C.4 Time spectra gated on the peaks of delayed γ rays from ^{167}Dy.

C.3 ^{169}Dy ($Z = 66,\ N = 103$)

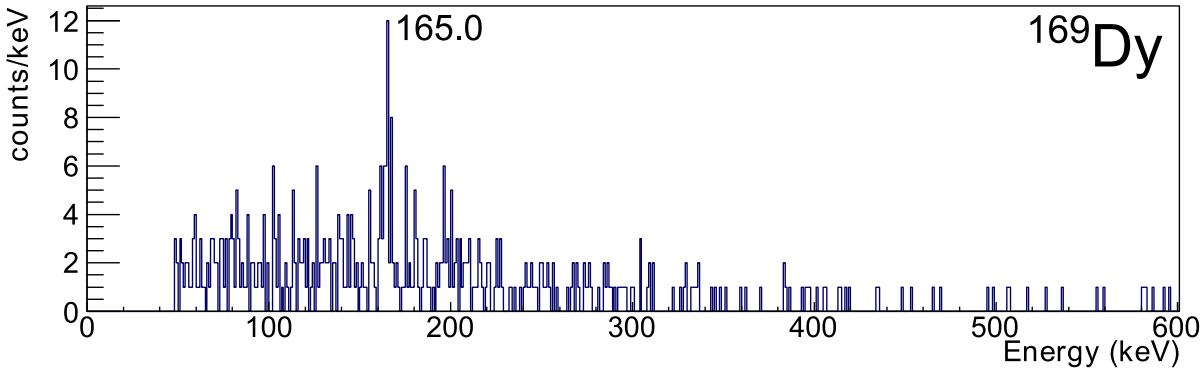

Figure C.5 Energy spectrum of delayed γ rays from ^{169}Dy.

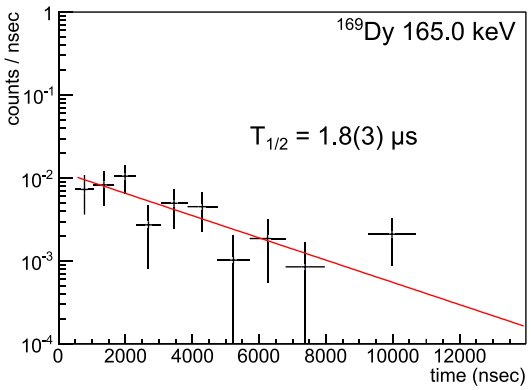

Figure C.6 Time spectra gated on the peaks of delayed γ rays from ^{169}Dy.

C.4 ^{170}Dy ($Z = 66,\ N = 104$)

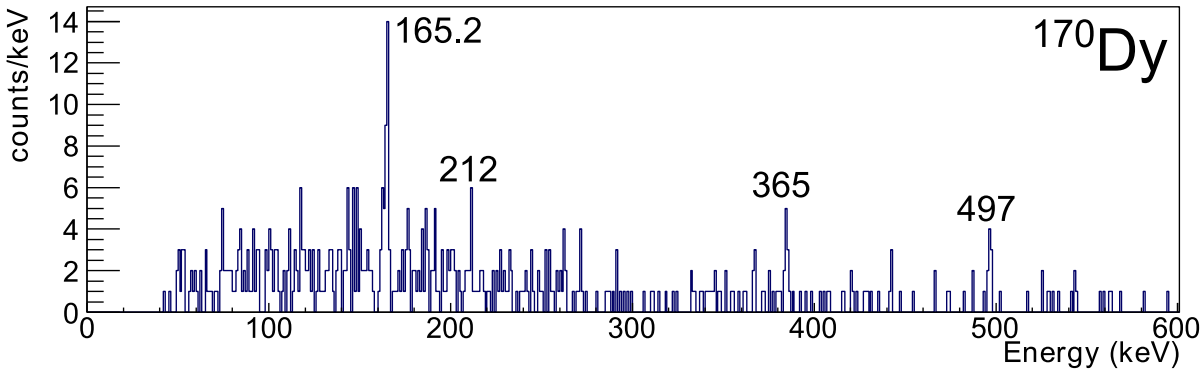

Figure C.7 Energy spectrum of delayed γ rays from ^{170}Dy.

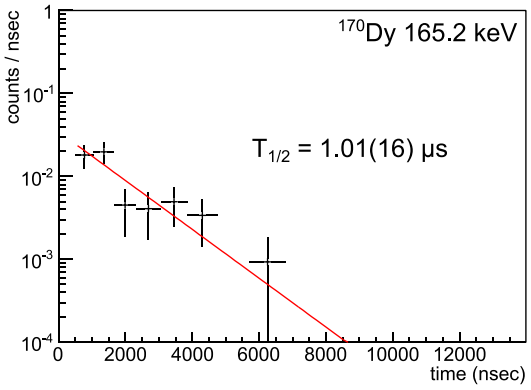

Figure C.8 Time spectra gated on the peaks of delayed γ rays from ^{170}Dy.

C.5 ^{162}Gd ($Z = 64,\ N = 98$)

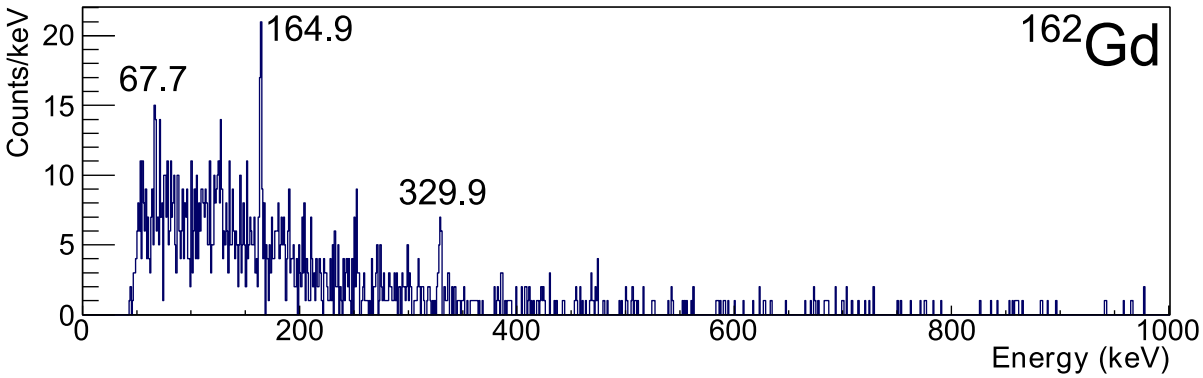

Figure C.9 Energy spectrum of delayed γ rays from ^{162}Gd.

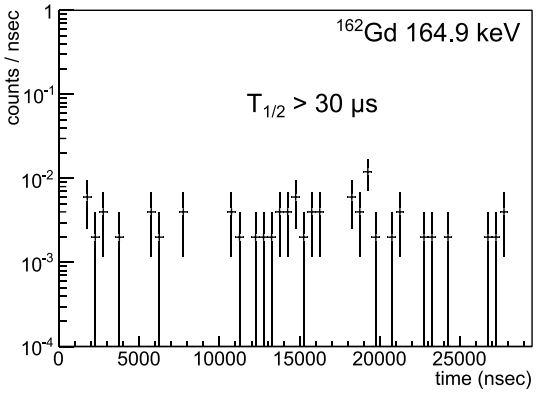

Figure C.10 Time spectra gated on the peaks of delayed γ rays from ^{162}Gd.

C.6 ^{165}Gd ($Z = 64,\ N = 101$)

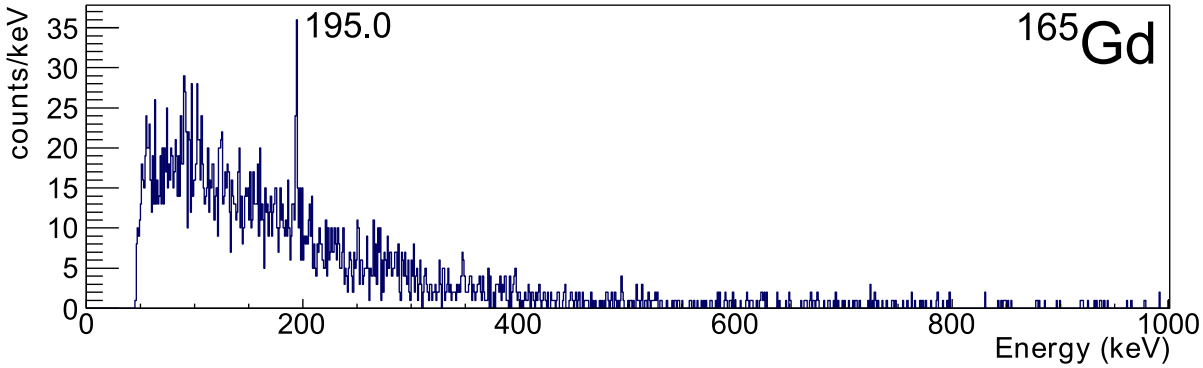

Figure C.11 Energy spectrum of delayed γ rays from ^{165}Gd.

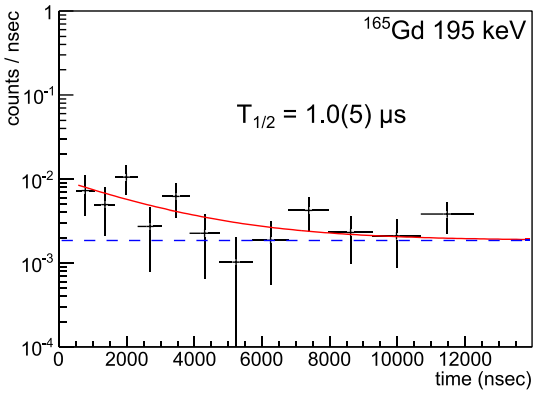

Figure C.12 Time spectra gated on the peaks of delayed γ rays from ^{165}Gd.

C.7 ^{166}Gd ($Z = 64,\ N = 102$)

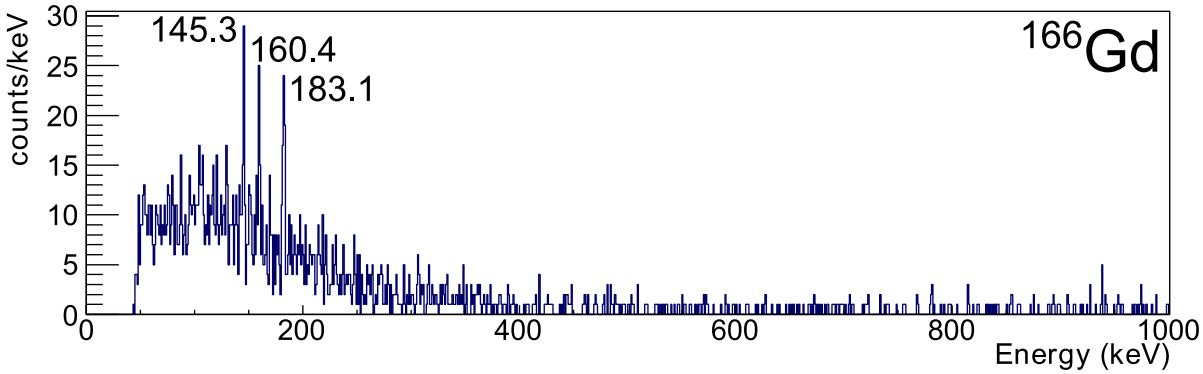

Figure C.13 Energy spectrum of delayed γ rays from ^{166}Gd.

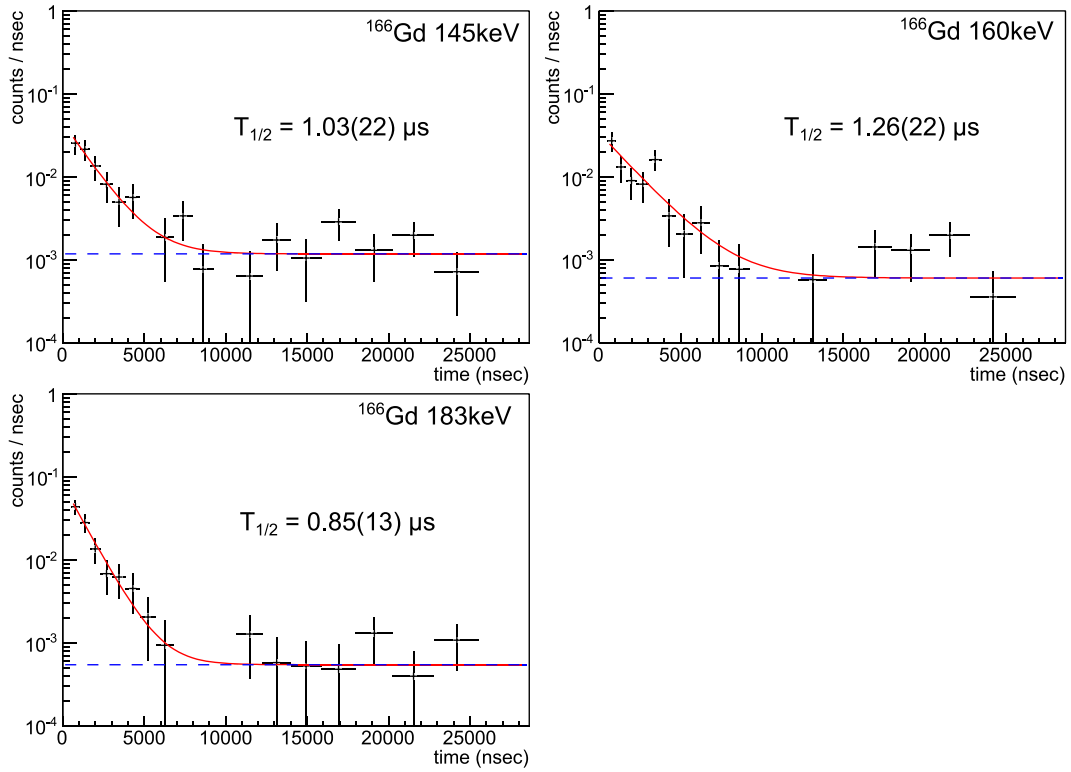

Figure C.14 Time spectra gated on the peaks of delayed γ rays from ^{166}Gd.

C.8 ^{164}Eu ($Z = 63,\ N = 101$)

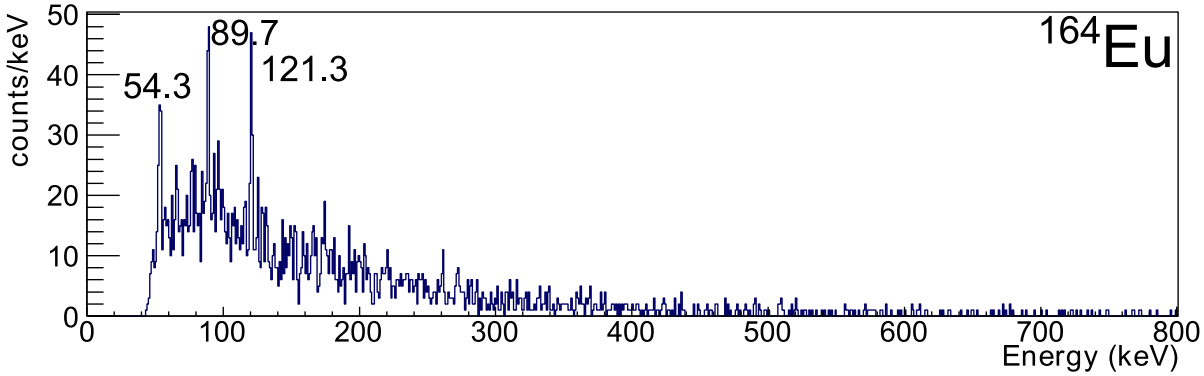

Figure C.15 Energy spectrum of delayed γ rays from ^{164}Eu.

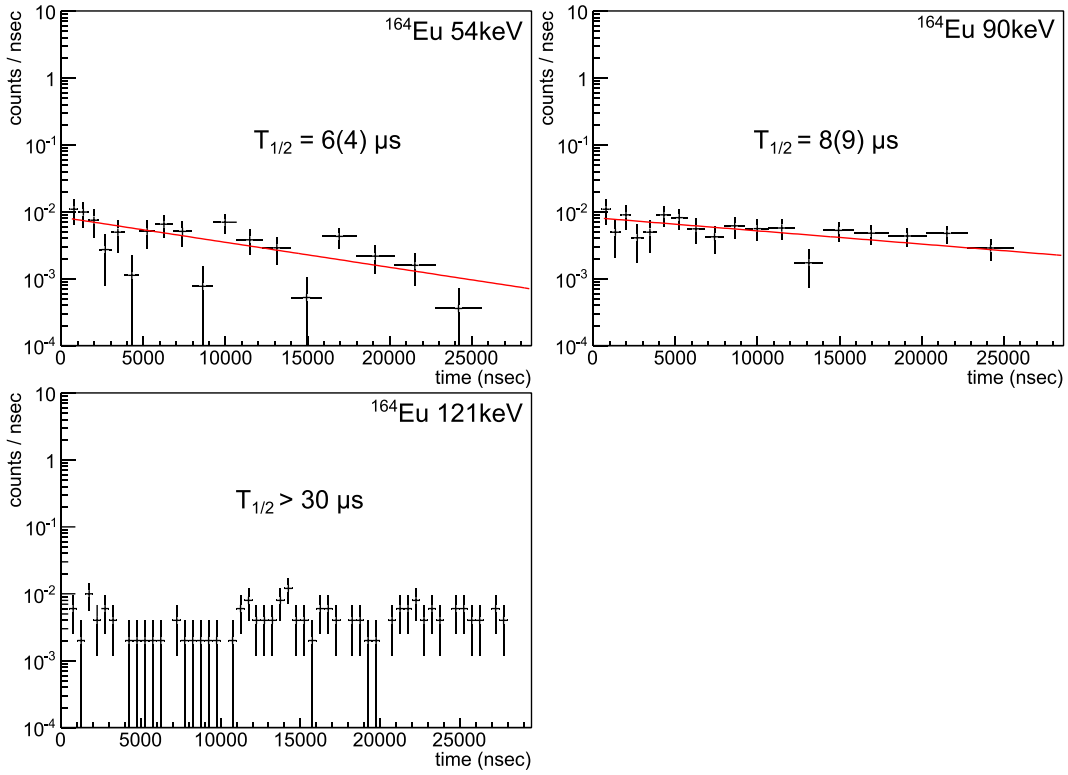

Figure C.16 Time spectra gated on the peaks of delayed γ rays from ^{164}Eu.

C.9 ^{161}Sm ($Z = 62,\ N = 99$)

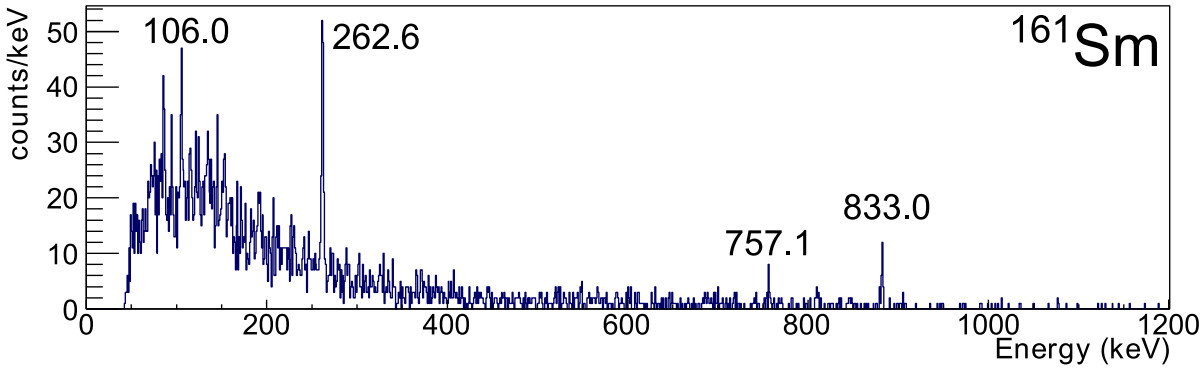

Figure C.17 Energy spectrum of delayed γ rays from ^{161}Sm.

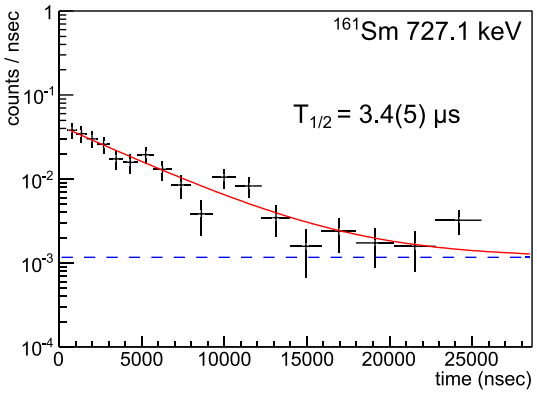

Figure C.18 Time spectra gated on the peaks of delayed γ rays from ^{161}Sm.

C.10 ^{158}Pm ($Z = 61,\ N = 97$)

In this nuclide, one delayed γ ray was observed at 121 keV with the half-life longer than the maximum time window of this measurement, 16 μs. The energy and timing spectra of the delayed γ ray in ^{158}Pm is shown in Figure C.19 and Figure C.20 respectively.

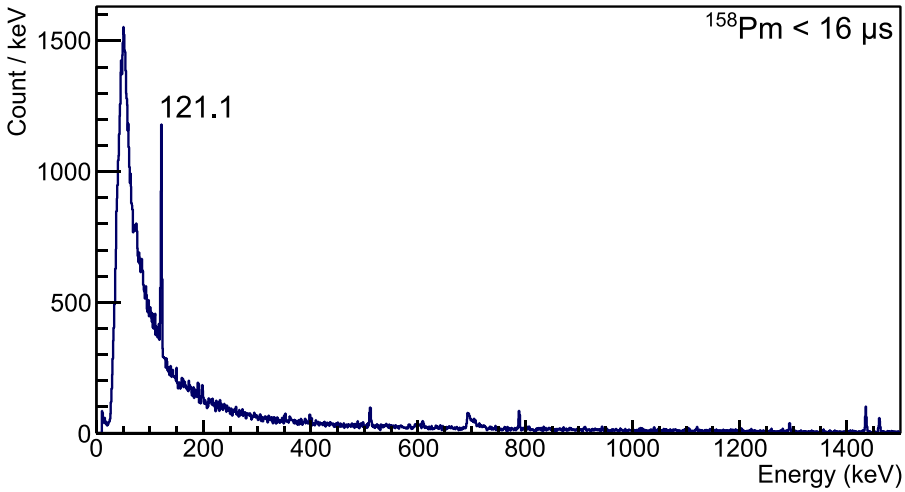

Figure C.19 Energy spectrum of delayed γ rays from ^{158}Pm. The time window is up to 16 μs after the implantation.

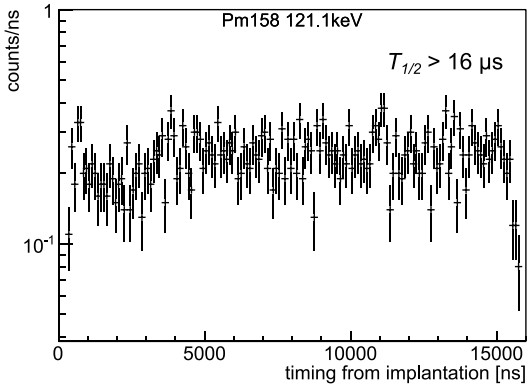

Figure C.20 Time spectra gated on the peaks of delayed γ rays from ^{158}Pm.

C.11 ^{159}Nd ($Z = 60,\ N = 99$)

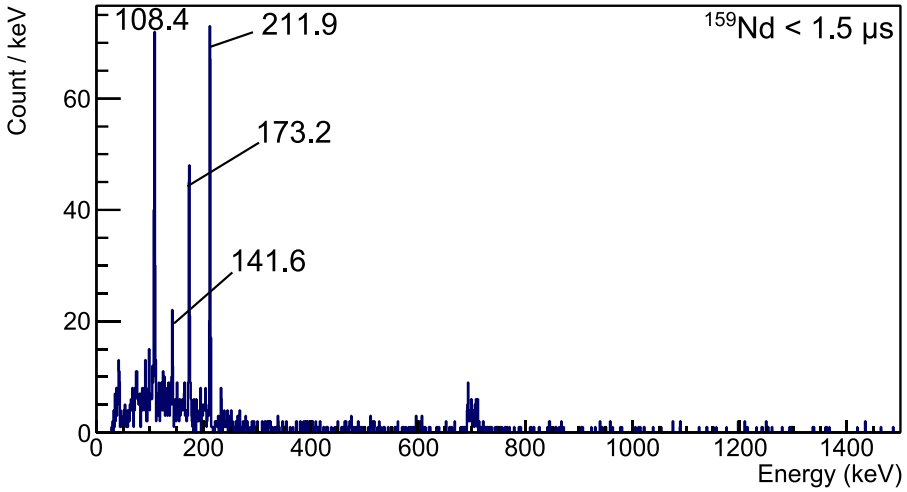

Figure C.21 Energy spectrum of delayed γ rays from ^{159}Nd. The time window is up to 1.5 μs after the implantation.

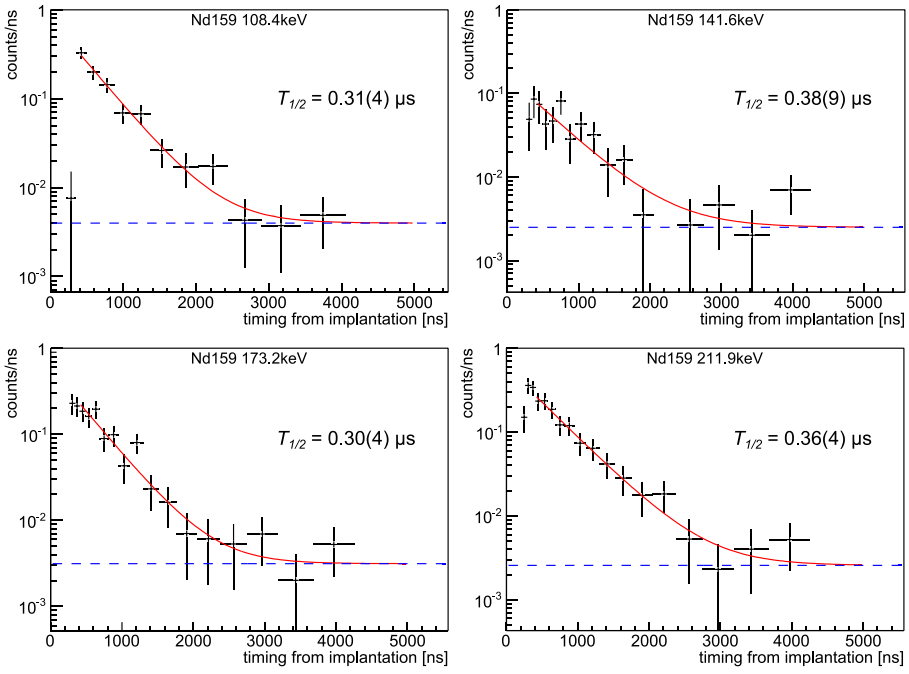

Figure C.22 Time spectra gated on the peaks of delayed γ rays from ^{159}Nd.

Table C.1 List of γ-ray coincidences in the isomeric decay of ^{159}Nd. Coincident γ rays are marked by ticks. The ticks with parenthesis indicate that there were some coincident events but the statistics was not sufficient to say it was significant.

Energy (keV)	108	141	173	212
108	gate	(✔)	(✔)	✔
141	(✔)	gate		
173	(✔)		gate	
212	✔			gate

C.12 ^{157}Pr ($Z = 59,\ N = 98$)

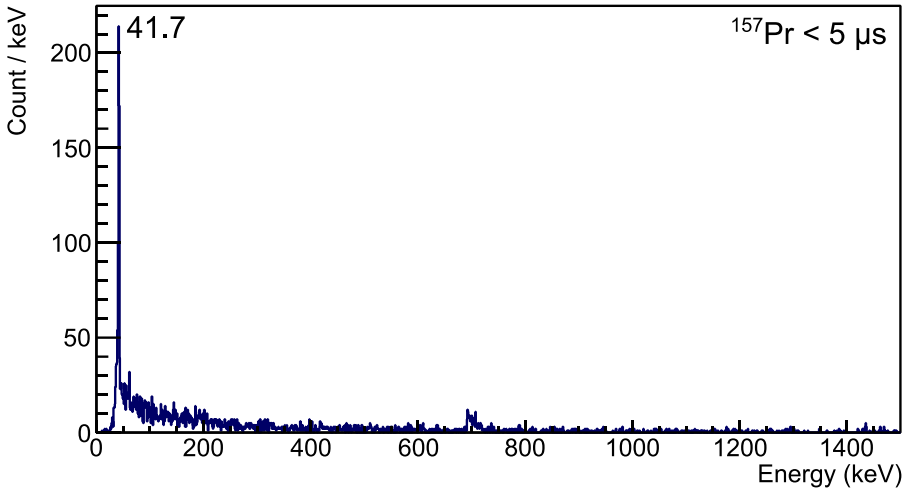

Figure C.23 Energy spectrum of delayed γ rays from ^{157}Pr. The time window is up to 5 μs after the implantation.

Reference

[1] S. Hilaire and M. Girod, Eur. Phys. J. A **33**, 237 (2007).

[2] M. G. Mayer, Phys. Rev. **75**, 1969 (1949).

[3] O. Haxel, J. H. D. Jensen, and H. E. Suess, Phys. Rev. **75**, 1766 (1949).

[4] H. Iwasaki, T. Motobayashi, H. Akiyoshi, Y. Ando, N. Fukuda, H. Fujiwara, Z. Fülöp, K. I. Hahn, Y. Higurashi, M. Hirai, I. Hisanaga, N. Iwasa, T. Kijima, A. Mengoni, T. Minemura, T. Nakamura, M. Notani, S. Ozawa, H. Sagawa, H. Sakurai, S. Shimoura, S. Takeuchi, T. Teranishi, Y. Yanagisawa, and M. Ishihara, Phys. Lett. B **491**, 8 (2000).

[5] H. Simon, D. Aleksandrov, T. Aumann, L. Axelsson, T. Baumann, M. J. G. Borge, L. V Chulkov, R. Collatz, J. Cub, W. Dostal, B. Eberlein, T. W. Elze, H. Emling, H. Geissel, A. Grünschloss, M. Hellström, J. Holeczek, R. Holzmann, B. Jonson, J. V Kratz, G. Kraus, R. Kulessa, Y. Leifels, A. Leistenschneider, T. Leth, I. Mukha, G. Münzenberg, F. Nickel, T. Nilsson, G. Nyman, B. Petersen, M. Pfützner, O. Tengblad, and M. V Zhukov, Phys. Rev. Lett. **83**, 1 (1999).

[6] D. Guillemaud-Mueller, C. Detraz, M. Langevin, and F. Naulin, Nucl. Phys. A **426**, 37 (1984).

[7] T. Motobayashi, Y. Ikeda, K. Ieki, M. Inoue, N. Iwasa, T. Kikuchi, M. Kurokawa, S. Moriya, S. Ogawa, H. Murakami, S. Shimoura, Y. Yanagisawa, T. Nakamura, Y. Watanabe, M. Ishihara, T. Teranishi, H. Okuno, and R. F. Casten, Phys. Lett. B **346**, 9 (1995).

[8] A. Ozawa, T. Kobayashi, T. Suzuki, K. Yoshida, and I. Tanihata, Phys. Rev. Lett. **84**, 5493 (2000).

[9] D. Steppenbeck, S. Takeuchi, N. Aoi, P. Doornenbal, M. Matsushita, H. Wang, H. Baba, N. Fukuda, S. Go, M. Honma, J. Lee, K. Matsui, S. Michimasa, T. Motobayashi, D. Nishimura, T. Otsuka, H. Sakurai, Y. Shiga, P. Söderström, T. Sumikama, H. Suzuki, R. Taniuchi, Y. Utsuno, J. J. Valiente-Dobón, and K. Yoneda, Nature **502**, 207 (2013).

[10] L. Satpathy and S. K. Patra, J. Phys. G Nucl. Part. Phys. **30**, 771 (2004).

[11] S. M. Burnett, A. M. Baxter, S. Hinds, F. Pribac, R. H. Spear, and W. J. Vermeer, Nucl. Phys. A **432**, 514 (1985).

[12] F. S. Stephens, R. M. Diamond, N. K. Glendenning, and J. de Boer, Phys. Rev. Lett. **24**, 1137 (1970).

[13] Z. Patel, P.-A. Söderström, Z. Podolyák, P. H. Regan, P. M. Walker, H. Watanabe, E. Ideguchi, G. S. Simpson, H. L. Liu, S. Nishimura, Q. Wu, F. R. Xu, F. Browne, P. Doornenbal, G. Lorusso, S. Rice, L. Sinclair, T. Sumikama, J. Wu, Z. Y. Xu, N. Aoi, H. Baba, F. L. Bello Garrote, G. Benzoni, R. Daido, Y. Fang, N. Fukuda, G. Gey, S. Go, A. Gottardo, N. Inabe, T. Isobe, D. Kameda, K. Kobayashi, M. Kobayashi, T. Komatsubara, I. Kojouharov, T. Kubo, N. Kurz, I. Kuti, Z. Li, M. Matsushita, S. Michimasa, C.-B. Moon, H. Nishibata, I. Nishizuka, A. Odahara, E. Şahin, H. Sakurai, H. Schaffner, H. Suzuki, H. Takeda, M. Tanaka, J. Taprogge, Z. Vajta, A. Yagi, and R. Yokoyama, Phys. Rev. Lett. **113**, 262502 (2014).

[14] P. Möller, J. R. Nix, W. D. Myers, and W. J. Swiatecki, At. Data Nucl. Data Tables **59**,

185 (1995).

[15] H. T. S. Schüler, Zeitschrift Für Phys. **457**, 457 (1935).

[16] M. Goldhaber and A. W. Sunyar, Phys. Rev. **83**, 906 (1951).

[17] A. Bohr and B. R. Mottelson, Phys. Rev. **90**, 717 (1953).

[18] C. F. v. Weizsäcker, Zeitschrift Für Phys. **96**, 431 (1935).

[19] H. A. Bethe and R. F. Bacher, Rev. Mod. Phys. **8**, 82 (1936).

[20] G. A. Lalazissis, S. Raman, and P. Ring, **71**, 1 (1999).

[21] S. Goriely, F. Tondeur, and J. M. Pearson, At. Data Nucl. Data Tables **77**, 311 (2001).

[22] R. F. Casten, D. D. Warner, D. S. Brenner, and R. L. Gill, Phys. Rev. Lett. **47**, 1433 (1981).

[23] S. G. Nilsson, Det K. Danske Vidensk. Selsk. Mat. Meddelelser **29**, (1955).

[24] G. D. Dracoulis, Nucl. Phys. A **752**, 213 (2005).

[25] G. S. Simpson, W. Urban, J. Genevey, R. Orlandi, J. A. Pinston, A. Scherillo, a. G. Smith, J. F. Smith, I. Ahmad, and J. P. Greene, Phys. Rev. C **80**, (2009).

[26] P. M. Walker, W. H. Bentley, S. R. Faber, R. M. Ronningen, R. B. Firestone, F. M. Bernthal, J. Borggreen, J. Pedersen, and G. Sletten, Nucl. Phys. A **365**, 61 (1981).

[27] C. Y. Wu, D. Cline, M. W. Simon, R. Teng, M. P. Carpenter, R. V. F. Janssens, and I. Wiedenhöver, Phys. Rev. C **68**, 1 (2003).

[28] W. C. Griffith, M. D. Swallows, T. H. Loftus, M. V. Romalis, B. R. Heckel, and E. N. Fortson, Phys. Rev. Lett. **102**, 1 (2009).

[29] J. Dobaczewski and J. Engel, Phys. Rev. Lett. **94**, 1 (2005).

[30] L. P. Gaffney, P. A. Butler, M. Scheck, A. B. Hayes, F. Wenander, M. Albers, B. Bastin, C. Bauer, A. Blazhev, S. Bönig, N. Bree, J. Cederkäll, T. Chupp, D. Cline, T. E. Cocolios, T. Davinson, H. De Witte, J. Diriken, T. Grahn, A. Herzan, M. Huyse, D. G. Jenkins, D. T. Joss, N. Kesteloot, J. Konki, M. Kowalczyk, T. Kröll, E. Kwan, R. Lutter, K. Moschner, P. Napiorkowski, J. Pakarinen, M. Pfeiffer, D. Radeck, P. Reiter, K. Reynders, S. V Rigby, L. M. Robledo, M. Rudigier, S. Sambi, M. Seidlitz, B. Siebeck, T. Stora, P. Thoele, P. Van Duppen, M. J. Vermeulen, M. von Schmid, D. Voulot, N. Warr, K. Wimmer, K. Wrzosek-Lipska, C. Y. Wu, and M. Zielinska, Nature **497**, 199 (2013).

[31] W. Urban, M. A. Jones, J. L. Durell, M. Leddy, W. R. Phillips, A. G. Smith, B. J. Varley, I. Ahmad, L. R. Morss, M. Bentaleb, E. Lubkiewicz, and N. Schulz, Nucl. Phys. A **613**, 107 (1997).

[32] P. A. Butler and W. Nazarewicz, Nucl. Phys. A **533**, 249 (1991).

[33] P. A. Butler and W. Nazarewicz, Rev. Mod. Phys. **68**, 349 (2008).

[34] J. L. Egido and L. M. Robledo, Nucl. Phys. A **545**, 589 (1992).

[35] S. Cwiok, J. Dudek, W. Nazarewicz, J. Skalski, and T. Werner, Comput. Phys. Commun. **46**, 379 (1987).

[36] D. L. Hendrie, N. K. Glendenning, B. G. Harvey, O. N. Jarvis, H. H. Duhm, J. Saudinos, and J. Mahoney, Phys. Lett. B **26**, 127 (1968).

[37] B. S. N. Singh, V. Nanal, and R. G. Pillay, Pramana – J. Physiscs **61**, 507 (2003).

[38] Y. D. Devi and V. K. B. Kota, Pramana – J. Physiscs **39**, 413 (1992).

[39] E. M. Burbidge, G. R. Burbidge, W. A. Fowler, and F. Hoyle, Rev. Mod. Phys. **29**, 547 (1957).

[40] R. Surman, J. Engel, J. Bennett, and B. Meyer, Phys. Rev. Lett. **79**, 1809 (1997).

[41] A. Rath, P. Stevenson, P. Regan, F. Xu, and P. Walker, Phys. Rev. C **68**, 1 (2003).

[42] M. Arnould, S. Goriely, and K. Takahashi, Phys. Rep. **450**, 97 (2007).

[43] S. Shibagaki, T. Kajino, G. J. Mathews, S. Chiba, S. Nishimura, and G. Lorusso, Astrophys. J. **816**, 1 (2015).

[44] S. Goriely, J.-L. Sida, J.-F. Lemaître, S. Panebianco, N. Dubray, S. Hilaire, A. Bauswein, and H.-T. Janka, Phys. Rev. Lett. **111**, 242502 (2013).

[45] D. Patel, A. G. Smith, G. S. Simpson, R. M. Wall, J. F. Smith, O. J. Onakanmi, I. Ahmad, J. P. Greene, M. P. Carpenter, T. Lauritsen, C. J. Lister, R. F. Janssens, F. G. Kondev, D. Seweryniak, B. J. P. Gall, O. Dorveaux, and B. Roux, J. Phys. G Nucl. Part. Phys. **28**, 649 (2002).

[46] S. K. Ghorui, B. B. Sahu, C. R. Praharaj, and S. K. Patra, Phys. Rev. C **85**, 064327 (2012).

[47] M. Wang, G. Audi, A. H. Wapstra, F. G. Kondev, M. MacCormick, X. Xu, and B. Pfeiffer, Chinese Physiscs C **1287**, 1603 (2012).

[48] G. Fioni, H. R. Faust, M. Gross, M. Hesse, P. Armbruster, F. Gönnenwein, and G. Münzenberg, Nucl. Instruments Methods Phys. Res. Sect. A **332**, 175 (1993).

[49] H. L. Ravn, Phys. Rep. **54**, 201 (1979).

[50] A. Shotter, Nucl. Instruments Methods Phys. Res. Sect. B Beam Interact. with Mater. Atoms **204**, 17 (2003).

[51] T. Kubo, Nucl. Instruments Methods Phys. Res. Sect. B Beam Interact. with Mater. Atoms **204**, 97 (2003).

[52] S. Nishimura, G. Lorusso, Z. Xu, J. Wu, R. Gernh, H. S. Jung, Y. K. Kwon, Z. Li, K. Steiger, and H. Sakurai, RIKEN Accel. Prog. Rep. **46**, 182 (2013).

[53] H. Kumagai, A. Ozawa, N. Fukuda, K. Sümmerer, and I. Tanihata, Nucl. Instruments Methods Phys. Res. Sect. A Accel. Spectrometers, Detect. Assoc. Equip. **470**, 562 (2001).

[54] K. Kimura, T. Izumikawa, R. Koyama, T. Ohnishi, T. Ohtsubo, a. Ozawa, W. Shinozaki, T. Suzuki, M. Takahashi, I. Tanihata, T. Yamaguchi, and Y. Yamaguchi, Nucl. Instruments Methods Phys. Res. Sect. A Accel. Spectrometers, Detect. Assoc. Equip. **538**, 608 (2005).

[55] S. Nishimura, Nucl. Phys. News **22**, 38 (2012).

[56] J. Eberth, P. Von Brentano, W. Teichert, H. G. Thomas, A. V. D. Werth, R. M. Lieder, H.

Jäger, H. Kämmerling, D. Kutchin, K. H. Maier, M. Berst, D. Gutknecht, and R. Henck, Prog. Part. Nucl. Phys. **28**, 495 (1992).

[57] E. V. D. Van Loef, P. Dorenbos, C. W. E. Van Eijk, K. W. Krämer, and H. U. Güdel, Nucl. Instruments Methods Phys. Res. Sect. A Accel. Spectrometers, Detect. Assoc. Equip. **486**, 254 (2002).

[58] O. J. Roberts, A. M. Bruce, P. H. Regan, Z. Podolyák, C. M. Townsley, J. F. Smith, K. F. Mulholland, and A. Smith, Nucl. Instruments Methods Phys. Res. Sect. A Accel. Spectrometers, Detect. Assoc. Equip. **748**, 91 (2014).

[59] S. Nishimura, Prog. Theor. Exp. Phys. **2012**, 3C006 (2012).

[60] H. Baba, T. Ichihara, T. Ohnishi, S. Takeuchi, K. Yoshida, Y. Watanabe, S. Ota, and S. Shimoura, RIKEN Accel. Prog. Rep. **43**, 222 (2010).

[61] http://www.xia.com/DGF-4C.html.

[62] Http://www.ces-Swap.com/single-Board-Computers/.

[63] N. Fukuda, T. Kubo, T. Ohnishi, N. Inabe, H. Takeda, D. Kameda, and H. Suzuki, Nucl. Instruments Methods Phys. Res. Sect. B Beam Interact. with Mater. Atoms **317**, 323 (2013).

[64] http://radware.phy.ornl.gov/gf3/.

[65] G. Audi, F. G. Kondev, M. Wang, B. Pfeiffer, X. Sun, J. Blachot, and M. MacCormick, Chinese Phys. C **36**, 1157 (2012).

[66] P. Möller, J. R. Nix, and K.-L. Kratz, At. Data Nucl. Data Tables **66**, 131 (1997).

[67] T. Kibédi, T. W. Burrows, M. B. Trzhaskovskaya, P. M. Davidson, and C. W. Nestor, Nucl. Instruments Methods Phys. Res. Sect. A Accel. Spectrometers, Detect. Assoc. Equip. **589**, 202 (2008).

[68] M. Hellström, H. Mach, B. Fogelberg, D. Jerrestam, and L. Spanier, Phys. Rev. C **43**, 1462 (1991).

[69] E. F. Jones, J. H. Hamilton, P. M. Gore, A. V. Ramayya, J. K. Hwang, and A. P. DeLima, Eur. Phys. J. A **25**, 467 (2005).

[70] G. D. Dracoulis, G. J. Lane, F. G. Kondev, H. Watanabe, D. Seweryniak, S. Zhu, M. P. Carpenter, C. J. Chiara, R. V. F. Janssens, T. Lauritsen, C. J. Lister, E. a. McCutchan, and I. Stefanescu, Phys. Rev. C **81**, 054313 (2010).

[71] G. Audi, O. Bersillon, J. Blachot, and A. H. Wapstra, Nucl. Phys. A **729**, 3 (2003).

[72] D. G. Burke, G. Løvhøiden, and E. R. Flynn, Nucl. Phys. A **318**, 77 (1979).

[73] R. C. Greenwood, R. G. Helmer, M. H. Putnam, and K. D. Watts, Nucl. Instruments Methods Phys. Res. Sect. A Accel. Spectrometers, Detect. Assoc. Equip. **390**, 95 (1997).

[74] R. B. Firestone, *Table of Isotopes Eighth Edition*, eighth edi (John Wiley & Sons, inc., 1996).

[75] G. Winter, L. Funke, K.-H. Kaun, P. Kemnitz, and H. Sodan, Nucl. Phys. A **176**, 609

(1971).

[76] J. Felsteiner and H. Lindeman, Phys. Rev. C **8**, 1929 (1973).

[77] M. Gasser, J. Kern, and O. Huber, Nucl. Phys. A **250**, 106 (1975).

[78] R.J.Gehrke, R.C.Greenwood, J.D.Baker, and D.H.Meikrantz, Radiochim. Acta **31**, 1 (1986).

[79] H.Mach, R.L.Gill, R.F.Casten, A.Piotrowski, A.Wolf, and J.A.Winger, Bull. Am. Phys. Soc. **32**, 1018 (1987).

[80] K. Okano, A. Taniguchi, S. Yamada, T. Sharshar, M. Shibata, and K. Yamauchi, Zeitschrift Für Phys. A **351**, 243 (1995).

[81] P.O.Aronsson, G.Skarnemark, and M.Skarestad, Inorg. Nucl. Chem. Lett. **10**, 499 (1974).

[82] Y. R. Letters, Phys. Rev. C **2**, 2410 (1970).

[83] G. Rudstam, K. Aleklett, and L. Sihver, At. Data Nucl. Data Tables **53**, 1 (1993).

[84] C. Ekström, L. Robertsson, G. Wannberg, and J. Heinemeier, Phys. Scr. **292**, 144 (1977).

[85] Y. Kawase and K. Okano, Zeitschrift Für Phys. A **330**, 231 (1988).

[86] R. C. Greenwood, R. A. Anderl, J. D. Cole, and H. Willmes, Phys. Rev. C **35**, 1965 (1987).

[87] R. A. Anderl, J. D. Cole, R. C. Greenwood, and C. W. Reich, Phys. Rev. C **36**, 1540 (1987).

[88] M. Shibata, O. Suematsu, Y. Kojima, K. Kawade, A. Taniguchi, and Y. Kawase, Eur. Phys. J. A **31**, 171 (2007).

[89] R. A. Y. Gunnink, Phys. Rev. **131**, 301 (1963).

[90] B. Pritychenko, M. Birch, B. Singh, and M. Horoi, At. Data Nucl. Data Tables **107**, 1 (2016).

[91] L. Satpathy and S. K. Patra, Nucl. Phys. A **722**, 24c (2003).

[92] O. E. nuclear structure Database, Http://www.nndc.bnl.gov/ensdf/.

[93] S. RAMAN, C. W. NESTOR, and P. TIKKANEN, At. Data Nucl. Data Tables **78**, 1 (2001).

[94] A. Bohr and B. R. Mottelson, *Nuclear Structure* (Benjamin, New York, 1969).

[95] A. H. Wapstra, G. Audi, and C. Thibault, Nucl. Phys. A **729**, 129 (2003).

[96] G. Audi, A. H. Wapstra, and C. Thibault, Nucl. Phys. A **729**, 337 (2003).

[97] F. G. Kondev, G. D. Dracoulis, and T. Kibédi, At. Data Nucl. Data Tables **103–104**, 50 (2015).

[98] K. Hara and Y. Sun, Int. J. Mod. Phys. **4**, 637 (1995).

[99] Y.-C. Yang, Y. Sun, S.-J. Zhu, M. Guidry, and C.-L. Wu, J. Phys. G Nucl. Part. Phys. **37**, 085110 (2010).

[100] Y. Sun and K. Hara, Comput. Phys. Commun. **104**, 245 (1997).

[101] A. Sobiczewski, Z. Patyk, S. Cwiok, and P. Rozmej, Nucl. Phys. A **485**, 16 (1988).

[102] T. Nakatsukasa, T. Inakura, and K. Yabana, Phys. Rev. C **76**, 024318 (2007).

[103] T. Inakura, T. Nakatsukasa, and K. Yabana, Phys. Rev. C **80**, 044301 (2009).

[104] J. Bartel, P. Quentin, M. Brack, C. Guet, and H.-B. Håkansson, Nucl. Phys. A **386**, 79 (1982).

[105] J. M. Blatt and V. F. Weisskopf, *Theoretical Nuclear Physics* (John Wiley and Sons, 1952).

[106] L. I. Rusinov, Sov. Phys. Uspekhi **4**, 282 (1961).

[107] K. E. G. Lobner, Phys. Lett. **26B**, 369 (1968).

[108] M. J. Martin, Nucl. Data Sheets **74**, ix (1995).

Acknowledgement

I would like to take this opportunity to express my sincere and great appreciations to the people who helped me accomplishing this work. This study was carried out as a collaboration of more than 20 institutes all over the world and many people have been involved to it. I acknowledge that there were also many indirect support from a lot of people. Even though I cannot write all my appreciations for each person here, I would like to thank all the people as much as possible, with my best sincere.

First of all, I would like to express my gratitude to my supervisor, Prof. S. Shimoura, for his instructive advices and patient support throughout the course of study. Five years of the experience studying in his laboratory have provided me chances to learn not only physics but also the way of studying as a researcher.

I would like to express my most sincere and greatest appreciate to Prof. E. Ideguchi, who have taken care of my study directly, throughout my course of study. He provided me many insightful advices from the preparation of experiments to writing the thesis. Without his help, I could not accomplish this work.

I am extremely grateful to all the collaborators of the two experiments: E. Ideguchi, G. Simpson, Mn. Tanaka, S. Nishimura, P. Doornenbal, P.-A. Söderström, G. Lorusso, Z. Y. Xu, J. Wu, T. Sumikama, N. Aoi, H. Baba, F. Bello, F. Browne, R. Daido, Y. Fang, N. Fukuda, G. Gey, S. Go, N. Inabe, T. Isobe, D. Kameda, K. Kobayashi, M. Kobayashi, T. Komatsubara, T. Kubo, I. Kuti, Z. Li, M. Matsushita, S. Michimasa, C.-B. Moon, H. Nishibata, I. Nishizuka, A. Odahara, Z. Patel, S. Rice, E. Sahin, L. Sinclair, H. Suzuki, H. Takeda, J. Taprogge, Zs. Vajta, H. Watanabe and A. Yagi. for RIBF-86 experement, D. Kameda, T. Kubo, N. Inabe, N. Fukuda, H. Takeda, H. Suzuki, K. Yoshida, K. Kusaka, K. Tanaka, Y. Yanagisawa, M. Ohtake, H. Sato, Y. Shimizu, H. Baba, M. Kurokawa, D. Nishimura, T. Ohnishi, N. Iwasa, A. Chiba, T. Yamada, E. Ideguchi, T. Fujii, S. Go, H. Nishibata, K. Ieki, D. Murai, S. Momota, Y. Sato, J. Hwang, S. Kim, O. B. Terasov, D. J. Morrissey, B. M. Sherrill, and G. Simpson for MS-11 experiment. I express my special thanks to Dr. D. Kameda who had taught me a lot about RIBF during MS-11 experiment and also on the data analysis from the beginning. I really appreciate for the many helps by all the other BigRIPS members. I learnt a lot of techniques for experiment and analysis from them. I also express my special thanks to the member of EURICA collaboration, Dr. S. Nishimura, Dr. P. Doornenbal, Dr. P.-A. Söderström, Dr. G. Lorusso, Dr. Z. Y. Xu, Dr. J. Wu, Dr. T. Sumikama and all the others. Without any of their contribution, this study could not be completed. I would like to thank the member of the group of Prof. A. Odahara at Osaka University. Discussions with Mr. H. Nishibata and Ms. A. Yagi were very practical and helped my analysis.

I would like to thank all the present and old members at CNS with whom I spent the daily life of research during my course of study. I had many precious advices and comments from the members of NUSPEQ group, Prof. S. Shimoura, Dr. S. Michimasa, Dr. M. Matsushita, Dr. K. Kisamori, Dr. S. Go, Mr. H. Miya, Mr. M. Takaki, Mr. T. Fujii, Mr. M. Kobayashi, Mr. K. Kobayashi, Mr. Y. Yamaguchi and Mr. S. Masuoka in the weekly meeting. I appreciate

Dr. S. Ota for reviewing this thesis. I also learnt a lot from him especially on data acquisition and programing for data analysis. I would like to thank my room mates and lunch mates at CNS, Dr. K. Kisamori, Mr. Y. Kiyokawa, Mr. Y. Kubota, Mr. M. Kobayashi, Mr. H. Tokieda and many others. I enjoyed daily discussions and talk with them. I express my gratitude to the secretaries in CNS: Ms. Y. Endo, Ms. M. Hirano, Ms. Y. Kishi, Ms. I. Yamamoto, Ms. Y. Soma, Mr. H. Yoshimura and Mr. M. Oki. I am grateful for their daily support to my research activity.

I would like to express my gratitude to Prof. H. Sakurai, who is my co-supervisor as the ALPS (Advanced Leading Graduate Course for Photon Science) program. It was a nice opportunity to have meetings with him every three month during the course, and I have got many precious advices there.

I really appreciate Dr. T. Inakura for the theoretical help for the study of octupole collectivity in neutron-rich Ba isotopes. The discussions with him was fruitful and deepen the understanding of the results.

I also greatly appreciate Dr. D. Steppenbeck for checking my English

At the end, I would like to thank all my friends and family. I appreciate especially my parents, for their encouragement and support over the years of my life.

The ALPS program by the University of Tokyo provided me financial and educational supports during my doctoral course. The last year of this work was supported by KAKENHI 15J10788 as the Grant-in-Aid for JSPS (Japan Society for the Promotion of Science) Fellows.